Datrier, Laurence Élise Hélène (2023) *Exploring the calibration of cosmological probes used in gravitational-wave and multi-messenger astronomy*. PhD thesis.

https://theses.gla.ac.uk/83608/

Exploring the calibration of cosmological probes used in gravitational-wave and multi-messenger astronomy

Laurence Élise Hélène Datrier
B.Sc., M.Sc.

Submitted in fulfilment of the requirements for the
Degree of Doctor of Philosophy

School of Physics and Astronomy
College of Science and Engineering
University of Glasgow

November 2022

Abstract

The field of gravitational wave astronomy has grown remarkably since the first direct detection of gravitational waves on 14th September 2015. The signal, originating from the merger of two black holes, was detected by the two US-based Advanced LIGO interferometers in Hanford (Washington State) and Livingston (Louisiana). The second observing run of the Advanced LIGO and Virgo detectors marked the first detection of a binary neutron star merger, along with its electromagnetic counterparts. The optical follow-up of the merger led to the first confirmed observations of a kilonova, an electromagnetic counterpart to binary neutron star and neutron star-black hole mergers whose existence was first predicted in 1970s. Following the multi-messenger observations of the binary neutron star merger GW170817, constraints were put on the rate of expansion of the Universe using both gravitational wave and electromagnetic data. These measurements could help us understand the current tension between early-Universe and late-Universe measurements of the Hubble constant H_0.

The use of gravitational wave signals for measuring the rate of expansion of the Universe was proposed by Schutz in 1986. Compact binary coalescences can be used as distance markers, a gravitational wave analogue to standard candles: "Standard Sirens". Measurements of the Hubble constant from standard sirens are independent from previous methods of constraining H_0. Bright sirens are gravitational wave signals that are detected coincidentally with electromagnetic signatures. These "bright" gravitational wave sirens are powerful cosmological probes, allowing us to extract information on both the distance and the redshift of the source. It is therefore important to maximise these coincident detections, and to carefully calibrate the data extracted from any standard siren.

The work presented in this thesis can be divided into three main topics, all under the umbrella of maximising scientific returns from observations of compact binary coalescences. These three topics are: kilonova parameter estimation, cosmology with gravitational waves, and calibration of advanced gravitational wave detectors.

We present work on inferring parameters from kilonova light curves. Ejecta parameters and information about the merging time of the progenitor is extracted from simulated kilonova light curves. We explore the consequence of neglecting some aspects of microphysics on the resulting parameter estimation.

We also present new results on the inference of the Hubble constant through the application of a robust test of galaxy catalogue completeness to the current gravitational wave cosmology pipeline. We explore the impact of adopting a robust estimate of the apparent magnitude threshold m_{thr} for the galaxy catalogues used in gravitational wave cosmology on the final inference of the Hubble constant H_0 from standard sirens, and compare the results to those obtained when adopting a conservative estimate for m_{thr}.

Finally, we present the first results from the prototype of a Newtonian Calibrator at the LIGO Hanford detector. Calibrating the LIGO detectors is crucial to the extraction of the gravitational wave source parameters that are used in cosmology with standard sirens.

Contents

List of Tables

List of Figures

Acknowledgements

I would firstly like to thank my supervisors, Martin Hendry and Graham Woan, for making it possible for me to undertake this PhD. I would also like to thank the rest of the IGR, especially the data analysis group, for their help and support throughout the past five years. In particular, I am grateful for the help, interesting discussions and rants about Gaussian Processes I have had with my office mates Daniel Williams and Fergus Hayes. I would also like to thank Rachel Gray for her help with understanding gwcosmo.

I would also like to thank all the wonderful people I met and worked with during my stay at LIGO Hanford in 2019 - that year was one of the best of my life, and I am very grateful for it. I would like to thank Rick Savage, Jeff Kissel, Sheila Dwyer and Jenne Driggers for the opportunity to work with them on projects at the site. I would also like to thank Michael Ross, Timesh Mistry, Jeff Kissel (again) and the rest of the calibration team for the opportunity to work on the Newtonian Calibrator.

I would like to thank Michael Coughlin for his help during my visit at Caltech in 2019. I am also grateful to Zoheyr Doctor for his help with Gaussian Processes.

I am also very grateful to Gavin Lamb for the opportunity to work on the impact of jet-ejecta interaction on inferred kilonova parameters - this was an interesting project to get involved in.

I would also like to thank all the friends and family without whom I could not have made it this far: Thi My Lien, Valériane, Soheb, Blair, Graeme, Calum, Cat, Sharan, Stu, Ewan, Aaron, Paul, Alan, Scott, Honi, Benas, and I am sure many others who I'm forgetting - if I did, coffee's on me next time we see each other!

Now, it's true that my cat cannot read and will therefore probably never see this, but in all fairness to him, I also doubt most of the humans mentioned here will ever read this thesis either. So, with this being said, I would still like to acknowledge my cat's support in warming my keyboard, attending several of my zoom meetings, and occasionally voicing what I interpreted to be rather strong opinions on the topic of kilonovae during said meetings.

Je remercie aussi ma famille, qui je pense ne lira jamais cette thèse (surtout maman qui ne comprend pas un mot d'Anglais) sauf cette page, pour leur soutien.

Declaration

This thesis is an account of work carried out throughout the duration of my PhD, starting from October 2017 until the present date (November 2022). This work was carried out at the University of Glasgow and at the LIGO Hanford detector in Washington State, USA. Unless stated otherwise the work presented in this thesis is my own. Chapters 1 and 2 are introductory material. The work in chapters 3, 4 and 5 makes use of pre-existing kilonova models and some existing python modules which are referenced in the text. The work in chapter 6 presents the implementation of an existing test of galaxy catalogue completeness into an existing pipeline for gravitational wave cosmology. Both are referenced in the text. The work in chapter 7 presents work undertaken as part of a group. This work was previously published as a paper. The introductory statement outlines my contributions towards this work.

This work was funded by the Science & Technology Funding Council (STFC) as part of a grant for a data-intensive Centre for Doctoral Training (CDT), the Scottish Data-Intensive Science Triangle (ScotDIST).

List of acronyms

BAT	Burst Alert Telescope
BBH	Binary Black Hole
BH	Black Hole
BNS	Binary Neutron Star
CAHA	Calar Alto Observatory
CBC	Compact Binary Coalescence
COBE	Cosmic BackgroundExplorer
DDF	Deep Drilling Field
DCC	Document Control Center
DES	Dark Energy Survey
EM	Electromagnetic
EoS	Equation of State
FAR	False Alarm Rate
GBM	Gamma-ray Burst Monitor
GCN	GRB Coordinates Network
GP, GPR	Gaussian Process, Gaussian Process Regression
GRB, sGRB	Gamma Ray Burst, Short Gamma Ray Burst
GW	Gravitational Wave
KN, KNe	Kilonova, Kilonovae
LIGO	Laser Interferometer Gravitational-Wave Observatory
LF	Luminosity Function
LSST	Legacy Survey of Space and Time (formerly Large Synoptic Survey Telescope)
MCMC	Markov Chain Monte Carlo
MMA	Multi-Messenger Astronomy
NOT	Nordic Optical Telescope
NESSAI	Nested Sampling with Artificial Intelligence
NSBH	Neutron Star-Black Hole
NS	Neutron Star
PE	Parameter Estimation

PDF	Probability Density Function
SN, SNe	Supernova, Supernovae
SNR	Signal to Noise Ratio
WFD	Wide Fast Deep
WMAP	Wilkinson Microwave Anisotropy Probe
XMM	High Throughput X-ray Spectroscopy Mission
ZTF	Zwicky Transient Facility

1 Introduction

> Everything starts somewhere, though many physicists disagree.
>
> Terry Pratchett, Hogfather

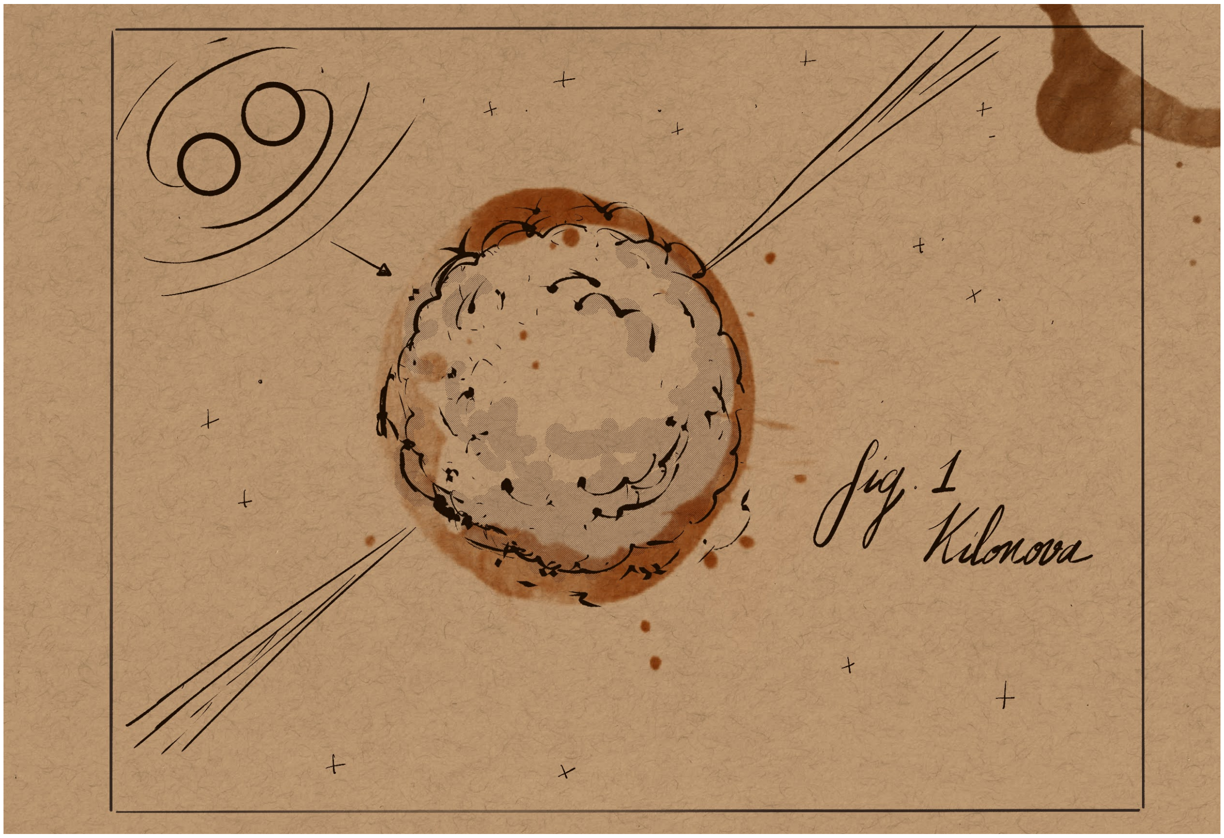

Gravitational waves are disturbances in spacetime that propagate at the speed of light. The search for these tiny ripples gave rise to a colossal international effort spanning decades. They were finally detected one hundred years after being first predicted. [1] The interferometric advanced gravitational wave detectors LIGO Hanford and LIGO Livingston detected the cosmic signal emanating from the distant merger of two black holes on 14th September 2015 at 09:50:45 UTC. Since this historic detection, the field of gravitational wave astronomy has blossomed, with

90 confirmed detections over three observing runs to date. Advanced Virgo and KAGRA joined the network of ground-based advanced gravitational wave observatories, with another LIGO detector planned in India.

There are many offshoots that originated from this historic detection. The discovery had ramifications for many fields of physics and astrophysics, bridging together experimental physics, astronomy, cosmology, theoretical physics and more. As a field, gravitational wave astronomy has exploded in recent years; it will continue to expand, with the LVK network currently under preparations for its fourth observing run (O4) set to start in Spring of 2023. [2]

Chapter 2 introduces the context for this detection and provides some background for much of the subsequent work presented in this thesis. The rest of this chapter focuses on the detection of the first binary neutron star merger, GW170817, the resulting optical and near-infrared counterparts to BNS mergers known as kilonovae and multi-messenger astronomy.

1.1 Gravitational Waves

Definition

Gravitational waves: Disturbances in spacetime travelling at the speed of light, generated by massive objects undergoing non-spherically and non-cylindrically symmetric acceleration. [3]

In 1915, physics was revolutionised by the publication of Einstein's Theory of General Relativity. [4] John Archibald Wheeler memorably summarises the underlying principle of the theory: *"Spacetime tells matter how to move; matter tells spacetime how to curve."* [5]

The existence of gravitational radiation arises as a natural consequence of Einstein's theory of general relativity. In 1916, only one year after he published his theory of general relativity, Einstein proposed a wave solution to his equations. [4, 6]

This wave solution demonstrates the existence of oscillations in the spacetime metric that propagate at the speed of light: gravitational waves.

1.1.1 Sources of gravitational waves

Gravitational waves are generated by any non-spherically and non-cylindrically symmetric accelerating mass-energy. [3, 7] These impart a quadrupole moment of mass, which in turn produces gravitational waves.

The effect of gravitational waves is infinitesimal. Because of this, only the most powerful astrophysical events in the Universe produce detectable gravitational waves. These events are generated by massive astrophysical objects undergoing rapid acceleration. While the luminosity of astrophysical signals observed in the EM spectrum scale inversely with the square of the distance, the amplitude of gravitational wave signals scales inversely with the distance.

Four different types of gravitational wave signals are expected from astrophysical systems: compact binary coalescences (CBCs), bursts, stochastic and continous waves.

Compact Binary Coalescences

Compact binary coalescences are the merger of two compact objects. Compact objects are extremely dense, heavy astrophysical objects. Black holes and neutron stars are compact stellar remnants that fall under that umbrella. CBCs make up all confirmed gravitational wave detections to date. CBCs present as a characteristic "chirp" signature, preceded by an inspiral phase.

Three types of compact binary coalescences have been detected:

- Binary Black Hole mergers (BBH)
- Binary Neutron Star mergers (BNS)
- Neutron Star-Black Hole mergers (NSBH)

Black holes are compact objects with a gravitational field so strong no object or signal can escape their pull. They were predicted by Schwarzschild in 1916 as a solution to Einstein's field equation for the gravitational fields of point masses. [8] Neutron stars are dense stars made up primarily of neutrons. They have a typical mass $\sim 0.5 - 3\ \mathrm{M}_{\odot}$ with typical radii of ~ 10 km. [9]

Mergers of stellar mass binary black holes are the most commonly detected systems. We can also expect other types of CBCs involving White Dwarfs (WD), with WD-NS/BH mergers expected to be common in our galaxy. [10] They do not, however, have as strong a signature as the previously described mergers, and their frequency makes them more appropriate targets for future space-based gravitational wave detectors. [11]

The work presented in this thesis focuses on compact binary coalescences.

Burst

Burst signals are another type of transient gravitational wave signal. They are weakly modelled transients of short duration. Burst searches make few assumptions on the shape of the gravitational waveform, being instead identified through the detection of excess-power signals and requiring signal coherence across several detectors. [12–14] Sources of bursts include core-collapse supernovae, pulsar glitches, cosmic string cusps and magnetar flares. [15, 16] No burst signal has been detected to date. Although one candidate burst signal, S200114f, generated a public alert during O3, further analysis found the signal not to be of astrophysical origin. [14]

Stochastic

Stochastic gravitational wave signals emerge from the multitude of incoherent gravitational wave signals that make up the astrophysical gravitational wave background. Along with incoherent signals from a background of distant compact mergers, primordial gravitational waves from the Big Bang are another potential source of stochastic gravitational waves. [17] An upper limit can be placed on the gravitational wave background from all-sky, all-frequency searches. [18,19]

Continuous

Continuous gravitational waves are emitted at a defined frequency over a long period of time. Neutron stars that are asymmetrical with regards to their rotation axis generate continuous gravitational waves as they spin. [20] These asymmetries are deformations on the surface of the neutron star. The non-detection of continuous waves puts constraints on the maximum strain of the signals, which translates to a limit on the maximum height of the deformations. [21]

1.1.2 Gravitational wave detectors

The search for gravitational waves started in the 1960s with the resonant bar detectors developed by Joseph Weber. These very early detectors were built to detect gravitational wave bursts from the collapse of supernovae. [7, 22] A detection was announced by Weber in 1969. The announcement was controversial, and the result could never be replicated by other teams. [23,24]

Following this unsuccessful venture into gravitational wave detection, laser interferometric gravitational wave detectors were proposed. [25, 26]

These interferometers would make use of optical path folding in their design in order to reach the arm lengths necessary for the detection of gravitational waves ($\sim$ 1000km), with the lasers making many round trips in the interferometer arms. [27] As gravitational waves travel through the interferometers, they distort space and change the optical path length L, inducing a differential length ΔL change in the arms called the strain h:

$$h = \frac{2\Delta L}{L} \tag{1.1}$$

The two Laser Interferometer Gravitational-wave Observatories (LIGO) were built in the 1990s, and began operating at design sensitivity in their data acquisition mode from November 2005 to September 2007. [28] The "Initial LIGO" observing runs did not yield any detections. The LIGO detectors were built as two identical interferometers with 4km arms, located in Washington State and Louisiana. Following the initial observing runs, the two detectors underwent major upgrades, and so began the era of Advanced LIGO, and of second generation gravitational wave detectors. The Advanced LIGO detectors have been operating and detecting gravitational waves since 2015.

The design of the Advanced LIGO interferometric detectors is based on a Michelson interferometer with 4km arms, with each arm containing a Fabry-Perot cavity to build up the phase shift produced by the change in length of the arms. [29]

Following Advanced LIGO's successful first observing runs, the Advanced VIRGO detector in Italy and KAGRA detector in Japan joined the network of ground-based gravitational wave detectors. [30,31] Virgo started observing at the end of the second observing run, while KAGRA joined at the end of the third observing run. Another detector with 600m arms, GEO600, is located in Germany. [32]

Figure 1.1: One arm of the LIGO Hanford detector in Washington State.

1.2 Detecting Gravitational Waves

The first direct detection of gravitational waves was made on 14th September 2015, almost exactly 100 years after they were first predicted by Albert Einstein. [4] The signal was observed simultaneously by the two LIGO detectors at 09:50:45 UTC on 14th September 2015. The source of the signal was the merger of two black holes at a luminosity distance of 410^{+160}_{-180}Mpc. [1]

1.2.1 Indirect detection

While GW150914 was the first direct detection of gravitational radiation, its existence had previously been inferred from the loss of orbital energy of binary pulsars. [33] The binary pulsar system PSR 1913+16 was discovered by Hulse and Taylor in 1975. [33] Monitoring of the system from 1975 to 1981 showed that the delays in pulse arrival from the system were consistent with orbital decay that matched predictions made by a loss of energy through gravitational radiation. [34]

1.2.2 Direct detection

The first direct detection of gravitational waves was made on 14th September 2015 at 09:50:45 UTC, during the first observing run (O1) of the Advanced LIGO detectors. [1] While the official start date for O1 was originally set for 18th September 2015, the detectors were at the time running in observing mode as part of Engineering Run 8, and the O1 dataset is defined as starting from 12th September 2015. [35, 36] Another two signals in the O1 data were later confirmed as gravitational wave events, GW151012 and GW151226 [37, 38]. The two signals also originated from the mergers of two black holes.

Since then, signals from binary neutron star mergers and neutron star-black hole mergers have also been detected by the LVK network. The latest data release of detected compact binary coalescences is GWTC-3, the third Gravitational Wave Transient Catalogue. It describes transient events detected up to the end of the third observing run. [2] GWTC-3 contains **90** events with $p_{astro} > 0.5$ across three observing runs.

Definition

p_{astro}**:** The inferred probability of a gravitational wave signal being of astrophysical compact binary coalescence origin.

1.2.3 GW170817

On 17th August 2017, the universe offered its most spectacular event yet to gravitational wave astronomers; two neutron stars merged, followed by a short Gamma Ray Burst (sGRB) and a kilonova. The event was observed all across the electromagnetic spectrum, in the X-ray, ultraviolet, optical, infrared, and radio bands. [39–49] The event was well-localised by the gravitational wave detector network, with a 90% confidence skymap spanning 28 deg^2 (initially 31 deg^2). It was measured at a distance of $d = 40^{+8}_{-14}$ Mpc. [40] The merger was found to have originated from the host galaxy NGC 4993. The luminosity distance measurement from GW170817 was consistent with several measurements of the distance to NGC 4993, the most precise of which being the measured surface brightness fluctuation distance $d = 40.7 \pm 1.8 \pm 1.9$ Mpc. [50–54]

The short Gamma Ray Burst associated with GW170817 was identified 1.7s after the gravitational wave "chirp", with the *FERMI* Gamma-ray Burst Monitor detected the sGRB 170817A at 12:41:06 UTC. The burst was also detected by the *INTernational Gamma-ray Astrophysics Laboratory* (*INTEGRAL*), with a 4.2σ association with the *FERMI* detected burst. [41, 42]

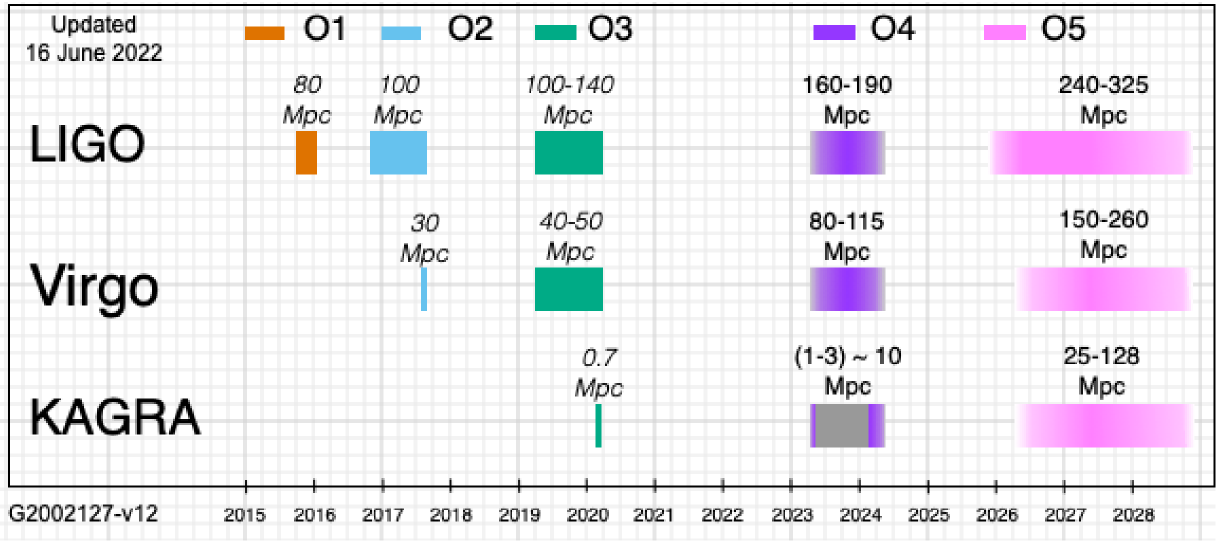

Figure 1.2: Plans for future observing runs of the LVK network with BNS observing range [56]

The optical counterpart to GW170817 was first detected by the SWOPE team and announced under the designation SSS17A. [55] A fast-fading transient coincident with the gravitational wave signal was observed 10.9 hours after the merger. The original search was carried out in the *i* band as theoretical predictions for kilonovae showed that the light curves would be very red. The discovery was disseminated through a GRB Coordinates Network notice (GCN) and subsequently observed by a plethora of other instruments.

1.2.4 Future observing runs

At the time of writing, the aLIGO detectors have completed three observing runs, with Virgo joining observations from the second observing run (O2) onwards and KAGRA joining the network towards the end of O3.

The next observing run, O4, is set to begin during Spring of 2023, with all four detectors joining the observing effort. Figure 1.2 shows a timeline of past and future runs with ground-based advanced detectors, with the planned detector sensitivity for binary neutron star mergers.

1.2.5 Future detectors

Ground-based detectors

Along with the planned Advanced LIGO detector in India and proposed upgrades to the current LIGO detectors, there are future plans for a third generation of ground-based gravitational wave detectors. Cosmic Explorer is a proposed design for a next-generation gravitational wave observatory with 40km arms. It will detect binary neutron star mergers beyond a redshift of 1. [57,58] The Einstein Telescope is a proposed European ground-based facility. The planned design is of a triangular, underground interferometer with 10km arms. [59]

Space-based detectors

The space-based gravitational wave detector LISA will explore the gravitational wave spectrum in a frequency window ranging from 0.1 to 100mHz, detecting sources like the mergers of supermassive black holes. The detector was designed as an interferometer in a 3-arm configuration, with each arm separated by 2.5 million km. Its orbit will be an Earth-trailing heliocentric orbit. [60] In December 2015, the LISA Pathfinder mission successfully demonstrated the technology that will be used for LISA. [61]

1.3 Multi-Messenger Astronomy

This section presents an overview of multi-messenger astronomy using gravitational waves and their electromagnetic counterparts, focusing on kilonovae.

1.3.1 Multi-Messenger Astronomy

The study of astronomy started with optical observations - detections made in the visible light spectrum. As the field advanced, this expanded to the observations of different parts of the electromagnetic spectrum. Astronomy stopped being bound to the optical realm in 1932, when Karl Jansky, then working at the Bell Telephone Laboratories, made the first radio observations of the Milky Way. [62] This was the start of multi-wavelength astronomy.

Photons are just one example of a cosmic messenger; the detection of cosmic rays in the 1910s by the Austrian physicist Victor Hess marked the true advent of multi-messenger astronomy. [63] Since then neutrinos of cosmic origin have been detected, first from the Sun and subsequently from a nearby supernova. [64, 65]

Definition

Multi-messenger astronomy: Observations of an astrophysical object, such as a compact binary coalescence, in more than one coincident "messenger": e.g. gravitational waves with an electromagnetic counterpart, electromagnetic observations with neutrinos, etc.

Gravitational waves are yet another cosmic messenger; a wholly different way of looking at the universe. As outlined in the previous section, they were only detected in 2015, a hundred years after being originally predicted. But it wasn’t until 2017 that the era of multi-messenger astronomy with GWs and EM truly began, with the coincident detection of a gravitational wave signal from two merging neutron stars, GW170817, and its electromagnetic counterparts.

1.3.2 Multi-Messenger Astronomy with Gravitational Waves

Observations of the binary neutron star merger GW170817 by both gravitational wave detectors and EM instruments heralded a new era of multi-messenger astronomy using gravitational waves and electromagnetic counterparts. Multi-messenger astronomy with gravitational waves offers complementary information about astrophysical objects. The observation of coincident signals from a source offers new insights into astrophysics, cosmology and fundamental physics. [66]

The observing campaign that followed the GW170817 alert was the first conclusive search for an electromagnetic counterpart to a gravitational wave signal. The observations confirmed binary neutron star mergers as the progenitors of kilonovae and short Gamma Ray Bursts (sGRB). The detection of a sGRB coincident with a gravitational wave signal allowed for the measurement of the speed of gravitational waves, and to place constraints on the mass of the graviton. [67]

Multi-messenger observations of BNS mergers with kilonovae can also constrain the neutron star equation of state. [68, 69]

These observations are also important in the field of cosmology, with EM-bright compact binary coalescences allowing us to place constraints on the rate of expansion of the Universe.

1.3.3 Kilonovae

Definition

Kilonova: Kilonovae are faint, rapidly fading optical and near-IR transients accompanying BNS or NSBH mergers. They are thermal transients powered by the radioactive decay of heavy unstable nuclei synthesised through rapid neutron capture.

Compact binary coalescences involving a neutron star can give rise to the ejection of neutron-rich matter. This ejected neutron-rich matter has a low electron fraction. These conditions are favourable for the synthesis of heavy elements (atomic mass greater than 140) called lanthanides through the rapid neutron capture process (r-process). The radioactive decay of these unstable heavy nuclei powers the optical and near-infrared thermal transients known as kilonovae, or macronovae. [70, 71] Kilonovae present themselves as a long-lived, supernova-like radiation following a compact binary coalescence. These radioactively-powered transients have a timescale of days to weeks, and are approximately isotropic. [72] They peak in the near-infrared at luminosities of $L_{peak} \sim 10^{41}$ erg s^{-1} and are powered by the decay of radioactive r-process material produced during the merger of two neutron stars, or a neutron star with a black hole. [73, 74] Depending on outcome of the merger, the kilonova peak can reach luminosities up to $L_{peak} \sim 10^{44}$ erg s^{-1} for some types of remnants. [75]

Kilonovae are an important actor in the nucleosynthesis of the universe. The decompression of the neutron rich matter ejected during the merger of two neutron stars, or of a neutron star with a black hole, gives rise to r-process nucleosynthesis. This nucleosynthesis process enriches the universe with heavy elements like platinum, gold, or the lesser-known strontium, the only element named after a place in Scotland. [75]

Definition

Nucleosynthesis: The process through which new atomic nuclei are created from existing nucleons and nuclei.

Neutron capture mechanisms

Definition

r-process: rapid neutron capture, a process through which a heavy seed nucleus undergoes a succession of rapid neutron captures.
s-process: slow neutron capture, a process through which a heavy seed nucleus undergoes neutron capture. Unstable isotopes typically undergo β-decay before capturing another neutron.

The s-process, slow neutron capture, takes place on long time-scales, ranging from ~ 100 years to $\sim 10^5$ years. It is responsible for the production of most isotopes with atomic mass $23 \leq A \leq 46$. [76, 77]

The r-process, rapid neutron capture, occurs on very short time-scales, with ∼0.01-10s between the β-decay processes in between neutron captures. [76] This process is believed to be responsible for the production of around half of the elements heavier than iron in the Universe. [78] These elements have to be formed via successive captures of neutrons. [79]

The mechanisms behind the r-process have been understood since the 1950s, but a problem remained: where in the Universe could we find an environment that was neutron-rich enough to support the nucleosynthesis of the heaviest elements?

Theorising the most neutron-rich environments

The existence of kilonovae was theorised before they were observed, as a solution to the formation site of some of the heaviest elements. The neutron-rich ejecta that results from the merger of compact star binaries was first predicted in the 1970s as the site of r-process (rapid neutron capture) and of the formation of many heavy elements with an atomic mass $A > 140$. [79–82] Born of the merger of a neutron star with either another neutron star or a black hole, they were theorised to be the only environment neutron-dense enough to support the kind of rapid neutron capture necessary for the formation of the heaviest elements. It wasn't until the 1990s that hydrodynamic simulations showed that these mergers would eject some matter; until then, the question of whether gravitationally-bound systems such as BNS could eject mass was still unresolved.

Simulations showed that the dynamically expelled neutron-rich mass in the merger of two neutron stars could reproduce heavy r-process elements past the platinum peak (A=195). [71,79,83] It then took until 2017 to make the first confirmed detection of a kilonova, despite candidate observations before, such as the potential optical transient detected in 2008 following the short GRB 080503. [84] Subsequent candidates were observed, first in 2013 accompanying GRB 130603B and in 2016 following GRB 160821B. [85,86]

Early models showed that only a merger of compact objects involving at least one neutron star would have a neutron density sufficient for the r-process to generate the very heaviest elements in the universe. Work on theoretical models of kilonova emission was first started by Li and Paczyński in 1998, who gave us our first model of kilonovae. [70] The model was a simple analytical one with parameterised heating, outputting the bolometric light curves for transients associated with binary neutron star mergers.

Shortly after this first model, the first hydrodynamical simulations of kilonovae were released. [71, 79, 83] More theoretical work was carried out on kilonova models, their ejection mechanisms and central engines in the 2000s and 2010s. [75, 87, 88] In 2013, it was proposed that lanthanides, the heavy elements present in kilonovae, would make the resulting radiation redder, dimmer and longer than previously thought. [74] The presence of those heavy elements increase the ejecta opacity by several orders of magnitude; the opacity of the ejecta is dominated by bound-bound transitions from the lanthanides, which have complex valence electron structures. These ions have a large number of strong lines that are very optically thick, therefore dominating the ejecta opacity despite their relatively low abundance. [89]

Kilonova modelling continues to be an active research topic, with ongoing major developments on ejection mechanisms and microphysics involved in the transients.

Progenitors of kilonovae

The progenitors of kilonovae are coalescing neutron star-neutron star or neutron star-black hole binaries. The nature of the resulting kilonova depends on the properties of the progenitor system.

In NSBH systems, a kilonova can only occur when the neutron star is tidally disrupted sufficiently far from the Schwarzschild radius of the black hole. This is related to both the tidal radius of the neutron star (which is related to the mass ratio of the system and the neutron star radius) and the radius of the innermost stable circular orbit (R_{isco}) of the black hole (which is related to the mass and spin of the black hole). If the neutron star is "swallowed whole" by the black hole, there is effectively zero mass ejected. Kilonovae that emerge from NSBH systems are mostly red and peak at $\sim$ 1 week post-merger. [75]

Several mechanisms for matter ejection have been identified in kilonovae arising from BNS systems. These depend on the parameters of the progenitor and the nature of the resulting merger remnant. The remnant consists of most (>90%) of the mass of the system. [91] Mass can be ejected dynamically through tidal forces and compression at the interface between the two

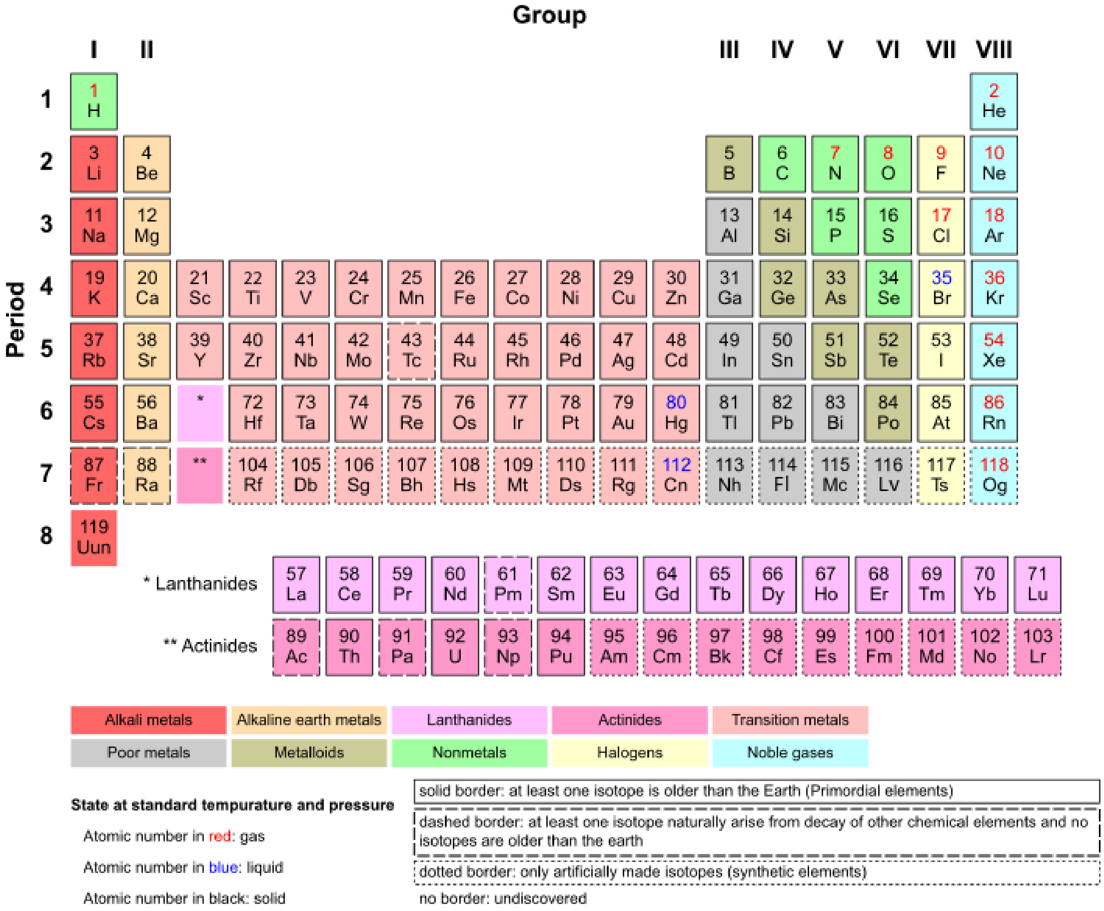

Period	I	II											III	IV	V	VI	VII	VIII
1	1 H																	2 He
2	3 Li	4 Be											5 B	6 C	7 N	8 O	9 F	10 Ne
3	11 Na	12 Mg											13 Al	14 Si	15 P	16 S	17 Cl	18 Ar
4	19 K	20 Ca	21 Sc	22 Ti	23 V	24 Cr	25 Mn	26 Fe	27 Co	28 Ni	29 Cu	30 Zn	31 Ga	32 Ge	33 As	34 Se	35 Br	36 Kr
5	37 Rb	38 Sr	39 Y	40 Zr	41 Nb	42 Mo	43 Tc	44 Ru	45 Rh	46 Pd	47 Ag	48 Cd	49 In	50 Sn	51 Sb	52 Te	53 I	54 Xe
6	55 Cs	56 Ba	*	72 Hf	73 Ta	74 W	75 Re	76 Os	77 Ir	78 Pt	79 Au	80 Hg	81 Tl	82 Pb	83 Bi	84 Po	85 At	86 Rn
7	87 Fr	88 Ra	**	104 Rf	105 Db	106 Sg	107 Bh	108 Hs	109 Mt	110 Ds	111 Rg	112 Cn	113 Nh	114 Fl	115 Mc	116 Lv	117 Ts	118 Og
8	119 Uun																	

* Lanthanides	57 La	58 Ce	59 Pr	60 Nd	61 Pm	62 Sm	63 Eu	64 Gd	65 Tb	66 Dy	67 Ho	68 Er	69 Tm	70 Yb	71 Lu
** Actinides	89 Ac	90 Th	91 Pa	92 U	93 Np	94 Pu	95 Am	96 Cm	97 Bk	98 Cf	99 Es	100 Fm	101 Md	102 No	103 Lr

Alkali metals	Alkaline earth metals	Lanthanides	Actinides	Transition metals
Poor metals	Metalloids	Nonmetals	Halogens	Noble gases

State at standard tempurature and pressure

Atomic number in red: gas

Atomic number in blue: liquid

Atomic number in black: solid

solid border: at least one isotope is older than the Earth (Primordial elements)

dashed border: at least one isotope naturally arise from decay of other chemical elements and no isotopes are older than the earth

dotted border: only artificially made isotopes (synthetic elements)

no border: undiscovered

Figure 1.3: The periodic table of elements, with lanthanides in light magenta. [90]

objects, or as disc wind ejecta, as matter forms an accretion disc. [75] The mass of the dynamically expelled ejecta strongly depends on the neutron star equation of state, on the total mass and on the mass ratio of the binary. [92] The nature of the disc wind ejecta is sensitive to the resulting merger remnant; should the remnant survive as a hot neutron star for tens of milliseconds, the neutrino irradiation will lower the neutron fraction, hereby suppressing lanthanide production and resulting in bluer disc winds. If it promptly collapses into a black hole, the neutrino irradiation will be suppressed, likely resulting in red winds. [93, 94] This red kilonova would peak on a timescale of ~ 3 days, whereas kilonovae that do not promptly collapse into a black hole peak with a timescale of $\lesssim 1$ day. [75]

Searches

Kilonovae are faint objects with a rapid decay, making untriggered searches difficult with current instruments. Due to this rapidly evolving nature, the best chance of detecting kilonovae is through triggered searches, either from gravitational wave or sGRB detections. Archival searches on previously released data were carried out following the detection of the kilonova AT 2017gfo. A search for kilonovae in the Dark Energy Survey data found no events. [95]

The rapid rise time of kilonovae allows us to distinguish them from supernovae. This characteristic short timescale makes prompt observations of kilonovae the best way to tell them apart from such contaminants. [96] Cuts on colour and rise time allow for the robust separation of kilonovae from other known types of transients. [97]

Three notable kilonova candidates were observed prior to AT 2017 gfo. In 2008, a bright short gamma-ray burst, GRB 080503, was accompanied by a faint optical counterpart consistent with a kilonova. [84] Another compelling candidate was observed in 2013 following GRB 130603B. [85] In 2016, an optical counterpart was observed following sGRB 160821B. The search included the *HST*, *XMM-Newton* and ground-based telescopes such as the Gran Telescopio Canarias (GTC), the Nordic Optical Telescope (NOT), the Telescopio Nazionale Galileo (TNG), the William Herschel Telescope (WHT), and the Karl G. Jansky Very Large Array (VLA). The observed kilonova and afterglow were associated with a host galaxy with redshift $z = 0.162$. [86]

In late 2021, another kilonova was detected following the long gamma ray burst GRB211211A. The event is notable as the kilonova was detected at 350Mpc and following a long gamma ray burst, rather than an sGRB. The GRB was identified simultaneously by *Swift*'s Burst Alert Telescope (BAT) and *Fermi*'s Gamma-ray Burst Monitor (GBM). The kilonova was detected following *Swift* observations of the GRB afterglow in the X-ray and ultra-violet. This triggered an optical observing campaign with the Nordic Optical Telescope (NOT) and the Calar Alto Observatory (CAHA). The observations found an uncatalogued transient rapidly fading following the detected GRB. Subsequent observations and analysis confirmed the mystery source to be a kilonova, whose brightness and colour was similar to those of the kilonova that accompanied

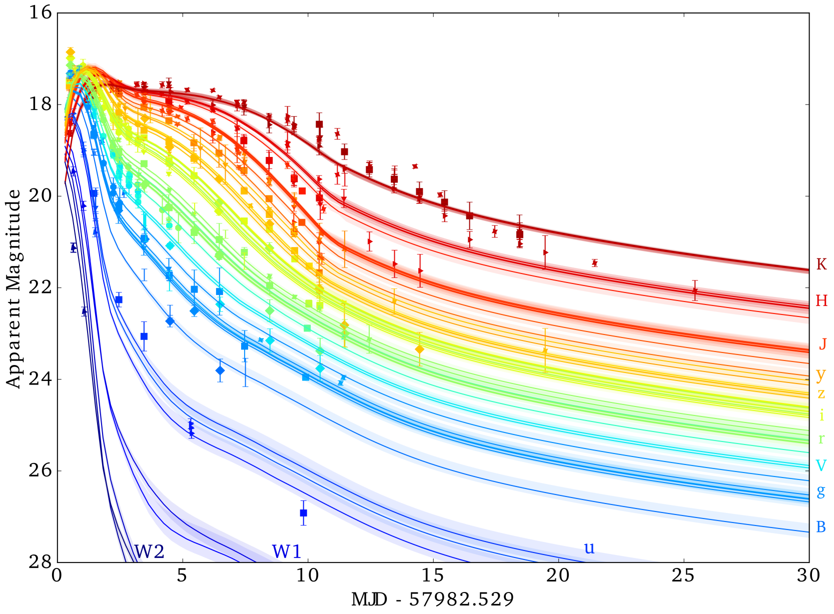

Figure 1.4: Unified data set - the light curves of AT 2017gfo. Figure from [99]

GW170817. [98]

AT 2017gfo

The detection of gravitational waves from the merger of two neutron stars, GW170817, on 17th August 2017 engendered an intensive follow-up search campaign for an accompanying optical signature to the merger. A kilonova associated with the merger was detected 11 hours after the merger. [40]

These observations showed that BNS mergers are a dominant site of r-process nucleosynthesis of heavy elements.

The light curves from the counterpart accompanying GW170817 were consistent with the release of multiple ejecta components with different lanthanide abundances. Analysis of late-time light curves showed that at least $0.05M_{\odot}$ of heavy elements were produced in the aftermath of the merger, confirming the role of neutron star mergers in r-process nucleosynthesis in the Universe. [100]

To date, AT 2017gfo is the only kilonova detection accompanied by a gravitational wave signal.

1.3.4 Multi-messenger Astronomy with the Vera Rubin Observatory

The Vera Rubin Observatory will survey the transient sky to unprecedented depths. With its first light planned in 2023, it will map the sky in the *ugrizY* bands for 10 years during the duration of its Legacy Survey of Space and Time. Exploring the transient sky is one of the LSST's four main science themes, the other three being probing dark energy and dark matter, taking an inventory of the Solar System, and mapping the Milky Way. [101] Based in northern Chile, it will have the capability to observe 10,000 deg^2 in a single filter band within three nights with its 3.2 Gigapixel camera and 9.6 deg^2 field of view. [101] During its ten year mission, each field will be visited every $\sim$4 days in one of the "ugrizY" filters. [102]

It is set to observe kilonovae to distances greater than those possible with the current generation of ground-based gravitational wave detector networks, with some kilonovae detectable up to 475Mpc. [103, 104] Kilonovae are hard to detect for current instruments due to their faint and rapidly evolving nature, making serendipitous discoveries particularly sensitive to uncontrollable factors such as the weather. [105] The LSST would be able to carry out GW-triggered EM follow-up campaigns to an unprecedented depth.

The Vera Rubin Observatory could be crucial in target of opportunity (ToO) observations of gravitational wave events during future observing runs. Along with detecting kilonovae following BNS and NSBH triggers, it could place deep constraints on optical emissions from binary black hole mergers. [106] While several mechanisms for EM emissions from BBHs have been proposed, and one candidate EM event has been observed following the BBH GW190521, none have been confirmed to date. [107–109] The wide coverage abilities of the LSST could also be crucial in detecting early emissions from kilonovae, which would be crucial to our understanding of the emission mechanisms of the transients. [110]

Definition

Vera Rubin Observatory: Previously known as Large Synoptic Survey Telescope. A planned astronomical observatory whose main mission will be carrying out an optical synoptic survey, the Legacy Survey of Space and Time (LSST). LSST will survey the transient sky at unprecedented depths.

Kilonovae from binary neutron star mergers on the observing horizon of aLIGO will be hard to detect even for 4m telescopes. [111] The Vera Rubin Observatory could unveil a population of kilonovae observed independently of any GW trigger.

LSST observations of kilonovae could also be optically triggered. If optimised, wide surveys like the Zwicky Transient Facility (ZTF) and LSST could serendipitously detect kilonovae several days post-merger. [112]

Under its current baseline strategy, the Wide Fast Deep (WFD) survey of the LSST is expected to detect a low number of kilonovae, with estimated rates between 27 and 70 events for the duration of the lifetime of the survey. [113, 114]

While ejecta parameters can be recovered from these serendipitous discoveries, so could a merger time and luminosity distance. If a serendipitous kilonova observation happens during a LIGO observing run, it could be linked to potential sub-threshold or single-detector signals.

2 | Cosmology

> Space is big. You just won't believe how vastly, hugely, mind-bogglingly big it is. I mean, you may think it's a long way down the road to the chemist's, but that's just peanuts to space.
>
> Douglas Adams, The Hitchhiker's Guide to the Galaxy

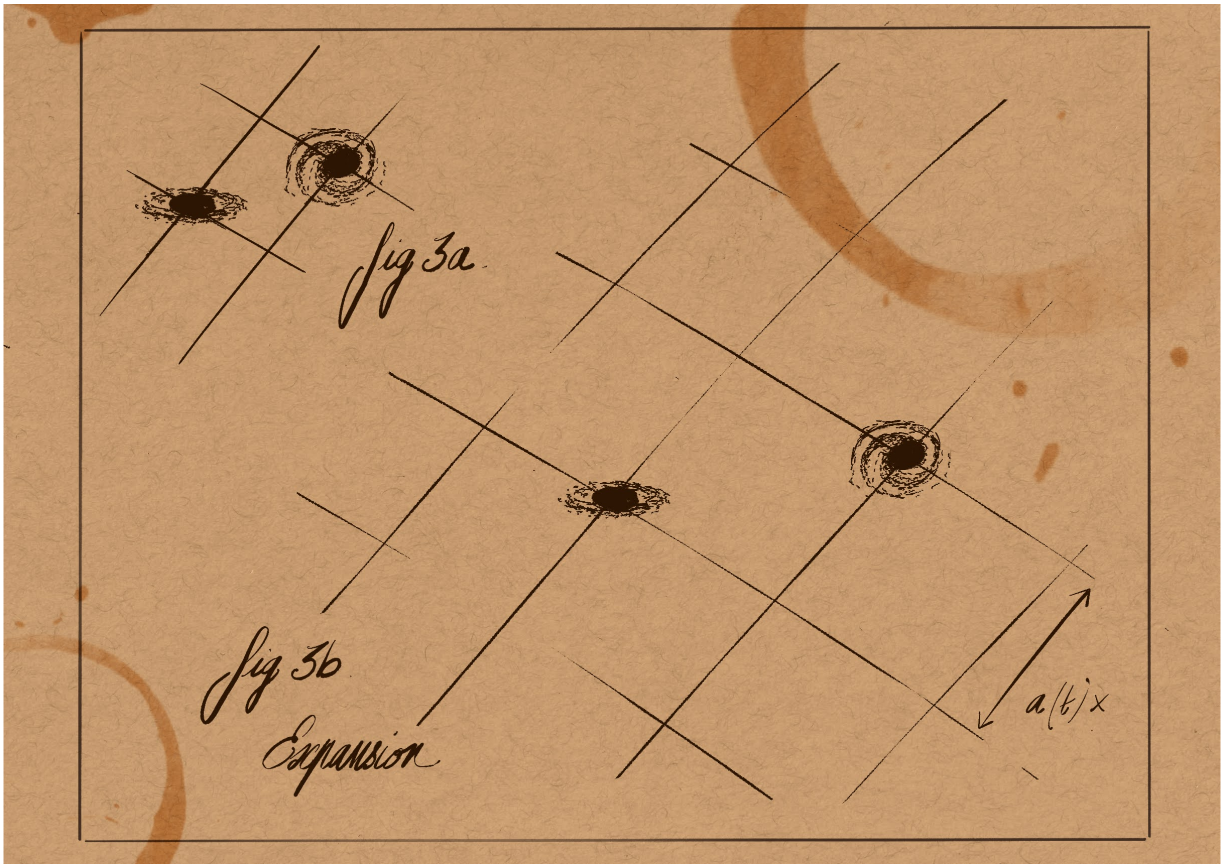

Chapter 1 introduces gravitational waves and multi-messenger astronomy. Multi-messenger astronomy with gravitational waves has applications in the field of cosmology, which will be the topic of chapter 6. This chapter introduces a brief history of cosmology, the Hubble constant and cosmology with gravitational waves.

2.1 A Brief History of Cosmology

The Cosmos is the entire Universe that surrounds us, and cosmology is its study. Cosmology has had its place in both science and spiritual belief for as long as people have been looking up and into the Cosmos. Throughout the ages, cosmology has been concerned with our place in the Universe, a curiosity arising naturally from observations of the night sky.

It was assumed for many millenia that the Earth occupied a very special, central place in the Universe. This was the basis of the Ancient Greek cosmological model developed by Ptolemy. In this cosmology, our home planet was placed at the centre of the Universe, orbited by the Sun, Moon and planets. The stars were resting in the background, static sources of light. In the 1500s, Copernicus challenged this view when he proposed the heliocentric model. Even then, this model still placed us in a special place, with the Sun at the centre of the Universe. [115]

Our understanding of the Cosmos went a step further with Newton, who believed other stars to be just like our own Sun, with their own orbiting planets around them. In 1785, the Herschels gave us our picture of the solar system as part of a galaxy. [115, 116] In their model, the solar system was still at the centre of the Milky Way.

In 1952, at a meeting of the International Astronomical Union, astronomer Walter Baade postulated that our galaxy was not unique or at the centre of the Universe, but rather a mundane galaxy among others, not occupying any special place in the Universe. He also postulated that the Universe was much larger than previously believed, doubling previous estimates. [115] It was therefore a long road to our contemporary understanding of the Cosmos and our place within it. The twentieth century heralded a new era of precision cosmology.

Cosmology is, at its core, the study of the Universe as a single system. Whereas astrophysics is more concerned with the underlying physics that govern objects and interactions within the Universe, the focus of cosmology is on the dynamical evolution of this single system.

This dynamical evolution of the whole Cosmos can be studied through models of the Universe and their physical parameters.

2.1.1 The Hubble constant

Gazing into the depths of the Cosmos, a peculiar phenomenon can be observed: astrophysical objects, like galaxies, seem to be moving away from us. Not only do they appear to be receding, but the rate at which they are moving away seemingly grows with increasing distances. This phenomenon was first observed by the astronomer Edwin Hubble in 1929. [117]

The Hubble constant is named after Edwin Hubble, who made the first measurement of the rate of expansion of the Universe in 1929. [117] From observations of nearby galaxies (referred

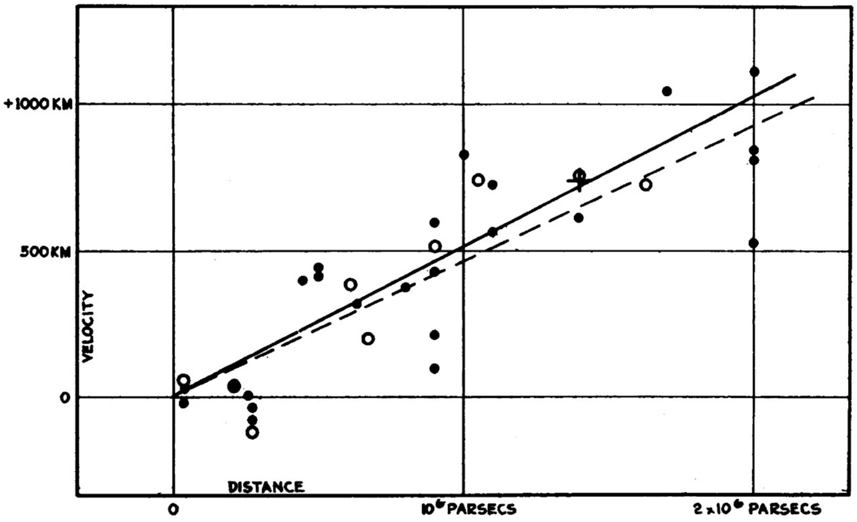

Figure 2.1: Edwin Hubble's original plot of the redshift-luminosity distance relationship. Figure from [117]

to as extra-galactic nebulae), Edwin Hubble first discovered that there was a relationship between the recession velocity v and distance r to nearby galaxies in 1929. From this work a constant of proportionality between the two quantities was introduced, bearing the astronomer's name: the Hubble constant H_0.

$$H_0 = \frac{v}{r}, \tag{2.1}$$

with v the radial velocity and r the distance. For small enough redshifts ($z \ll 1$), $v = cz$, and we can approximate the proper distance between galaxies r to the luminosity distance d_L. This gives us the more familiar form of Hubble's law:

$$d_L = \frac{cz}{H_0}. \tag{2.2}$$

Definition

The Hubble constant: The Hubble constant describes the rate of the expansion of the Universe. It is measured in units of kilometres per second per megaparsec ($\mathrm{km\,s^{-1}\,Mpc^{-1}}$)

While Edwin Hubble's observations were the first observational evidence for an expanding Universe, the phenomenon had been predicted by theory before. [118, 119] Indeed, the Hubble constant can be derived from Friedmann's equations. [119–121] Starting from Einstein's field equations, Alexander Friedmann derived a set of equations which describe the expansion of an isotropic and homogeneous Universe.

Friedmann's 1922 work, seven years prior to Edwin Hubble's paper on the recession velocity of nearby galaxies, describes the evolution of the relative expansion of the Universe through the introduction of a scale factor $a(t)$. This scale factor describes the relationship between the proper separation of two objects at an arbitrary time t, $x(t)$, and the proper separation between the same two objects at present day, x_0.

$$a(t) = \frac{x(t)}{x_0} \tag{2.3}$$

We can define the Hubble parameter in terms of this scale factor:

$$H \equiv \frac{\dot{a}(t)}{a(t)} \tag{2.4}$$

The relationship between the redshift and scale factor of the Universe can be derived from the Friedmann-Lemaître-Robertson-Walker (FLRW) metric. In the metric, spatial coordinates are comoving; this means objects remain at fixed coordinates, with the expansion characterised only by the scale factor $a(t)$. [115, 119, 120, 122–125]

$$ds^2 = -c^2dt^2 + a^2(t)\left[\frac{dr}{1-kr^2} + r^2(d\theta^2 + \sin^2\theta d\phi^2)\right] \tag{2.5}$$

where k is the curvature of the Universe. For light propagation:

$$ds = 0. \tag{2.6}$$

For a radially propagating ray, travelling from $r = 0$ to $r = r_0$, this means that $d\theta = d\phi = 0$. Setting this and $ds = 0$ in equation 2.5:

$$\frac{cdt}{a(t)} = \frac{dr}{\sqrt{1-kr^2}}. \tag{2.7}$$

To derive the time taken for the light to travel from $r = 0$ to $r = r_0$, we integrate equation 2.7.

$$\int_{t_e}^{t_r} \frac{cdt}{a(t)} = \int_0^{r_0} \frac{dr}{\sqrt{1-kr^2}}, \tag{2.8}$$

where t_e is the time at emission of the propagating ray and t_r the time at reception at $r = r_0$.

Now, we can imagine a second light ray being emitted from $r = 0$ and received at $r = r_0$ shortly after the first one. Since the galaxies are comoving and therefore in the same coordinates, the emission and reception times would, respectively, be t_e+dt_e and t_r+dt_r. We then have:

$$\int_{t_e+dt_e}^{t_r+dt_r} \frac{cdt}{a(t)} = \int_0^{r_0} \frac{dr}{\sqrt{1-kr^2}}. \tag{2.9}$$

The left-hand sides of equation 2.8 and equation 2.9 are equal, allowing us to write the following expression:

$$\int_{t_e}^{t_r} \frac{cdt}{a(t)} = \int_{t_e+dt_e}^{t_r+dt_r} \frac{cdt}{a(t)}. \tag{2.10}$$

Now, since the areas under the curve determined by $\frac{c}{a(t)}$ are the same from t_e to t_r and t_e+dt_e and t_r+dt_r, and the area from t_e+dt_e to t_r is common to both, we can conclude that the area from t_e to t_e+dt_e is equal to the area from t_r to t_r+dt_r. We can then write:

$$\int_{t_e}^{t_e+dt_e} \frac{cdt}{a(t)} = \int_{t_r}^{t_r+dt_r} \frac{cdt}{a(t)}. \tag{2.11}$$

The slices considered are narrow, which means we can approximate the area under the curve to that of a rectangle. This gives us the expression:

$$\frac{dt_r}{a(t_r)} = \frac{dt_e}{a(t_e)}. \tag{2.12}$$

Now, assuming an expanding Universe, $a(t_r) > a(t_e)$ for any t_e. Therefore $dt_r > dt_e$; the time interval increases with the expansion of the Universe.

We can picture that each propagating light ray is actually a crest of a wavelength. Then, we have the wavelength $\lambda \propto dt \propto a(t)$, giving us:

$$\frac{\lambda_r}{\lambda_e} = \frac{a(t_r)}{a(t_e)}. \tag{2.13}$$

For an observer on earth, $t_r = t_0$. The redshift is defined as:

$$\frac{a(t_0)}{a(t_e)} \equiv 1+z. \tag{2.14}$$

The expansion of the Universe results in an increase of the proper distance between galaxies with a large separation. When galaxies have small separations, they tend to form gravitationally bound systems like clusters. These systems are subject to peculiar velocities. [126] Since the recession velocity of galaxies is proportional to our distance to them, the effect of peculiar velocities v_{pec} is most noticeable for nearby objects. At sufficiently small luminosity distances, we can have $v_{pec} >> v_H$, with v_H the velocity of the Hubble flow. [127, 128]

This recession speed of a galaxy cannot be directly measured. The way to measure it is through the galaxy's redshift. As a galaxy moves away from us, or as the space between two galaxies expands, their characteristic absorption and emission lines get shifted towards redder wavelengths. Conversely, when a galaxy moves towards us, these lines shift towards bluer wavelengths (we can then speak of blueshift). [115] This technique was first used by Slipher in 1912, who used measurements of the redshift of the Andromeda galaxy to determine the velocity at which our galactic neighbour was moving towards us. [129]

To be more specific, the redshift z of an object is defined as the fractional Doppler shift of its emitted light due to radial motion. [130] The cosmological redshift of an object is defined as the redshift contribution from the expansion of the Universe. Since there is a relationship between the distance of an object and how fast the Universe is expanding at that point, cosmological redshift can be used as a distance marker. It should be noted that this is not quite true; as the rate of expansion of the Universe evolves with time, so does the redshift. The imparted change is however very small, especially compared to the changes in redshift due to the change in peculiar velocity of either the source or the observer. [131]

Edwin Hubble originally measured the value of his eponymous constant to be $H_0 = 500$ km s^{-1} Mpc^{-1}. [117] Issues with the calibration used in estimating the Hubble were raised in 1958 by cosmologist Allan Sandage. His work gave us the first reasonable estimate for the Hubble constant, with a measured value of $H_0 = 75$ km s^{-1} Mpc^{-1}. [132]

2.1.2 The Standard Model of Cosmology

The study of the Universe as a system relies on certain assumptions about its structure. These assumptions are known as the Cosmological Principle.

The Cosmological Principle states that, on large scales ($>$ 300Mpc), the Universe is spatially both homogeneous and isotropic. These assumptions underpin the standard model of cosmology. This means that the place we occupy in the Universe is not a special one. No matter what point in the Universe you stand on, it will look the same (**homogeneity**); no matter what direction you look in, it will look the same (**isotropy**).

Definition

The Cosmological Principle: On large scales, the Universe looks isotropic and homogeneous.

The cosmological principle holds up on large scales, as observed by redshift surveys like the Sloan Digital Sky Survey. While there is structure on smaller scales such as filaments, voids and clustering, on those larger scales there is no distinguishable structure.

While the expansion of the Universe had been known about for a longer time, up until 1998, this expansion was believed to be decelarating due to gravity. The deceleration was quantified by the parameter q_0. [133] It therefore came as a surprise that the expansion of the Universe was actually accelerating. [134, 135] This supported a non-zero cosmological constant Λ, previously considered to be a "blunder" in Einstein's equations.

The paper, published in 1998, presented observations of high-redshift Type Ia supernovae which showed that their luminosity distances were 10 to 15% larger than what would be expected in a $\Lambda = 0$ Universe. [135]

The standard model of cosmology is referred to as the ΛCDM (Λ Cold Dark Matter) model. This model underlies much of modern cosmology, including some methods for measuring the Hubble constant.

2.2 Methods for Measuring the Hubble Constant

This section briefly introduces methods for measuring the Hubble constant. The two main methods of measuring the Hubble constant are from local observations (late Universe) and from early Universe observations. Local observations are inferred directly on scales $>$ 100Mpc. [136] Early Universe methods are indirect and rely on assuming a (ΛCDM) Universe.

2.2.1 The Cosmic Microwave Background

The Hubble constant can be measured from observations of the early Universe.

The Cosmic Microwave Background was first observed in 1964 as a faint radiation filling the sky in all directions. The discovery was made with the Holmdel Horn Antenna at the Crawford Hill Laboratory.[1] The discovery was first reported in 1965. [139]

The CMB is radiation from the epoch of recombination which has travelled and cooled down to a present temperature of $T_0 = 2.725 \pm 0.001K$. [115] On large angular scales, it contains the imprints or primordial gravitational potential fluctuations. [140, 141]

The ability to obtain a measurement for H_0 from measurements of the CMB comes from the fact that the cosmological principle is not *quite* exact; small irregularities, called anisotropies, are expected in the CMB. These anisotropies, tiny differences in temperature in the CMB of the order of $\frac{\Delta T}{T} \sim 10^{-5}$, were first detected by the COBE mission in 1992. [115, 140]

The Planck mission, a successor to the Wilkinson Microwave Anisotropy Probe (WMAP) and Cosmic Background Explorer (COBE) satellites, measures anisotropies in the cosmic microwave background. [142, 143] The physical scale of anisotropies and the temperature at which the CMBR is emitted can be predicted theoretically. By measuring the angular scale of anisotropies and their temperature, it is possible to estimate the distance and redshift of the CMB, which in turn can give us an estimate of the Hubble constant. The angular power spectrum of the Uni-

---

[1] It is amusing to note that the CMB was first thought to be pigeon excrement on the antenna rather than of astrophysical origin - two pigeons had set up inside the antenna. However, after trapping the birds and cleaning the equipment, the signal persisted. [137] More than 50 years later, birds masquerading as signals of astrophysical origin are still an ongoing issue, with a mysterious signal at the LIGO Hanford detector turning out to be thirsty ravens pecking at ice on the cryogenic pumps. [138]

verse was found to be consistent with an inflationary, spatially flat ΛCDM model specified by 6 parameters. [144–146]

At the time of writing, the latest measurements from Planck give a Hubble constant of $H_0 = 67.4 \pm 0.5$ km s^{-1} Mpc^{-1} [143]

2.2.2 Standard candles

Local measurements of the Hubble constant require that we determine the distance to astrophysical objects. For very distant objects, this is not straightforward; in order to use luminosity-distance relationships, we need a reference for how bright an object is supposed to be.

Enter the cosmic distance ladder: a succession of methods for measuring the distance to far-out astrophysical objects, with each "rung" of the ladder defined by how nearby the objects are. The distance to nearby objects can be measured using parallax. [147]

Standard candles are astrophysical systems from which a luminosity distance can be obtained, due to their well-known, characteristic luminosities. The luminosity distance d_L relates an object's observed flux F to its intrinsic luminosity L.

Type Ia supernovae

Type Ia supernovae allow us to probe the Universe well into the smooth Hubble flow, making them powerful distance indicators. They are extremely luminous point sources generated by the thermonuclear explosions of white dwarfs. [148, 149] Because all Type Ia are the result of the same process, they have characteristic, well-known light curves.

At the time of writing, the latest local measurement of the Hubble constant released by the SHoES team with Hubble Space Telescope observations of type Ia supernovae gives a Hubble constant value of $H_0 = 73.04 \pm 1.04$ km s^{-1} Mpc^{-1}. [150]

Cepheid variable stars

Cepheids are luminous variable stars that undergo pulsations. The relationship between the period of their variability and their pulsation, the period-luminosity relationship, makes them ideal for measuring distances. [151] They were first observed by astronomer Henrietta Swann Leavitt in 1908. [152] Her observations of 1777 variable stars in the Magellanic clouds led to the discovery that the luminosity of these stars was related to their pulsation period. [153, 154] This Cepheid period-luminosity relationship, or Leavitt Law, makes Cepheid variable stars a powerful tool for measuring distances to nearby galaxies.

2.2.3 The Hubble tension

Early Universe and local measurements of the Hubble constant are in disagreement. At the time of writing, the Hubble tension has passed 5σ. [150]

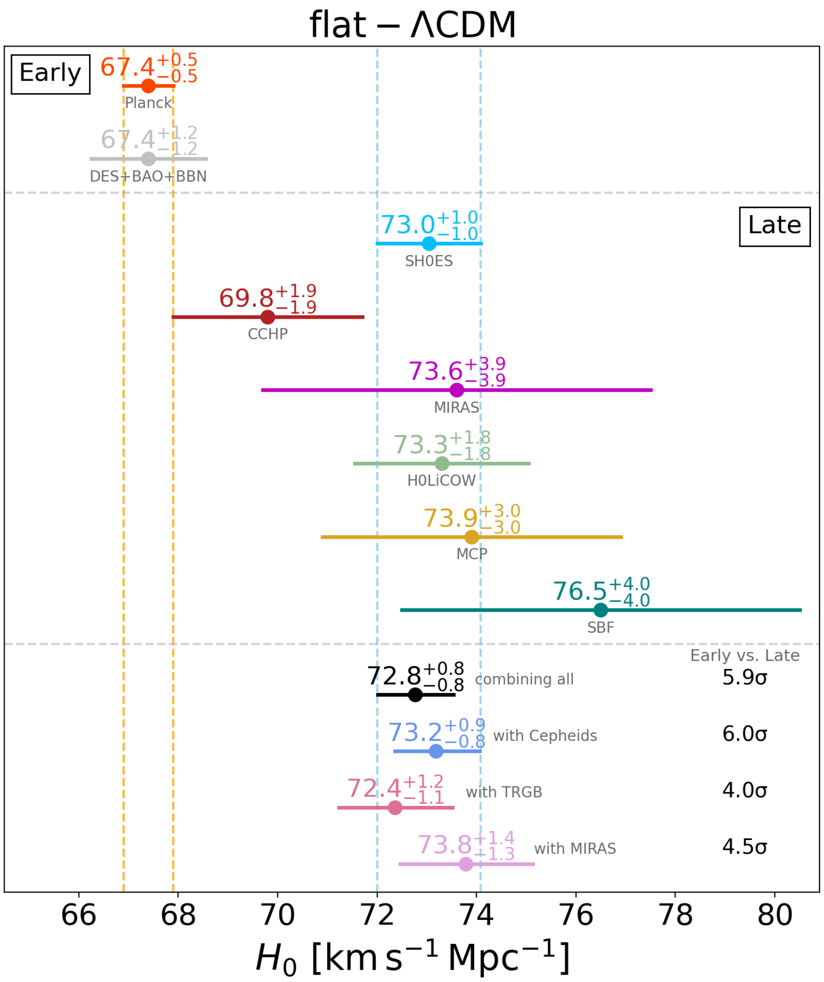

Figure 2.2: Plot illustrating the current state of the Hubble constant, with early vs late Universe measurements. Figure generated with code from [155], updated with the latest SH0ES results from [150]

Figure 2.2 shows the latest measurements of the Hubble constant from early- and late-Universe methods. This tension could spell trouble for the ΛCDM model, or could indicate the presence of some unaccounted-for systematics. This makes independent measurements of the Hubble constant which do not rely on model assumptions or the cosmic distance ladder an important tool for understanding the discrepancies between different H_0 measurements.

2.3 Cosmology with Gravitational Waves

Section 2.2 presented an overview of methods for measuring the Hubble constant. A third method, analogous to standard candles, makes use of gravitational wave signals as cosmological probes. This method is independent of the other methods described in the previous section, and could become an important tool in understanding the tension between the local and early Universe measurements of the Hubble constant. At the time of writing, the latest Hubble constant measurement from gravitational waves comes from the analysis of the GWTC-3 data, with a value of $H_0 = 68^{+12}_{-8}$ km s^{-1} Mpc^{-1} using the redshifted masses, and $H_0 = 68^{+8}_{-6}$ km s^{-1} Mpc^{-1} for the galaxy catalogue method. [156]

The idea of using the gravitational wave emission from mergers of compact objects to probe cosmological parameters pre-dates the direct detection of gravitational waves by $\sim$30 years. In 1986, Bernard Schutz proposed that gravitational waves from compact binary coalescences could be a new, independent cosmological probe. [157] These would later be known as standard sirens, the gravitational wave counterpart to standard candles. Similarly to standard candles, standard sirens yield a luminosity distance. The paper outlines a method for measuring the Hubble constant H_0 using binary neutron star mergers as dark sirens - standard sirens without an accompanying electromagnetic counterpart.

However, unlike standard candles, which depend on knowledge of other rungs of the cosmic distance ladder for calibration, compact binary coalescences are calibrated by general relativity. While the distance estimates obtained from gravitational waveforms have large uncertainties (up fo $\sim$40%), this self-calibration means that standard sirens are not subject to the same astrophysical systematics as standard candles, making them a powerful tool for cosmography. [158] Gravitational wave signals from compact binary coalescences are, essentially, a self-calibrating distance ruler, yielding absolute distances from their waveforms.

As the orbits of compact binary systems shrink during their inspiral phase, they lose energy in the form of gravitational radiation. Information on the luminosity distance can be obtained from this GW signal, and if observed by a network of detectors, then the host galaxy of the event can be localised, giving us information about the redshift. The luminosity distance obtained from the source is an absolute distance, under the assumption that the binary coalescence waveform is accurately described by general relativity. [158]

Because the inspiral phase of CBCs is well-modelled, and thanks to breakthroughs in the field of numerical relativity, it is possible to obtain a distance from the entire gravitational wave waveform of a CBC. [159–162]

If we take a BNS system located at a distance $d_L = 100r_{100}$ Mpc and emitting gravitational waves at a frequency of $100f_{100}$ Hz, we have:

$$r_{100} = 7.8 f_{100}^{-2}(\langle h_{23}\rangle \tau)^{-1}, \tag{2.15}$$

where τ is a measure of the timescale on which the frequency of the binary changes and $\langle h_{23}\rangle = \langle h\rangle * 10^{23}$, and $\langle h\rangle$ is the root mean square amplitude, or strain, of the gravitational waves, averaged over all detector and source orientations. [157] From this equation, we can see that the luminosity distance of the system is dependent on the measured strain h and the frequency f_{100}.

While some redshift information is obtained from gravitational wave events, it is degenerate with the chirp mass, meaning it is important to obtain redshift information through other means for inferring cosmological parameters. [157, 163] For binary neutron stars, in the case where no electromagnetic counterpart is observed and the host galaxy not resolved, it is possible to use the narrow mass distribution of neutron stars to get a redshift distribution for the system. [164] However, the redshift obtained from this method would contain contributions from the velocity of the system along with the velocity of the Hubble flow.

Definition

Chirp Mass: The chirp mass of a compact binary coalescence is well measured from its gravitational waveform. It is a combination of the component masses m_1 and m_2 of the system, with $\mathscr{M} = \frac{(m_1m_2)^{3/5}}{(m_1+m_2)^{1/5}}$. It's affected by the redshift of the system; the redshifted chirp mass is $\mathscr{M}_{\ddagger} = (1+z)\mathscr{M}$ for a system with redshift z and chirp mass $\mathscr{M}$.

Another method of obtaining the redshift, proposed by Schutz, is to use galaxy catalogues to assign a probable host galaxy to a gravitational wave event. With this method, each potential host galaxy is assigned a probability of being the true host of the GW signal for a range of values of the Hubble constants. When we marginalise over all potential hosts and using several gravitational wave events, an estimate of the Hubble constant can be obtained. [157, 165]

Gravitational wave cosmology offers an independent method for measuring the Hubble constant, making it an important tool in starting to understand the Hubble tension.

3 | Methods for parameter estimation

> I often think that the night is more alive
> and more richly colored than the day.
>
> Vincent Van Gogh

This chapter outlines methods used for parameter estimation, in particular inferring ejecta parameters from kilonova light curves. It is divided into four main sections: Bayesian inference, kilonova models, Gaussian Process Regression and parameter estimation.

3.1 Bayesian Inference

The principles of data analysis for gravitational wave astrophysics rely on applications of **Bayesian inference**. Bayesian inference is an approach to probability used extensively in many fields of astronomy and astrophysics, including gravitational wave astronomy. This section introduces the history and principles of Bayesian inference. The methods used in this thesis make use of these principles.

3.1.1 History

The unusual history of Bayesian inference starts in the eighteenth century with the work of reverend Thomas Bayes. He developed a theory to estimate the probability of an event occurring knowing how many times it had occurred in the past. Largely unnoticed at the time, the work was published posthumously by Richard Price, along with amended and added material. [166] The theory was also rediscovered independently and given its mathematical form by French polymath Pierre Simon Laplace. [167] The Bayesian approach to probability then resurfaced in the twentieth century with many successful applications, from decision-making to optimising searches for the wreckage of planes.

Bayesian inference was not always met with widespread acceptance; in the nineteenth century, it was met with virulent backlash in the context of the Dreyfus affair, when French mathematician Henri Poincare used Bayesian reasoning to refute the accusations made against Alfred Dreyfus. [167]

Bayesian inference knew a resurgence during World War II, with the release of Harold Jeffrey's *The Theory of Probability*. [168] The code for the German enciphering machine Enigma was cracked by Alan Turing using a Bayesian inference technique that he developed. [167, 168]

Bayesian probability can be understood as "Probability Theory as logic"[1], as opposed to frequentist approaches which focus more on calculating frequencies of random variables as probability, relying on "identical repeats". [169]

Nowadays, many scientific fields rely on the application of **Bayesian inference** for statistical analyses. There are many advantages to using Bayesian inference in the physical sciences. It particularly shines in the fields of modern astrophysics and cosmology. Some of the reasons for this are: [170]

- The models used in cosmology and astrophysics are increasingly complex, requiring efficient and sophisticated inference tools. This is also a consequence of the recent data explosion in cosmology.
- The field requires an approach that can effectively deal with incomplete data and biases such as selection effects
- The limited resources of the field; strategies need to be optimised to maximise scientific returns
- Astronomy and cosmology often have limited, complex and sometimes poor data which cannot always be improved.

Bayesian inference is also used extensively for data analysis in gravitational wave astronomy. It is useful in helping discriminate gravitational wave signals from astrophysical sources from noise, and for dealing with the high-dimensional parameter spaces of compact binary coalescences.

Definition

Bayesian Inference: An approach to probability based on "plausibility" of a hypothesis A conditional on B, $p(A|B)$. In Bayesian inference, our degree of uncertainty is encoded into probability distributions for model parameters or hypotheses. [169]

Any use of Bayesian inference stems from the application of **Bayes' Theorem**. This equation, also known as Bayes' rule, can be derived from basic rules of sum and product probabilities, which are outlined in the sections below.

---

[1] A wonderfully humourous example can be found in xkcd

3.1.2 Principles of Bayesian inference

The sum rule and the product rule

Bayes' theorem can be derived from two basic rules of probability: the sum rule and the product rule.

$$p(A|B)+p(\overline{A}|B)=1, \tag{3.1}$$

and

$$p(A,B|C)=p(A|C)p(B|A,C)=p(B|C)p(A|B,C), \tag{3.2}$$

in which $p(A|B)$ is the probability that A is true given B, and $p(\overline{A}|B)$ is the probability that A is not true given B. Given that, in this situation, there are only two possible outcomes (either A is true or it isn't), and that the product $A\overline{A}$ is always false (the two propositions, A is true and A isn't true, cannot be true at the same time) the sum of these probabilities must add up to 1. The two propositions governing the sum rule are of the Aristotelian logical type. [171]

$p(A,B|C)$ is the probability of A and B being true given C. This is known as the joint probability of A and B. The product rule can be derived through extended logic. [169]

Bayes' Theorem

When combining these rules, we arrive at the expression of Bayes's theorem seen in equation 3.3.

$$p(H|D,I)=\frac{p(H|I)p(D|H,I)}{p(D|I)}, \tag{3.3}$$

where:

- H is our hypothesis,
- D is the data,
- I is the background information,
- $p(H|D,I)$ is the posterior,
- $p(H|I)$ is the prior,
- $p(D|H,I)$ is the likelihood,
- $p(D|I)$ is the marginal likelihood, or evidence.

3.1.3 Marginalisation

Marginalisation offers a way of dealing with nuisance parameters. If a distribution depends on parameters that are of little or no interest to us, these are called nuisance parameters.

In Bayesian inference, these nuisance parameters are dealt with through marginalisation: that is, integrating through the entire parameter space for the nuisance parameters.

For example, for a probability $p(X)$ depending on a continuous parameter H:

$$p(X) = \int_H p(X,H)dH, \tag{3.4}$$

$$p(X) = \int_H p(X|H)p(H)dH. \tag{3.5}$$

Marginalisation can also be applied to the discrete case, with $p(X)$ depending on a parameter H that can take n values H_i:

$$p(X) = \sum_{i=1}^{n} p(X|H_i)p(H_i) \tag{3.6}$$

This is especially useful for the denominator, or marginal likelihood, of Bayes' theorem. Applying marginalisation to the marginal likelihood as defined in equation 3.3, in the discrete case with a hypothesis H_i, we can define the extended Bayes' theorem:

$$p(D|I) = \sum_{i=1}^{n} p(D|H_i,I)p(H_i), \tag{3.7}$$

$$p(H_j|D,I) = \frac{p(H_j|I)p(D|H_j,I)}{\sum\limits_{i=1}^{n} p(D|H_i,I)p(H_i)}. \tag{3.8}$$

3.2 Kilonova Models

An overview of kilonovae, including searches, models and detections, was presented in chapter 1.

Kilonovae can produce a diverse range of light curves. [172] These light curves differ depending on the parameters of the kilonova ejecta that emerges from the merger of two neutron stars, or of a neutron star with a black hole. The composition and other parameters of this ejecta vary depending on the parameters of the merger, including the outcome of the merger and nature of the remnant. [75] Outcomes of this type of merger, such as prompt collapse to a black hole or magnetars accelerating ejecta, vary and influence the resulting light curves. [172]

During the merger of two neutron stars or a neutron star with a black hole, matter can be flung through different ejection mechanisms and with different parameters. The resulting kilonova light curves will be dependent on these parameters. Inferring the ejecta parameters from kilonova light curves requires that we have accurate models of kilonovae.

Kilonova models vary in complexity and in the number of ejection mechanisms they incorporate. These can range from toy models, which are often simple analytical equations, to complex models that are the results of simulations taking into account many mass ejection mechanisms and microphysics. [75]

The first kilonova model, with parameterised heating, was released in 1998 by Li and Paczyński. [70] The model was a simple analytical model predicting the bolometric luminosities of a transient resulting from a neutron star merger. Twenty years later, the 1990s saw the advent of the first hydrodynamics simulations of kilonovae. [71, 83]

Since then, kilonova modelling has been a very active field of astrophysics, especially expanding following the first confirmed detection of a kilonova from the merger of two neutron stars following the gravitational wave event GW170817. [40]

In order to infer ejecta parameters from kilonova observations, we need models that can predict the observed light curves as a function of ejecta parameters and time post-merger. The models used in the analysis presented in subsequent chapters are the 1-dimensional radiative transfer models developed in 2017 by Kasen et al. [94] They are time-resolved spectra obtained through the use of a Monte Carlo code that solves the multi-wavelength radiation transport equation in a relativistically expanding medium. [94, 173, 174] These models identify two components, each with different mechanisms for mass ejection in a binary neutron star merger:

- A dynamical mechanism (blue component): the ejecta matter is expelled during the merger, as tidal forces on the orbital place and shock heating at the contact interface of the two stars fling out matter from the neutron stars. Tidal forces peel away matter from the surface of the approaching stars, while shock heating squeezes additional matter into the polar regions. [71, 94, 175, 176]

- A "wind" mechanism (red component): roughly one second after the merger, matter from the accretion disc around the merger remnant is blown away in winds at lower velocities than the squeezed component. [177–182] This component is sensitive to the fate of the merger remnant, and can result in blue (remnant survives as hot NS for tens of milliseconds) or red (prompt collapse to a BH) winds. [94]

The red component is made up primarily of heavy r-process elements (elements whose atomic mass is greater than 140), while the blue component is made primarily of lighter r-process elements. The models are generated from synthesised observables obtained by numerically solving the Boltzmann equation for relativistic radiation transport in radioactive plasma. [94] The

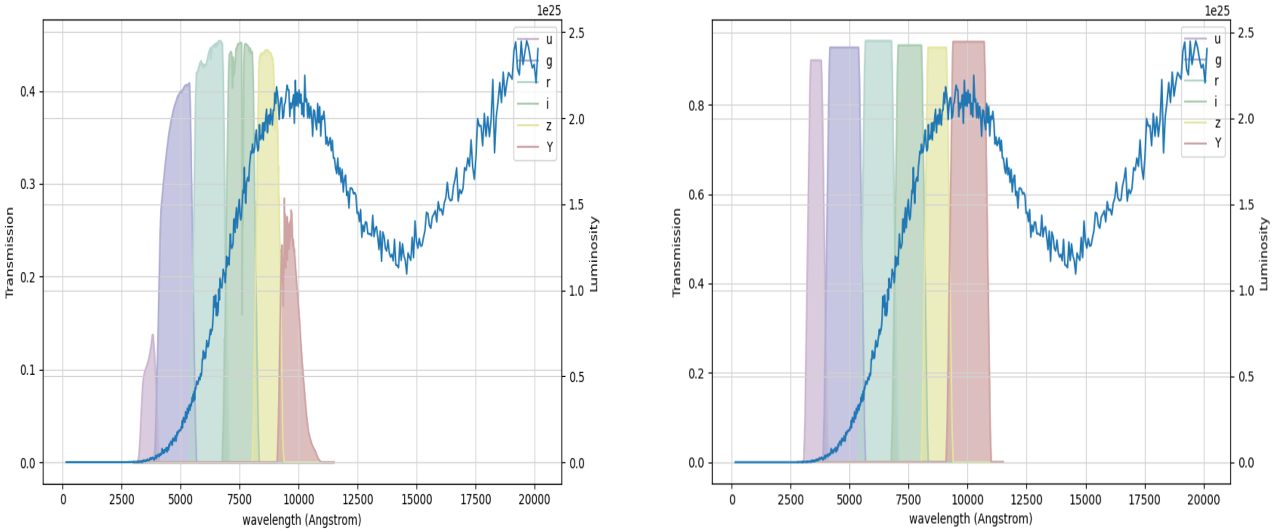

Figure 3.1: Example of a time-resolved spectrum for a kilonova taken from the grid of models by Kasen et al. Both the baseline ideal transmission filters (right) and total transmission filters taking into account instrumental effects (left) are presented. The filters are obtained from the baseline LSST throughputs. [183]

two components that make up the light curves are spatially distinct. The parameters for each component are the ejecta mass m_{ej}, ejecta velocity v_{ej}, and lanthanide fraction X_{lan}.

3.3 Gaussian Processes

Section 3.1 presented a brief introduction to Bayesian inference. The following section introduces Gaussian Process Regression, a regression scheme that applies principles of Bayesian inference.

The kilonova models used in the work presented in this chapter and the two following chapters are the results of radiative transfer simulations. These are generated for a finite grid of ejecta parameters, and are computationally expensive to generate. While parameter estimation is possible using the grid of discrete models, this results in awkward posterior distributions, multi-modalities and degeneracies.

In order to use this finite number of kilonova light curves for parameter estimation, it is therefore best to implement an interpolating scheme for the light curves, making it possible to generate light curves for any given set of physical parameters.

Two approaches are possible: interpolating the spectra, or interpolating the resulting broadband light curves. We choose to interpolate the light curves rather than the spectra. Work on interpolating the time-resolved spectra using Gaussian Process Regression can be found in [68].

There are a number of existing interpolating schemes, such as linear interpolation or nearestneighbour interpolation. Gaussian Process Regression is a powerful non-linear interpolating scheme, which we use in this work.

Gaussian processes are a stochastic process defined as a collection of random variables, any finite number of which have a joint Gaussian distribution - hence the name "Gaussian Process". They are used to infer directly in function space, by describing a distribution over functions. [184] They offer a flexible and robust way of interpolating data. They are completely defined by a set of two functions: a mean function and a covariance function.

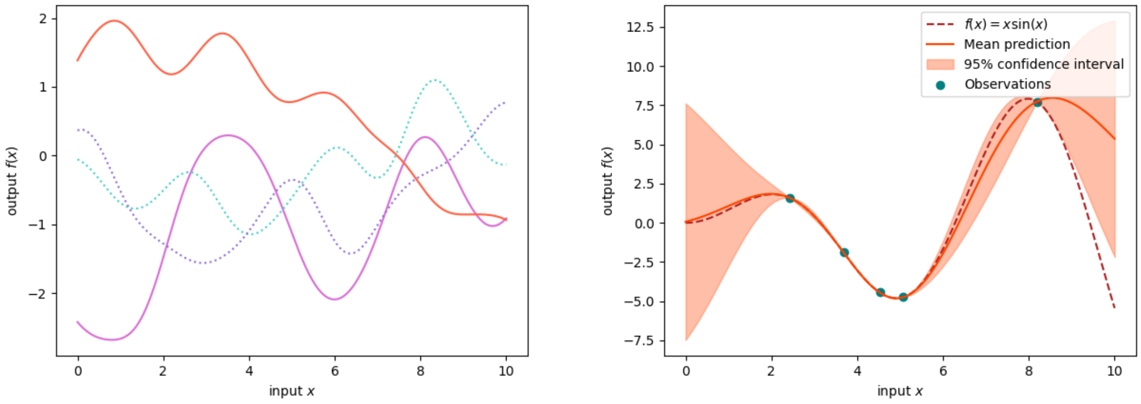

Figure 3.2: Functions drawn from GP prior (left) and posterior (right) i.e. prior conditioned by 5 noiseless data points drawn from a real function $f(x) = x \sin x$.

Gaussian Processes make use of covariance functions, which encode our assumptions about the shape of the underlying function defining the model. [184] The untrained covariance function defines our prior for the Gaussian Process. When the Gaussian Process is trained, the posterior distribution of functions is updated using data points from the models. This training can be done on either noiseless or noisy data points.

Figure 3.2 shows an example of Gaussian Process Regression. The left-hand side plot shows sample functions drawn from the kernel of the Gaussian Process, which constitutes the prior. The right-hand side plot shows one of these functions conditioned on five noiseless data points.

3.3.1 Training a Gaussian Process on kilonova light curves

The kilonova models used for training the Gaussian Process are the ones described in section 3.2. These models are time-resolved spectra, which are convolved with LSST filters to produce light curves in the *griz* bands. The original dataset consists of 329 light curves for times up to 25 days post-merger with a 0.1 day time resolution.

Light curves are generated using the time-resolved spectra and LSST *griz* filters. Figure 3.1 shows an example of a time-resolved spectrum from one of the kilonova models, with the *ugrizY* LSST filters. To get expected magnitudes for astronomical objects, the baseline ideal filters are convolved with the time-resolved spectra. [183] In order to smoothe out the numerical noise (due to the Monte Carlo sampling) present in the models, the light curves are smoothed with a rolling 0.5 day window. Data points beyond $t = 10$ days are discarded for training, along with any data points where the models become completely unreliable - this is marked by a sudden, sharp drop in the light curve.

The kilonova ejecta becomes optically thin at times well beyond the light curve peak. At these times, the model is less reliable due to the approximation of local thermodynamic equilibrium breaking down. [94] Because the models are less reliable at later times, we only train the Gaussian Process and run parameter estimation on the first 10 days post-merger.

We train the Gaussian Process on light curves generated from these spectra rather than the spectra directly. This is to allow for quicker inference using broadband observations in the time domain. This also makes the training, especially the choice of kernel function, more straightforward. A different Gaussian Process is trained on each filter band.

The smoothed *griz* light curves are found in figure 3.3. The figure shows all one component light curves, including those with a lanthanide fraction of $X_{lan} = 10^{-9}$, which are discarded in the training. This is due to the large gap in the parameter space between light curves with $X_{lan} = 10^{-5}$ and $X_{lan} = 10^{-9}$. Considering this subset of the models allows for better interpolation from the Gaussian Process. This also helps reduce the amount of data points used, which is important for training Gaussian Processes. There are 55 light curves (out of 329) with $X_{lan} = 10^{-9}$.

The complexity of Gaussian Processes goes with N^2, with N the number of data points. The complexity of GPRs also increases sharply with dimensionality. [184]

Two methods are used to get around the complexity of the dataset:

- Downsampling the data
- Using a Hierarchical Off-Diagonal Low-Rank (HODLR) solver

The kernel is chosen to be an addition of two exponential squared quadratics, one acting on all dimensions and one acting on the time dimension only. This is to reflect the variation in length scale for the time dimension, capturing both the rapid peak of the kilonova at 1-2 days post-merger and the slow decay in magnitude of the light curve.

3.3.2 Training and optimising a Gaussian Process

Solver

We use a HODLR solver implemented within the **`george`** python module. [185] The HODLR solver is based on the Hierarchical Off-Diagonal Low-Rank structure. For n-dimensional problems, the inversion of an $n \times n$ covariance matrix is required. With standard methods, the complexity of this matrix inversion goes with $\mathscr{O}(n^3)$. The HODLR solver offers an $\mathscr{O}(n \log^2 n)$

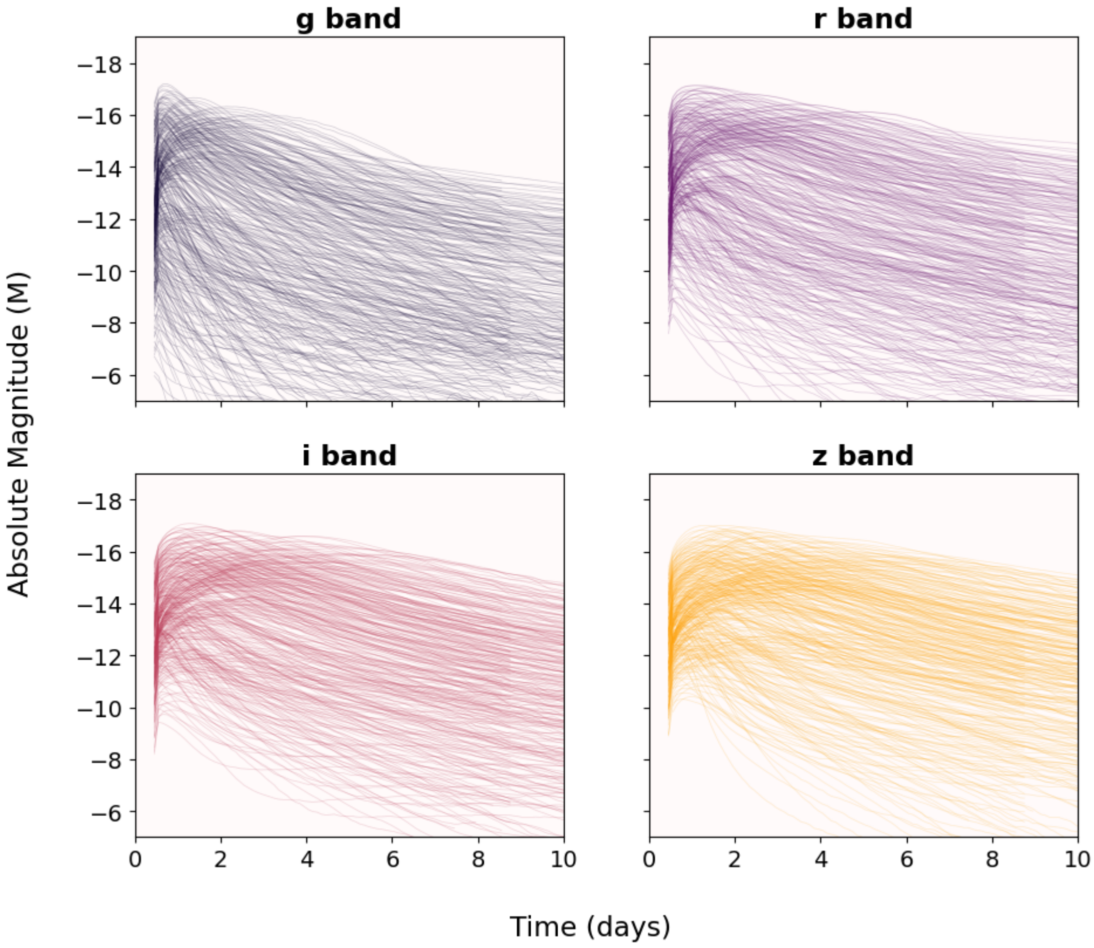

Figure 3.3: Smoothed models for *griz* bands. These are single-component light curves generated from time-resolved spectra using the filters seen in figure 3.1, smoothed with a rolling mean with a 0.5 day window.

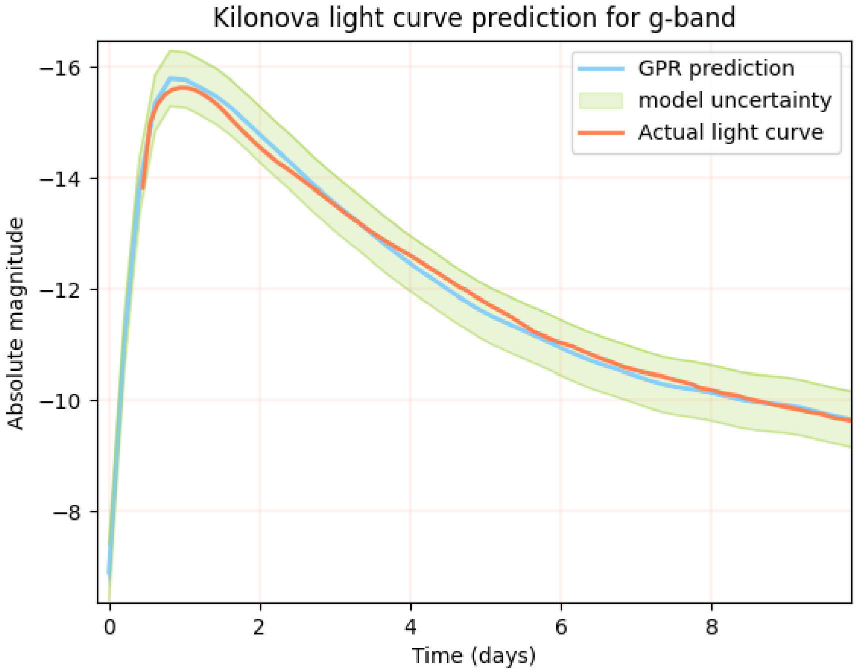

Figure 3.4: GPR predictions for a kilonova light curve using LSST g-band, with ejecta parameters m_{ej} = 0.05 $M_\odot$, v_{ej} = 0.1 c and $X_{lan} = 10^{-4}$. Holdout validation with this set of parameters removed from the training.

algorithm for factorising matrices. This method can be applied to any choice of covariance function.

The kilonova models can be treated as a 5-dimensional grid. The x-parameters fed into the Gaussian process are time (t), lanthanide fraction (X_{lan}), ejecta mass (m_{ej}) and ejecta velocity (v_{ej}). The y-axis is the absolute magnitude corresponding to these parameters and the band the GPR is being trained on. There is a separate trained GPR for each band used in the analysis, here the *griz* bands.

Hyperparameters

As described previously, Gaussian Processes are trained using what we call a kernel as a prior in the function space. This kernel will be different depending on the shape and dimensionality of the dataset.

For the dataset in this problem, we choose a combination of two kernels. The first kernel acts on all 4 x-dimensions, while the second kernel acts only on the time dimension.

Two kernels act on the time dimension in order to capture both the rapidly peaking epoch of the kilonova light curve (∼1-2 days) and its subsequent slow decay. Only one of the kernels acts on the other dimensions. The lengthscales of this kernel for each physical parameter relates to the spacing of the parameter grid from the models used for training.

With this problem, we hand-tune the hyperparameters and verify the trained model with holdout validation, where one part of the dataset is excluded from the training. For some datasets, optimisation of the hyperparameters can be done systematically through optimising the cross-validation likelihood and the marginalised log-likelihood.

An example of the output from a GPR trained on the g-band data is presented in figure 3.4, along with the true light curve. The figure shows an example of holdout validation of the training; the light curve corresponding to a specific set of parameters is removed from the training dataset, and the results from the trained GPR for this set of parameters are shown against the corresponding true light curve.

3.4 Parameter Estimation on Light Curves

The kilonova parameters are inferred from the light curves for different observing bands.

Using the Gaussian process trained on kilonova models, one can define a function that defines an apparent magnitude

$$m = \mathscr{F}(\theta_{KN}, t, x, d_L), \tag{3.9}$$

with x the band, t the time in days post-merger, d_L the luminosity distance and θ_{KN} the ejecta parameters. These ejecta parameters are m_{ej}, v_{ej} and X_{lan}. Each magnitude m is generated by the trained GPR.

The likelihood of the parameters given the observed data is then

$$p(\theta|\mathscr{D}) = \prod\prod p(\mathscr{D}_{GPR}|\mathscr{D}, \theta), \tag{3.10}$$

where $\mathscr{D}_{GPR}$ is the set of magnitudes m_{GPR} corresponding to the ejecta parameters θ, time t, luminosity distance d_L and observing band x. To get the log-likelihood in the parameter estimation code, we evaluate the log probability density function for each sample of parameters θ giving a set of magnitudes $\mathscr{D}_{GPR}$

$$\sum_{band=x_i}^{x_n} \sum_{i=0}^{N} \log\sigma - \frac{1}{2}\log(2\pi) - \frac{1}{2}\left(\frac{m_{N,x_i} - m_{N,x_i}^{GPR}}{\sigma}\right)^2 \tag{3.11}$$

for N observations in a set of n bands $x_1 \dots x_n$, with m_{N,x_i} the simulated observations, m_{N,x_i}^{GPR} the observations generated by a GPR corresponding to a set of sampled parameters θ, and $\sigma = 1$mag the uncertainty on the models.

We use `NESSAI` as a fast sampler. [186] `NESSAI` is a sampler developed by Williams et al. which uses a machine learning algorithm known as normalising flows. Normalising flows are generative models that produce tractable distributions, allowing for efficient and robust sampling. Normalising flows work by transforming a specified, simple probability distribution into a more complex distribution through an invertible mapping. [187]

While `NESSAI` was originally developed for parameter estimation for gravitational wave astronomy, it is well-adapted to any problems where the likelihood is computationally expensive, as is the case here. Instead of using computationally expensive techniques like Markov Chain Monte Carlo (MCMC) or Nested Sampling, `NESSAI` makes use of a modified nested sampling algorithm that uses normalising flows for proposal. Other methods like parallel tempering, which could deal with degeneracies, had been used in previous instances of the code, but it was found that `NESSAI` greatly reduces the time taken for the parallel estimation code to run. [188,189]

4 | Kilonova parameter estimation

> Alors ce sera pour toi comme si riaient toutes les étoiles.
>
> Antoine de Saint-Exupéry, Le Petit Prince

This chapter presents the results of parameter estimation on kilonova light curves using the method outlined in chapter 3. It is split into two main sections. In the first section, we apply the methodology previously described to real data from the AT 2017gfo DECam observations. In the second section, we apply the methodology to simulated light curves. This second section focuses on recovering a merger time from simulated light curves generated using a Gaussian Process trained on models.

The first observing run of the Advanced LIGO detectors revealed 103 sub-threshold BNS candidates with a false alarm rate (FAR) of less than 1/day. Of these none were identified as unambiguous gravitational wave signals. Correlating such sub-threshold candidates with electromagnetic counterparts could help identify real signals. [190] The large number of sub-threshold candidates even in just the first observing run means Target of Opportunity dedicated follow-ups might not be possible for every BNS candidate. It is therefore more likely that a correlated EM signal would be a serendipitous discovery. With dedicated survey strategies, a number of kilonovae associated with sub-threshold signals could be detected, although this number would be affected by the duty cycles of the interferometers. [114]

There is also scope for GW searches from EM triggers. These searches typically require time windows obtained from the EM signals. There are already pipelines in place searching LIGO data for coincident BNS signals triggered by sGRB. Existing pipelines, like RAVEN, search *FERMI* GBM data for transient events that are temporally coincident with LIGO CBC triggers. [191, 192] Burst searches for signals accompanying supernovae are optically triggered, with a search window of $\sim$1.5 days [193]

We focus on the *griz* bands, which are the most commonly used in kilonova detection strategies and also make up for the bulk of LSST observations during the main survey. Observations in the *griz* bands make up for 73% of observations for the baseline strategy for the LSST survey. This makes these four bands ideal for serendipitous, non-triggered kilonova detections throughout the duration of the main survey. [114, 194]

Several observing strategies have been proposed for serendipitous kilonova discoveries. In one strategy, nightly *gi* observations are used 20 nights a month, in two blocks of 10 nights. [113] Other strategies focus on any nightly pairs of observations with an increase in cadence for multi-band observations. [114] Similar strategies have also been proposed for other deep surveys, for example the Zwicky Transient Facility (ZTF), a survey that currently observes the sky with a $\sim$3 day cadence. Proposed strategies favour nightly *gri* observations in order to maximise serendipitous observations of kilonovae with wide surveys such as ZTF, with a 470% improvement in number of detected kilonovae for nightly observations compared to a 3-5 day cadence. [112, 195] For more distant kilonovae, the *izY* bands are favoured. [196] In this work we focus on two cadences (nightly and every 5 nights) for different band filter pairs.

4.1 Parameter Estimation on Real Kilonova Light Curves

Using the DECam light curves for AT 2017gfo, we can test the method outlined in the previous chapter on real data, looking at the effect of band and start of observations on the recovered parameters. We choose to run the analysis on a set of observations from one instrument only in the *griz* band as this replicates a scenario close to that of the simulated ones with LSST light curves.

The dataset used in this analysis is presented in [197]. It is the result of an EM follow-up campaign for the GW signal GW170817 by the Dark Energy Camera (DECam) in the i and z bands over a 70deg^2 area. The transient AT 2017gfo was first detected by DECam in the i and z bands at 11.4hrs post-merger. This initial detection was followed-up by observations in the *ugrizY* bands. Of this dataset, we use the *griz* observations for up to 10 days post-merger.

4.1.1 Inferring ejecta parameters

The method outlined in the previous section is tested on observations of the kilonova associated with GW170817, AT 2017gfo. We use the DECam *griz* observations up to 10 days post-merger. As previously discussed, at later times the models are less reliable due to the ejecta becoming optically thin, meaning that the local thermodynamic equilibrium approximation breaks down. [94] This is why we only consider times up to 10 days post-merger.

We first run the parameter estimation code on the full light curves up to $t = 10$ days post-merger to recover only the ejecta parameters. The luminosity distance d_L is fixed at $d_L = 40$ Mpc, as is the merger time with the first observations at $t_0 = 11.4$ hrs. The uncertainty on the models is assumed to be Gaussian, with $1\sigma = 1$ mag. This conservative uncertainty budget captures hard-to-quantify uncertainties in the models used for this analysis, such as uncertainties on the electron fraction and heating rate which can result in differences in the predicted luminosities. [68, 198, 199]

The priors on the ejecta parameters are the following:

- X_{lan}^{red} log uniform 10^{-2} to 10^{-1}, X_{lan}^{blue} log uniform 10^{-5} to 10^{-2}.
- m_{ej} uniform from 0.001 to 0.1 $M_{\odot}$.
- v_{ej} uniform from 0.05 to 0.3 c with $v_{ej}^{blue} > v_{ej}^{red}$.

The priors are chosen to be uninformative and are guided by the shape of the parameter grid for the underlying models. The models are computed for values of X_{lan} distributed uniformly in log-space, and values of v_{ej} and m_{ej} are uniformly distibuted. The lower and upper bounds are determined by the lower and upper bounds of the computed light curves, as the Gaussian Process performs best as an interpolating scheme, with extrapolated light curves being unreliable.

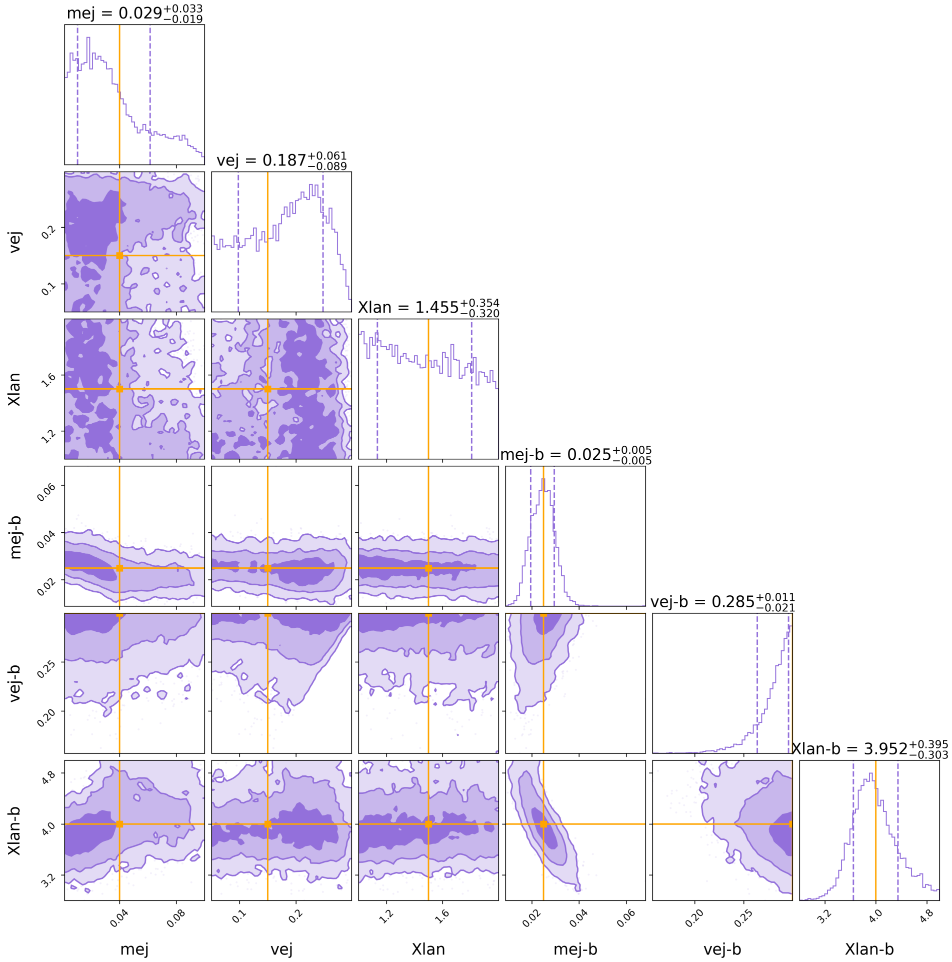

Figure 4.1: Full parameter estimation for *griz* AT 2017gfo DECam observations. True values (in orange) for ejecta parameters are taken from the best fit from the original work by Kasen et al. [94]. The data is fitted to a two-component kilonova light curve, with each component (red and blue) having its set of parameters $(m_{ej}, v_{ej}, X_{lan})$.The distance d_L is fixed and taken to be 40 Mpc.

Figure 4.1 shows the aforementioned parameter estimation on the kilonova ejecta parameters, using the AT 2017gfo *griz* DECam data and with a fixed t_0 and d_L. The corner plot shows posteriors for the inferred ejecta parameters, along with the best fit values taken from the original paper accompanying the models that were used for training the Gaussian Process, taken from [94]. The data is fitted to a two-component ("red"/lanthanide-rich and "blue"/lanthanide-poor) model. While not much information is recovered for some parameters, like $X_{lan,red}$ and $v_{ej,red}$, the final results are in good agreement with the best fit parameters from the original analysis, shown in orange on the figure.

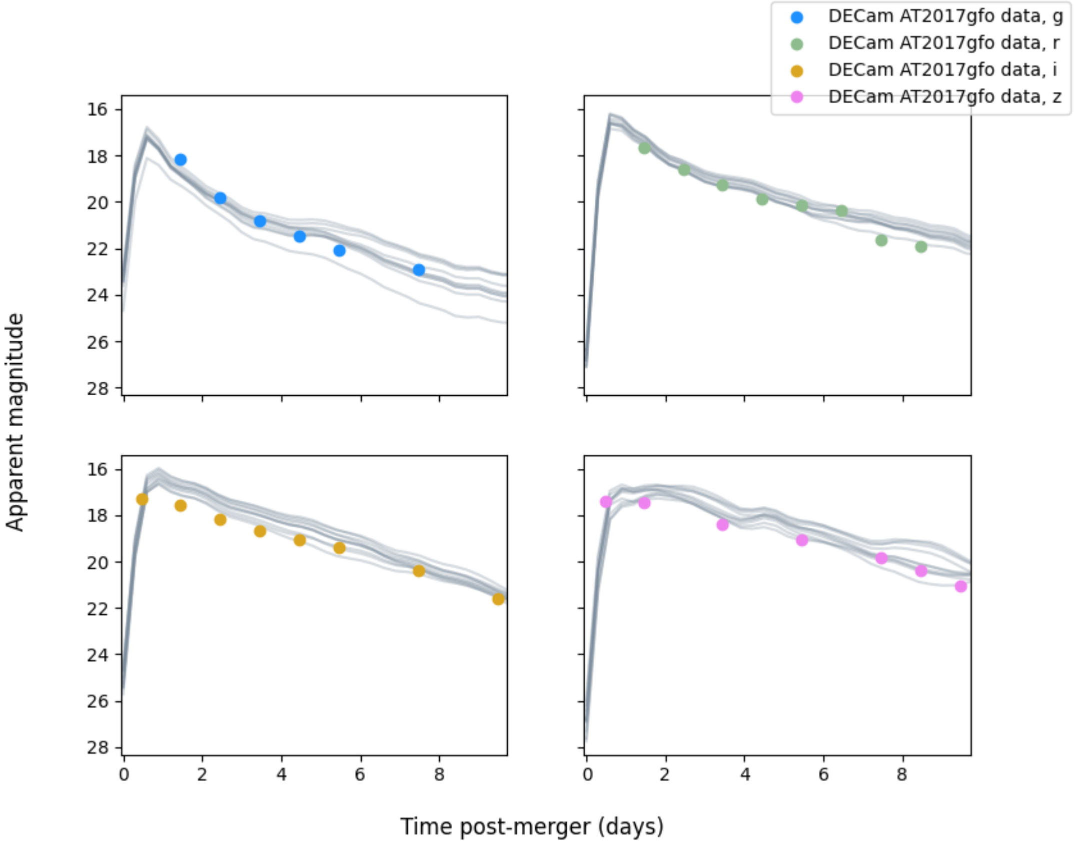

Figure 4.2: Light curves generated from posterior samples for the best fit to AT 2017gfo against *griz* AT 2017gfo DECam observations for 0 to 10 days. Each light grey line represents a posterior sample, while the filled circles are observations made by DECam during the GW170817 follow-up.

Figure 4.2 shows light curves generated from parameters sampled from the posterior in figure 4.1 against the DECam observations of AT 2017gfo in the *griz* bands. Figure 4.3 shows the same data with the light curves corresponding to the best fit parameters from table 4.1. We show 1mag uncertainties, which are used in the parameter estimation, around the best fit. The best-fit light curves are a good fit to the *griz* data.

Table 4.1 shows results from the parameter inference for our analysis on the DECam *griz* data for AT 2017gfo and other analyses presented in [94] and [68]. The results of our parameter estimation on the *griz* DECam data points are in good agreement with previous analyses. Differences in the final results can be due to the different datasets used; we only use the DECam

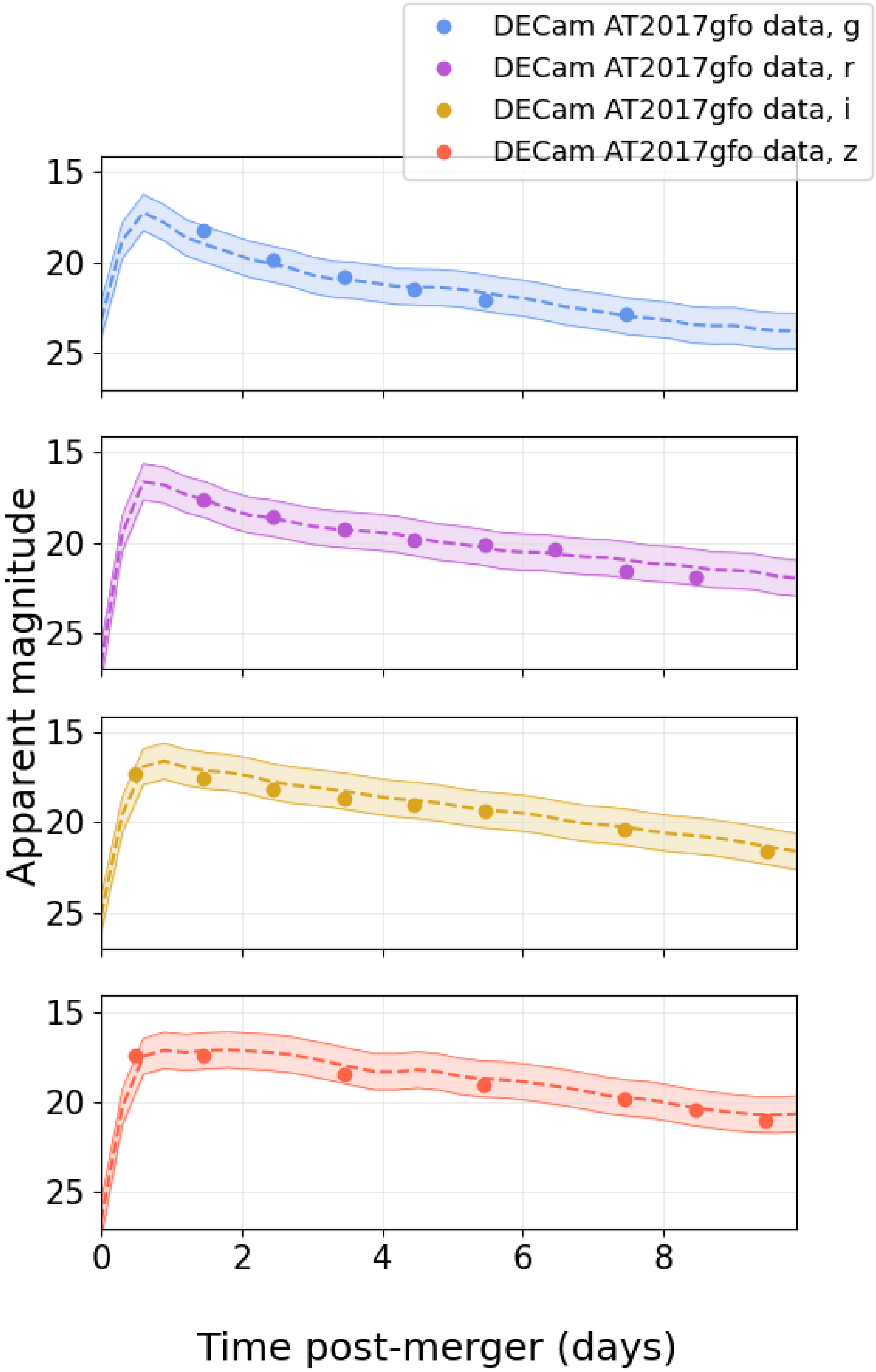

Figure 4.3: Light curves for the best fit parameters with 1 mag uncertainty vs *griz* AT 2017gfo DECam observations. The dashed lines are kilonova light curves generated for the best fit parameters to AT 2017gfo. These parameters can be found in table 4.1. The solid lines draw out a 1 mag uncertainty around the best fits, while the filled circles are the actual observations from DECam.

Parameter	Kasen	Coughlin	This work
m_{ej} (red) ($M_\odot$)	0.04	$0.03^{+0.02}_{-0.01}$	$0.03^{+0.03}_{-0.02}$
v_{ej} (red) (c)	0.15	$0.10^{+0.08}_{-0.06}$	$0.19^{+0.06}_{-0.09}$
$\log_{10}(X_{lan})$ (red)	-1.5	$-1.61^{+0.96}_{-1.04}$	$-1.46^{+0.35}_{-0.32}$
m_{ej} (blue) ($M_\odot$)	0.025	$0.024^{+0.01}_{-0.01}$	$0.025^{+0.005}_{-0.005}$
v_{ej} (blue) (c)	0.3	$0.17^{+0.09}_{-0.1}$	$0.28^{+0.01}_{-0.02}$
$\log_{10}(X_{lan})$ (blue)	-4	$-4.73^{+0.42}_{-0.20}$	$-3.95^{+0.40}_{-0.30}$

Table 4.1: Table of results for AT 2017gfo ejecta parameters. This table shows the best fit results from [94] and [68]. The analysis in this work is run only on the *griz* DECam observations up to 10 days post-merger, while the other fits are on the full dataset of observations.

griz dataset, while the other two analyses use the full dataset for AT 2017gfo observations. The full dataset is shown in figure 1.4.

Varying d_L

The previous parameter estimation was run for a fixed luminosity distance $d_L = 40$ Mpc. In this section, we allow d_L to vary by making it a parameter of the generated light curves. Figure 4.4 shows the ejecta parameter posteriors for a flat prior on d_L with 40% uncertainty bounds around $d_L = 40$ Mpc. This uncertainty is larger than the uncertainty from the gravitational wave luminosity distance obtained from GW170817 $d_L = 40^{+7}_{-15}$ Mpc, but is typical of d_L inferred from gravitational wave events. [39] The priors on all ejecta parameters are the same as described previously for the parameter estimation with a fixed luminosity distance.

The resulting inferred parameters are similar to the parameters inferred without varying d_L, with the recovered ejecta parameters still in good agreement with other analyses.

Figure 4.5 shows the PE for a wider prior on d_L (uniform from 0 to 100 Mpc). The posteriors are similar to the posteriors for the tighter prior on d_L and for a fixed d_L.

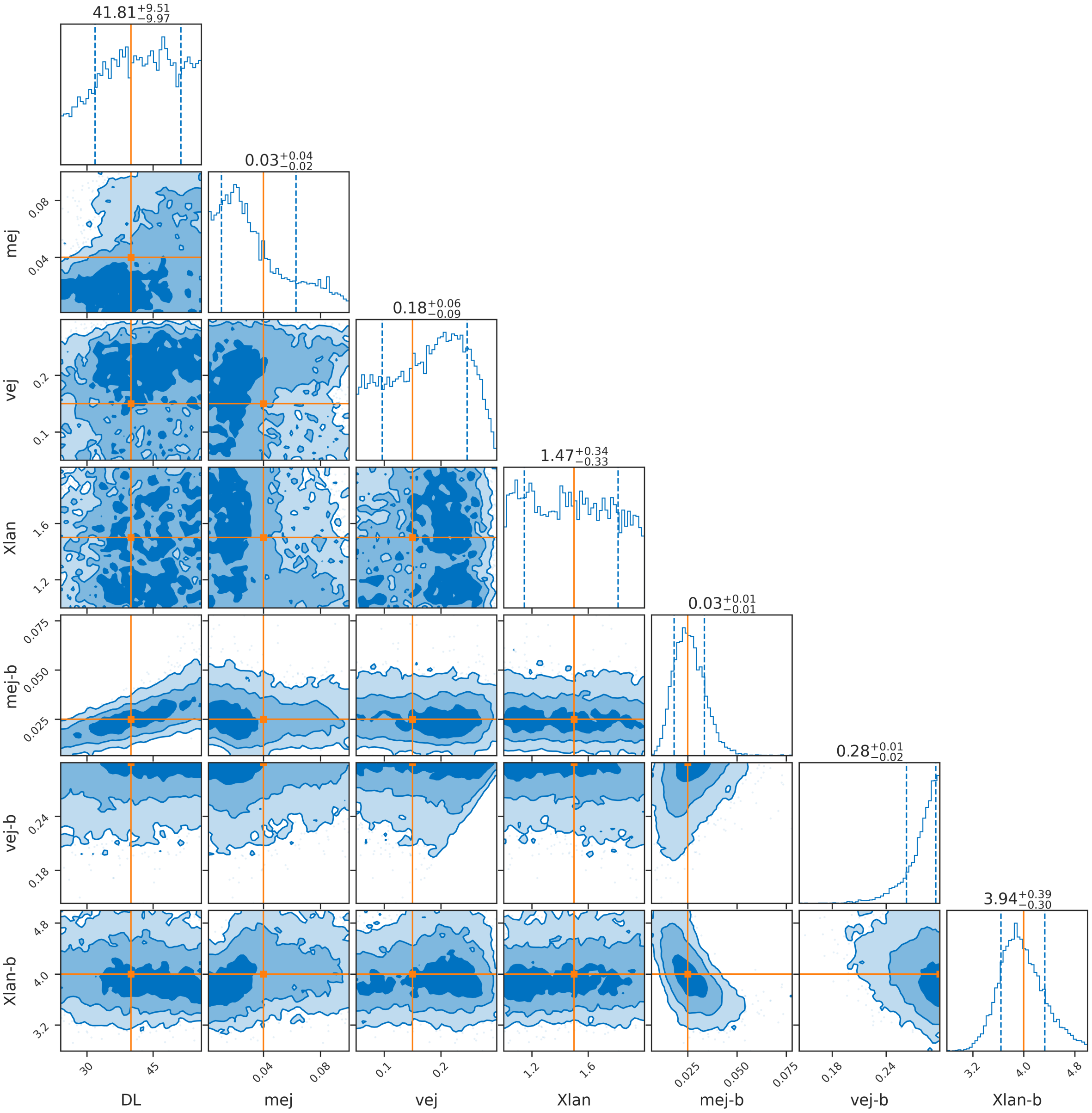

Figure 4.4: Ejecta parameter estimation from AT 2017gfo observations in the *griz* bands with a tight prior on d_L (uniform from 24 to 56 Mpc).

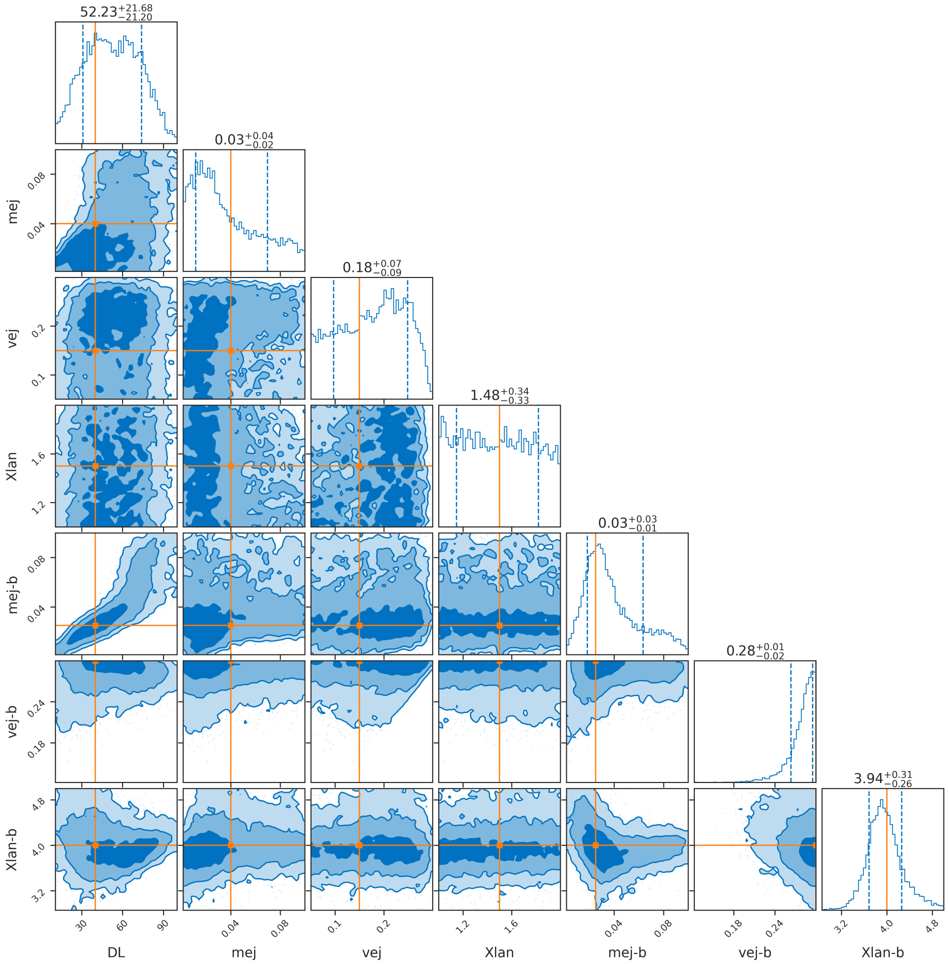

Figure 4.5: Ejecta parameter estimation from AT 2017gfo observations in the *griz* bands with a wider prior on d_L (uniform from 10 to 100 Mpc).

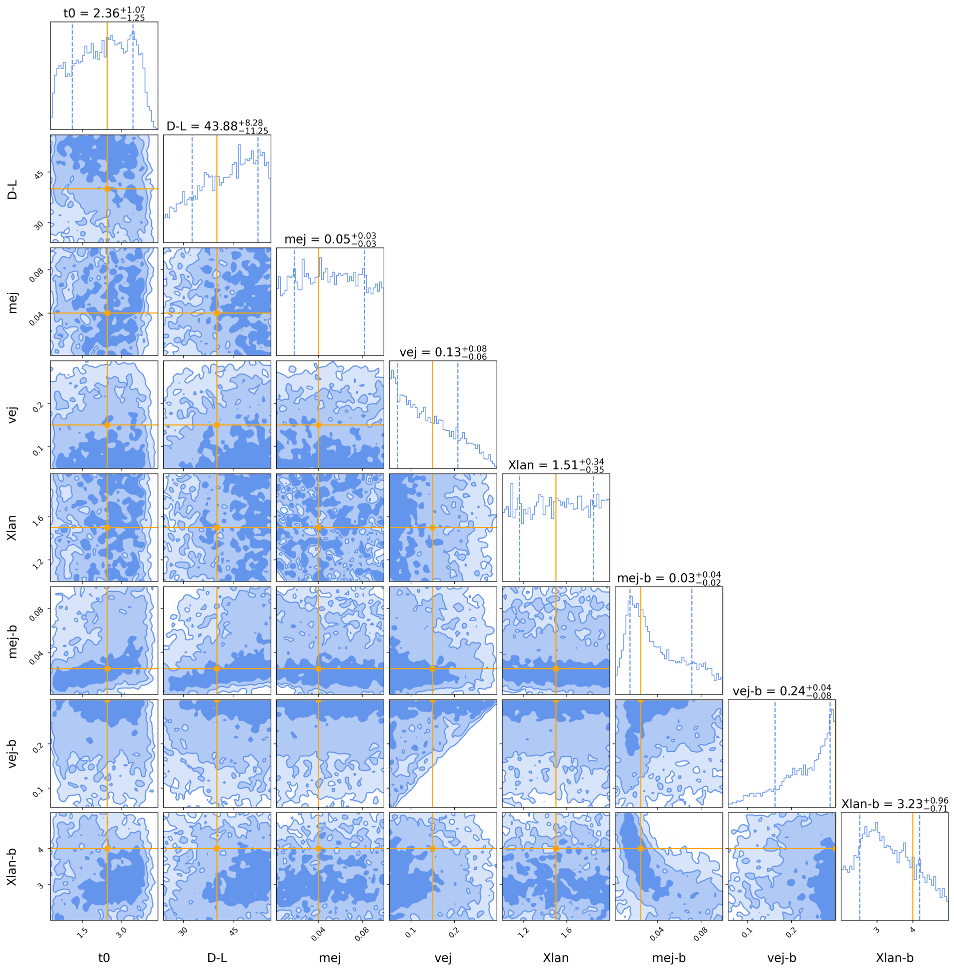

Figure 4.6: Full parameter estimation for *ri* bands on AT 2017gfo DECam observations, with a starting time t_0 2.45 days post-merger. Real values for ejecta parameters are taken from Kasen(2017) [94]. True d_L taken to be 40 Mpc.

4.1.2 Recovering the merger time from truncated AT 2017gfo light curves

The light curves are truncated in time and the parameter estimation code is run for various starting times of observations. This serves as a test of the applicability of the method on real data. The aim is to recover a merger time t_0 from observations that are incomplete, starting several days after the merger.

The priors are the following:

- d_L uniform 24 to 56 Mpc
- t_0 uniform 0 to 10 days

As previously described, the prior on d_L is uniform and corresponds to 40% bounds on d_L.

Figure 4.7 shows results on t_0 for different starting times of observations and band combinations. The results show that information is recovered on the merger time t_0 in all cases, and that the prompt start of observations post-merger matters more than the choice of pair of bands. The

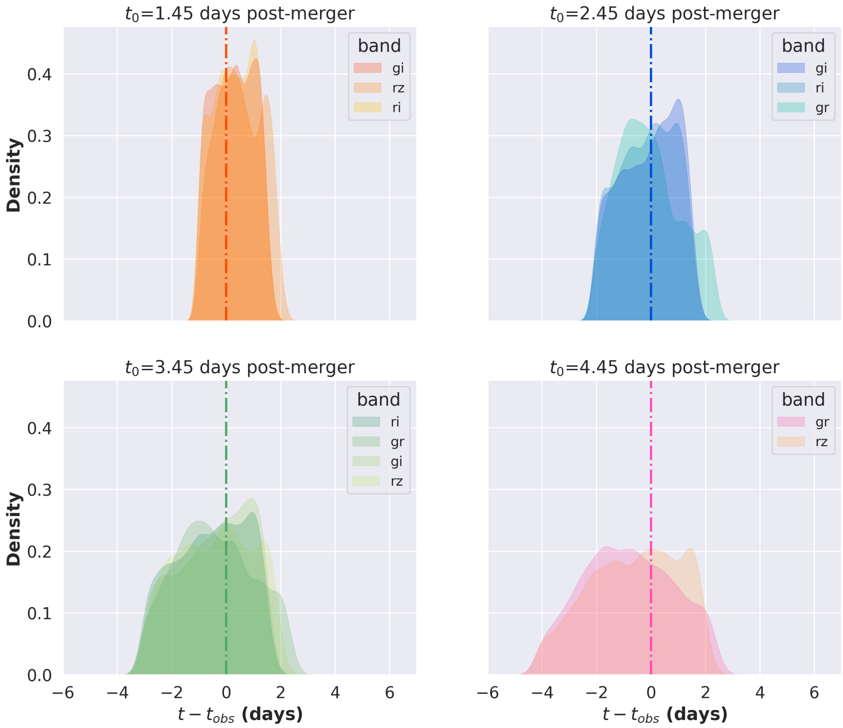

Figure 4.7: Results of merger time inference on the AT 2017gfo DECam observations for different starting times of observations and observing bands.

resulting posterior on t_0 is $t_0 = 1.72^{+0.86}_{-0.88}$ days for the *ri* bands with the actual t_0 being $t_0 = 1.45$ days. The results are similar for other bands, with a recovered 68.3% interval of ∼1.8 days. For light curves truncated at 2.45 days, the recovered merger time is $t_0 = 2.30^{+1.15}_{-1.20}$ days for the *ri* bands. For light curves truncated at 4.45 days, we get $t_0 = 3.82^{+1.89}_{-1.82}$ days in the *rz* bands, with a similar posterior in other band combinations.

With the starting time of observations and cadence being equal, no choice of band combination prevails over the others. However, at larger distances d_L, this choice might become more important in order to increase chances of detection and number of observations. Figure 4.6 shows an example of a complete corner plot for this analysis, with observations in the *ri* bands and the light curves being truncated so that the earliest observation is at $t_0 = 2.45$ days post-merger. All corner plots from the results in 4.7 can be found in Appendix B.

The results serve as a proof of principle for the parameter estimation pipeline.

4.2 Detectability of Kilonovae with LSST

The rest of the work presented in this chapter focuses on recovering a merger time t_0 from simulated serendipitous kilonova observations.

With the baseline2018a cadence for the main survey of the LSST, only ~ 7.5 serendipitous kilonova observations are expected. [113] In the baseline main survey strategy, each field is visited ~ 825, with visits spread over the *ugrizY* filters. [102] However, there are existing proposed strategies to maximise the detection of kilonovae during the main Wide Fast Deep survey. One such strategy, proposed by [113], could yield close to 300 GW170817-like kilonovae throughout the WFD survey.

However, not all kilonovae are expected to be as bright as GW170817, and will present some variation in colour. In this section we estimate the fraction of kilonovae detectable by the LSST for a range of ejecta parameters, over various times t and luminosity distances d_L.

Using the trained Gaussian Process, a large number of kilonova light curves is produced. Each light curve is made up of two components, a red (lanthanide-rich) and blue (lanthanide-poor) component. There is a total of 6 parameters for each light curve, sampled from priors determined by the bounds defined by the parameter grid from the models the GPR is trained on.

All 800 light curves generated for estimating the detectability can be seen in Figure 4.8. Each kilonova is the sum of two light curves forming the red and blue components.

$$m = -2.5\log_{10}(10^{-0.4m_{blue}} + 10^{-0.4m_{red}}) \tag{4.1}$$

We adapt the detectability criteria outlined in [200]:

- At least two filter bands have at least one observation,
- There is at least one observation at least 20 days before,

	u	g	r	i	z	Y
WFD	23.9	25.0	24.7	24.0	23.3	22.1

Table 4.2: LSST design single-visit limiting magnitudes for the WFD baseline survey. [201]

- There is at least one observation 20 days after.

We assume that the conditions for the second and third detection criteria are met in the baseline survey.

Figure 4.9 shows the fraction of these kilonovae detectable in different bands and band combinations as a function of time. Detectability here is defined as the apparent magnitude of the kilonova being higher than the single exposure LSST magnitude threshold for the quoted luminosity distance. It's important to note that "detectability" is not the same as the detection criteria used for kilonovae, but rather just whether the apparent magnitude makes it above the limiting magnitude of the WFD single-visits.

The limiting magnitudes are presented in table 4.2. These are the design limiting magnitudes for single-visit exposures in the baseline Wide Fast Deep (WFD) survey.

This shows that even for late-time observations associated with events close to the aLIGO event horizon, some kilonovae might still be detectable. This is consistent with other work, which found some kilonovae to be detectable up to 475 Mpc with wide-field surveys like the LSST. [104].

Results of the parameter estimation are only presented for kilonovae with apparent magnitudes above the LSST WFD threshold for a single visit. This favours certain observing strategies, band combinations and cadences, especially at higher distances and t_0. While Target of Opportunity observing strategies, such as the ones used in the follow-up of gravitational wave signals, could use longer exposure times, we stick to the WFD single visit thresholds as we are considering serendipitous kilonova observations.

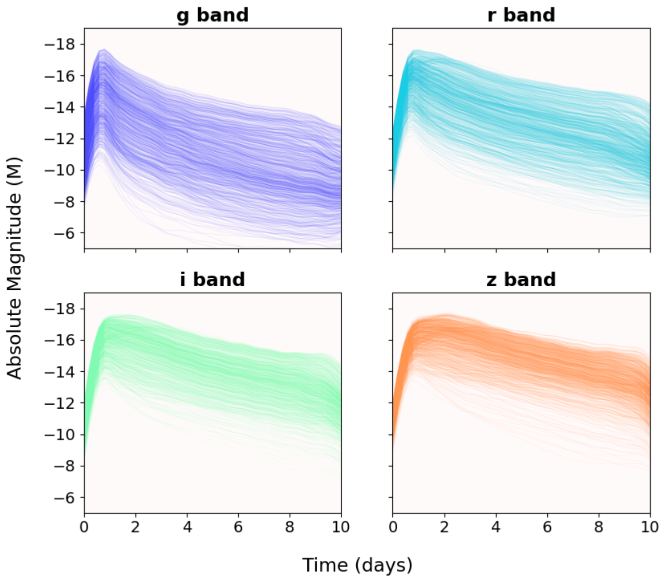

Figure 4.8: Kilonova light curves generated by a trained Gaussian Process. Each light curve is made up of two components (red and blue).

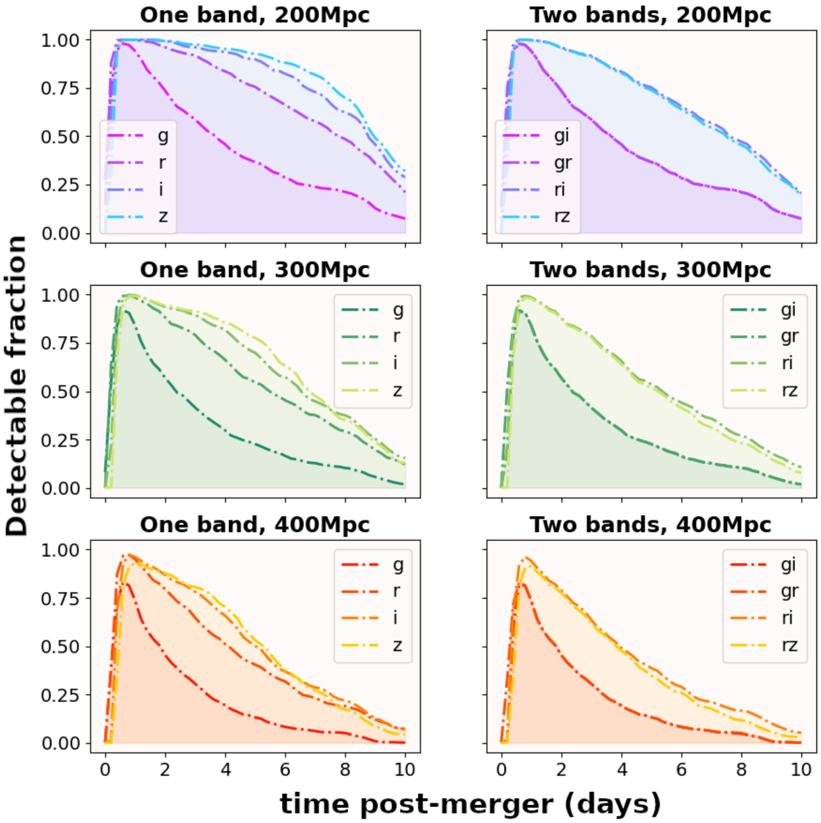

Figure 4.9: Detectability of kilonovae at various d_L in one band and two-band combinations.

4.3 Results on Simulated Light Curves

In this section we explore parameter estimation on simulated light curves. The light curves are simulated using the trained Gaussian Process, as described in chapter 3.

We assume a fixed luminosity distance d_L, under the assumption that the host galaxy is identifiable for each kilonova observation. In the AT 2017gfo analysis, the effect of a larger prior on d_L was minimal on the recovery of the other parameters. We test 4 different luminosity distances, at $d_L =$100, 200, 300 and 400Mpc.

The parameter estimation is run for two different kilonova light curves, with the main difference between the two kilonovae being on the ejecta mass of each component. We label them "blue" and "red", with the "blue" kilonova having a higher ejecta mass for the blue component, and the "red" kilonova having a higher red ejecta mass with a more subdued blue component. Table 4.3 shows a list of ejecta parameters for the two light curves considered in this analysis. Figure 4.10 shows the light *griz* light curves for the kilonova corresponding to the aforementioned ejecta parameters. These were chosen for this analysis as they are bright kilonovae, but have some variations in colour, as seen by the variations in brightness for some of the bands.

Kilonova	Ejecta mass	Ejecta velocity	Lanthanide fraction	Ejecta mass (blue)	Ejecta velocity (blue)	Lanthanide fraction(blue)
Blue	0.02 $M_\odot$	0.19 c	$10^{-1.48}$	0.07 $M_\odot$	0.24 c	$10^{-4.0}$
Red	0.09 $M_\odot$	0.20 c	$10^{-1.5}$	0.04 $M_\odot$	0.25 c	$10^{-4.0}$

Table 4.3: Ejecta parameters for the two kilonova light curves considered in this analysis.

4.3.1 Effect of cadence and band choice

We explore the effect of cadence on recovering the merger time. Two different cadences are considered, a nightly cadence and a cadence of 5 days. Most serendipitous observing strategies advocate for at least a nightly cadence over a limited time. [113, 114, 195, 196] The prior on t_0 is kept to be uniform over $0-10$ days for both cadences:

- If we assume follow-up from an internal (or external EM) trigger, the prior on t_0 would be larger than the one determined by the cadence.
- If we assume "blocks" of observations on consecutive nights for limited amounts of time, that area of the sky would not have been visited regularly prior to initial detection.

Figure 4.11 shows a direct cadence comparison for observations in the *rz* bands for a "red" kilonova at 300 Mpc. The importance of adopting a fast cadence for parameter estimation is evident from the posteriors on t_0. For a first observation at $t_0 = 1$ day post-merger, the 68.3%

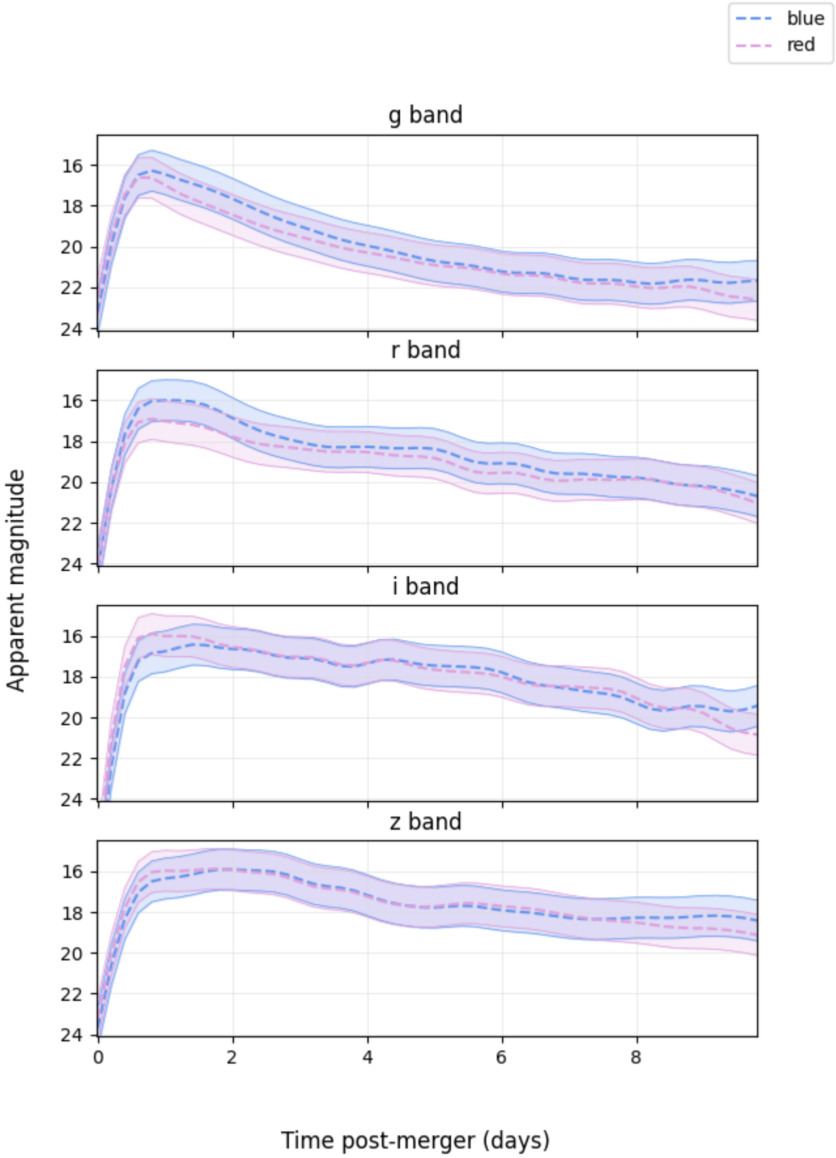

Figure 4.10: The *griz* light curves for the simulated kilonovae the parameter estimation is run on. Shown with 1 mag uncertainty for $d_L = 40$ Mpc.

confidence interval for the recovered merger time is $t_0 = 1.37^{+0.58}_{-0.56}$ at a 1 day cadence against $2.15^{+1.13}_{-1.14}$ day at a 5 day cadence. The effect of cadence is noticeable for early time detections at all luminosity distances. Figure 4.12 shows the same posteriors presented differently, with the posterior on t_0 rather than $t_0 - t_{obs}$, with t_{obs} the actual start of observations.

The effect of cadence is also noticeable at greater luminosity distances and later time observations. This is due to the increase in number of observations; the greatest difference to the final posterior comes from the total number of observations.

For distant kilonova candidates, a follow-up observation on the next night would make the greatest difference to detectability and parameter estimation on the light curves. All results for all band combinations, luminosity distances and kilonovae are found in Appendix B.

The largest difference from the choice of pair of bands is on detectability. The t_0 posterior is more dependent on the number of observations than which bands are used. This could also be seen in the inference on AT 2017gfo light curves, seen in figure 4.7.

Figures 4.13 and 4.14 show results on the inferred t_0 for a 5 day cadence at 300 Mpc, for different band pairs. We can see that while the g band limits the detectability of the kilonova, with no detection at $t_0 = 5$ days post-merger, it constrains the merger time better than other bands. This is understood as a selection effect. As seen in figure 4.9, the fraction of detectable kilonovae falls off more sharply for the g band than any other band. Therefore, a kilonova detection in this band already provides some tighter constraints on the merger time t_0.

The effect of band choice matters less for high cadence observations, as seen in figures 4.16 and 4.15. This is because the high cadence maximises the number of observations. The best results which do not compromise detectability, with both kilonovae still detectable at $t_{obs} = 5$ days post-merger, are on the iz bands.

The choice of bands matters more at slow cadences and for early time observations. Taking the example of the blue kilonova at 200 Mpc, there is little appreciable difference in the posteriors on the recovered t_0 when $t_{obs} = 1$ day post-merger at a nightly cadence. The recovered t_0 in the gi bands is $t_0 = 1.03^{+0.42}_{-0.42}$ days for a 1 day cadence and $t_0 = 1.39^{+0.70}_{-0.71}$ days for a 5 day cadence. In the iz bands, $t_0 = 1.14^{+0.48}_{-0.46}$ days for a 1 day cadence and $t_0 = 2.23^{+1.26}_{-1.15}$ days for a 5 day cadence. The posterior is significantly wider for the 5 day cadence in the iz bands, and more biased.

We find that detectability increases in the riz bands. The effect can be seen particularly for late time observations of kilonovae at distances of $300 - 400$ Mpc.

Figures 4.17 and 4.18 show a direct comparison of the choice of bands for a blue kilonova at 400 and 200 Mpc, for two different cadences.

The full results can be found in Appendix B. We only show a subset of the results here.

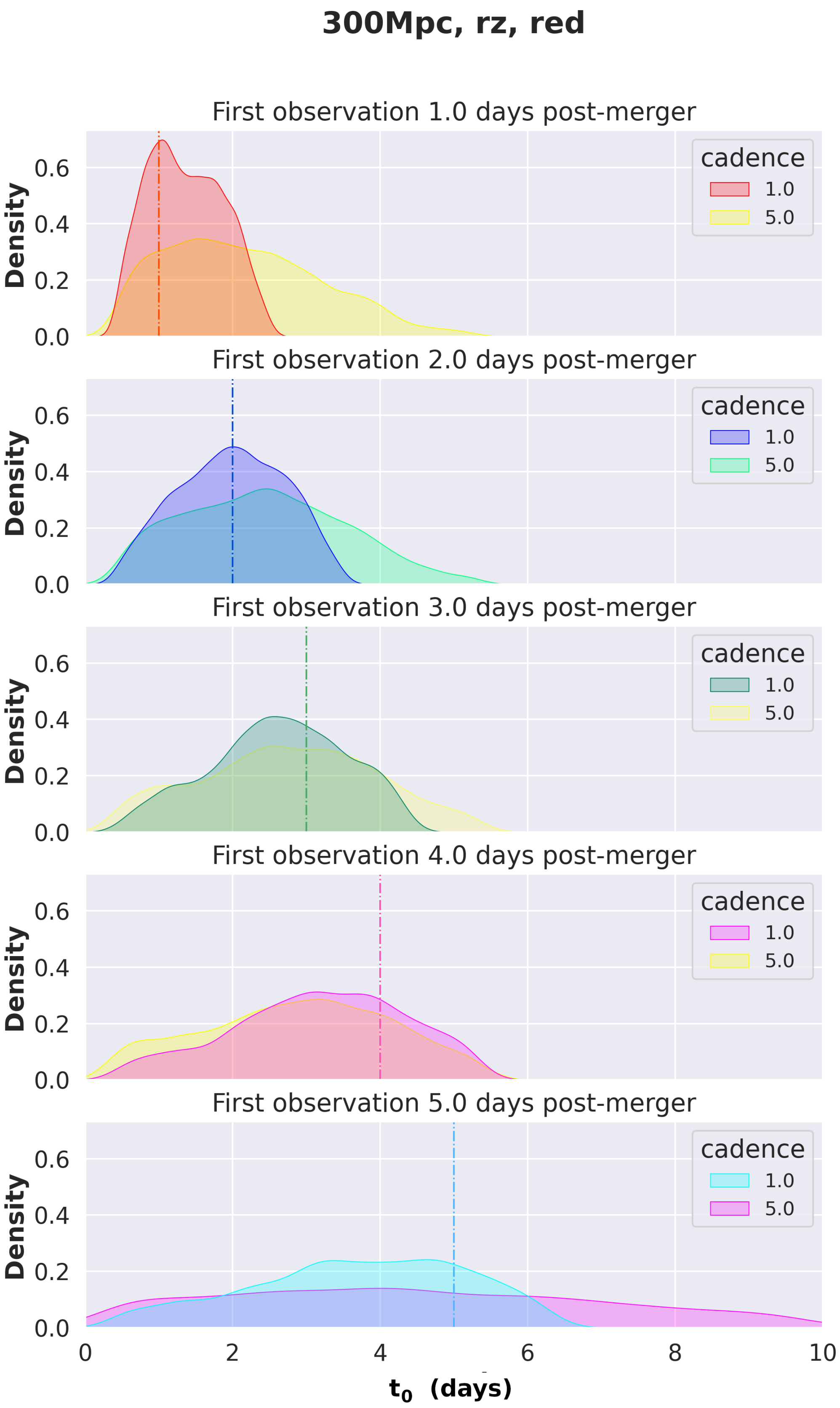

Figure 4.11: Effect of cadence on recovery of t_0 for a "red" kilonova at 300 Mpc in the rz bands. Each panel shows a different time for the first observation t_0 in days post-merger.

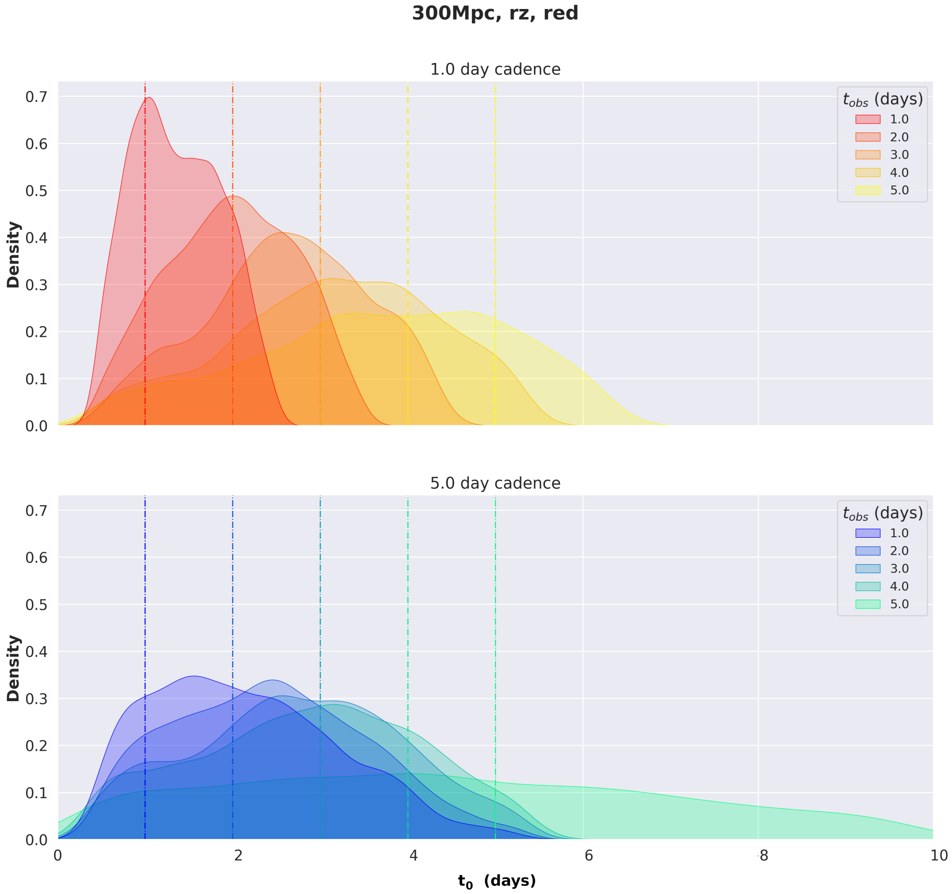

Figure 4.12: Effect of cadence on recovery of t_0 for a "red" kilonova at 300 Mpc in the rz bands.

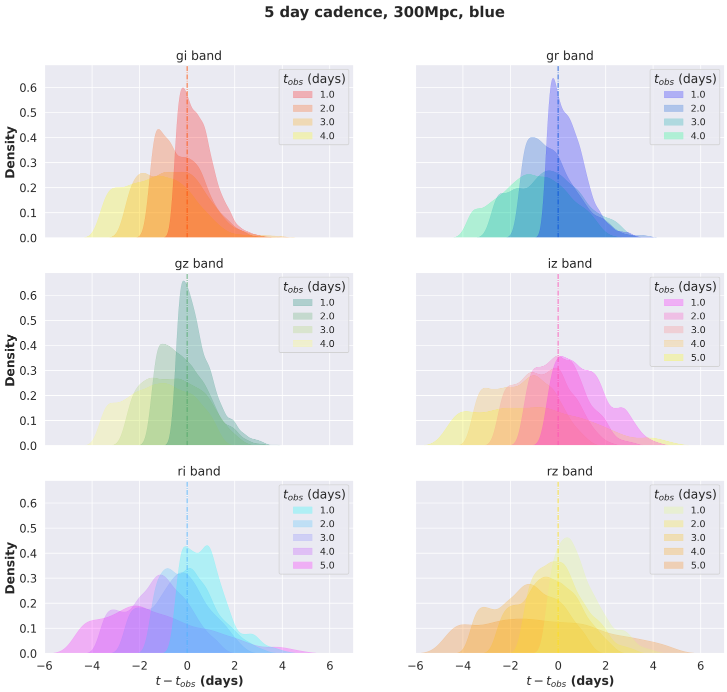

Figure 4.13: Results on t_0 for the "blue" kilonova, with a 5 day cadence at 300 Mpc. Results are shown for 6 different two band combinations, for five different t_0. Where a result is not included, the kilonova did not meet the criteria for detectability outlined previously.

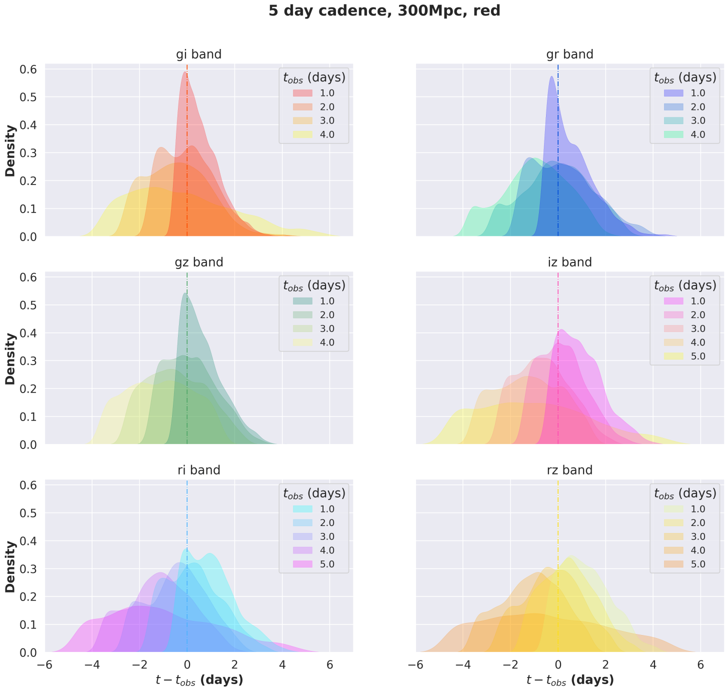

Figure 4.14: Results on t_0 for the "red" kilonova, with a 5 day cadence at 300 Mpc.

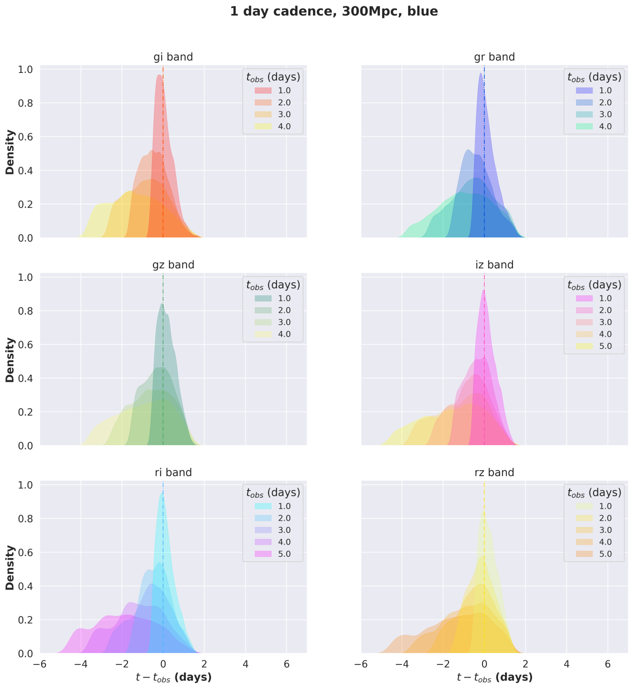

Figure 4.15: Results on t_0 for the "blue" kilonova, with a 1 day cadence at 300 Mpc.

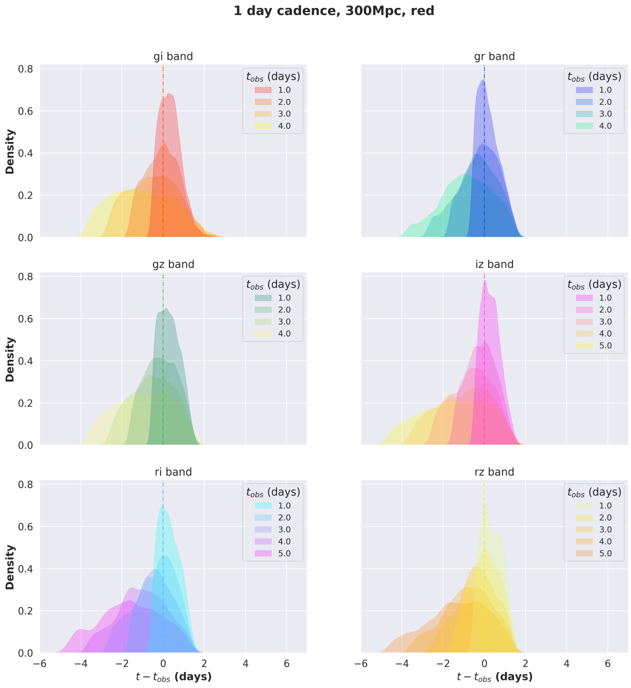

Figure 4.16: Results on t_0 for the "red" kilonova, with a 1 day cadence at 300 Mpc.

4.4 Conclusions

In this chapter, we have presented results from a parameter estimation pipeline that makes use of Gaussian Process Regression as an interpolating scheme for kilonova light curves obtained from two-component radiative transfer models. We applied this pipeline to real data and performed parameter estimation on the DECam observations of the kilonova AT 2017gfo to recover ejecta parameters. The recovered parameters were in good agreement with two previous studies that used the same models for parameter estimation. Discrepancies can be explained by the fact that other studies performed the parameter estimation on a larger dataset, including observations from many instruments.

The focus of this chapter was on recovering a posterior on t_0, the merger time of a binary neutron star, from incomplete kilonova light curves. The analysis was first performed on truncated DECam light curves for AT 2017gfo, fitting all parameters along with t_0. This was done for different band pairs from *griz*, and different times for t_{obs} the time of the first observation. No band combination seemed to prevail in this analysis, with the recovered posterior on t_0 being similar for all pairs of bands considered. For observations starting from $\sim$ 1.5 to 2.5 days post-merger, the recovered posterior on t_0 gave a time window of $\sim$ 1.5-2 days, similar to the GW search window for optically-triggered burst signals. At later times, from $\sim$ 3.5 to 4.5 days post-merger, we obtained a 68.3% credible interval on t_0 of $\sim$ 3-4 days.

We applied the same methodology to simulated observations and tested different band combinations for kilonovae at varying distances and with different starts of observations t_{obs} ranging from 1 to 5 days post-merger. Results were presented for two different cadences of observations, nightly and every 5 days. The distances considered in this section were greater than that of AT 2017gfo, ranging from 100 to 400 Mpc.

Overall, we found that we could recover some information on t_0 from the truncated light curves, even for distant kilonovae with late time observations. While some bands such as the *g*-band seem to constrain t_0 more than others, especially at early times and for nearby kilonovae, this could simply be due to selection effects. The luminosity in the *g*-band drops off sharply, already placing constraints on the kilonova parameter estimation due to the fact that the kilonova was detectable. Overall, the *riz* bands are better for maximising detectability and number of observations, with *iz* the best band combination for both detectability and the recovered t_0.

Cadence was found to be more important than the choice of bands in recovering a posterior on t_0. For a kilonova at 200 Mpc and a nightly cadence, a time window of $\sim$ 1 day could be recovered for a first observation at $t_{obs} = 1$ day post-merger. With a 5 day cadence, this estimate increased to a window of $\sim$ 2.5 days. At later times, with $t_{obs} = 5$ days post-merger, the posteriors on t_0 are uninformative for a 5 day cadence, and the window is $\sim$ 3-5 days for a nightly cadence. The estimated t_0 is more biased for late time observations.

The recovered posterior on t_0, along with information on the localisation, could inform searches for gravitational wave signals, or give more weight to sub-threshold events. Information can be recovered even from later time observations, which could open the way for GW searches from serendipitous discoveries of kilonovae and maximise prospects for multi-messenger astronomy.

There are however some caveats and sources of bias in this analysis, coming from the fact that the results are model-dependent.

The parameter estimation presented here makes use of one-dimensional models. It should be noted that the viewing angle of a kilonova will have an effect on the observed brightness, especially during early times. The peak luminosity could be up to $\sim 20\%$ brighter depending on the viewing angle. This would mostly affect the earlier-time observations. The model uncertainties are also large, with $\sigma = 1$ mag.

Another potential issue is that we only consider the models up to 10 days post-merger, after which they become unreliable. This has a limiting effect on the number of observations considered in this work for simulated light curves. This could lead to less informative posteriors on the light curves for late time observations.

However, while the analysis is model-dependent, we could still recover posteriors on t_0 from real data, by performing the analysis on AT 2017gfo light curves. Kilonovae are however expected to produce a diverse range of light curves, and the models used in this analysis might not provide as good a fit to future observations.

There is still potential for kilonova-triggered gravitational wave searches, and high cadence searches will be the key to these searches. Real-life observations would have localisation information which could be incorporated in a search pipeline, along with the information on the merger time t_0. The pipeline for parameter estimation, which incorporates Gaussian Process Regression and the use of `NESSAI`, could be modified in the future for different kilonova models.

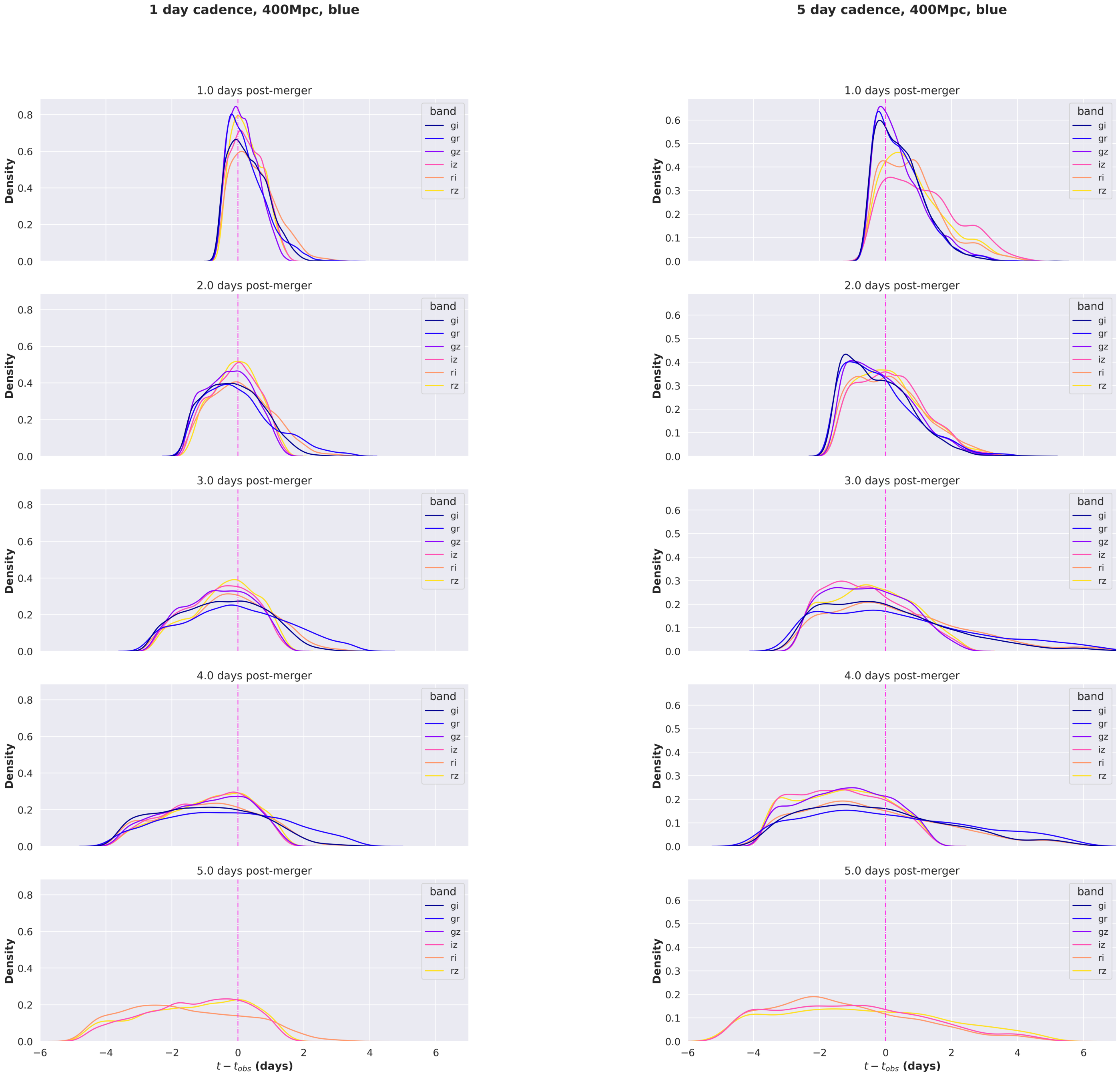

Figure 4.17: Comparison of pairs of bands for a "blue" kilonova at 400 Mpc. The figures show results for a 1 day cadence and for a 5 day cadence. Where band combinations are not present, the kilonova did not meet the detection criteria.

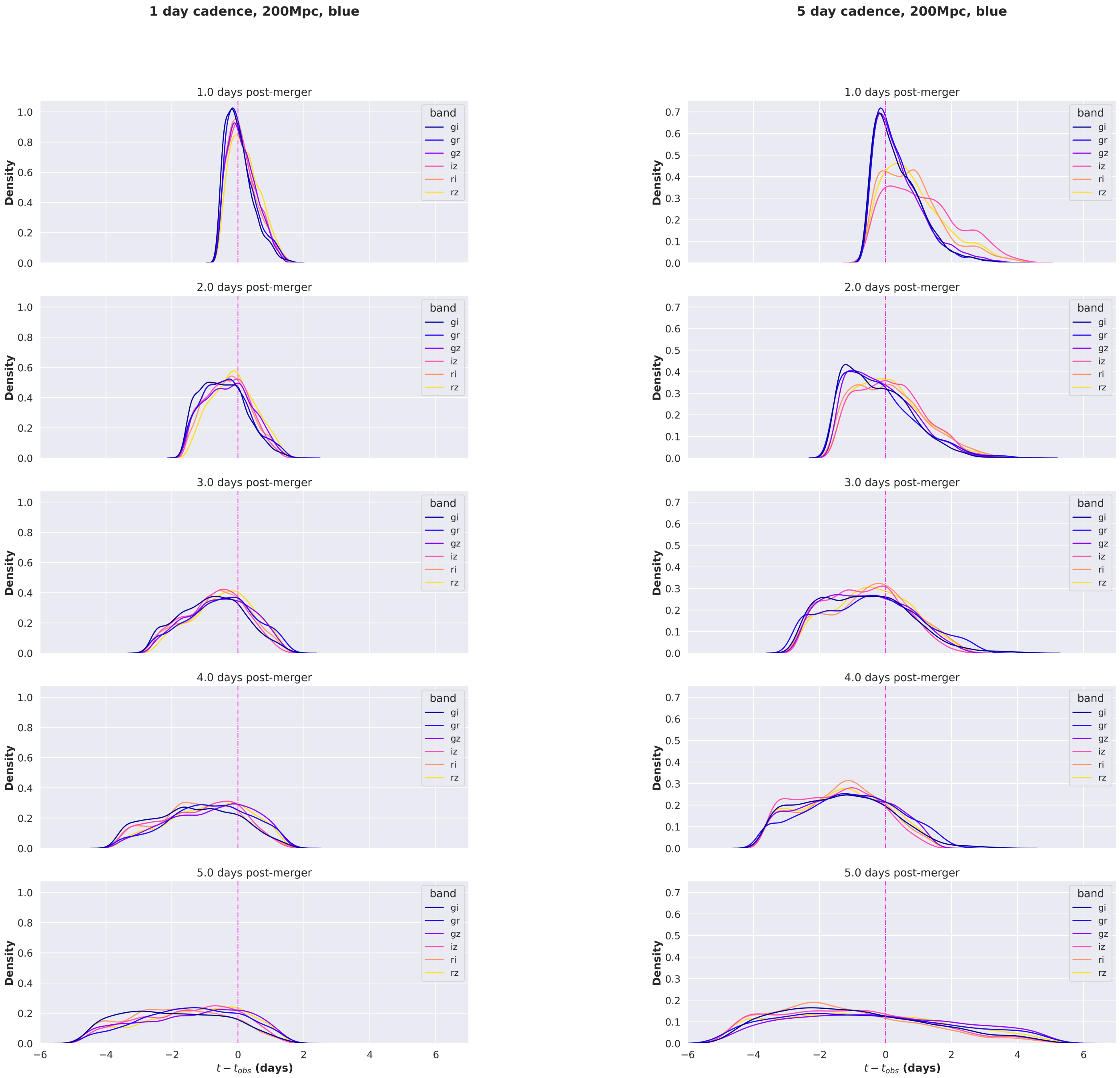

Figure 4.18: Comparison of pairs of bands for a "blue" kilonova at 200 Mpc. The figures show results for a 1 day cadence and for a 5 day cadence. Where band combinations are not present, the kilonova did not meet the detection criteria.

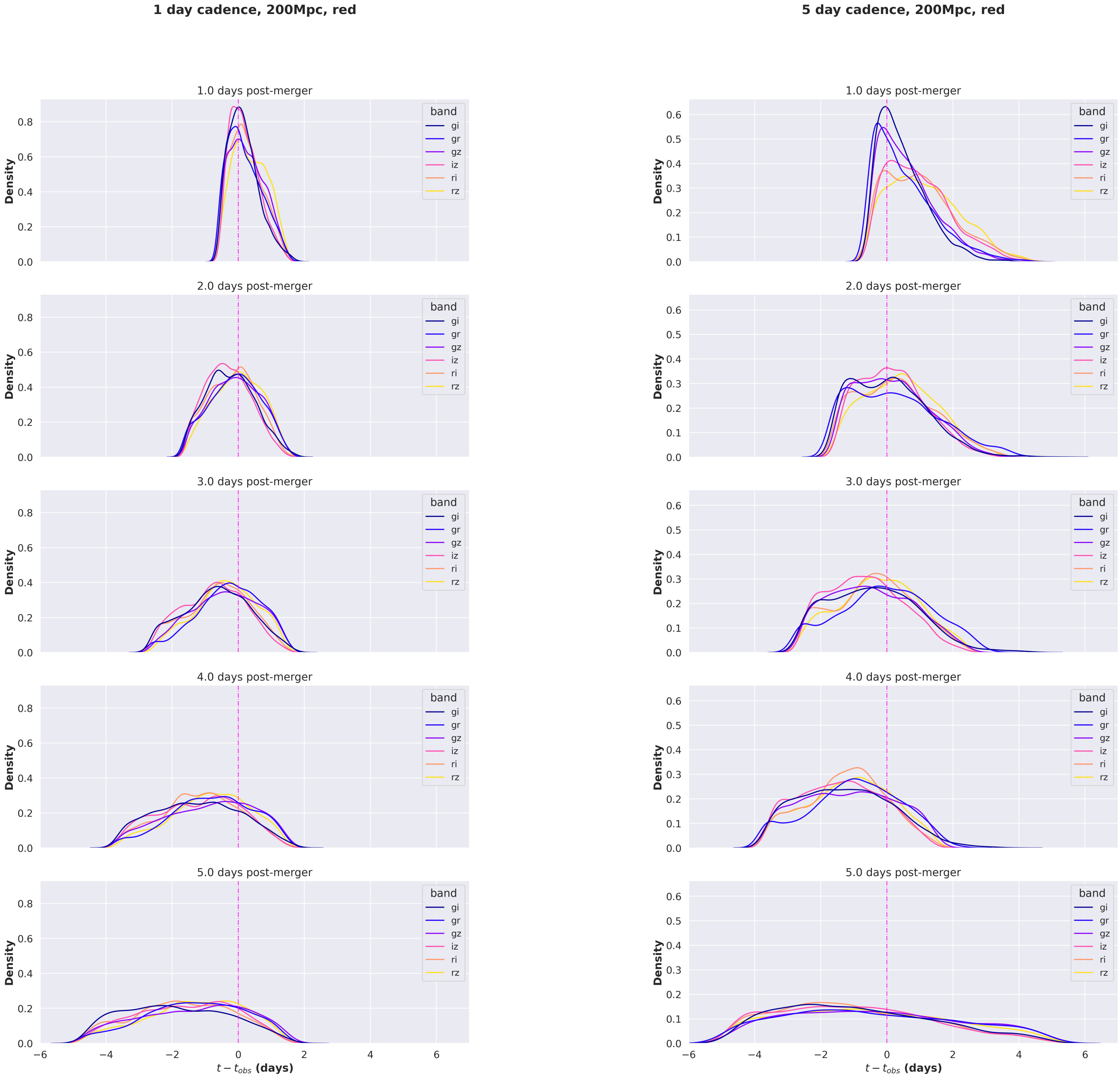

Figure 4.19: Comparison of pairs of bands for a "red" kilonova at 200 Mpc. The figures show results for a 1 day cadence and for a 5 day cadence. Where band combinations are not present, the kilonova did not meet the detection criteria.

5 | Inferring the ejecta parameters of a kilonova with jet-ejecta interaction

> Les gens ont des étoiles qui ne sont pas les mêmes.
>
> Antoine de Saint-Exupéry, Le Petit Prince

Chapter 3 introduced a methodology for inferring the ejecta parameters of a kilonova from observed light curves. Chapter 4 presents the results of applying this methodology for obtaining a posterior on the merger time of two neutron stars t_0 from late observations of kilonovae. This chapter presents another application of the methodology introduced in chapter 3: parameter estimation on kilonova models that incorporate different physics, namely taking into account the effect of a relativistic jet interacting with the previously released ejecta matter. This parameter estimation can quantify the effect of neglecting this effect on the recovery of ejecta parameters from kilonova light curves. Kilonova modelling requires a lot of microphysics, not all of which is modelled in the models we use for parameter estimation. If the effect of jet-ejecta interaction is ignored, the recovered posteriors for the ejecta parameters could be biased.

5.1 Kilonovae and Jets

The physics underlying kilonovae is complex, and many physical phenomena and ejection mechanisms need to be taken into account to accurately model the emission coming from the transients. Accurate models require detailed microphysics, accurate radiative transfer simulations and a solid understanding of the underlying nuclear physics. [96] The study of kilonovae and their light curves ties in many different areas of physics and astrophysics: numerical relativity, hydrodynamics, radiative transfer...

Different kilonova models tend to take into account different parameters and physical phenomena, with not all models taking into account all parameters, mass ejection mechanisms and microphysics that would come into play in a real kilonova. Depending on models, different mechanisms for mass ejection, interactions and microphysics are modelled, and others neglected. One oft-neglected phenomenon in many kilonova models is the effect of a relativistic jet interacting with the previously ejected matter on the resulting EM radiation. The work presented in this chapter is based on work on the effect of jets on resulting kilonova light curves that can be found in [202]. This section presents of short summary of this work. Previous work had been carried out on "jetted" kilonovae, but the analysis in [202] uses actual simulations as initial conditions for the kilonova wind and dynamics. [177, 203–209] The work presented in [202] explores the hydrodynamic interaction of a relativistic jet with neutrino-driven winds from a long-lived neutron star merger remnant.

5.1.1 Relativistic jets in neutron star mergers

Compact binary mergers involving at least one neutron star are often accompanied by short Gamma Ray Bursts (sGRBs). [210] The sGRBs accompanying BNS and NS-BH mergers are thought to originate from energy dissipation in ultrarelativistic jets. [211] If matter is previously ejected as a kilonova, the highly collimated, relativistic jets launched in those mergers can interact with the ejecta. [212]

The interaction of jets with the ejecta in BNS is somewhat comparable to the interaction present in long-duration GRBs, where an ultra-relativistic jet has to tunnel through a collapsing star. [213–215] However, these two scenarios are not identical, due to the nature of the dynamical ejecta from a BNS, which, unlike a collapsar whose size is fixed, is an expanding outflow. [207]

Neutron-rich kilonova ejecta contain a sizable quantity of lanthanides. These elements have high opacities and can obscure some of the kilonova emission and make the resulting light curves redder, dimmer and longer. [74, 89] This high-opacity material effectively acts as a "curtain", obscuring the blue radiation and making the kilonova peak in the red. A relativistic jet could potentially "punch" through the high opacity material, allowing some of the underlying blue emission to shine through at earlier times. [202] This mechanism would make the kilonova look brighter and bluer to an observer, especially at early times.

5.1.2 An excess of blue in AT 2017gfo

The kilonova AT 2017gfo associated with the gravitational wave event GW170817 was brighter in the bluer bands than models predicted. Several physical mechanisms have been proposed to explain this excess of blue radiation These include spiral density waves generating a spiral-wave wind [216], a strongly-magnetised hypermassive neutron star remnant (magnetar). [179] Jets interacting with the ejecta could also cause the brightening of a kilonova in the blue bands. Simulations show that it is likely GW170817 had a successful jet. [207] The radio and X-ray emission accompanying the kilonova AT 2017gfo is interpreted as coming from a relativistic jet observed slightly-off axis and interacting with the surrounding matter from the ejecta. [48, 211, 217, 218]

The mechanism described previously, through which a relativistic jet allows for bluer emission at early times, is a potential explanation for the blue excess seen in the kilonova that accompanied GW170817. This would be an important consideration for inferring the physical parameters of the ejecta. If no jet is assumed, then the resulting PE could wrongly infer the parameters to compensate for the excess radiation. This effect could impact the recovered ejecta velocities, masses and lanthanide fractions

When modelling this mechanism, the modelled light curves result in a better fit for the early blue emission from the kilonova that accompanied GW170817.

5.1.3 Models of jetted kilonovae

The kilonova models used in the analysis presented in this chapter were computed from the POSSIS code developed by Bulla. [219] For comparison, models that only have the wind component of a kilonova are also used. Both models have the same parameters, differing only in the presence of a jet. We will refer to the models where a jet is present as "jetted kilonova" models. These were computed for the analysis presented in [202]. Only the kilonova emission is modelled, with no jet afterglow present in the simulation.

The jetted kilonova models have different jet luminosities and were computed for different viewing angles. They are also computed for different disc compositions, with a "lanthanide-rich" and a "lanthanide-free" kilonova.

The simulations presented in [202] show that a jet would punch through the high opacity, lanthanide-rich material, allowing the underlying radiation to escape more easily along the jet axis. The effect is most pronounced during the first 3 days post-merger and for more luminous jets, making the light curves brighter in the near-ultraviolet and in the short optical wavelengths, where the line opacities are higher. The angle-dependence of the resulting radiation is also mitigated by the presence of a jet, which makes the emission more isotropic. [202] This increase in isotropy is explained by the jet introducing its own viewing angle dependence - the high-opacity curtain is pushed away by the jet in the polar axis, meaning radiation can escape more easily along the jet axis than in the wind-only kilonovae. This seemingly erases the viewing angle dependence that is seen in the absence of a jet.

The work presented in this paper qualitatively shows that jets could incur a blue brightening of a kilonova at early times. While not as bright as the observed AT 2017gfo light curves, the predicted lanthanide-rich light curves with a powerful jet have peaks $\sim 0.5 - 1.0$ mag dimmer than observations and have a similar decay. [202]

The models are independent from the models used for parameter estimation in this analysis, providing a good cross-check for parameter estimation. As in previous sections, the models used for this analysis are the ones developed by Kasen et al. [94] These models do not take into account any viewing-angle dependence. However, using these for parameter estimation can still allow us to make a qualitative statement on the effect of the jet-ejecta interaction on the final recovered posteriors for the ejecta parameters.

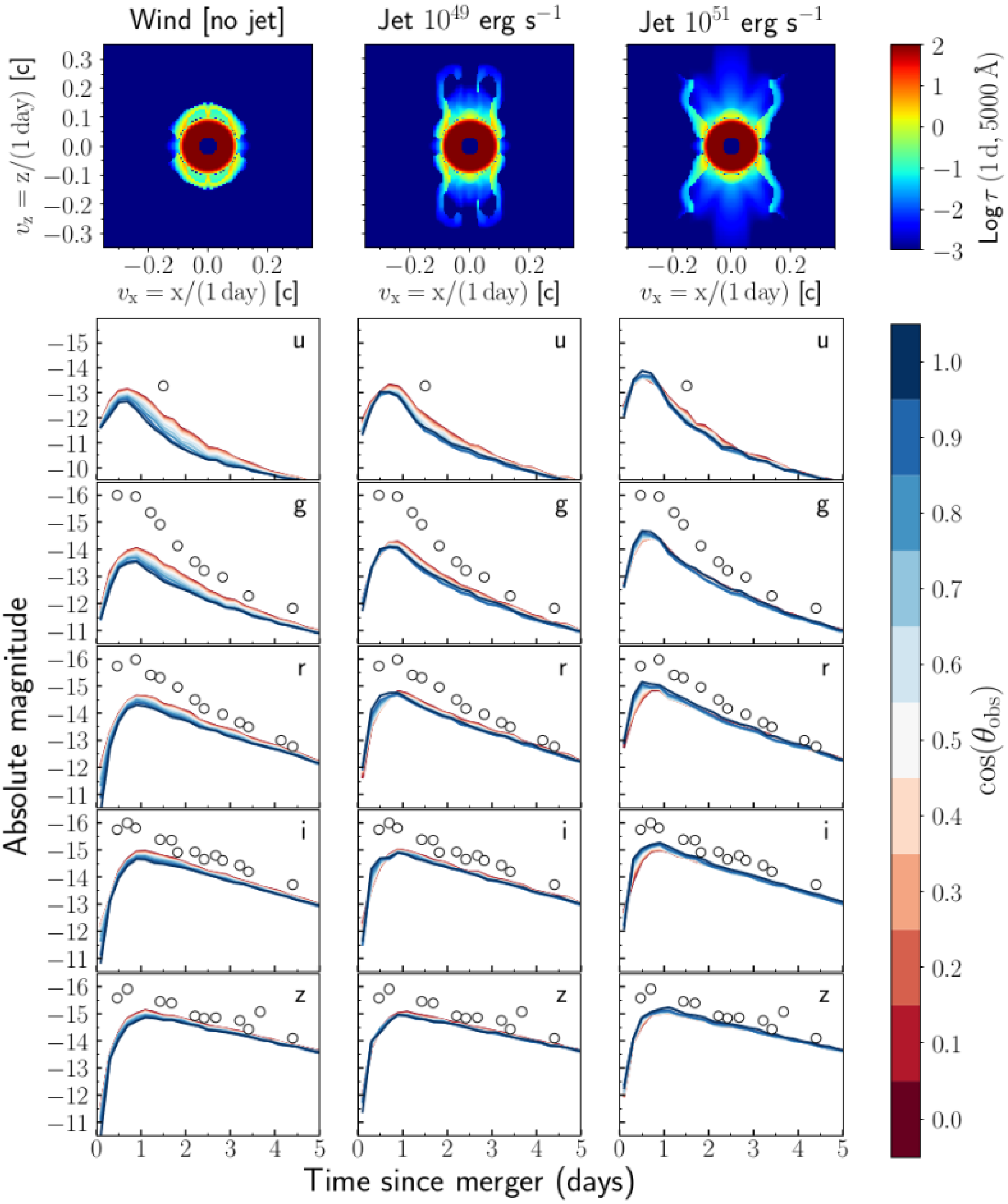

Figure 5.1: *ugriz* light curves for a lanthanide-rich composition with a jet. Three models are presented: wind-only, 10^{49} erg s^{-1} jet and 10^{51} erg s^{-1} jet. The data points are AT 2017-gfo light curves. From Nativi et al. (2021) [202]

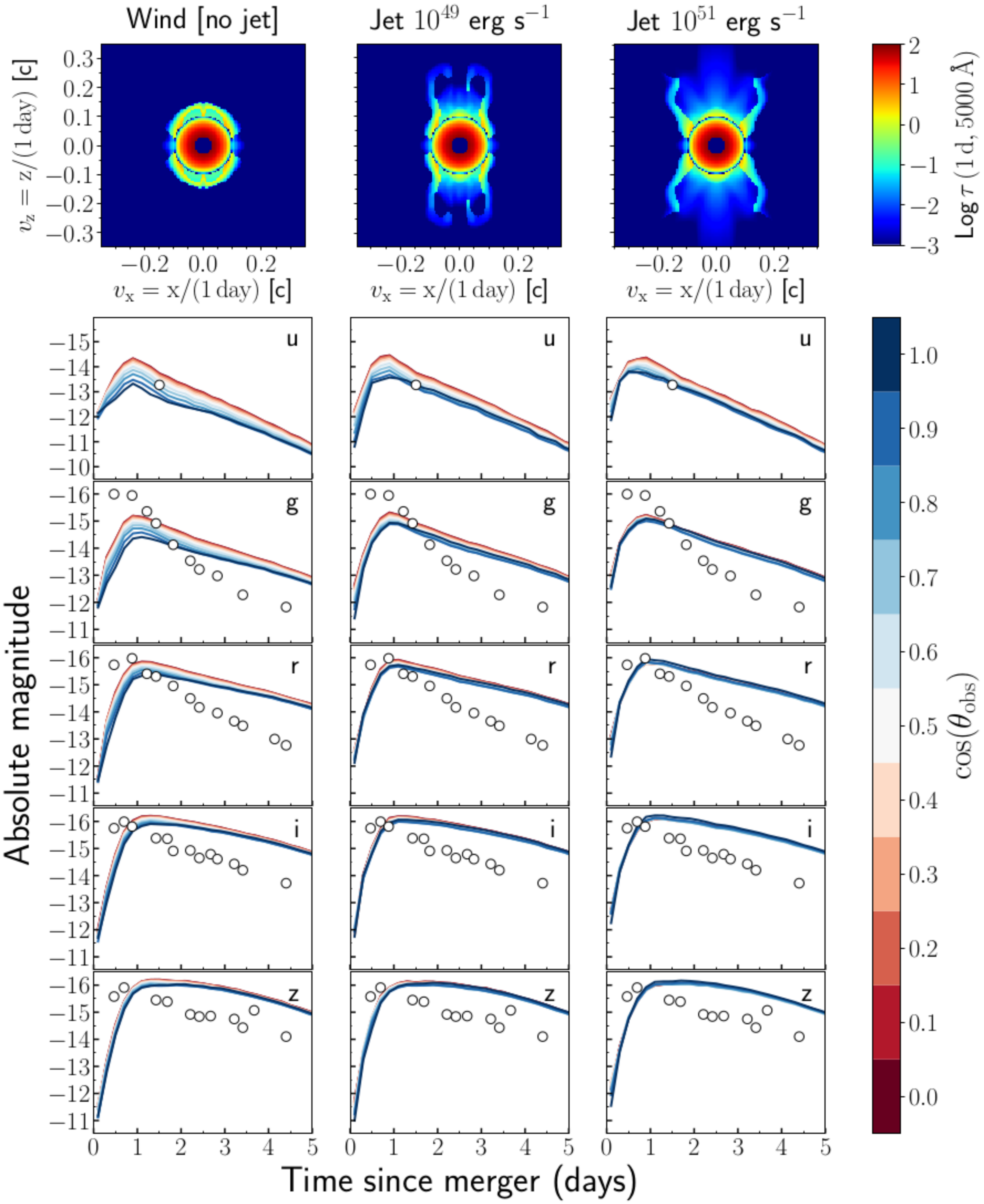

Figure 5.2: *ugriz* light curves for a lanthanide-free composition with a jet. Three models are presented: wind-only, 10^{49} erg s^{-1} jet and 10^{51} erg s^{-1} jet. The data points are AT 2017-gfo light curves. From Nativi et al. (2021) [202]

5.2 Parameter Estimation on Kilonova Light Curves With and Without a Jet

The previous section introduced relativistic jets and the effect of their interaction with the previously ejected matter in a kilonova, making the resulting light curves appear brighter and bluer at early times.

If parameter estimation is carried out on kilonova light curves without taking into account the effect of the interaction of a relativistic jet with the ejecta, then the resulting ejecta parameters could be biased. We run the previously described parameter estimation method on the models described in section 5.1. The models that the Gaussian Process is trained on do not take into account any potential effects from a relativistic jet, nor do they take into account the effect of viewing angle.

The presence of a strong jet, however, makes the emission appear more isotropic, with less angle-dependence on the light curves when a jet is present, as seen in figures 5.1 and 5.2.

As in previous sections, the parameter estimation is run for a kilonova with two components, red and blue (wind and dynamical). While the models in [202] are wind-only, we found that the wind-only component of the Kasen models was a poor fit, especially for the lanthanide-free models. The inferred parameters are the ejecta mass, lanthanide fraction, and ejecta velocity $(m_{ej}, v_{ej}, X_{lan})$ for each component. The luminosity distance is fixed at $d_L = 40$ Mpc.

5.2.1 Parameter estimation on early time emission

The parameter estimation is first performed on the first 3 days of observations with a 12h cadence, where the effect of the jet on the resulting emission is most prominent. Subsequently, the effect of the jet on kilonova light curves becomes negligible. This is not necessarily a realistic observing scenario, but it is chosen as it best exemplifies the effect of the jet's interaction with the ejecta on the resulting light curves. The effect of the jet will be most noticeable at early times and with well-sampled light curves.

Figures 5.3,5.4 and 5.6 show the results of the parameter estimation for two lanthanide-free kilonova models: one only taking into account the wind component, and one that has a jet with an initial luminosity $L_j = 10^{51}$ erg s^{-1}, viewed at an angle $\cos\theta_{obs} = 1.0$. Figures 5.7, 5.8 and 5.10 show the same set-up but for a lanthanide-rich kilonova.

We choose these parameters for the jet luminosity and viewing angle as they provide the largest difference in observed magnitude between the wind-only and jetted models. This can be seen in figures 5.2 and 5.1. The resulting light curves are most affected by the jet interaction in the lanthanide-rich case. The parameter estimation is run on the *griz* bands, which are common bands in optical searches for kilonovae, with the redder *riz* commonly used for detecting kilonovae and $g+z$ commonly used for constraining the colour evolution of kilono-

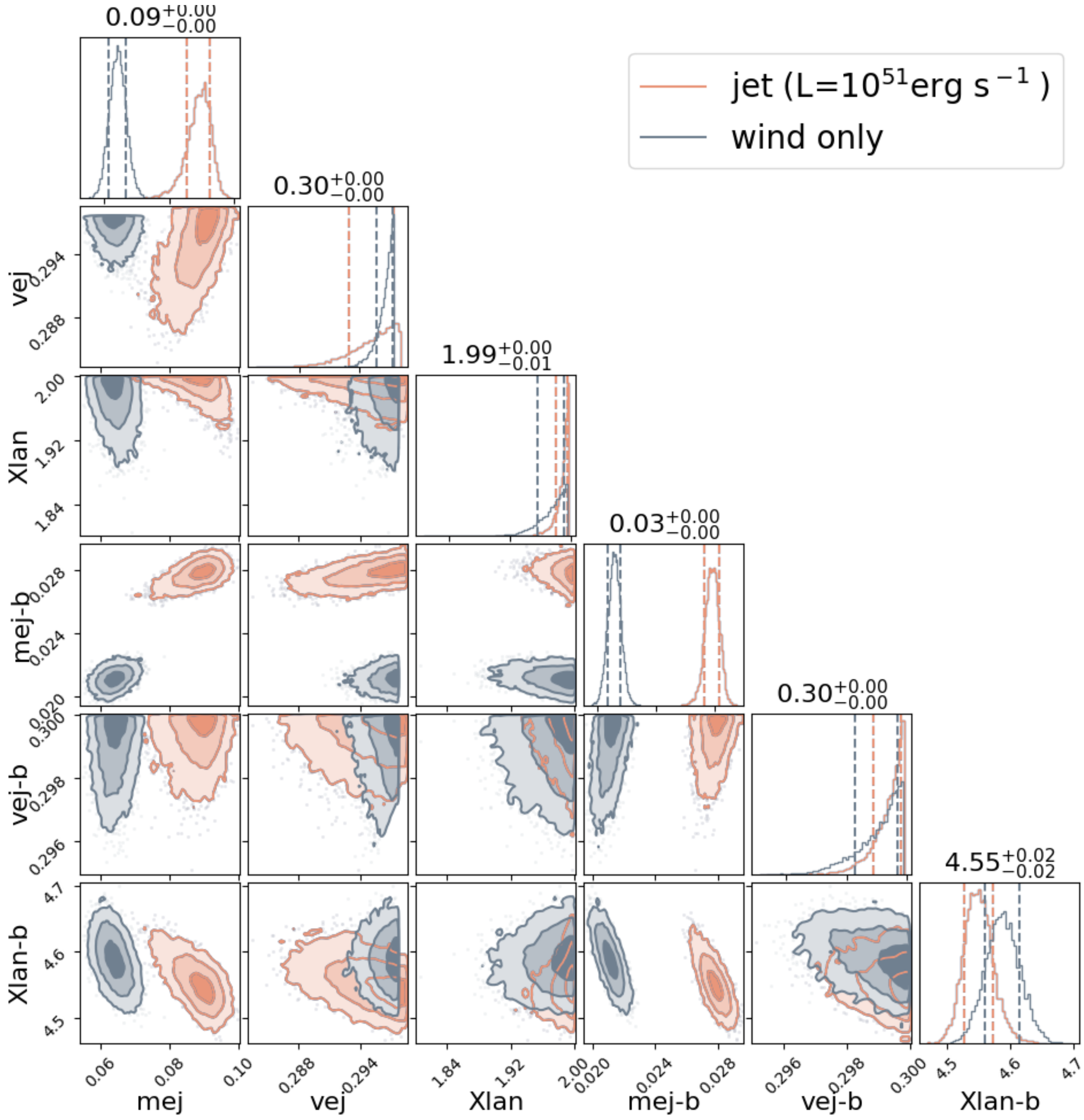

Figure 5.3: Corner plot for parameter estimation on kilonovae with and without a jet. 12h cadence, *griz* bands, over 3 days. 0.1 magnitude uncertainty. Both models are for lanthanide-free kilonovae with $\cos\theta_{obs} = 1.0$. The jetted kilonova has a jet luminosity $L_j = 10^{51}$ erg s^{-1}. The results are for the ejecta parameter of two components, a red component and a blue component.

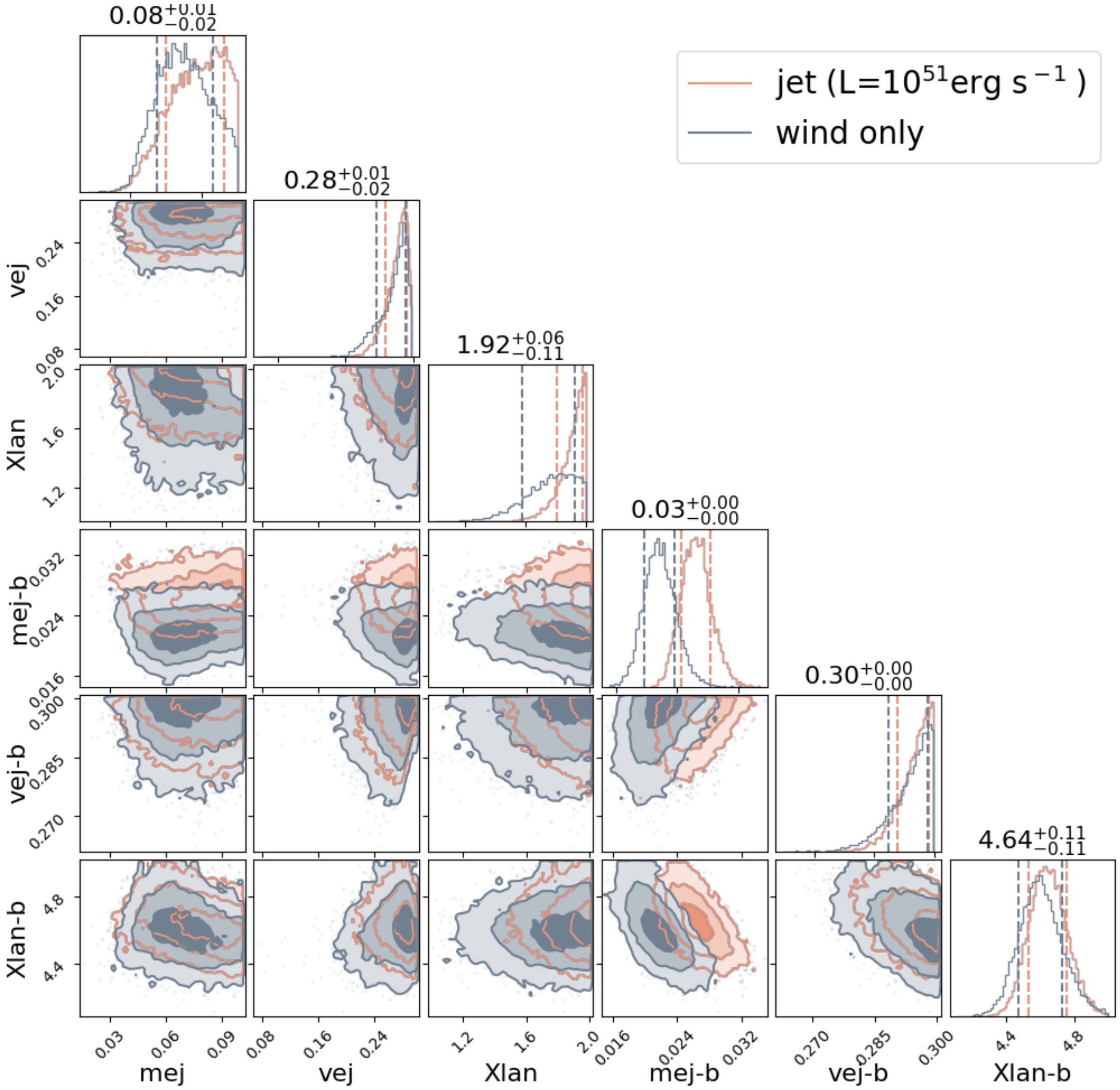

Figure 5.4: Corner plot for parameter estimation on kilonovae with and without a jet. 12h cadence, *griz* bands, over 3 days. 0.5 magnitude uncertainty. Both models are for lanthanide-free kilonovae with $\cos\theta_{obs} = 1.0$. The jetted kilonova has a jet luminosity $L_j = 10^{51}$ erg s^{-1}. The results are for the ejecta parameter of two components, a red component and a blue component.

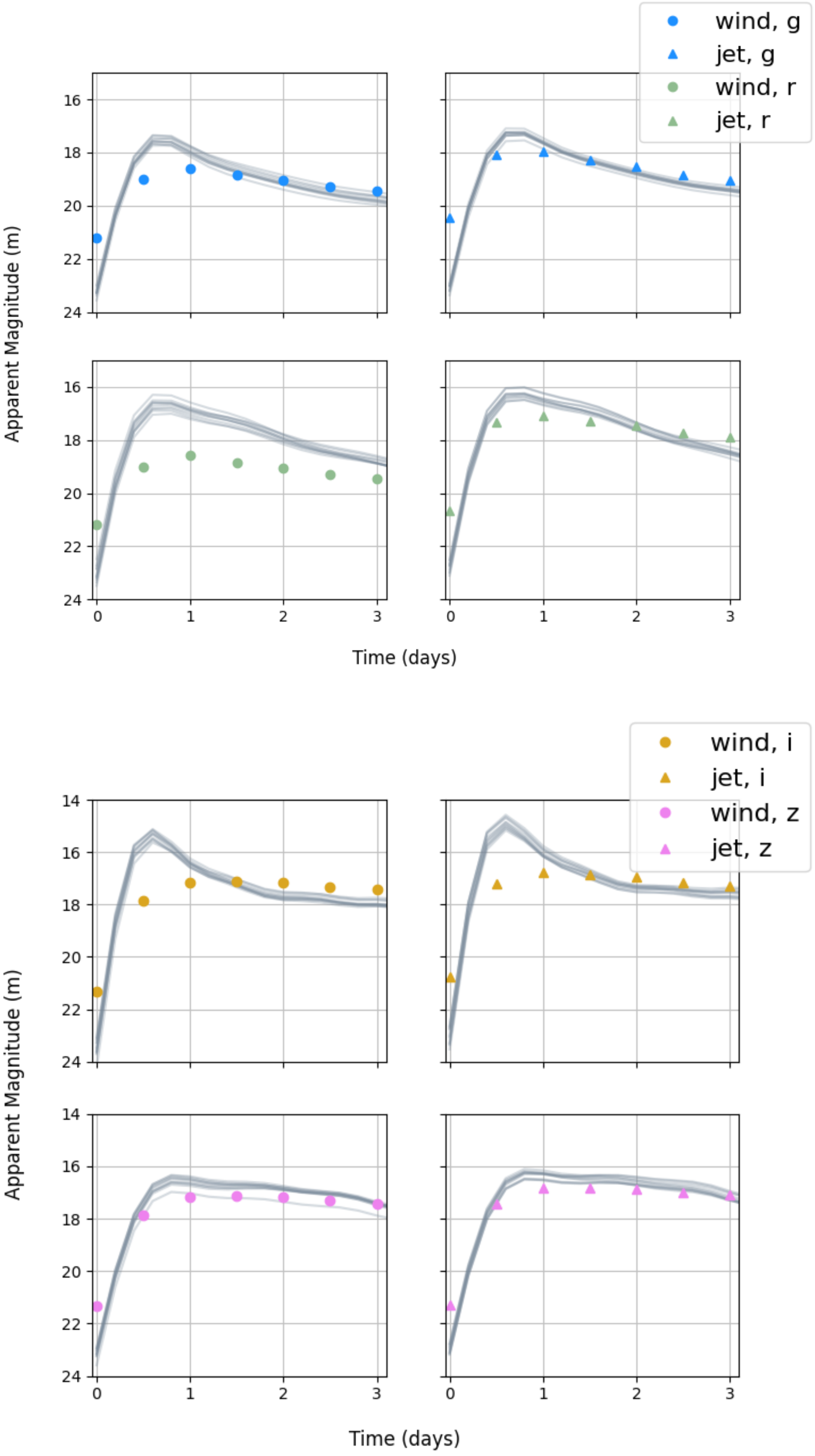

Figure 5.5: Models of wind-only and jetted kilonova with light curves generated from posterior samples. Each grey line is a light curve generated from a posterior sample of kilonova parameters, while the solid data points are the simulated observations from the kilonova models presented in [202]. The simulated observations are for a lanthanide-free kilonova with a viewing angle $\cos\theta_{obs} = 1.0$ and jet luminosity $L_j = 10^{51}$ erg s^{-1} for the jetted case.

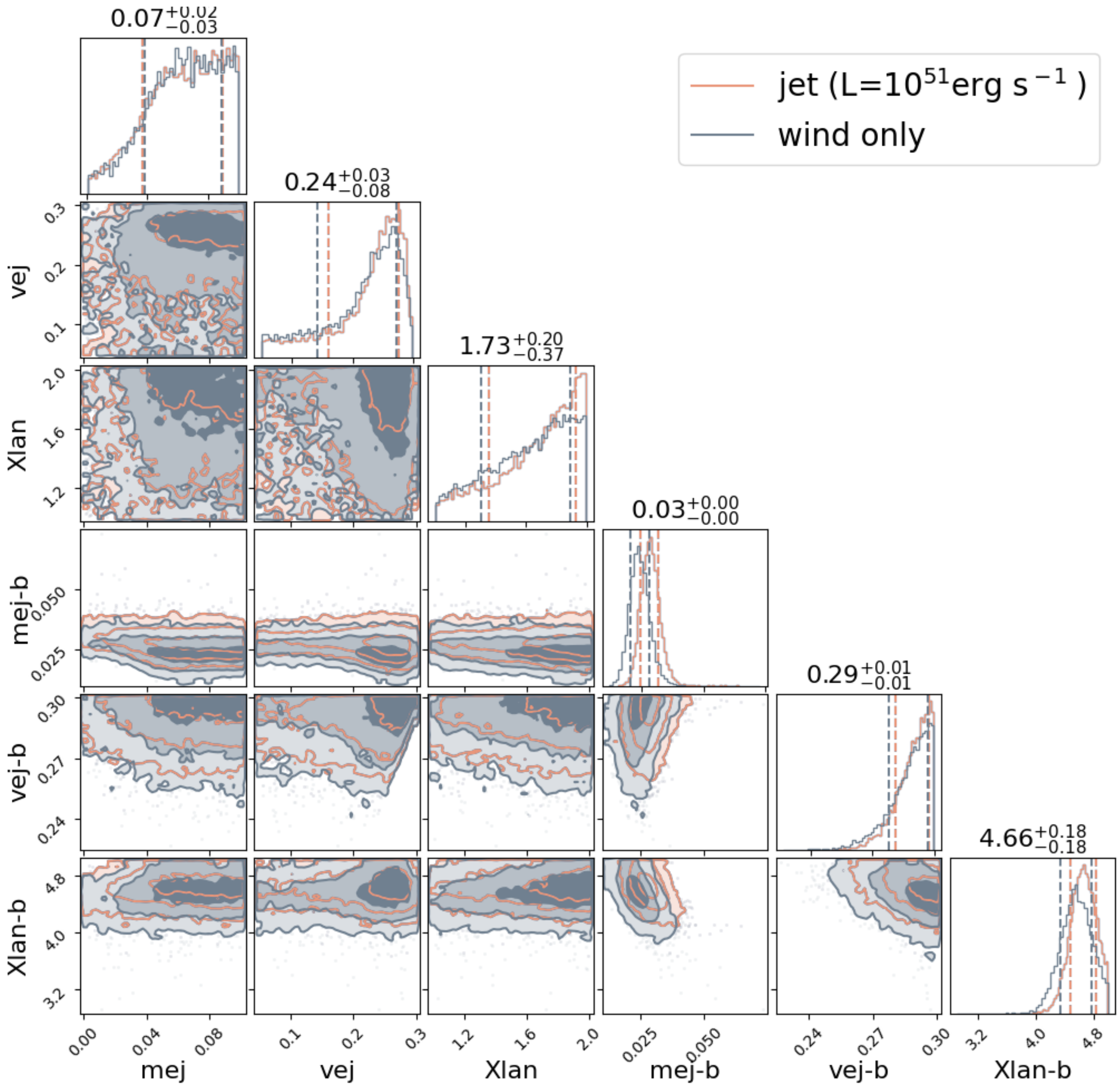

Figure 5.6: Corner plot for parameter estimation on kilonova with and without a jet. 12h cadence, *griz* bands, over 3 days. 1.0 magnitude uncertainty. Both models are for lanthanide-free kilonovae with $\cos\theta_{obs} = 1.0$. The jetted kilonova has a jet luminosity $L_j = 10^{51}$ erg s^{-1}. The results are for the ejecta parameter of two components, a red component and a blue component.

vae. [106, 113, 114, 195] Results are shown for three different uncertainties on the models used for the parameter estimation: $\sigma_m = 0.1$, 0.5 and 1.0 mag.

The results show that the ejecta mass is overestimated when not taking into account the effect of the jet on the kilonova light curves. The recovery of other ejecta parameters is also affected, particularly the ejecta velocity v_{ej}. Since the jet allows the some radiation to shine through the lanthanide curtain early, this can be expected; the effect of the jet could essentially look like the blue component of the ejecta is being flung out at a higher velocity.

Figure 5.9 shows samples drawn from the parameter estimation fitted to the lanthanide-rich models with and without the jet. These posterior samples are taken from the posteriors in figure 5.8, with a 0.5 mag uncertainty on the models. Figure 5.5 shows a similar fit for the lanthanide-free model, with samples taken from figure 5.4. From the figure, we can see that the light curves drawn from the posteriors are a good fit to the bluer g and r bands, especially for the jetted kilonova. However, the fit is less accurate for the redder bands, especially at very early times.

It is important to note that the models used for the parameter estimation do not take into account any effect from viewing angles, which could affect the peak luminosity by $\sim 20\%$ [94] The models used for simulating observations are also wind-only, missing some of the very early tidal ejecta. It can be seen from the samples plots that the wind-only posterior draws have an excess brightness at the peak compared to the Bulla models. The jetted kilonovae are seemingly more isotropic, and the posterior samples are a better fit. It is however still possible to make qualitative statements about the recovered ejecta parameters by taking the parameters for the wind-only kilonova as the "true" parameters of the kilonova.

The effect of the jet interaction on the recovered parameters is most noticeable when the model uncertainty is small, as can be seen in figures 5.3 and 5.7. However, even when using the standard, conservative uncertainty used in chapter 4 of $\sigma = 1.0$ mag, there is a noticeable discrepancy in the recovered ejecta mass for the blue component of the ejecta. This can be seen in figures 5.6 and 5.10.

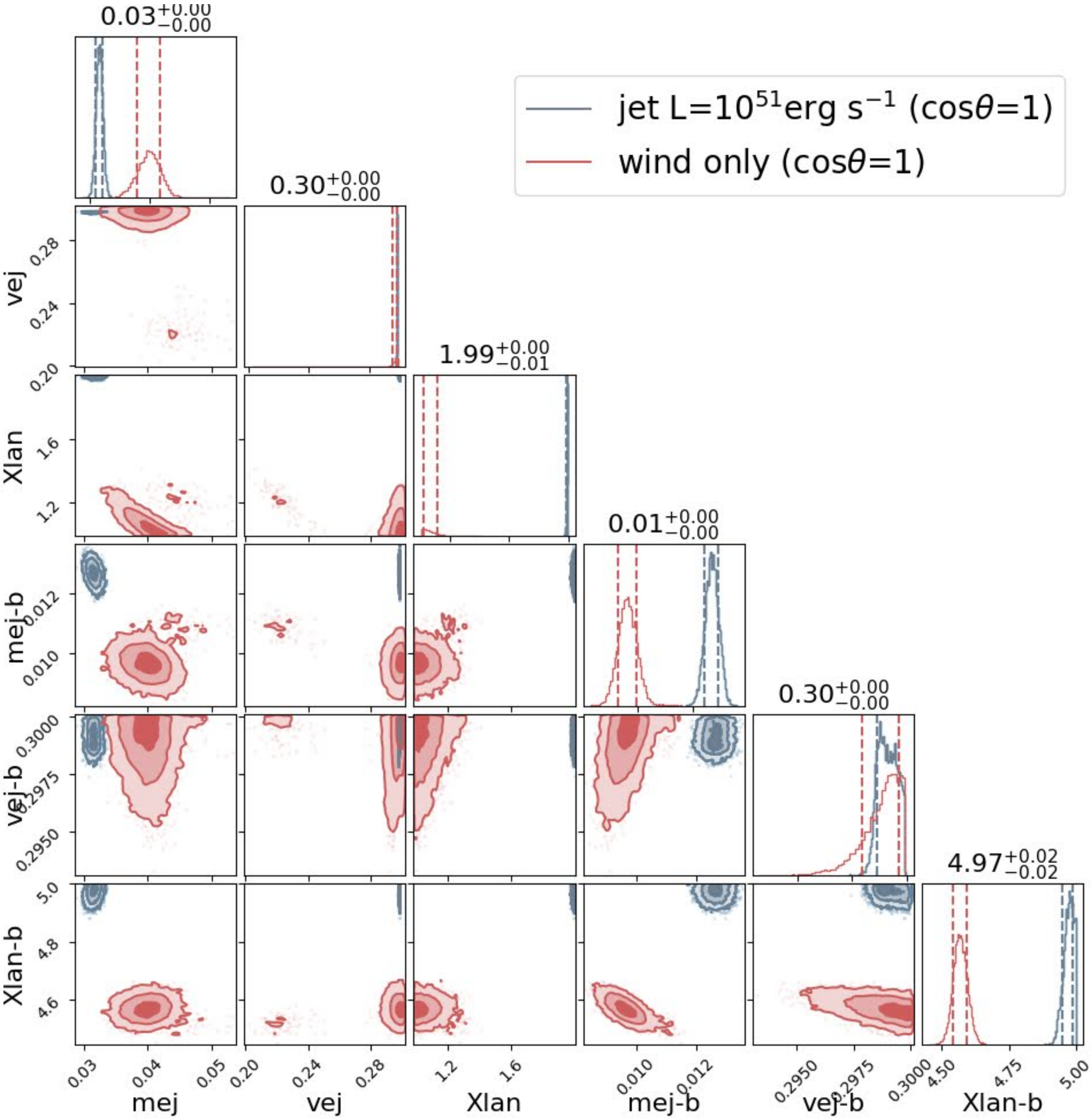

Figure 5.7: Corner plot for parameter estimation on kilonova with and without a jet. 12h cadence, *griz* bands, over 3 days. 0.1 magnitude uncertainty. Both models are for lanthanide-rich kilonovae with $\cos\theta_{obs} = 1.0$. The jetted kilonova has a jet luminosity $L_j = 10^{51}$ erg s^{-1}. The results are for the ejecta parameter of two components, a red component and a blue component.

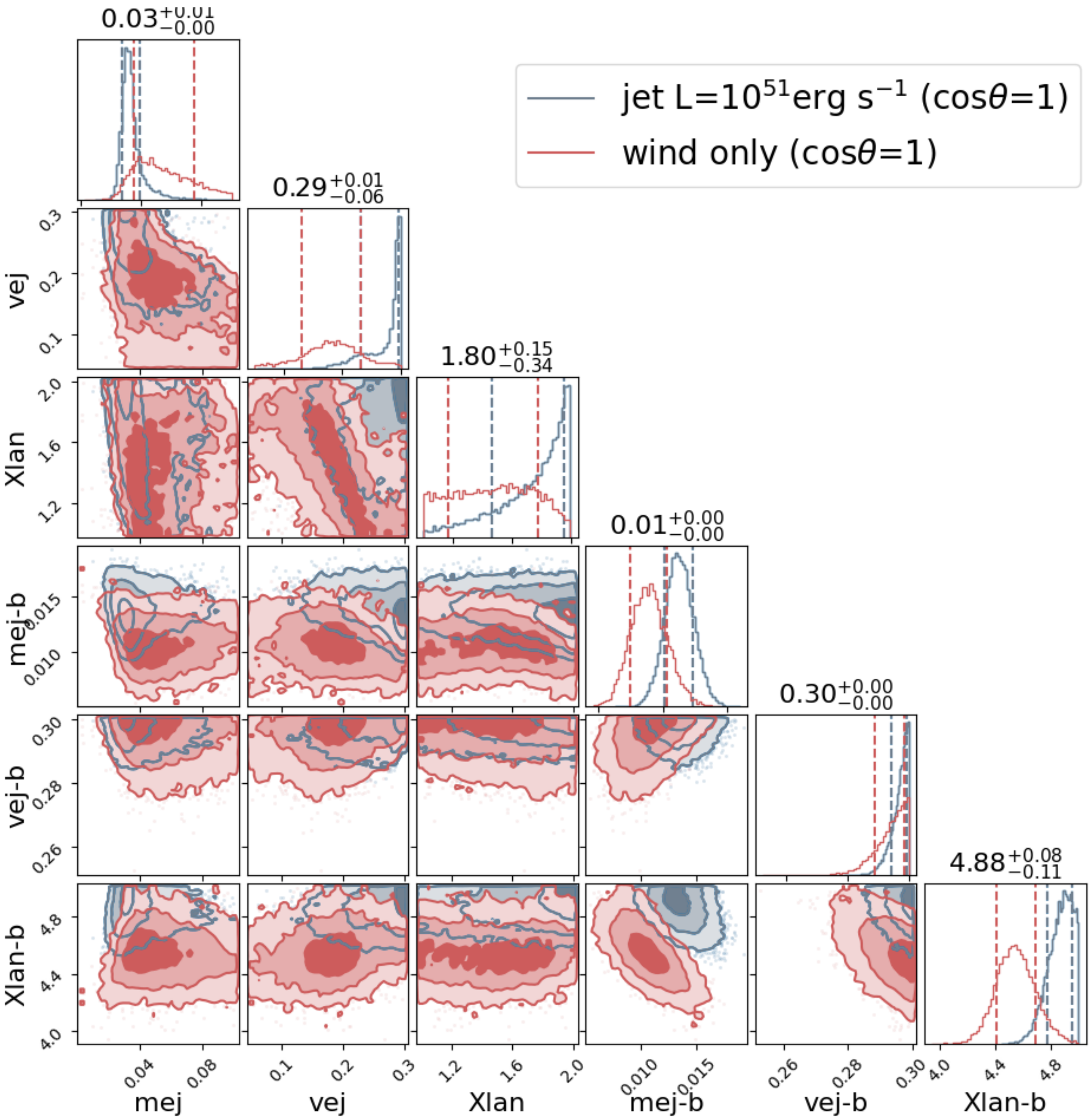

Figure 5.8: Corner plot for parameter estimation on kilonova with and without a jet. 12h cadence, *griz* bands, over 3 days. 0.5 magnitude uncertainty. Both models are for lanthanide-rich kilonovae with $\cos\theta_{obs} = 1.0$. The jetted kilonova has a jet luminosity $L_j = 10^{51}$ erg s^{-1}. The results are for the ejecta parameter of two components, a red component and a blue component.

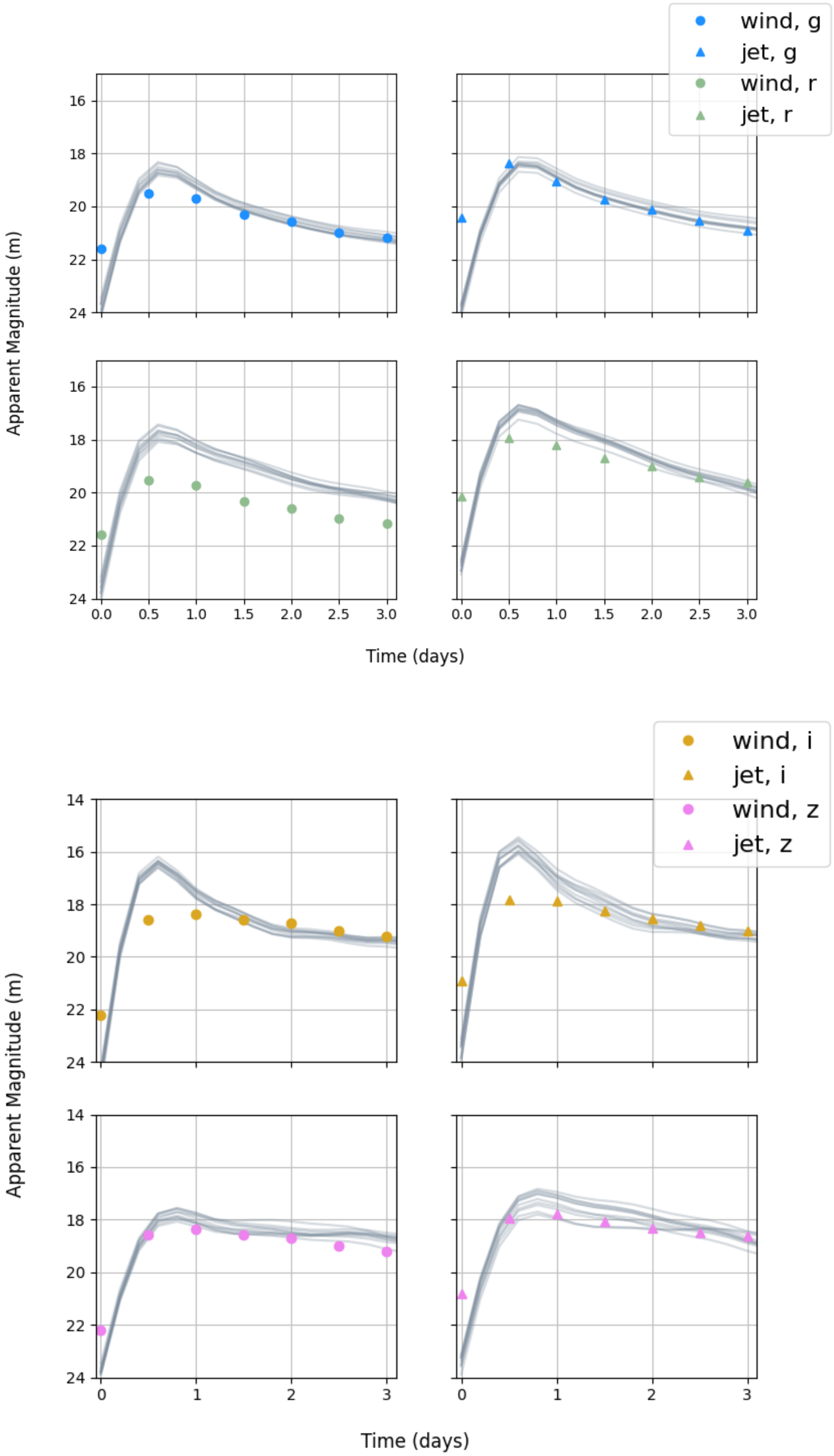

Figure 5.9: Models of wind-only and jetted kilonova with light curves generated from posterior samples. Each grey line is a light curve generated from a posterior sample of kilonova parameters, while the solid data points are the simulated observations from the kilonova models presented in [202]. The simulated observations are for a lanthanide-rich kilonova with a viewing angle $\cos\theta_{obs} = 1.0$ and jet luminosity $L_j = 10^{51}$ erg s^{-1} for the jetted case.

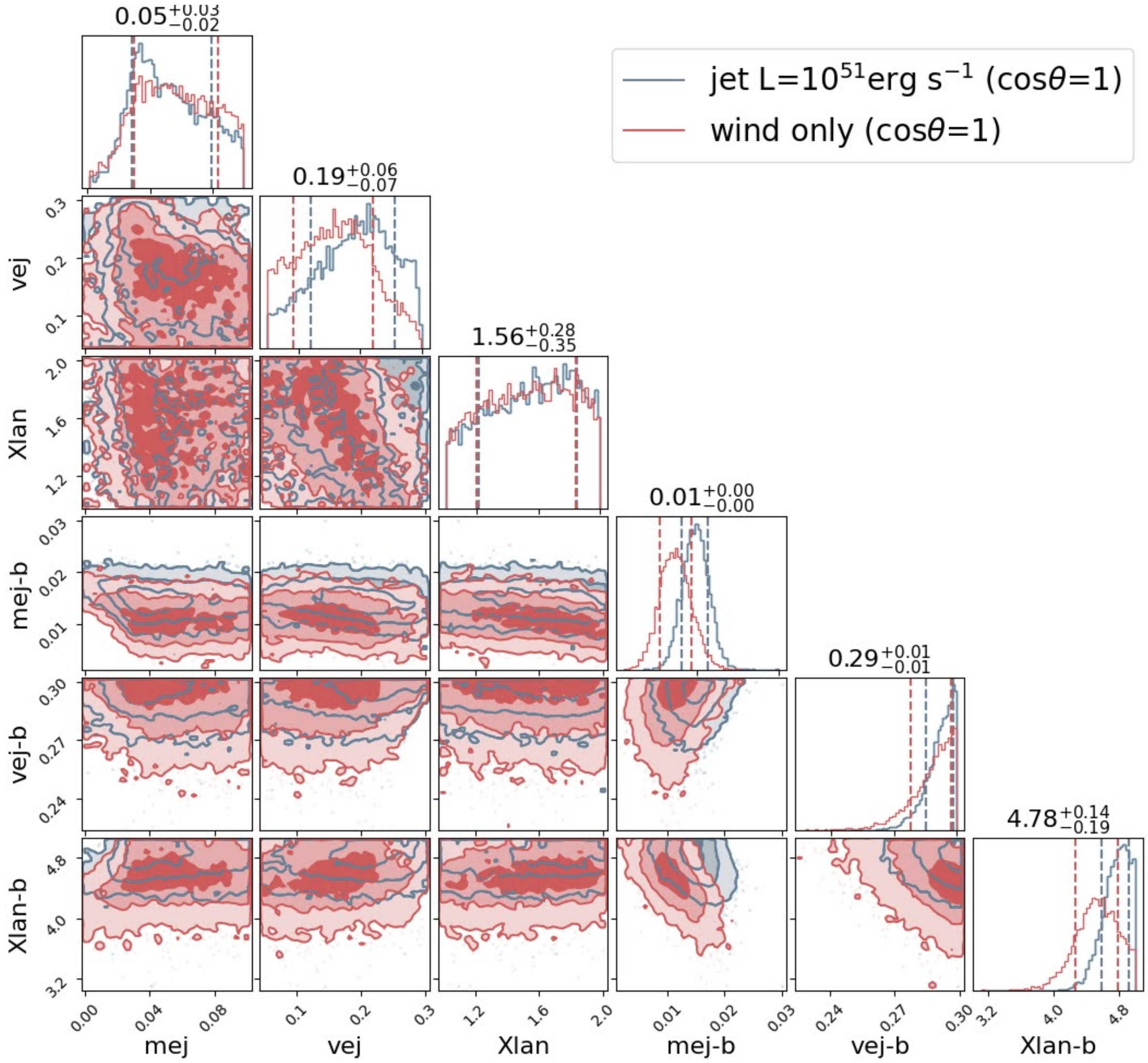

Figure 5.10: Corner plot for parameter estimation on kilonova with and without a jet. 12h cadence, *griz* bands, over 3 days. 1.0 magnitude uncertainty. Both models are for lanthanide-rich kilonovae with $\cos\theta_{obs} = 1.0$. The jetted kilonova has a jet luminosity $L_j = 10^{51}$ erg s^{-1}. The results are for the ejecta parameter of two components, a red component and a blue component.

5.2.2 Parameter estimation on lanthanide-rich kilonovae

Going forward, the analysis is performed with a more realistic cadence of 1 day, with observations being considered up to 7 days post-merger. The same bands, *griz*, are considered. Along with the lanthanide fraction, there are two other parameters that come into play for this analysis: the viewing angle of the kilonova and the luminosity of the jet. The starting time of observations is taken to be the same as with GW170817, at $t_0 \sim 0.4$days. Figure 5.1 shows light curves as a function of viewing angle for a jet-disrupted kilonova with a lanthanide-rich ejecta. The effect of the viewing angle is most pronounced in the *u* band, which is not considered in this analysis, as we focus on the most common bands for kilonova observations, *griz*.

In this section we present results of the previously described parameter estimation on lanthanide-rich kilonovae. These kilonovae have a higher fraction of the heavy elements (atomic mass over 140) called lanthanides. As the jet "punches" through the lanthanide curtain, we expect the fraction of lanthanides present in the kilonova ejecta to have an effect on the bias in recovered parameters. This is because the lanthanide-rich material contributes to the red emission from the kilonova; so if a jet has to drill through more lanthanide-rich material, we expect a greater difference in the resulting light curves than when the ejecta is lanthanide-free.

Models for two different jet luminosities are presented in [202]. The most luminous jet considered in the analysis has a luminosity $L_j = 10^{51}$ erg s^{-1}. The effect of the jet-ejecta interaction on the resulting emission is dependent on the jet's luminosity. The more energetic the jet, the brighter and bluer the resulting light curve will be. Powerful jets also make the radiation appear more isotropic.

Using the parameter inference method described in previous chapter, we perform a full parameter estimation on kilonova models with and without a jet interacting with the surrounding wind ("jetted" vs "wind-only").

Figure 5.11 shows results for two jetted kilonovae and a wind-only kilonova at an observing angle $\cos\theta_{obs} = 1.0$. There is a much larger bias in the recovered parameters with the more luminous jet, especially in the recovered ejecta velocity. The more luminous jet allows more radiation to escape from the kilonova earlier, making the ejecta appear faster when the effect of a jet is ignored. The parameter posteriors for a jetted kilonova with jet luminosity $L_j = 10^{49}$ erg s^{-1} have some significant overlap with the wind-only scenario. For a more luminous jet, there is a large bias in recovering the parameters.

Figures 5.12 and 5.13 show results comparing posteriors for a wind-only kilonova and a jetted kilonova with jet luminosity $L_j = 10^{51}$ erg s^{-1} for two different viewing angles $\cos\theta_{obs} = 0.0$ and 1.0. The effect of the jet interaction on the recovered posteriors is more pronounced for $\cos\theta_{obs} = 1.0$. Figure 5.14 compares the jetted kilonova with $L_j = 10^{51}$ erg s^{-1} and $\cos\theta_{obs} = 1.0$ to two wind-only kilonovae, each with a different viewing angle.

All final results are summarised in table 5.1, showing the 90% credible interval for each parameter. The table shows the inferred v_{ej} and m_{ej} of the two components for all three kilonovae

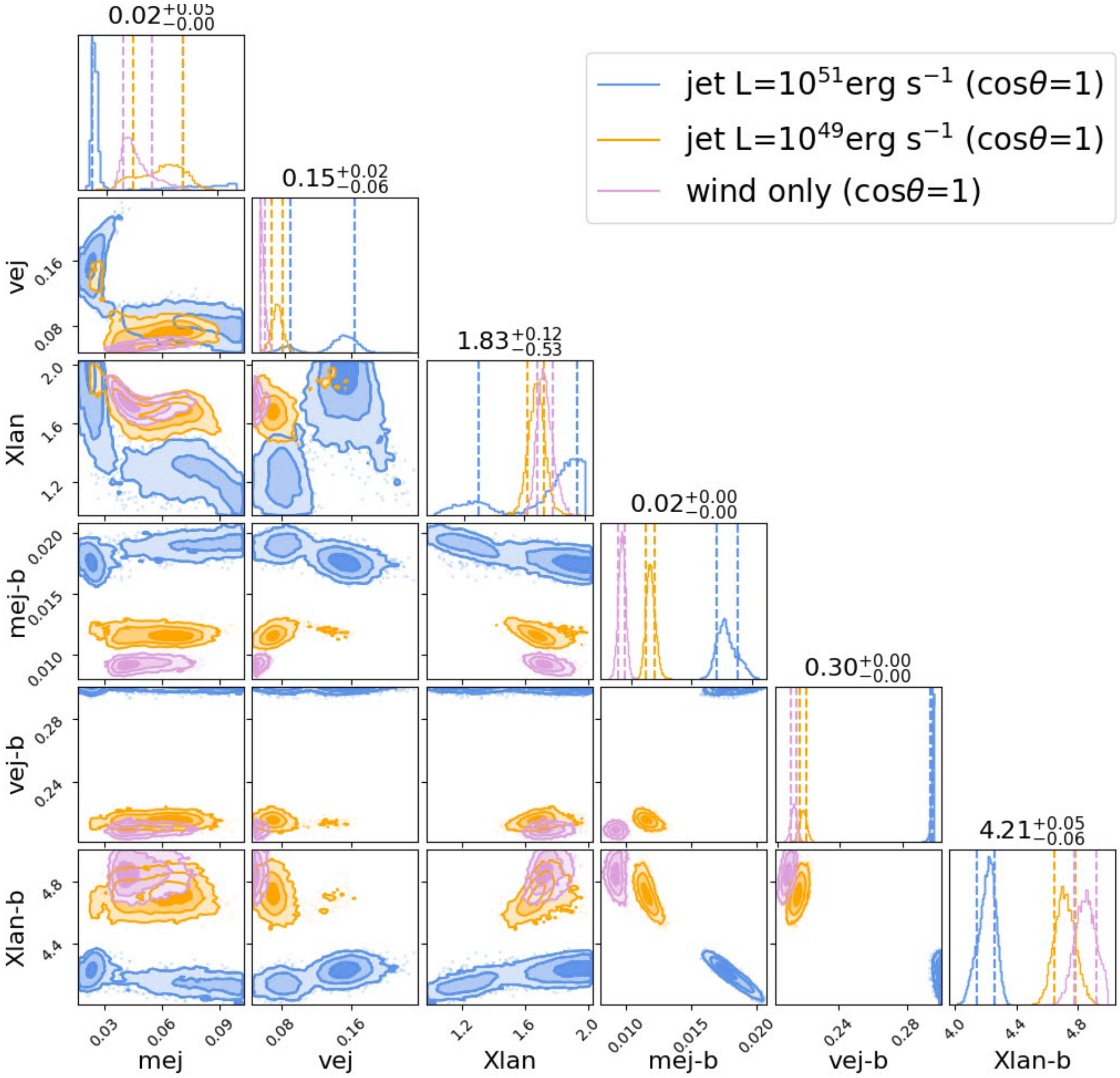

Figure 5.11: Corner plot for parameter estimation on lanthanide-rich kilonova with $cos\theta = 1.0$ with and without a jet. The uncertainty on the models is taken to be 0.1 mag. This corner plot compares the wind-only kilonova parameters to the two jetted kilonovae, with luminosities $L_j = 10^{49}$ and 10^{51} erg s^{-1}

(wind-only, jet with luminosity $L_j = 10^{49}$ erg s^{-1} and $L_j = 10^{51}$ erg s^{-1}) and for two viewing angles ($\cos\theta_{obs} = 1$ and $\cos\theta_{obs} = 0$). Most of the recovered parameters are similar when considering a viewing angle $\cos\theta_{obs} = 0$. The ejecta mass for the blue component is overestimated by 16% in the presence of a strong jet with luminosity $L_j = 10^{51}$ erg s^{-1}. When considering a viewing angle of $\cos\theta_{obs} = 1$, the ejecta mass for the red component is underestimated by a factor of $\sim$2 while the ejecta mass for the blue component is overestimated by a factor of $\sim$2. The ejecta velocity for both components is also overestimated in the presence of a strong jet.

$\cos\theta_{obs} = 0$	Wind-only	Jet $L_j = 10^{49}$erg s^{-1}	Jet $L_j = 10^{51}$erg s^{-1}
Ejecta mass (red) ($M_\odot$)	$0.0332^{+0.004}_{-0.002}$	$0.0331^{+0.004}_{-0.002}$	$0.0338^{+0.020}_{-0.008}$
Ejecta mass (blue) ($M_\odot$)	$0.0106^{+0.0005}_{-0.0005}$	$0.0111^{+0.0005}_{-0.0005}$	$0.0126^{+0.0007}_{-0.0008}$
Ejecta velocity (red) (c)	$0.054^{+0.006}_{-0.003}$	$0.055^{+0.007}_{-0.004}$	$0.08^{+0.04}_{-0.02}$
Ejecta velocity (blue) (c)	$0.214^{+0.003}_{-0.003}$	$0.216^{+0.003}_{-0.003}$	$0.216^{+0.004}_{-0.003}$
$\cos\theta_{obs} = 1$	Wind-only	Jet $L_j = 10^{49}$erg s^{-1}	Jet $L_j = 10^{51}$erg s^{-1}
Ejecta mass (red) ($M_\odot$)	$0.044^{+0.02}_{-0.008}$	$0.06^{+0.02}_{-0.02}$	$0.024^{+0.07}_{-0.003}$
Ejecta mass (blue) ($M_\odot$)	$0.0092^{+0.0005}_{-0.0005}$	$0.0117^{+0.0007}_{-0.0006}$	$0.018^{+0.002}_{-0.001}$
Ejecta velocity (red) (c)	$0.053^{+0.007}_{-0.003}$	$0.07^{+0.01}_{-0.01}$	$0.15^{+0.03}_{-0.07}$
Ejecta velocity (blue) (c)	$0.210^{+0.003}_{-0.003}$	$0.216^{+0.004}_{-0.004}$	$0.2992^{+0.0007}_{-0.0020}$

Table 5.1: Table of results for lanthanide-rich kilonovae. The lanthanide fraction X_{lan} is omitted from this table.

5.2.3 Parameter estimation on lanthanide-free kilonovae

The previous results show ejecta parameter estimation for a jetted and a wind-only kilonova for a lanthanide-rich ejecta. In this section, we present results for the "lanthanide-free" case. The kilonovae considered in this analysis have a lower fraction of heavy elements. This means the kilonova in this scenario is brighter, especially in the bluer bands. This can be seen when comparing figures 5.2 and 5.1. All other variables (jet luminosity, viewing angle) are the same as previously. As before, a 1 day cadence is used over 7 days in the *griz* bands and the uncertainty

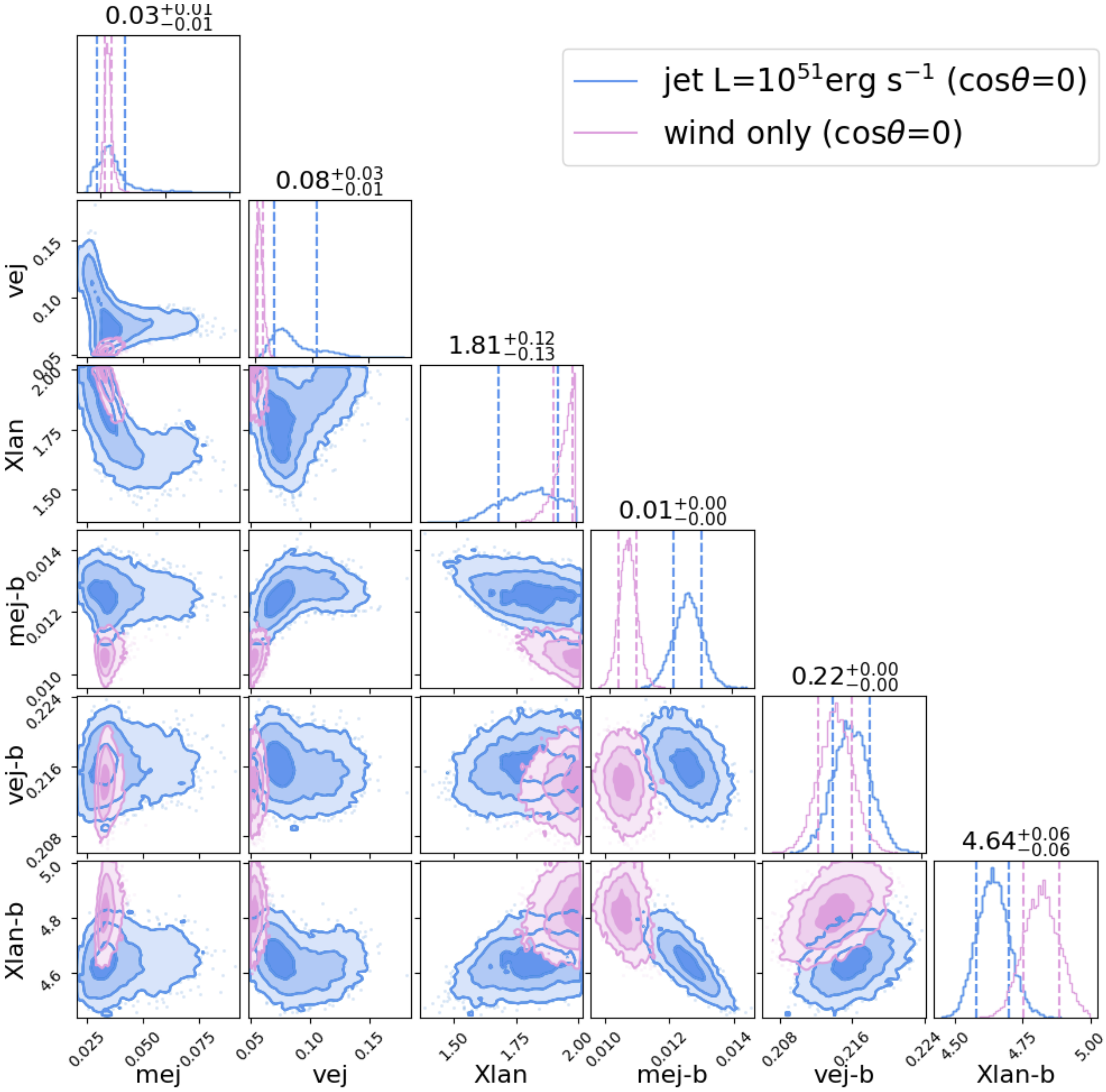

Figure 5.12: Corner plot for parameter estimation on kilonova with and without a jet. 1 day cadence, *griz* bands, over 7 days. 0.1 magnitude uncertainty. This is for a lanthanide-rich model with a jet $L_j = 10^{51}$ erg s^{-1} and $\cos\theta_{obs} = 0$.

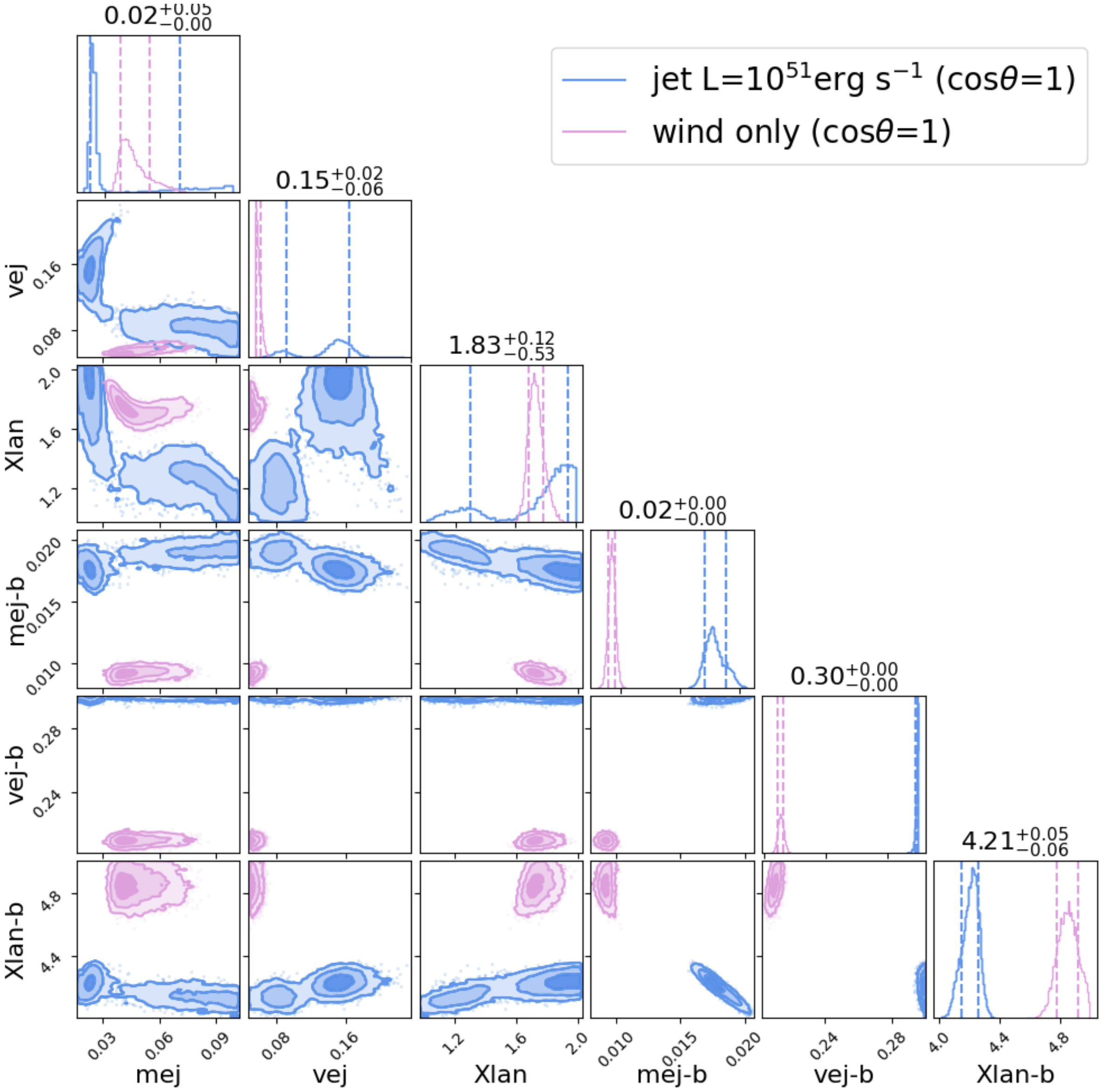

Figure 5.13: Corner plot for parameter estimation on kilonova with and without a jet. 1 day cadence, *griz* bands, over 7 days. 0.1 magnitude uncertainty. This is for a lanthanide-rich model with a jet $L_j = 10^{51}$ erg s^{-1} and $\cos\theta_{obs} = 1$.

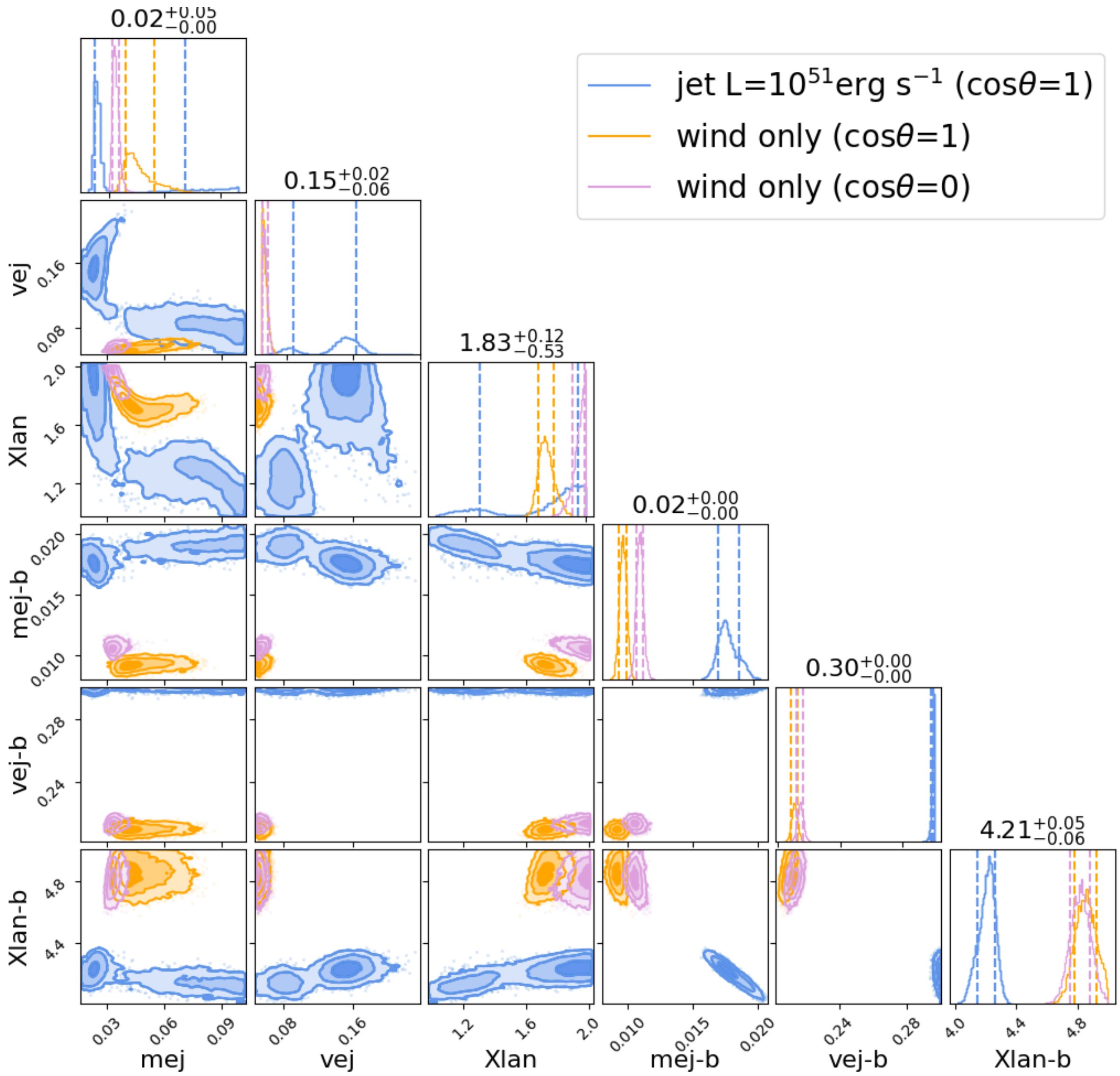

Figure 5.14: Results of the parameter estimation on a jetted kilonova ($L_j = 10^{51}$ erg s^{-1}, $\cos\theta_{obs} = 1$) and two wind-only kilonovae with different $\cos\theta_{obs}$. All results for a lanthanide-richLR composition.

on the models is taken to be $\sigma = 0.1$ mag.

Figure 5.15 shows results for two lanthanide-free kilonovae, one wind-only kilonova and a kilonova with a jet with luminosity $L_j = 10^{51}$ erg s^{-1}. Both have a viewing angle $\cos\theta_{obs} = 0$. The results show some multi-modalities in the parameters for the red component. For the blue component, v_{ej} is slightly overestimated in the jetted kilonova compared to the wind-only one, but the recovered ejecta mass m_{ej} is similar.

Figure 5.15 shows the same scenario as previously described but with a viewing angle $\cos\theta_{obs} = 1$. As before with the lanthanide-rich kilonovae, in the presence of a jet the recovered ejecta mass m_{ej} for the blue component is affected, with the mass being overestimated in the models with interaction from a powerful jet. The effect is less pronounced than in the lanthanide-rich models. However, all results show an overestimation of the ejecta velocity v_{ej} for the blue component in strongly jetted kilonovae.

Figures 5.17 and 5.18 show the results of parameter estimation on those same lanthanide-free kilonovae, for jetted kilonovae and wind-only kilonovae with different viewing angles. The jet makes the radiation more isotropic, meaning that some information on the viewing angle is lost, with the blue component of the jetted kilonova in both cases being more similar to the wind-only kilonova with $\cos\theta_{obs} = 0$. The loss of this viewing-angle information from jetted kilonovae could have implications for other fields (for example, cosmology) that rely on recovering angle information from EM counterparts.

Compared to the lanthanide-rich results, there is little difference in the recovered lanthanide fraction X_{lan}. However, the ejecta mass for the blue component differs significantly, implying the presence of more lanthanide-free material shining through the kilonova as the jet punches through. All results still show that the ejecta mass for the blue component is slightly overestimated in the presence of a powerful jet, though to varying degrees depending on the initial conditions of the kilonova wind.

All results of the parameter estimation on m_{ej} and v_{ej} for lanthanide-free kilonovae are summarised in table 5.2. As was the case in table 5.1, the 90% credible intervals are presented for each parameter, and the results are shown for the three different kilonovae and for two viewing angles. For both viewing angles ($\cos\theta_{obs} = 0$ and $\cos\theta_{obs} = 1$), the ejecta velocity on the red component seems to be overestimated in the presence of a jet, but the uncertainties are very large. For a viewing angle $\cos\theta_{obs} = 0$, the red component ejecta mass is again overestimated in the presence of a jet, but the uncertainties are large enough to make this result unreliable. Other parameters for this viewing angle are similar with or without a jet. For $\cos\theta_{obs} = 1$, the presence of a strong jet mostly impacts the recovered blue component ejecta mass, with the mass being overestimated by $\sim 17\%$ in the presence of a jet with luminosity $L_j = 10^{51}$ erg s^{-1}.

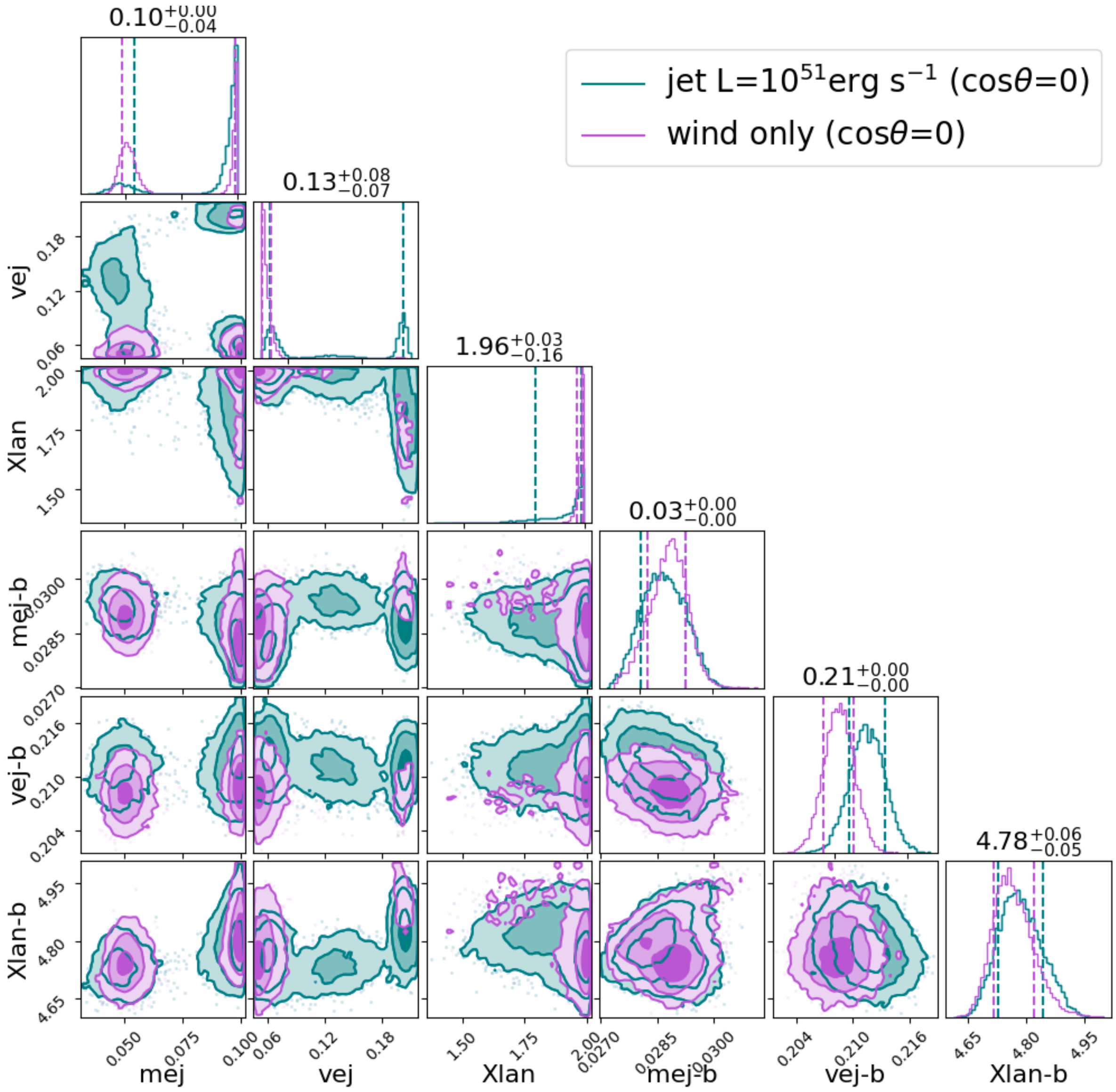

Figure 5.15: Corner plot for parameter estimation on kilonova with and without a jet. 1 day cadence, *griz* bands, over 7 days. 0.1 magnitude uncertainty. This is for a lanthanide-free model with a jet 10^{51} erg s^{-1} and $\cos\theta_{obs} = 0$.

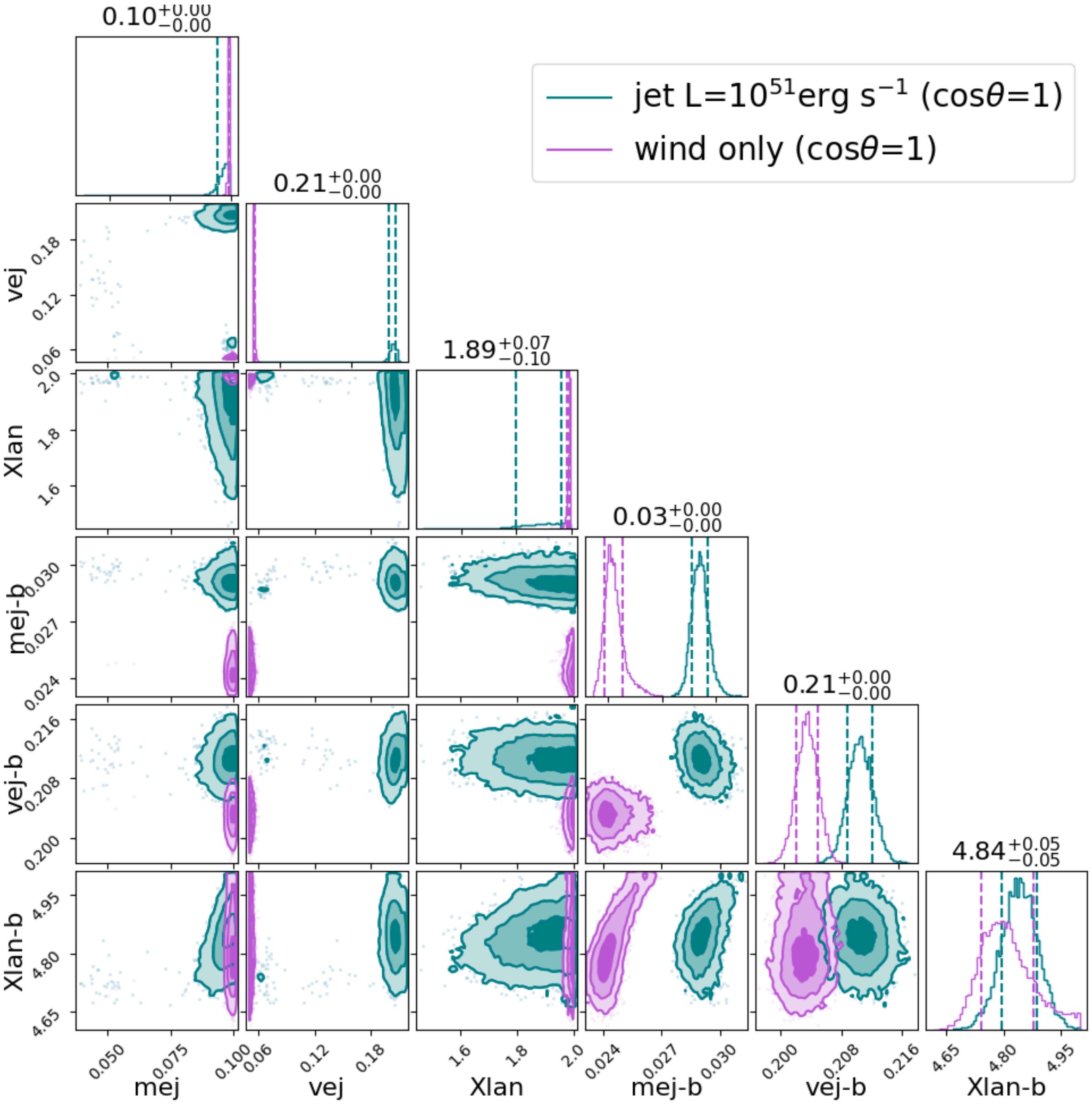

Figure 5.16: Corner plot for parameter estimation on kilonova with and without a jet. 1 day cadence, *griz* bands, over 7 days. 0.1 magnitude uncertainty. This is for a lanthanide-free model with a jet 10^{51} erg s^{-1} and $\cos\theta_{obs} = 1$.

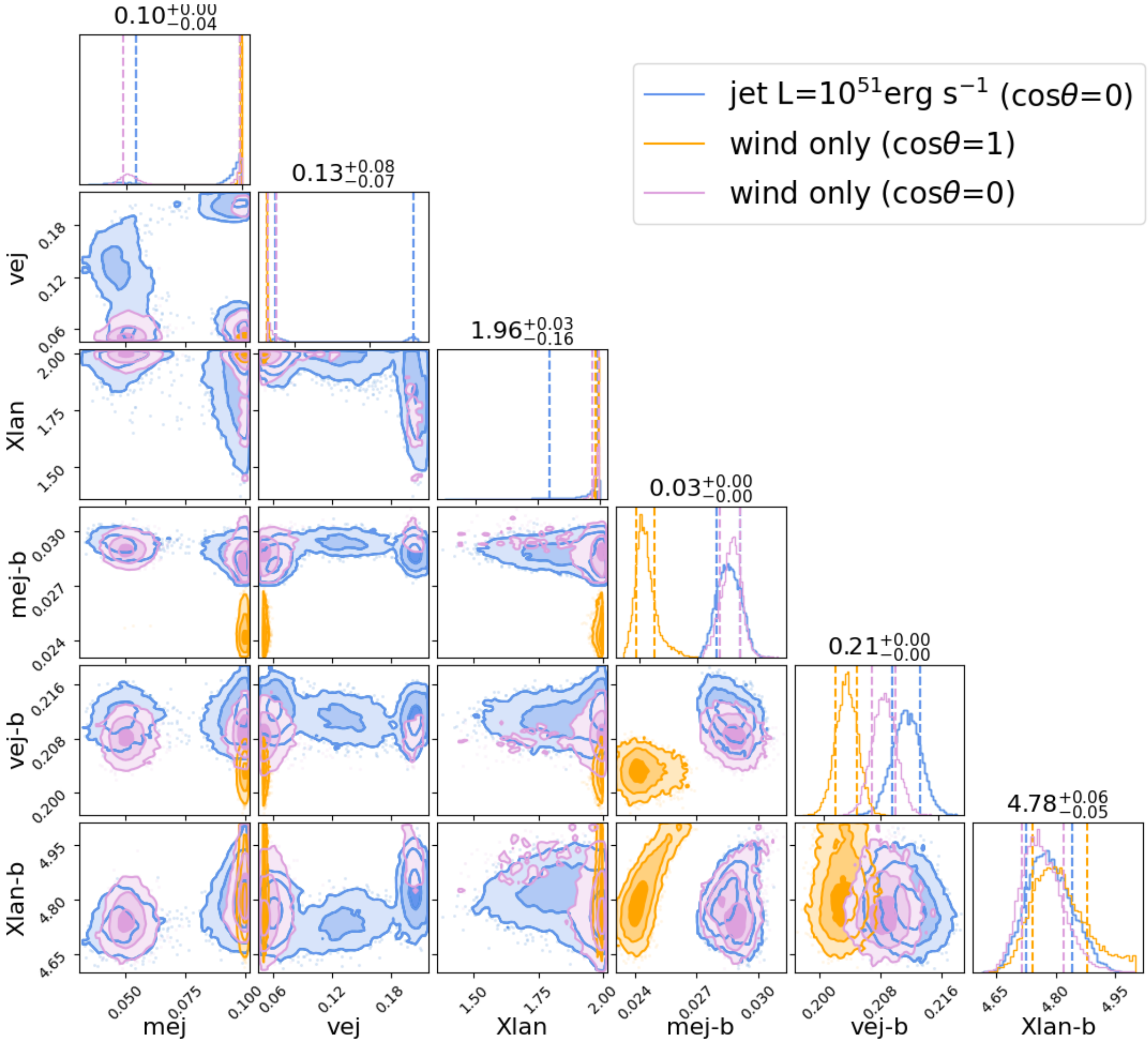

Figure 5.17: Results of the parameter estimation on a jetted kilonova ($L_j = 10^{51}$ erg s^{-1}, $\cos\theta_{obs} = 0$) and two wind-only kilonovae with different $\cos\theta_{obs}$. All results for a lanthanide-free composition.

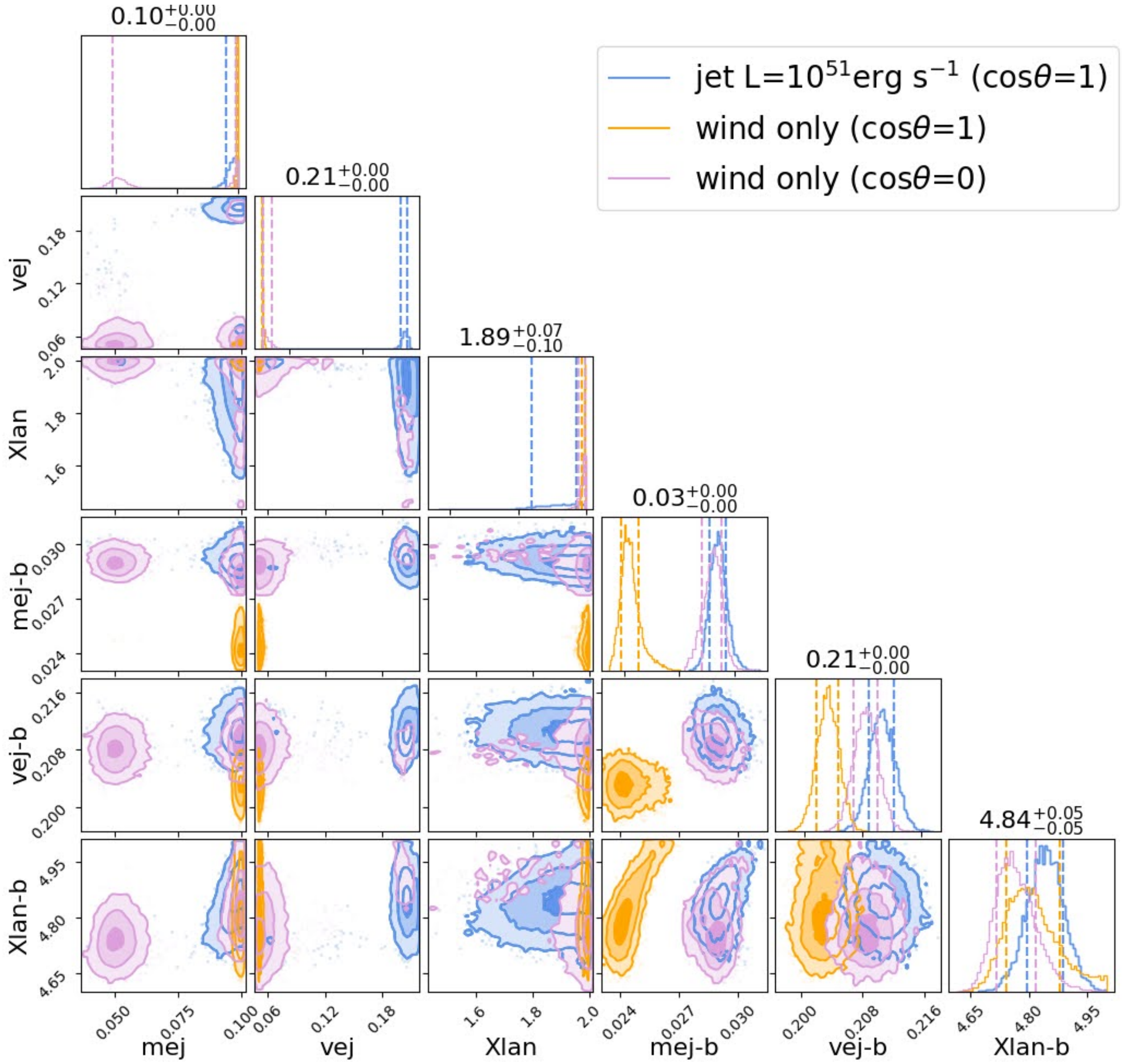

Figure 5.18: Results of the parameter estimation on a jetted kilonova ($L_j = 10^{51}$ erg s^{-1}, $\cos\theta_{obs} = 1$) and two wind-only kilonovae with different $\cos\theta_{obs}$. All results for a lanthanide-free composition.

$\cos\theta_{obs} = 0$	Wind-only	Jet $L_j = 10^{49}$erg s^{-1}	Jet $L_j = 10^{51}$erg s^{-1}
Ejecta mass (red) ($M_\odot$)	$0.054^{+0.05}_{-0.008}$	$0.098^{+0.002}_{-0.05}$	$0.0977^{+0.003}_{-0.05}$
Ejecta mass (blue) ($M_\odot$)	$0.0288^{+0.0008}_{-0.0009}$	$0.0292^{+0.0010}_{-0.001}$	$0.0286^{+0.0010}_{-0.0009}$
Ejecta velocity (red) (c)	$0.055^{+0.01}_{-0.004}$	$0.13^{+0.08}_{-0.08}$	$0.13^{+0.08}_{-0.07}$
Ejecta velocity (blue) (c)	$0.208^{+0.003}_{-0.003}$	$0.212^{+0.003}_{-0.003}$	$0.212^{+0.003}_{-0.003}$
$\cos\theta_{obs} = 1$	Wind-only	Jet $L_j = 10^{49}$erg s^{-1}	Jet $L_j = 10^{51}$erg s^{-1}
Ejecta mass (red) ($M_\odot$)	$0.0996^{+0.0003}_{-0.0009}$	$0.0993^{+0.0005}_{-0.002}$	$0.097^{+0.002}_{-0.005}$
Ejecta mass (blue) ($M_\odot$)	$0.0242^{+0.001}_{-0.0007}$	$0.0273^{+0.0008}_{-0.0007}$	$0.0291^{+0.0008}_{-0.0007}$
Ejecta velocity (red) (c)	$0.0509^{+0.002}_{-0.0006}$	$0.054^{+0.008}_{-0.003}$	$0.2^{+0.2}_{-0.007}$
Ejecta velocity (blue) (c)	$0.203^{+0.002}_{-0.003}$	$0.208^{+0.003}_{-0.003}$	$0.211^{+0.003}_{-0.003}$

Table 5.2: Table of results for lanthanide-free kilonovae. The lanthanide fraction X_{lan} is omitted from this table.

5.3 Conclusions

The results of this analysis qualitatively show that if the potential effect of the interaction of a relativistic jet with the surrounding material is not taken into account, the ejecta parameters recovered from kilonova light curves will be biased. This is especially true of the ejecta velocity and ejecta mass, with the effect being most pronounced in line of sight viewing angles and for more powerful jets. The viewing angle dependence of the bias comes from the jet introducing its own viewing angle dependency, with the radiation escaping more easily along the jet axis. This makes the radiation appear more isotropic.

This also means that some viewing angle information could be lost if the jet-ejecta interaction is not taken into account. The presence of a jet could make the resulting light curve look like that of a kilonova with a different viewing angle.

While the results of this analysis are strongly model-dependent, by taking the results of the parameter estimation on the wind-only kilonova as the "true" ejecta parameters, it is possible to make qualitative statements about the impact of ignoring jet-ejecta interaction.

Lanthanide-rich kilonovae, especially, show a large discrepancy in the recovered parameters when neglecting the effect of a jet, especially when observed in the polar axis. In the case of a lanthanide-rich kilonova with a strong jet and observed in the plane of the polar axis, the estimate for the ejecta mass m_{ej} of the blue component is doubled.

It should be noted, however, that kilonova modelling is a rapidly evolving field, and any results from parameter estimation runs is model-dependent. There are several discrepancies between the models used in this work, and neither incorporate all effects observable in the emission from a real kilonova. This can be seen in the fits in figures 5.9 and 5.5, where the light curves generated from the posteriors on the inferred parameters are not a very good fit to the models presented in [202].

The jetted models do not incorporate jet afterglow emission that would be seen in real observations. These models also neglect the very neutron-rich matter first ejected tidal dynamical ejecta that covers the orbital plane of the binary. On the other hand, the models used in the parameter estimation identify several mechanisms for the ejection of matter. The models used for the parameter estimation are also 1-dimensional, but the simulations of the jetted and wind-only kilonovae that are used to simulate observations are 3-dimensional. Viewing angle dependence could affect the resulting peak luminosity by $\sim 20\%$.

The real model uncertainties are also large, with the standard model uncertainty on the Kasen models taken to be $\sigma = 1$ mag. This work presented results for small model uncertainties, with $\sigma = 0.1$ mag. However, it can still be seen in the parameter estimation runs where $\sigma = 1$ mag that the ejecta mass is overestimated in the presence of a jet, compared to the models that are wind-only.

While the results are mostly qualitative, we can still see a clear trend in the discrepancy between the inferred parameters for the wind-only and the jetted kilonovae. The results illustrate the impact of neglecting the effect of jet-ejecta interaction on parameter estimation from kilonova light curves. Depending on the scenario, the ejecta mass could be overestimated by up to a factor of $\sim$2. Since the mass of the ejecta from BNS systems is dependent on parameters of the progenitor system and on the neutron star EOS, it is an important parameter to constrain accurately.

As future simulations improve and incorporate more kilonova physics, the pipeline could be adapted to new models for further, more quantitative studies of the impact of jet-ejecta interaction on the recovered kilonova parameters.

6 | Gravitational Wave Cosmology

> In the beginning there was nothing,
> which exploded.
>
> Terry Pratchett

This section introduces work done for implementation into the **`gwcosmo`** pipeline. It builds upon previous work done by Gray et al. [220] to refine the treatment of the probability of the host galaxy associated with a gravitational wave event being within a galaxy catalogue, $p(G|D_{GW}, x_{GW})$.

Chapter 2 presented an overview of modern cosmology, including a brief introduction to cosmology with gravitational waves. This chapter goes more in-depth on methods for measuring the Hubble constant using standard sirens, and presents the implementation of a robust statistical test of galaxy catalogue completeness into one of the current gravitational wave cosmology pipelines for inferring the Hubble constant.

6.1 Gravitational Wave Cosmology with Standard Sirens

With the detection of GW150914, prospects for gravitational wave cosmology started to become a reality. With observations of many compact binary coalescences, a precise estimate of the Hubble constant could be obtained, through either statistical means or by the identification of electromagnetic counterparts (such as kilonovae) to gravitational wave signals.

The best result from a single gravitational wave event to date comes from GW170817, which was accompanied by electromagnetic signatures that allowed astronomers to determine which host galaxy the signal originated from. A redshift could then be obtained from the host galaxy. Since GW170817 had an accompanying EM signal, it is known as a "bright siren". The rest of the chapter will focus on the treatment of "dark sirens", gravitational wave signals which do not have a confirmed detection of a coincident electromagnetic signature. This is the case for all signals detected to date, except GW170817. [40,221] The event GW190521, then S190521g, had a candidate EM counterpart, ZTF19abanrhr, a flare detected by ZTF. [109] Using the uniquely identified host galaxy associated with the potential counterpart of GW190521, a standard siren

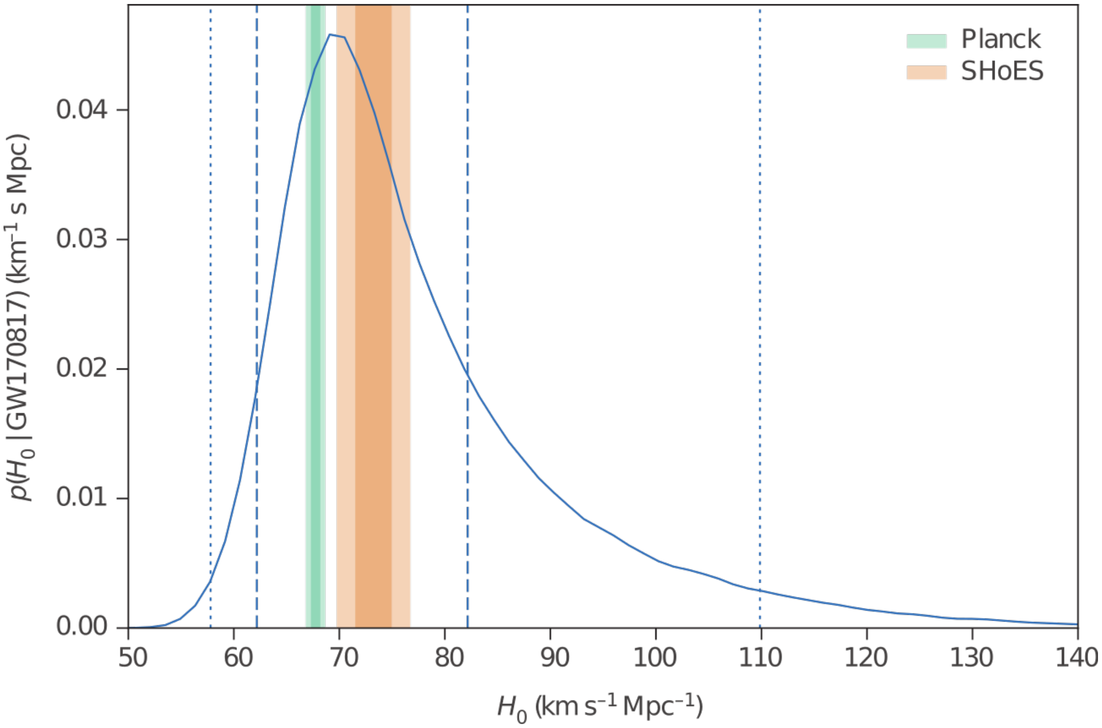

Figure 6.1: The 2017 result for H_0 from GW170817 [221]. The shaded regions show the latest SHoEs and Planck results at the time of publication. Figure from [221].

measurement of H_0 found $H_0 = 48^{+24}_{-10}$ km s^{-1} Mpc^{-1} [222] However, the association between the electromagnetic event ZTF19abanrhr and GW190521 is not confirmed.

The binary neutron star merger GW170817 was accompanied by the observation of an optical counterpart (kilonova) and a short GRB. [40] The detection of these coincident EM signals allowed for the identification of the event's host galaxy, NGC 4993. Redshift information was then obtained from host spectroscopy. [40]. The identification of the host galaxy was independent of H_0.

The result obtained from GW170817 gives a Hubble constant of $H_0 = 70^{+10}_{-8}$ km s^{-1} Mpc^{-1} [221] Figure 6.1 shows the 2017 measurement of the Hubble constant using the luminosity distance from the waveform of the binary neutron star merger GW170817 and the redshift from the identified host galaxy NGC 4993. [221]

6.1.1 Dark sirens

In the case of GW170817, the identification of the host galaxy from the accompanying electromagnetic signals generated by the event allowed for the easy obtention of redshift information for the event.

In the case where no EM counterpart is detected, redshift information can still be obtained through statistical means. This is the original method proposed by Schutz, relying on the use of galaxy catalogues for obtaining redshift information about the gravitational wave source. [157]

The rest of this chapter focuses on this statistical method, using redshift information from galaxy catalogues as part of a pipeline for inferring the Hubble constant. This is not the only statistical method for inferring H_0. There is a second method for inferring H_0 using standard sirens in the absence of an EM counterpart; this method jointly fits the cosmological parameters and the source population properties of binary black holes, and does not make use of any galaxy catalogue. [156, 223]

6.1.2 The galaxy catalogue method and `gwcosmo`

One of the statistical methods for inferring H_0 from compact binary coalescences with no EM counterpart is known as the galaxy catalogue method. It should be noted that this method is subject to biases, mostly due to assumptions about the BBH source mass distribution. [156] In this method, a probable host galaxy from a catalogue is associated to each gravitational wave event, providing a redshift. The uncertainty in the host galaxy is marginalised over for each GW event.

This galaxy catalogue is the one currently used in the **`gwcosmo`** pipeline. A full description of the methodology of the pipeline can be found in [224]. **`gwcosmo`** is a python package used for inferring H_0 from gravitational wave observations. It makes use of two methods: the EM counterpart method (for the treatment of "bright sirens"), and the previously mentioned galaxy catalogue method (for the treatment of "dark sirens"). The treatment of dark sirens implements the method outlined by Schutz in [157].

Figure 6.2 presents a network diagram of the workings of the Bayesian framework of **`gwcosmo`**. The parameters are:

- H_0 the Hubble constant
- M the absolute magnitude of galaxies
- z the galaxy redshifts
- Ω the cosmological parameters
- d_L the luminosity distance
- s the GW source
- m the apparent magnitude of galaxies
- m_{thr} the catalogue's limiting apparent magnitude
- x_{GW} the GW data associated with the GW source
- ρ_{thr} the gravitational wave SNR threshold

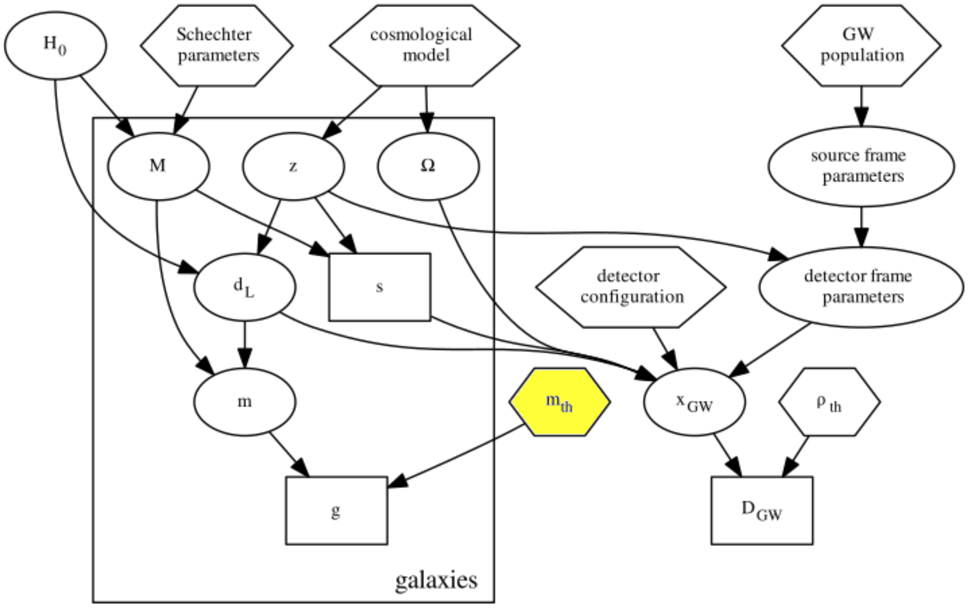

Figure 6.2: Network diagram of the parameters included in the **gwcosmo** methodology, from [224]. The magnitude threshold for the galaxy catalogue m_{thr} is highlighted, showing which other parameters this feeds into. The boxed in parameters are inferred individually for every galaxy considered. The magnitude threshold m_{thr} acts on which galaxies are considered g.

- D_{GW} indicating that a gravitational wave signal was detected; x_{GW} passed detection threshold ρ_{GW}
- g the galaxies

The diagram shows every parameter that goes into the final posterior on H_0, and how they relate to each other. The galaxy catalogue method for statistical inference of the Hubble constant relies on the identification of potential host galaxies in the skymap defined by the gravitational wave event. The gravitational wave data provides a luminosity distance while each galaxy provides a redshift. The probability for each galaxy with redshift z to be the host is tested for a range of values of H_0 using the relationship $d_L = \frac{cz}{H_0}$. Marginalised over all galaxies, we obtain a posterior on the Hubble constant. With a large number of gravitational wave events, the final posterior will converge around the true H_0, as the redshift and distance information associated with each true host galaxy will be associated with the same, true, value of the Hubble constant.

$$p(H_0|x_{GW}, D) \propto p(H_0) \prod_i^N p(x_{GW}|D, H_0), \tag{6.1}$$

with x_{GW} the gravitational wave data, $\mathscr{D}$ corresponding to the data being above a detection threshold SNR $\rho_{thr} = 12$, and N the number of detections.

In order to use galaxy catalogues to obtain statistical information about the redshift of a gravitational wave event's redshift, we need to know how complete the catalogue used is. If a galaxy catalogue is not complete to the limit of gravitational wave detectability, the host galaxy of the event might lie outwith the catalogue. Assuming a complete catalogue would therefore introduce large systematics due to the assumption that the host galaxy of an event would necessarily be in the catalogue. Therefore, it is necessary to carefully estimate the completeness of any galaxy catalogue used in this method.

Figure 6.2 shows a network diagram of the parameters that feed into the **gwcosmo**, showing where the galaxy catalogue completeness and m_{thr} come into play. A complete derivation of the Bayesian formalism behind the **gwcosmo** pipeline can be found in [224].

We summarise the most relevant parts of the equations that involve the probability of the host galaxy of the event being in the galaxy catalogue, and thus the apparent magnitude threshold m_{thr}.

In order to get a final posterior on H_0, we need to marginalise the probability of the data over the two propositions G and $\overline{G}$, with:

- g representing proposition G and $\overline{G}$
- G representing that the host galaxy is within the galaxy catalogue
- $\overline{G}$ representing that the host galaxy is outwith the galaxy catalogue

In the **gwcosmo** pipeline, these depend on the apparent magnitude threshold of the catalogue.

$$p(x_{GW}|D,H_0) = \sum_g p(x_{GW}|g,D,H_0)p(g|D,H_0). \tag{6.2}$$

$p(G|z,\Omega,M,m,D,s,H_0)$ is approximated to a Heaviside step function around the apparent magnitude threshold m_{thr}, corresponding to a sharp cut-off on apparent magnitude.

$$p(G|D,s,H_0) = \frac{\int_0^{z(M,m_{thr},H_0)} dz \int d\Omega p(D|z,\Omega,s,H_0)p(s|z)p(z)p(\Omega)p(s|M,H_0)p(M|H_0)}{\int\int\int p(D|z,\Omega,s,H_0)p(s|z)p(z)p(\Omega)p(s|M,H_0)p(M|H_0)dzd\Omega dM}. \tag{6.3}$$

Equation 6.3 is, for a given Hubble constant H_0, the probability that the host galaxy for a gravitational wave event is contained within the catalogue.

This is not the only part of the **gwcosmo** pipeline that is affected by the choice of m_{thr}; galaxies with apparent magnitudes below the threshold are discarded in the analysis.

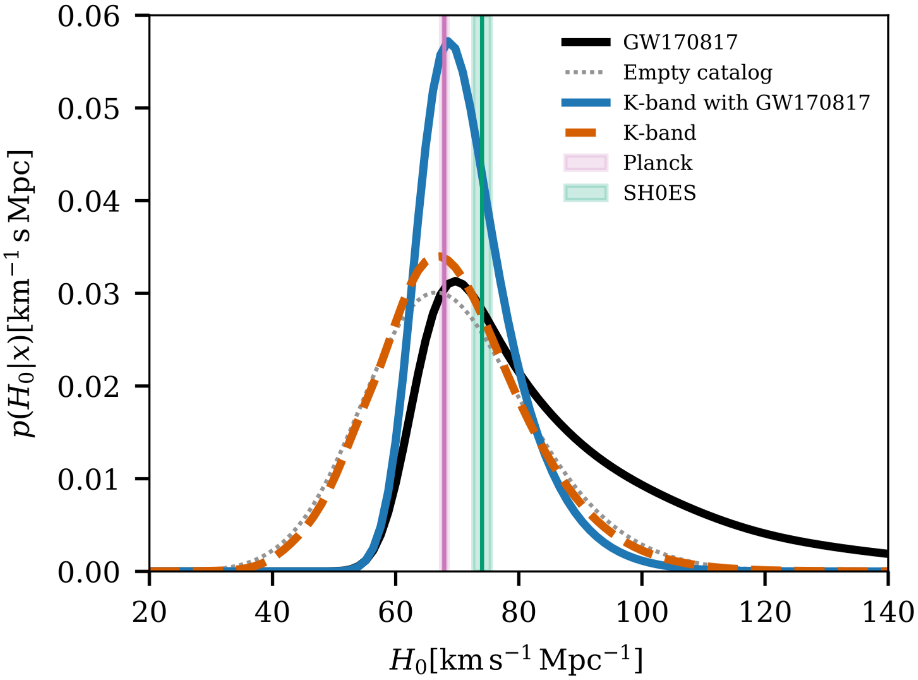

Figure 6.3: The latest posterior on H_0 from standard sirens, using 42 compact binary coalescences from GWTC-3 and GW170817. These results are obtained using the galaxy catalogue method with the K-band of the GLADE+ catalogue. Figure from [156].

6.1.3 Current measurements of H_0 with `gwcosmo`.

The latest measurements of H_0 come from the GWTC-3 analysis. [2,156] GWTC-3 encompasses all above-threshold events to date, from O1 to the end of O3b. The results for the catalogue method are presented in Figure 6.3.

Previous results were obtained from GWTC-1, the first Gravitational Wave Transient Catalogue. GWTC-1 contains eleven events, of which ten are binary black hole coalescences, and one is the binary neutron star merger GW170817. [37] Of these eleven events, only seven are used for H_0 studies. The final result from this analysis was $H_0 = 69^{+16}_{-8}$ km s^{-1} Mpc^{-1}, a 4% improvement over the GW170817-only result. [225]

The latest results come from the analysis of the transient catalogue GWTC-3. Of the 90 events that make up the catalogue, 47 were used for this analysis. The final result using `gwcosmo` yielded $H_0 = 68^{+8}_{-6}$ km s^{-1} Mpc^{-1}. [156] This latest result represents an improvement of 42% with respect to the GWTC-1 result and 20% with respect to the GWTC-2 result.

6.2 Galaxy Catalogues

Galaxy catalogues are the output of large surveys of either the full sky or an area of the sky. They can also vary in their depth and observing band. Choosing the appropriate galaxy catalogue is important for the inference of H_0 from dark sirens. The catalogue needs to cover the full sky, or, for individual events, it needs to cover the full GW skymap. The observed band is also important, as some bands have a better-understood luminosity function. Some bands adhere better to the assumption of a universal luminosity function; for example, in redder bands, the galaxy brightness may be less affected by e.g. recent bursts of star formation that might depend on the position and redshift of the galaxy.

6.2.1 Galaxy catalogues and completeness

Galaxy catalogues are essentially an inventory of galaxies. Due to limitations on measured flux, no galaxy catalogue is complete.

Understanding the intrinsic properties of galaxy populations is one of the major challenges of observational cosmology. The extraction of these properties is affected by selection effects due to the limiting flux on observations of galaxies. [226]

Definition

Completeness: The completeness of a galaxy catalogue is a measure of the number of galaxies in a survey compared to the expected number of galaxies. This is dependent on colour, direction and luminosity distance. For a sample of galaxies with a given absolute magnitude M, the apparent magnitude completeness of the sample will be primarily dependent on luminosity distance, and indirectly on the redshift via the Hubble constant.

Section 6.3 goes into more detail about ways to determine the completeness of a galaxy catalogue, focusing on a robust statistical test described by Rauzy. [226] This is a test of completeness in terms of the limiting apparent magnitude of a survey.

6.2.2 GLADE and GLADE+

The Galaxy List for the Advanced Detector Era (GLADE) and GLADE+ catalogues are near-full-sky galaxy catalogues compiled especially for multi-messenger astronomy with advanced gravitational wave detectors. [227, 228] They are constructed from several surveys chosen for depth and sky coverage.

Figure 6.5 shows the B-band completeness of the GLADE+ and GLADE 2.4 catalogues. In this figure, the completeness is calculated based on the expected galaxy density. The expected galaxy density is calculated under the assumption that galaxies are uniformly distributed in comoving volume. This method means that completeness can go above 100%, if the total luminosity at a certain d_L is higher than the expected one. In the case of the GLADE and GLADE+ catalogues, this is caused by local overdensities of galaxies around the Milky Way. [228]

The GLADE+ catalogue contains 22.5 million galaxies. It is made up of the GWGC, 2MPZ, 2MASS XSC, HyperLEDA and WISExSCOSPZ galaxy catalogues. Also included is the SDSS-

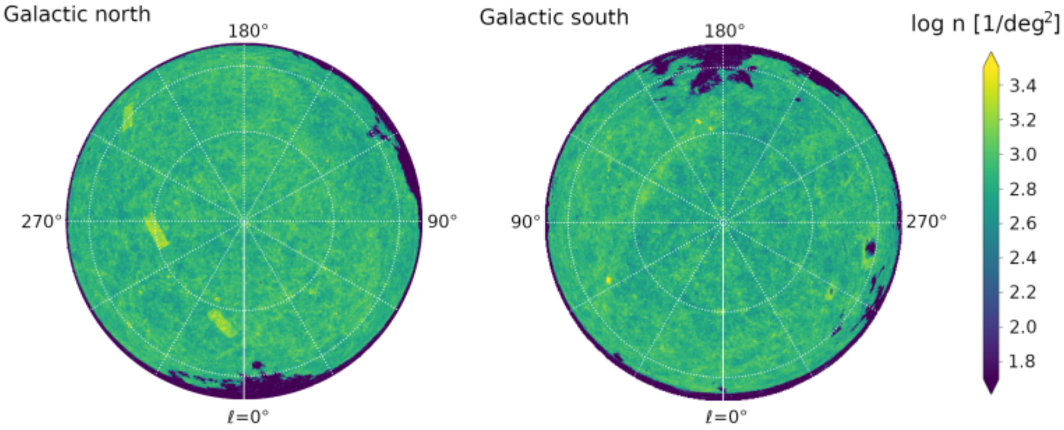

Figure 6.4: From [228], galaxy number density of GLADE+.

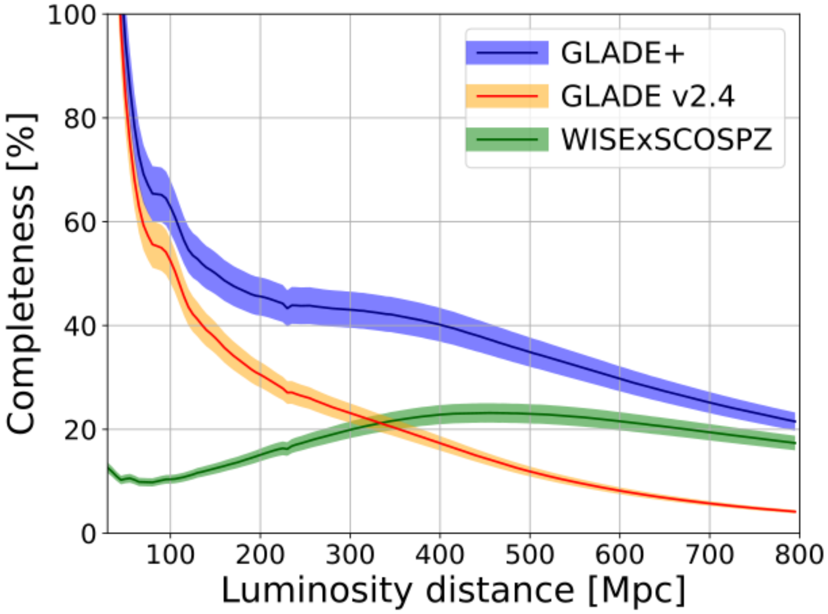

Figure 6.5: The normalised integrated B-luminosity completeness of the GLADE+ catalogue and its constituents as a function of luminosity distance d_L. The y-axis shows the completeness as a percentage. The completeness is determined as a function of number of observed galaxies compared to number of expected galaxies, under the assumptions that galaxies are uniformly distributed in comoving volume. Where there are overdensities due to clustering/structure in a catalogue, the completeness of a catalogue can therefore go over 100%. Figure from [228].

DR16Q quasar catalogue. It's complete up to a luminosity distance of $d_L = 47^{+4}_{-2}$Mpc and contains bright galaxies up to 90% of the total expected B-band and K-band luminosities up to ∼130Mpc. [228]

6.2.3 DES-Y1

The DES-Y1 catalogue is a deeper catalogue by the Dark Energy Survey. Unlike GLADE and GLADE+, this is not a survey with full-sky coverage. This means it is not appropriate as a general purpose galaxy catalogue for use with gravitational wave events; it can however be used for events for which the localisation is encompassed within the area mapped by the survey.

The Dark Energy Survey is a five-year survey mapping galaxies across an area 5000 deg^2. It comprises of around 300 million galaxies in five different filter bands $grizY$. For this analysis, the publicly available year 1 survey is used (DES-Y1 or Y1A1 GOLD). [229, 230]

The DES-Y1 catalogue consists of ∼137 million objects over ∼1800 deg^2 in the DES $grizY$ filters. The 10σ limiting magnitudes for galaxies are $g = 23.4$, $r = 23.2$, $i = 22.5$, $z = 21.8$ and $Y = 20.1$. [229] The catalogue includes photometric redshift estimates. The gravitational wave event GW170814 originated from within the area mapped by the DES-Y1 survey. It is a much deeper catalogue than GLADE with its deepest overall limiting magnitude being in the g-band, with $m_{thr} = 23.4$.

GW170814 was the first gravitational wave event to be detected by a network of three detectors, having been detected by both LIGO detectors at Hanford and Livingston and by Virgo. This triple-coincident detection means the BBH was very well-localised, with a 90% credible region of 60 deg^2. [231]

The initial skymap of 87 deg^2 was searched using the Dark Energy Camera and compared to pre-existing fields to look for potential optical counterparts to the event. The sky localisation was completely contained within the DES footprint. [232] However, no counterpart was found.

In the analysis of GW170814 with **`gwcosmo`**, we use the g-band data from DES, as it is the band in which the survey is most complete, with the 95% completeness magnitude limit in the g- band quoted at 23.72 mag in a sample of high quality objects. [230]

The DES-Y1 catalogue is only used in the GWTC-1 analysis and only for the gravitational wave event GW170814. It is not used in the subsequent GWTC-3 analysis, which exclusively uses the K-band of the GLADE+ catalogue. DES-Y1 does not contain K-band luminosities and therefore cannot be used in that final analysis, which covers all events above $SNR = 12$ detected to date. However, it is a useful test of the difference in posterior when using the robust method of estimating the completeness. As surveys become deeper, more gravitational wave events could lie in host galaxies that would be discarded if our estimate of the completeness of the catalogue were too conservative.

6.3 A Robust Test of Completeness for GLADE and GLADE+

In this section, we present a robust statistical test of galaxy catalogue completeness developed by Rauzy. [226] This test of completeness is adapted to and applied to the `gwcosmo` pipeline.

6.3.1 Testing the completeness of a galaxy catalogue

Galaxy catalogues are typically limited by a threshold on detectable apparent fluxes. [226] This means any galaxy catalogue will contain more objects that are closer and/or brighter. The completeness of a catalogue in magnitude and redshift is not only affected by the detection threshold, but also by other complex observational selection effects such as galaxy colour and size. This makes determining the completeness of a galaxy catalogue a complex issue. One way of dealing with the incompleteness of a galaxy catalogue is by obtaining an estimate of its apparent magnitude threshold. There are other methods such as by comparing the observed galaxy number density to the expected value. [233]

In the latest instance of `gwcosmo`, the completeness of the GLADE and GLADE+ galaxy catalogues is determined on a grid of HEALpix-defined "pixels", as the threshold apparent magnitude m_{thr} is strongly affected by direction. [220, 234] This is true of any galaxy catalogue that covers the whole sky. The issue is more pronounced for catalogues like GLADE and GLADE+, which are composites of different surveys with different depths and sky coverage. The catalogue pixels are determined using HEALpix, a framework for discretising large galaxy surveys into spherical maps. [234]

The current `gwcosmo` analysis uses the **median** apparent magnitude as a threshold for estimating the completeness of the catalogue. While this method avoids biases that would be introduced by taking the faintest galaxy as a completeness threshold, it is a very conservative estimate. This method effectively discards half of the galaxies in the GLADE and GLADE+ catalogues, some of which could potentially be host galaxies of GW events. To maximise scientific returns from the use of galaxy catalogues for cosmology with gravitational waves, it is necessary to introduce an unbiased but not overly conservative estimate of its magnitude threshold.

6.3.2 A robust test of galaxy catalogue completeness

As described in the previous subsection, determining the completeness of a galaxy catalogue is a non-trivial issue, and the apparent magnitude threshold is an important parameter in the methodology behind the `gwcosmo` pipeline.

We outline a robust method for testing the completeness of a galaxy catalogue in apparent magnitude. The method outlined below is fully described in [226]. Here we present an overview of this statistical test and its application.

Essentially, this method defines a statistical test that can determine at which test magnitude threshold a galaxy catalogue is emptier than expected, by comparing the number of galaxies in two samples from the galaxy catalogue rather than comparing it to the expected number of galaxies, which would need to be obtained from a luminosity function. The test relies on the evaluation of a statistic which tests for completeness, T_C, for different test apparent magnitude thresholds m_{test}.

This method builds upon a statistical test first proposed by Efron and Petrosian in 1992. [235] This statistical test was originally intended to test for independence in truncated data, and applied to redshift-magnitude surveys to test for statistical independence between redshift and absolute magnitude. In [226], the test is applied to galaxy catalogues for obtaining a robust estimate of the apparent magnitude threshold m_{thr} of a redshift-magnitude survey. One advantage of this method is that, unlike some of the methods for assessing completeness described previously, it does not assume any underlying luminosity function; rather, it assumes that there is a universal luminosity function that describes the entirety of the catalogue. The exact form of this universal luminosity function does not matter with this approach; this makes it an appropriate method for estimating galaxy catalogue completeness with minimal information about the LF.

Since no a-priori assumptions are made about the redshift-space distribution of the tested sample, this method is not affected by clustering or the evolution of the mean number density of galaxies. [226]

This method requires both apparent magnitude and redshift samples for each galaxy in the catalogue. From the (m_i, z_i) samples for each galaxy, one can define a luminosity distance $d_{L,i}$, an absolute magnitude M_i and a distance modulus μ_i:

$$d_{L,i} = \frac{cz_i}{H_0}, \tag{6.4}$$

$$M_i = m_i + 5 - 25\log_{10}(d_{L,i}), \tag{6.5}$$

and

$$\mu_i = 5\log_{10}(d_{L,i}) + 25, \tag{6.6}$$

with c in km s^{-1} and $d_{L,i}$ in Mpc. Equations 6.4,6.5 and 6.6 assume a Hubble constant H_0; however, this choice does not affect the resulting calculated magnitude threshold m_{thr}. The assumed Hubble constant is only used in intermediate steps, with no change to the final result on the statistic T_C and the inferred m_{thr}. We assume a Hubble constant $H_0 = 70.0$ km s^{-1} Mpc^{-1} for these steps, once again emphasising that this has no bearing on the final result. Changing the value of H_0 changes the values of both the calculated M and d_L used in the intermediate steps of the calculation. Since the final inferred magnitude threshold m_{thr} then depends only on the apparent magnitude-redshift samples, choosing any value for H_0 will result in the same m_{thr}.

The robust test of completeness requires testing several test magnitude limits m_{test} to find the true threshold m_{thr}.

For each galaxy in the sample with an absolute magnitude M and an apparent magnitude m:

$$\mu = m - M. \tag{6.7}$$

We can define $M_{lim}(\mu)$ such that:

$$M_{lim}(\mu) = m_{lim} - \mu. \tag{6.8}$$

This defines the maximum absolute magnitude, $M_{lim}(\mu)$, for which a galaxy with a given distance modulus μ would be visible in the sample.

For each galaxy with (M_i, μ_i), and assuming a test magnitude limit m_{test}, we can define a random variable ζ_i, defined as:

$$\zeta = \frac{F(M)}{(F(M_{lim}(\mu))} \tag{6.9}$$

where F is the cumulative luminosity function. The variable ζ is distributed within the interval $[0,1]$ and independent of the sample.

This is equivalent to

$$\zeta_i = \frac{r_i}{n_i + 1}, \tag{6.10}$$

where for each galaxy i we have

$$r_i = S1 \qquad\qquad n_i = S1 \cup S2, \tag{6.11}$$

where $S1$ is the area drawn out by $\mu < \mu_i$ and $M < M_i$, while $S2$ is defined by $\mu > \mu_i$ and $M^i_{lim} > M > M_i$. r and n are integrals corresponding to the number of galaxies in those areas. Figure 6.6 illustrates the areas $S1$ and $S2$ along with the (M, μ) samples in one pixel of the B-band of GLADE+. In each subsample $S1$ and $S2$, M and μ are independent (by construction).

It is proven in [235] that the variables ζ_i are independent under the null hypothesis. The expectation E_i and variance V_i of each random statistic ζ_i are:

$$E_i = \frac{1}{2} \text{ and } V_i = \frac{n_i - 1}{12(n_i + 1)}. \tag{6.12}$$

We define the quantity T_C

$$T_C = \frac{\sum_{i=1}^{N} (\zeta_i - \frac{1}{2})}{\sum_{i=1}^{N} V_i}. \tag{6.13}$$

The expectation of T_C is 0 and its variance is unity. It can be estimated without any a-priori assumptions about the form of the luminosity function. If the statistic is complete, then it follows a Gaussian distribution around zero; T_C starts going systematically negative when there is a deficit of galaxies fainter than $M_{lim}(\mu)$. This deficit is caused by the test magnitude m_{test} being larger than the true magnitude threshold m_{thr}.

The statistic T_C becoming very negative is therefore indicative of catalogue incompleteness. This is a result of the region $S2$ being emptier than the region $S1$. Following Rauzy, we take $T_C = -3$ as a threshold for determining the magnitude threshold for catalogue completeness.

Figure 6.8 shows samples of distance modulus μ and absolute magnitude M for a single pixel in the B-band of the GLADE galaxy catalogue. Each dot represents a galaxy. The orange line represents a completeness cut-off based on the median apparent magnitude, while the red line shows the robust apparent magnitude threshold. Figure 6.7 shows the T_C statistic over a range of test limiting apparent magnitudes for the same pixel.

Since the properties of the T_C statistic hold for any 3-dimensional redshift-space distribution and is therefore not affected by clustering and galaxy density evolution, it is well adapted to sub-samples of galaxies from the composite catalogues GLADE and GLADE+. [226]

6.4 Applying the Robust Test of Completeness to Galaxy Catalogues for `gwcosmo`

In this section, we present an application of the previously outlined method to galaxy catalogues used for cosmology with gravitational waves, along with its implementation into the **`gwcosmo`** pipeline.

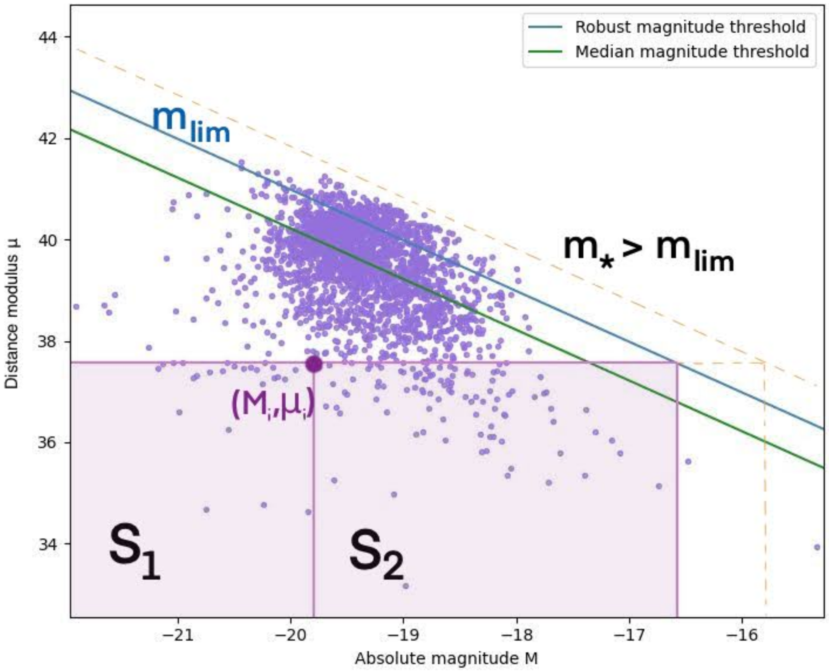

Figure 6.6: Illustrating the S1 and S2 areas for a single pixel in the GLADE+ B-band. M vs μ with S1 and S2 for a galaxy (M_i,μ_i). The solid blue and green lines show, respectively, the robust and median apparent magnitude thresholds for this sample of galaxies. The orange line shows a test limit magnitude m_*.

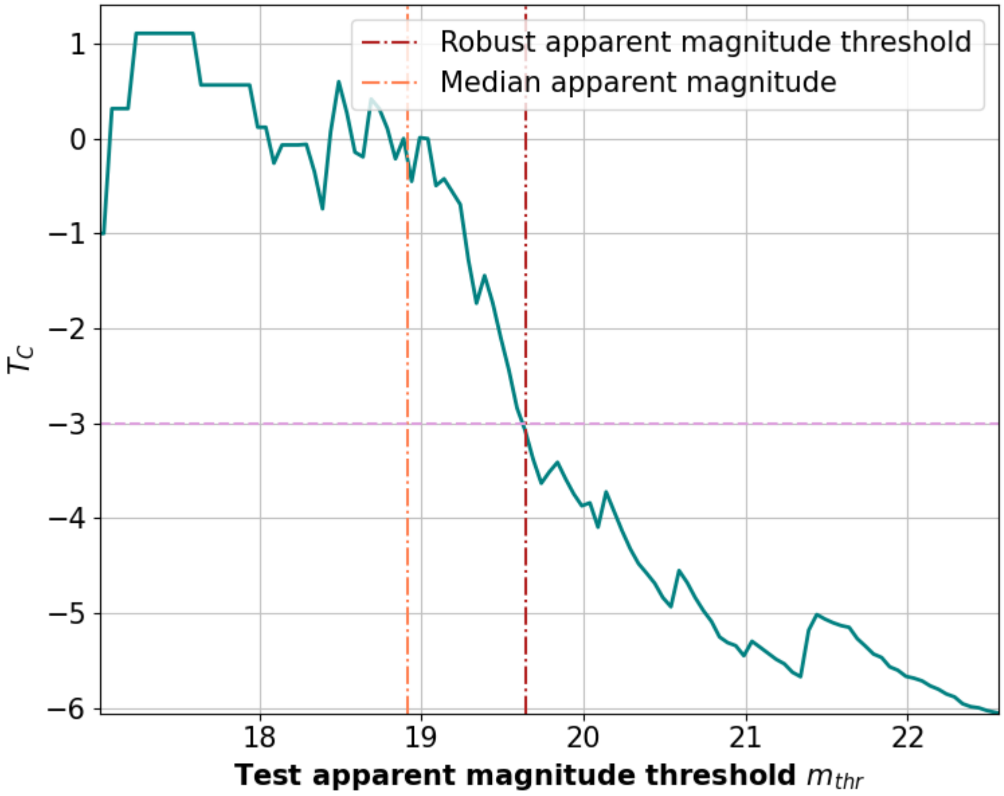

Figure 6.7: T_C statistic over a range of test limiting apparent magnitude m_{test} for a single "pixel" of the GLADE catalogue with $N_{side} = 32$. This shows the characteristic drop-off of the T_C statistic when reaching the true m_{thr}. The threshold on T_C is taken to be -3. This shows the resulting estimated apparent magnitude threshold m_{thr} against the median apparent magnitude.

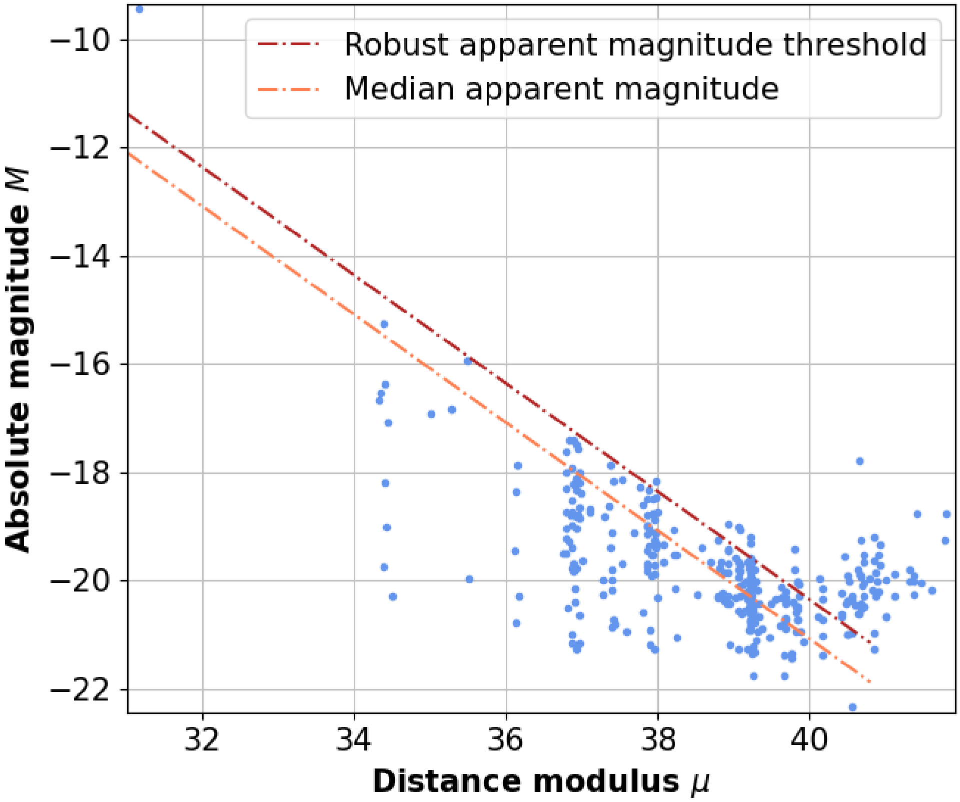

Figure 6.8: (M, μ) samples for the same single pixel in the GLADE B-band as shown in Figure 6.7. The dash-dotted lines show the median and robust apparent magnitude thresholds for this pixel. The apparent structure in the distribution of μ comes from limits on the precision for μ (truncation errors).

6.4.1 Implementing the robust test into `gwcosmo`

The method described in section 6.3 is implemented into the **`gwcosmo`** package for use with the GLADE, GLADE+ and DES galaxy catalogues. While the statistical test itself is straightforward, some finer points of its application must be considered in the implementation.

Sub-sampling for large numbers of galaxies

In the B-band, the GLADE and GLADE+ catalogues contain millions of galaxies. The complexity of the robust test described previously goes up with $\mathcal{N}^2$, making it computationally expensive and slow to determine the completeness of each individual pixel containing thousands of galaxies.

To get around this, we sample a subset of 400 galaxies with (m_i, z_i) multiple times and evaluate m_{thr} for each subset of galaxies. The final m_{thr} is taken to be the mean of the evaluated m_{thr} for the different random subsamples.

This method needs only be used with the B-band, as both GLADE and GLADE+ do not contain many galaxies per pixel in the K-band. The sparseness of GLADE+ in the K-band can be seen in the histogram in figure 6.20.

Selecting test apparent magnitude thresholds

In order to apply the robust test, we must choose some test magnitude thresholds. We choose to calculate T_C for apparent magnitudes from $m_{median} - 0.5$ to $m_{median} + 4$ with a 0.05 mag step. After testing, this was found to be the best range to determine m_{thr} without sacrificing too much efficiency during the runs.

Redshift uncertainties

The GLADE and GLADE+ catalogues have corresponding photometric redshifts and redshift uncertainties for each galaxy surveyed. A subset of galaxies in the survey have spectroscopically determined redshifts, resulting in a much smaller redshift uncertainty.

To propagate redshift uncertainties to the magnitude threshold estimate, we make the following two assumptions:

- The galaxies have a redshift
- The redshift uncertainties are Gaussian

We therefore assume the uncertainties on the galaxy redshifts are described by a truncated Gaussian. The distribution is truncated to only allow positive redshift values (we assume every galaxy has a redshift).

In order to sample over the redshift distributions, the magnitude threshold m_{thr} is estimated for several samples of (m_i, z_i) for each pixel. This in turn returns a range of m_{thr} values.

Magnitude uncertainties

Just as with redshifts, the magnitudes m_i associated with each galaxy also carry an uncertainty. None of the current methods for estimating the magnitude threshold of GLADE and GLADE+ currently implement apparent magnitude uncertainties on individual galaxies. Future work should focus on implementing these, alongside obtaining uncertainties on m_{thr}. Ignoring apparent magnitude uncertainties on individual galaxies in this work allows for a more direct comparison to the median method of estimating galaxy catalogue completeness.

Uncertainties on the magnitude threshold

Unlike the median method for catalogue completeness, the robust method relies on both the apparent magnitude and redshift of each galaxy. This means having to deal with photometric redshift uncertainties early on in the analysis.

For large numbers of galaxies, the effect of uncertainties is small as the uncertainties on z tend to average out. However, the GLADE+ catalogue is complete to a much brighter apparent magnitude in the K-band than in the B-band, meaning there is a lower number of galaxies in each pixel, increasing the impact of photometric redshift uncertainties on the inference of m_{thr}.

The comparative sparseness of GLADE+ in the K-band will become apparent in later sections when we apply the robust method. The increased impact of the photometric redshift uncertainties would result in a larger uncertainty on the inferred apparent magnitude threshold. In order to carry out a rigorous analysis, future instances of **`gwcosmo`** will therefore need to implement uncertainties on the magnitude threshold.

6.4.2 Magnitude threshold maps of GLADE and GLADE+

The method described above is applied to **`gwcosmo`**. The analysis will use the GLADE, GLADE+ and DES-Y1 catalogues. As the DES-Y1 catalogue is only used for one event and in the GWTC-1 analysis only, this subsection focuses on the application of the robust method to the GLADE and GLADE+ catalogues.

GLADE and GLADE+ are galaxy catalogues compiled from several surveys. Because of this, they do not have a straightforward distribution of galaxies and therefore have a non-uniform completeness throughout their sky coverage. [227, 228] This means that in order to obtain the most accurate result, we cannot assume a single magnitude threshold throughout the entire catalogue, or even throughout the patch of sky contained by each event's skymap. A full description of the pixelated method for **`gwcosmo`**, along with GWTC-1 results, can be found in [220].

The catalogues are divided into HEALpix pixels. HEALpix (Hierarchical Equal Area iso-Latitude Pixelization) is a data structure with an associated library of algorithms allowing for the discrete spherical mapping of galaxy catalogues and other large astronomical datasets. It effectively divides catalogues into a grid of "pixels". The grid resolution is determined by the parameter N_{side}. For a given N_{side}, a HEALpix map will contain a number of pixels N_{pix}. [234]

$$N_{pix} = 12N_{side}^2 \,, \tag{6.14}$$

with the same area Ω_{pix}:

$$\Omega_{pix} = \frac{\pi}{3N_{side}^2} \,. \tag{6.15}$$

At an N_{side} of 32, each pixel for GLADE and GLADE+ covers a region spanning approximately 3.36 deg^2, with a total number of pixels of 12,288. [220, 236] The HEALpix maps in `gwcosmo` are implemented using the healpy package, a python wrapper for the HEALpix library. [234, 237]

Figure 6.9 shows m_{thr} maps of the GLADE+ catalogue in the B-band for a HEALpix N_{side} of 32.

Figures 6.10 and 6.11 show maps of apparent magnitude threshold for the K-band of the GLADE catalogue for different grid resolutions. Figure 6.12 shows $m_{thr}^{robust} - m_{thr}^{median}$ for the K-band in two different resolutions, illustrating that the catalogue has a deeper limit when applying the robust method of estimating galaxy catalogue completeness.

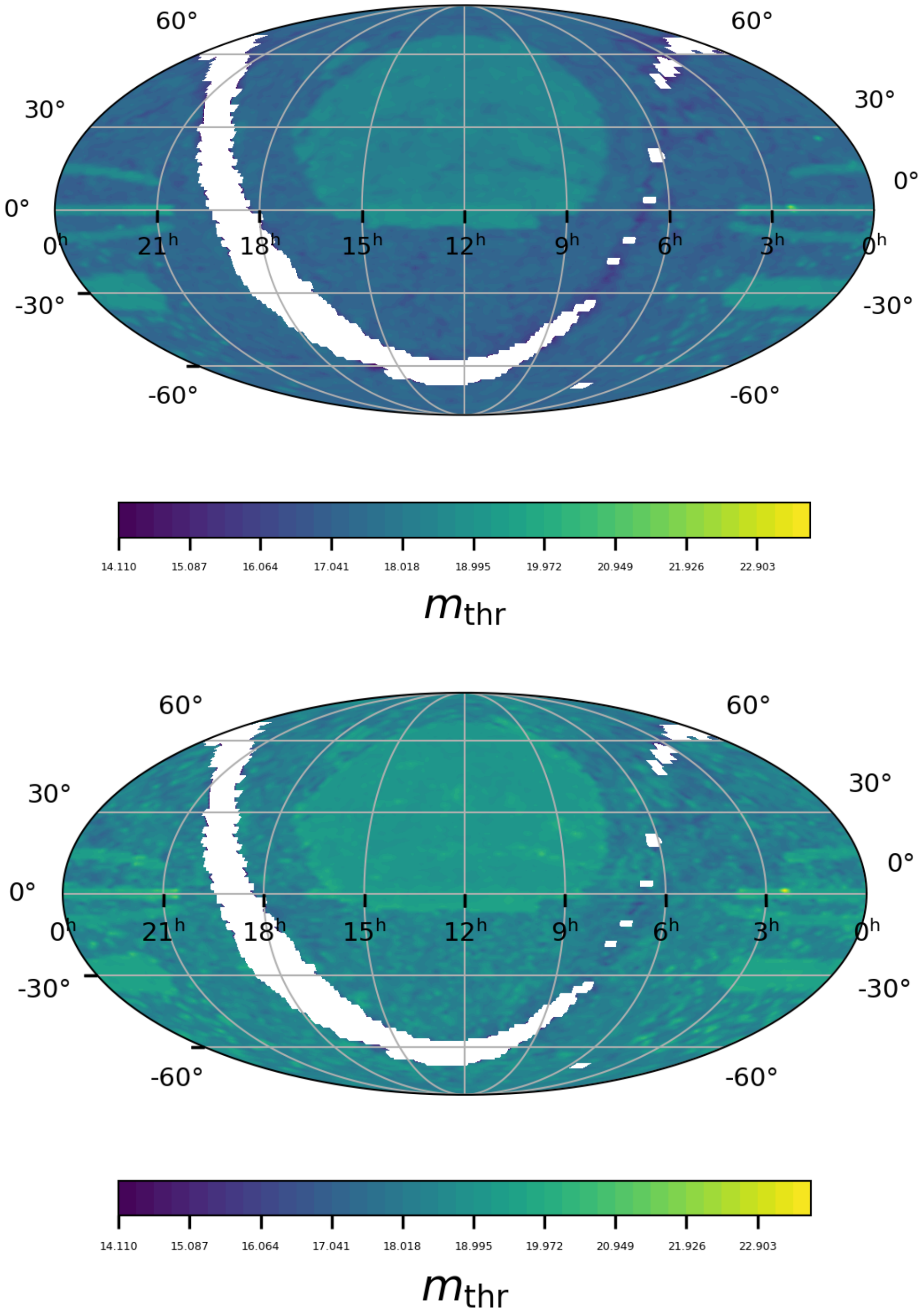

Figure 6.9: A map of magnitude thresholds m_{thr} for the GLADE+ B-band data, comparing the median and robust methods. The size of the pixels corresponds to a HEALpix pixel size of $N_{side} = 32$. Both scales are the same to illustrate the difference in m_{thr}. Blank pixels are "empty" pixels, containing fewer than 10 galaxies. These are not considered for analysis.

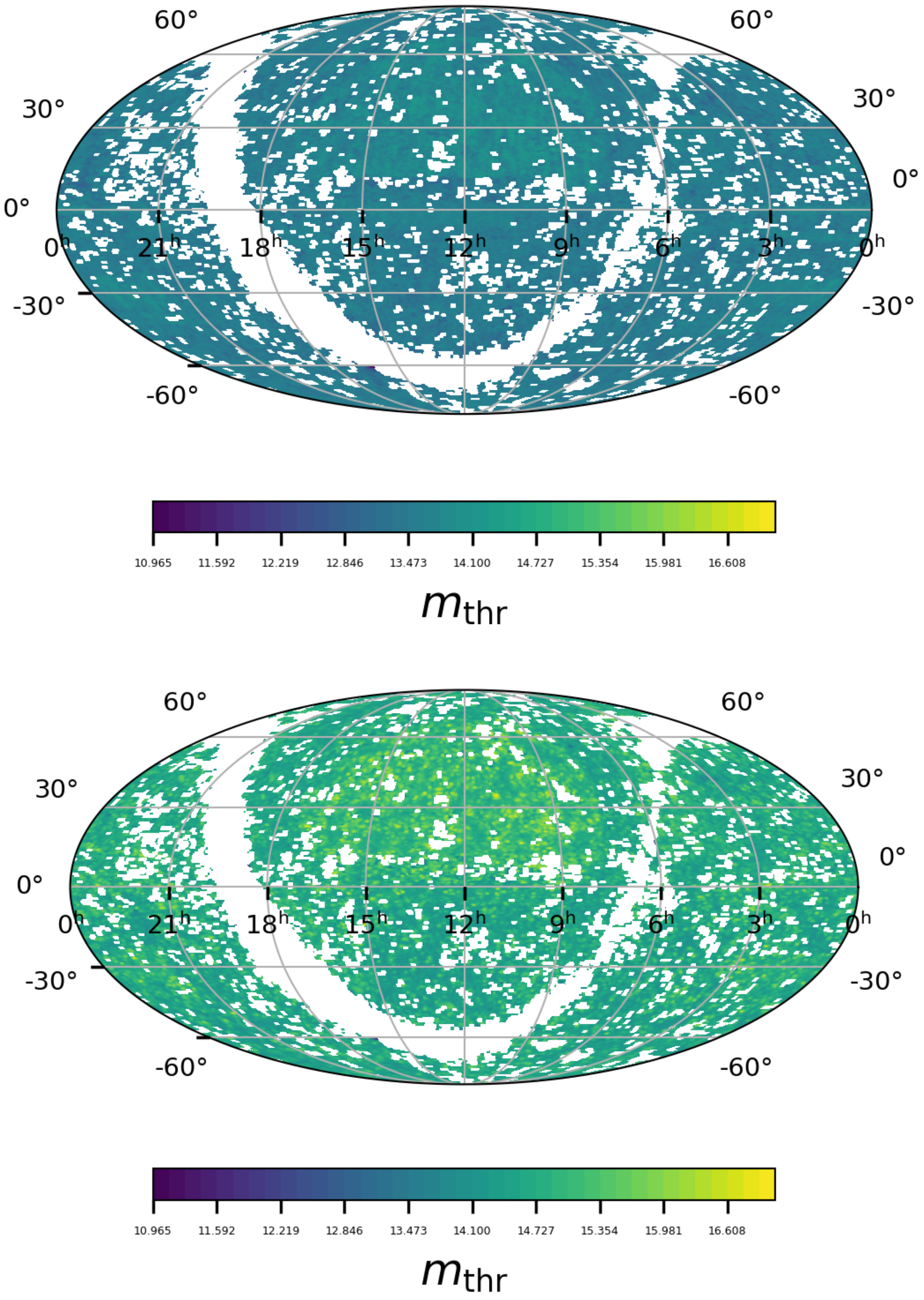

Figure 6.10: A map of magnitude thresholds m_{thr} for the GLADE+ K-band data, comparing the median and robust methods. The size of the pixels corresponds to a HEALpix pixel size of $N_{side} = 64$. Both scales are the same to illustrate the difference in m_{thr}. Blank pixels are "empty" pixels, containing fewer than 10 galaxies. These are not considered for analysis. This map represents the smallest pixel size used in the analysis.

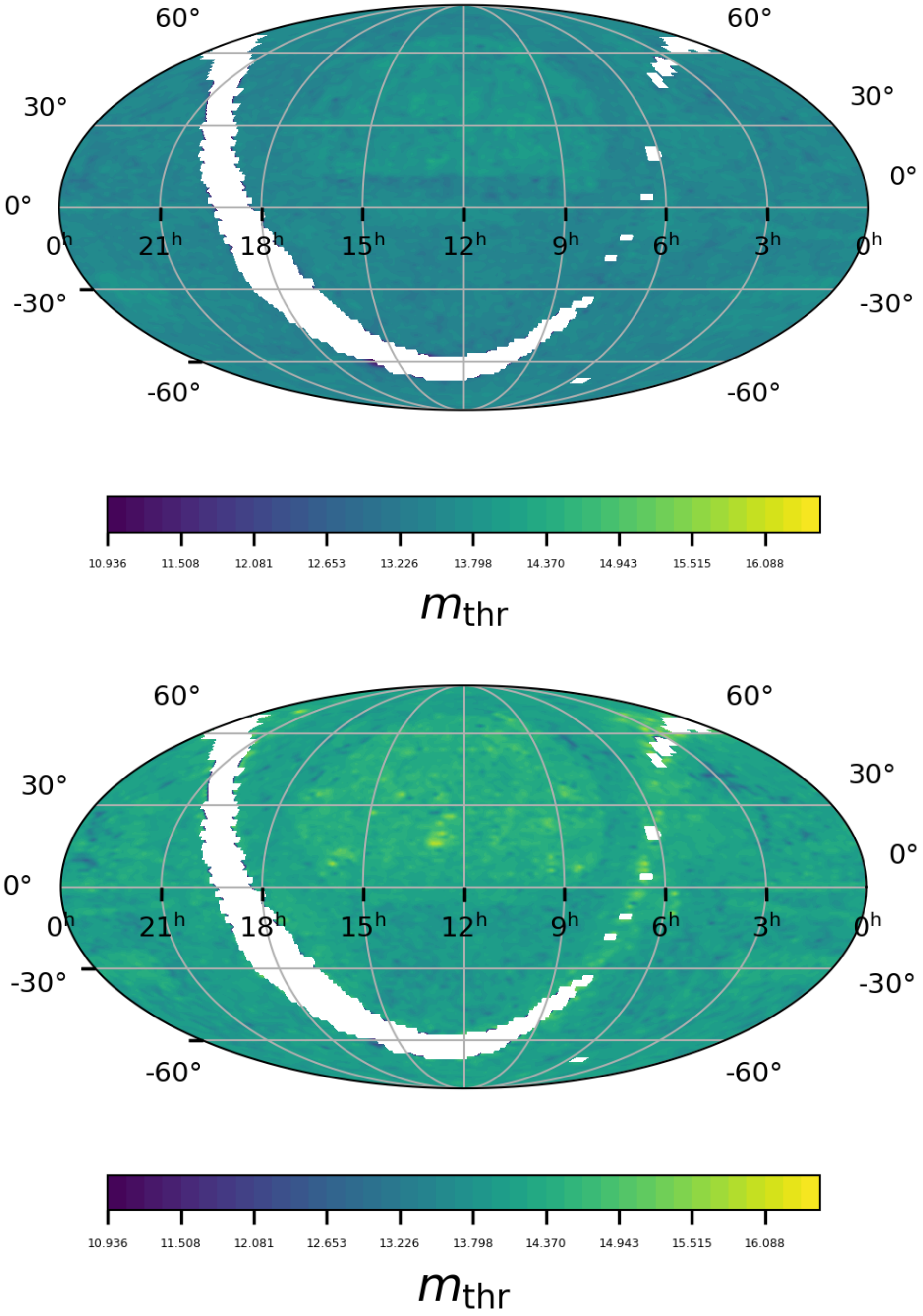

Figure 6.11: A map of magnitude thresholds m_{thr} for the GLADE+ K-band data, comparing the median and robust methods. The size of the pixels corresponds to a HEALpix pixel size of $N_{side} = 32$. Both scales are the same to illustrate the difference in m_{thr}. Blank pixels are "empty" pixels, containing fewer than 10 galaxies. These are not considered for analysis.

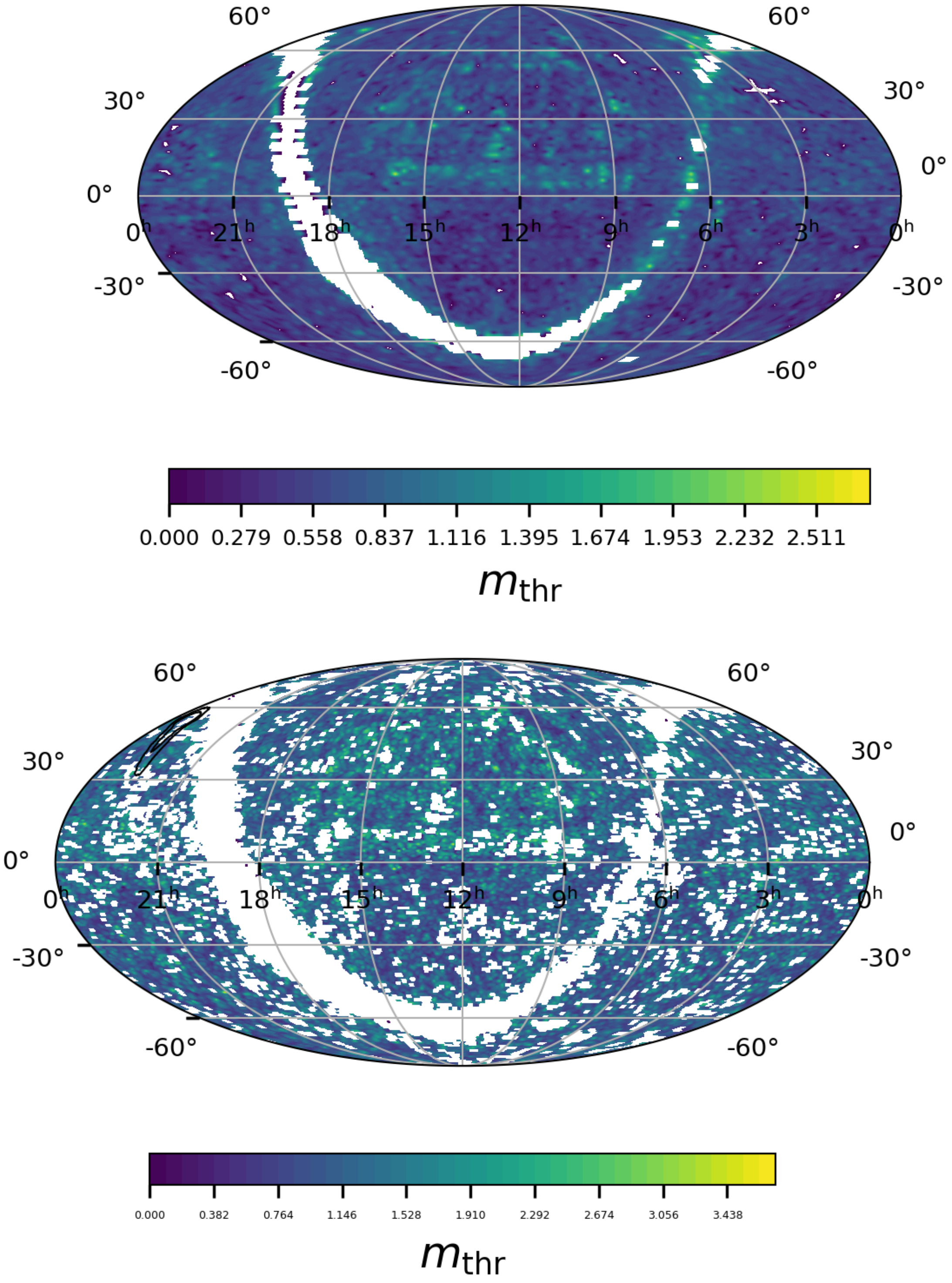

Figure 6.12: Map illustrating the difference in m_{thr} between the median and robust methods. This is a map for the GLADE+ K-band with HEALpix $N_{side} = 32$ (top) and $N_{side} = 64$ (bottom)

6.5 Results of a Robust Analysis of GWTC-1 with the GLADE and GLADE+ B-bands

The current **`gwcosmo`** analysis uses the median apparent magnitude from galaxies in the sample as the apparent magnitude cut-off for catalogue completeness. This method is overly conservative and throws out many potential host galaxies. To maximise results from the galaxy catalogue method, we need to apply a non-biased but accurate estimate of the apparent magnitude threshold m_{thr}

The previous sections introduced the **`gwcosmo`** pipeline, the role of galaxy catalogue incompleteness and a robust statistical test for estimating m_{thr}, along with its application to the GLADE and GLADE+ catalogues.

These tools allow us to re-run the cosmological inference analysis with the galaxy catalogue method using a more robust estimate of incompleteness. We first run the analysis on the GWTC-1 data, which is made up of the brightest events from the O1 and O2 runs. This represents seven events, out of the eleven detected, in total: six BBHs and the BNS event GW170817. Since GW170817 is a bright siren, having an associated EM counterpart and a clearly identified host galaxy, the resulting posterior for this event is unaffected by the change in magnitude threshold incurred by the robust analysis.

This analysis was firstly done using the B-band luminosities of galaxies in the GLADE catalogue. We can compare the analysis results for two separate scenarios: one with a pixelated galaxy catalogue, and one with an unpixelated galaxy catalogue.

The cosmology analysis for the detected gravitational wave events up to the end of the second observing run (O2) is re-run on the O1 and O2 events above a certain SNR threshold. Table 6.2 shows a list of events used in this analysis. The data for this analysis comes from the GWTC-1 catalogue of gravitational wave events. [37] Only the brightest events from the GWTC-1 catalogue are used for this analysis, with the threshold signal-to-noise ratio so that $SNR > 12$ [225]

The events in the analysis have corresponding skymaps which show the localisation of the event. In the case of GW170814, the skymap overlaps with the DES-Y1 catalogue, a deeper galaxy survey. The g-band of DES-Y1 is used for this event.

The analysis is done using the statistical method of inferring H_0 for all events but GW170817, which had an optical counterpart that allowed us to get redshift information. The posterior for GW170817 is taken from the analyses in [156, 225].

6.5.1 An unpixelated skymap case study

The original GWTC-1 analysis was done using "unpixelated" galaxy catalogues. Rather than breaking down the galaxy catalogue into HEALpix pixels and treating each pixel within the

Event name	Type	d_L	SNR
GW150914	BBH	440^{+150}_{-170}	24.4
GW151012	BBH	1080^{+550}_{-490}	10.0
GW151226	BBH	450^{+180}_{-190}	13.1
GW170104	BBH	990^{+440}_{-430}	13.0
GW170608	BBH	320^{+120}_{-110}	15.4
GW170729	BBH	2840^{+1400}_{-1360}	10.8
GW170809	BBH	1030^{+320}_{-390}	12.4
GW170814	BBH	600^{+150}_{-220}	16.3
GW170817	**BNS**	40^{+7}_{-15}	**33.0**
GW170818	BBH	1060^{+420}_{-380}	11.3
GW170823	BBH	1940^{+970}_{-900}	11.5

Table 6.2: Table of GWTC-1 events, which includes the subset of seven events considered for this analysis. [37] Events in the grey rows are not considered. The resulting dataset consists of six binary black hole mergers and one binary neutron star merger. GW170817 is a bright siren and unaffected by the robust analysis as the redshift information is obtained from the electromagnetic counterpart.

skymap of the event, the subsample of galaxies contained within the event skymap was considered as a whole for determining m_{thr}. [225] We can test the robust method of completeness on an event using an unpixelated catalogue. This method is no longer used, with the pixelated method now favoured. Regardless, it serves as a good test of the impact of the robust method.

In the unpixelated **`gwcosmo`** pipeline, a single apparent magnitude threshold m_{thr} is calculated for the sample of all galaxies that are contained within the skymap of the event. We run the pipeline on GW150914 using both the median and robust methods of estimating m_{thr}, applied to the event's unpixelated GLADE map.

Figure 6.13 shows the H_0 posteriors for GW150914 when using an unpixelated GLADE catalogue. There is a clear difference in the final posterior, illustrating the effect of an increasing apparent magnitude threshold.

This method is much more subject to biases if m_{thr} is not treated carefully, therefore only serves as a proof of concept. Since GLADE and GLADE+ vary with directionality, the robust method is more adapted to the pixelated galaxy catalogues - it could overestimate the magnitude threshold for some parts of the skymap associated with the GW event.

6.5.2 GWTC-1 with pixelated galaxy catalogues

In this section we present the analysis of O1 and O2 events with a pixelated GLADE catalogue, using B-band luminosities. We also present results for the same analysis using the GLADE+ B-band luminosities.

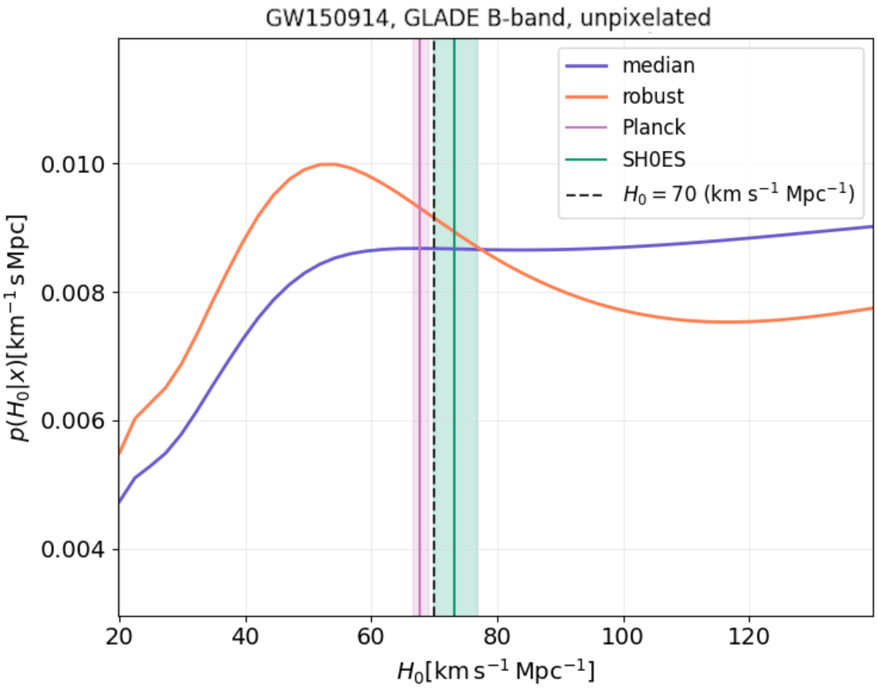

Figure 6.13: Posterior on H_0 for GW150914 using the unpixelated B-band of the GLADE catalogue.

In the pixelated case, the galaxy catalogue is divided into equal HEALpix pixels and a magnitude threshold is computed for each pixel. More detail on how the catalogues are divided into pixels can be found in section 6.4.2. The pipeline is then run on each pixel that overlaps with the event's skymap, and combined at the end. This allows for a more accurate assessment of the probability of the host galaxy being within the catalogue $p(G|D_{GW}, x_{GW})$, along with taking into account the directional variability in depth of composite catalogues like GLADE and GLADE+. A full overview of the pixelated pipeline, along with new results from the GWTC-1 analysis originally presented in [37], can be found in [220]. This method differs from previous methods of dealing with non-uniform galaxy catalogue completeness, such as the one presented in [233].

Figure 6.14 shows results for the GWTC-1 pixelated analysis using the robust method and the median magnitude method. There is a slight difference in the final posterior, with the width of the final posterior on H_0 being 1.3% narrower for the 68.3% percentile when considering only dark sirens. The final posterior with GW170817 is 3.4% narrower using the robust method.

Figure 6.17 shows the same analysis as previously using the GLADE+ B-band instead of the GLADE B-band. GW170814 remains unchanged, being analysed using the DES catalogue. For this analysis, the final posterior on H_0 is 5.1% narrower when considering only dark sirens, and 7.1% narrower when considering both dark and bright sirens. This is a clear improvement when using the robust method.

We see that in the pixelated case, the application of the robust method of galaxy catalogue

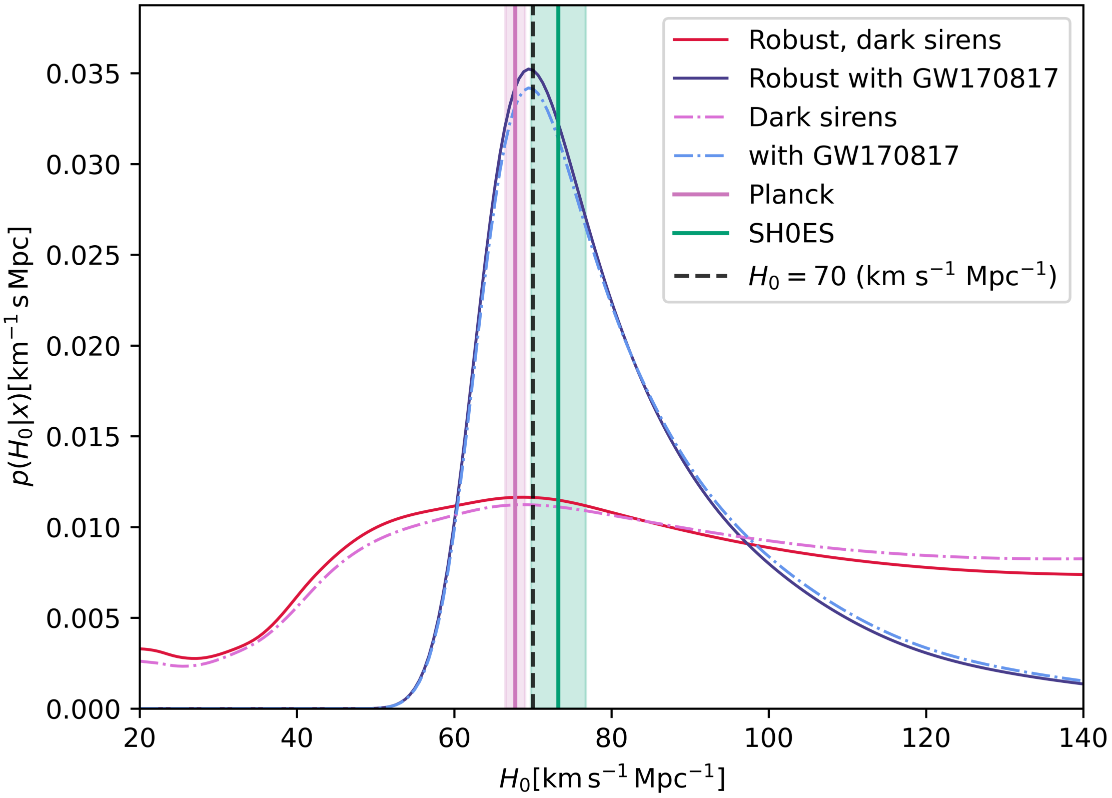

Figure 6.14: Final posteriors on H_0 for the GWTC-1 dataset using the B-band of the GLADE catalogue. Dashed lines show results for the median method, and solid lines show the robust method. The "Dark Sirens" dataset consists of the 6 BBHs above the SNR threshold from the O1 and O2 observing runs.

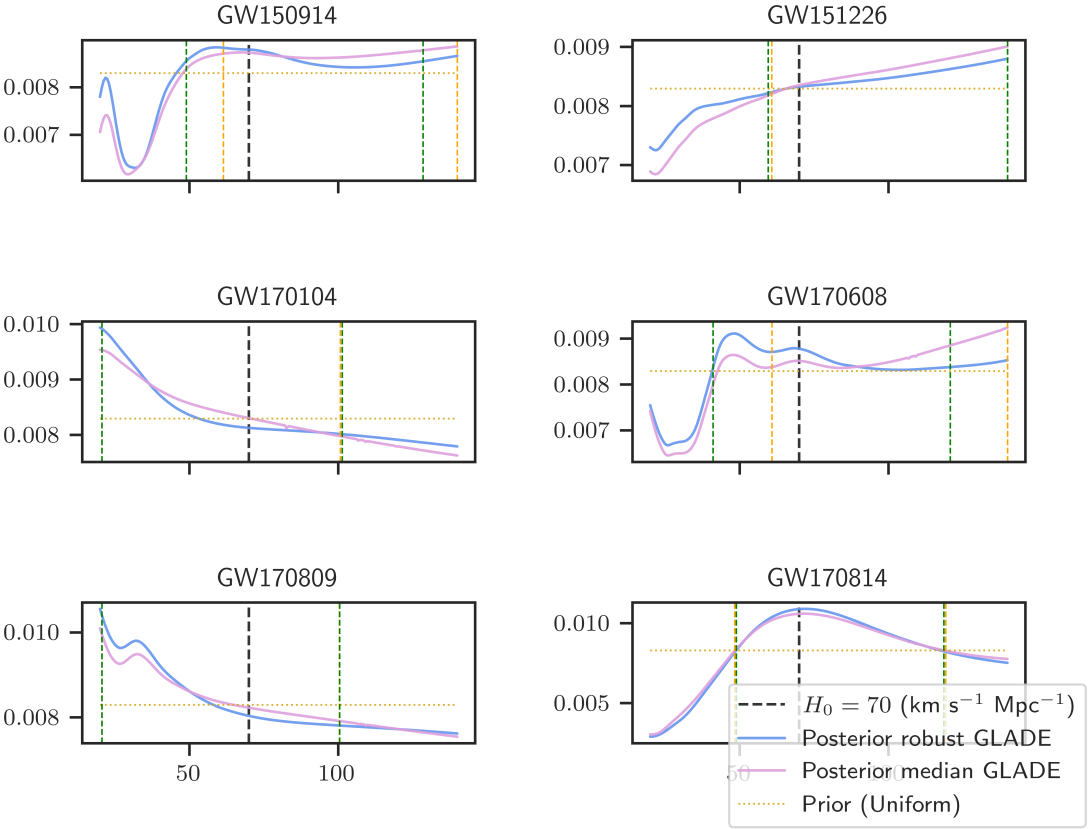

Figure 6.15: Final posteriors on H_0 for each event in the GWTC-1 dataset using the B-band of the GLADE catalogue. Dashed lines show results for the median method, and solid lines who the robust method. GW170814 is included in the plot but is analysed using the DES-Y1 catalogue.

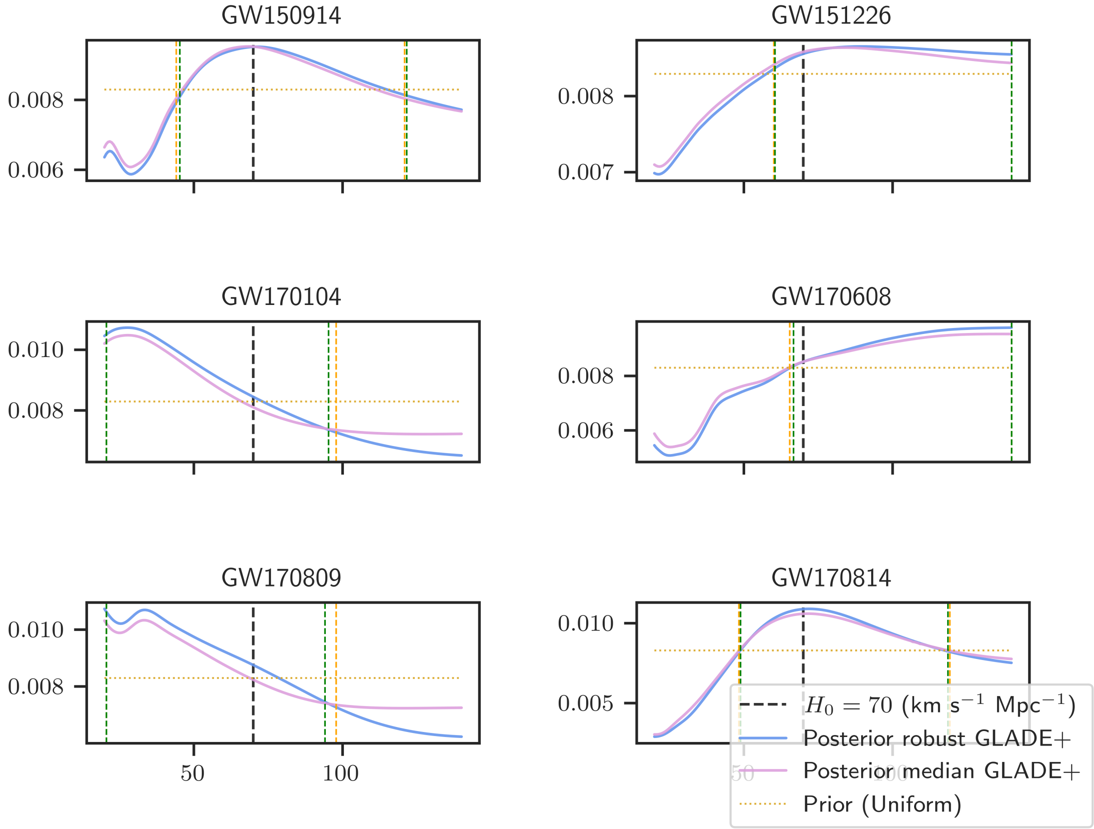

Figure 6.16: Final posteriors on H_0 for each event in the GWTC-1 dataset using the B-band of the GLADE+ catalogue. Dashed lines show results for the median method, and solid lines who the robust method. GW170814 is included in the plot but is analysed using the DES-Y1 catalogue.

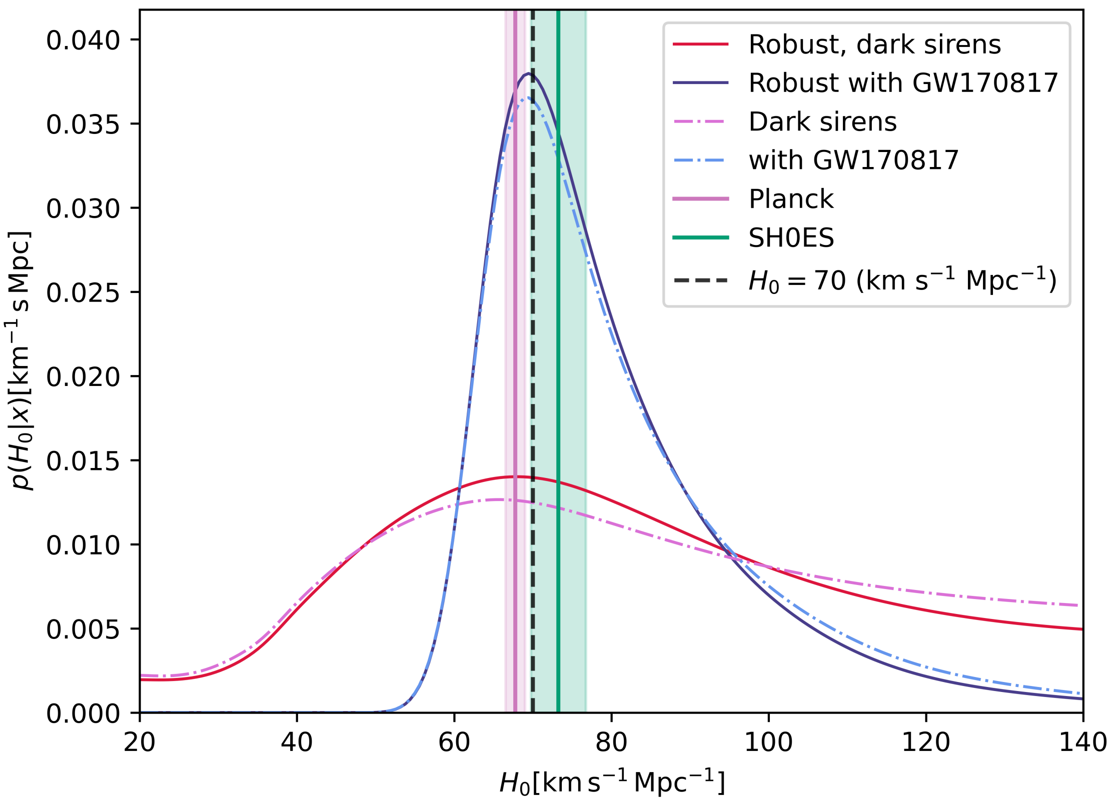

Figure 6.17: Final posteriors on H_0 for the GWTC-1 dataset using the B-band of the GLADE+ catalogue. Dashed lines show results for the median method, and solid lines who the robust method.

Catalogue	Method	Result (Dark sirens)	Result (all)
GLADE	median	68.8^{+47}_{-21}	69.6^{+19}_{-8}
GLADE	robust	68.7^{+43}_{-24}	69.5^{+18}_{-9}
GLADE+	median	64.4^{+43}_{-21}	69.4^{+16}_{-8}
GLADE+	robust	67.4^{+36}_{-24}	69.3^{+17}_{-8}

Table 6.3: Final results for H_0 values from the GWTC-1 data, using different methods and catalogues.

completeness results in an improved posterior on H_0.

Figure 6.18 shows the H_0 posterior for the GW170814 event only using the g-band of the DES-Y1 catalogue. As previously discussed, the DES-Y1 catalogue is much deeper than GLADE and GLADE+, with the pixels that make up the GW170814 sky localisation area having an apparent magnitude threshold ~ 25 when evaluated with the robust method. By comparison the most complete pixels for GLADE go down to an apparent magnitude of ~ 21 in the B-band. This makes GW170814 the most informative dark siren of this analysis.

6.6 Results of a Robust Analysis of GWTC-3 with the GLADE+ K-band

The **`gwcosmo`** analysis on GWTC-3, the third catalogue of gravitational wave events which encompasses all events detected from O1 to O3b, was done using the K-band of the GLADE+ catalogue. [2, 156]

While the GLADE+ catalogue is less complete in the K-band, it was found to be subject to fewer biases than an analysis with the B-band due to the behaviour of its luminosity function. Figure 6.19 shows the assumed and observed luminosity functions for the GLADE+ B- and K-bands. It can be seen from this plot that the galaxy distributions in the K-band follow the assumed luminosity function more closely than in the B-band.

The GWTC-3 analysis uses 47 gravitational wave events above a threshold SNR of 11, including the events described in table 6.2. The analysis of GW170814 is done using GLADE+ rather than DES, as DES does not contain K-band data for galaxies, with DECam observations only being in the *grizY* filters. Of the 47 selected events, 42 are BBH, 2 are BNS (GW170817 and GW190425), 2 are NSBH (GW200105 and GW 200115) and one is the asymmetric mass binary GW190814. [39, 156, 238–240]

The GLADE+ catalogue is less complete in the K-band than in the B-band. This means that each pixel will contain fewer galaxies. This means no re-sampling methods are needed for

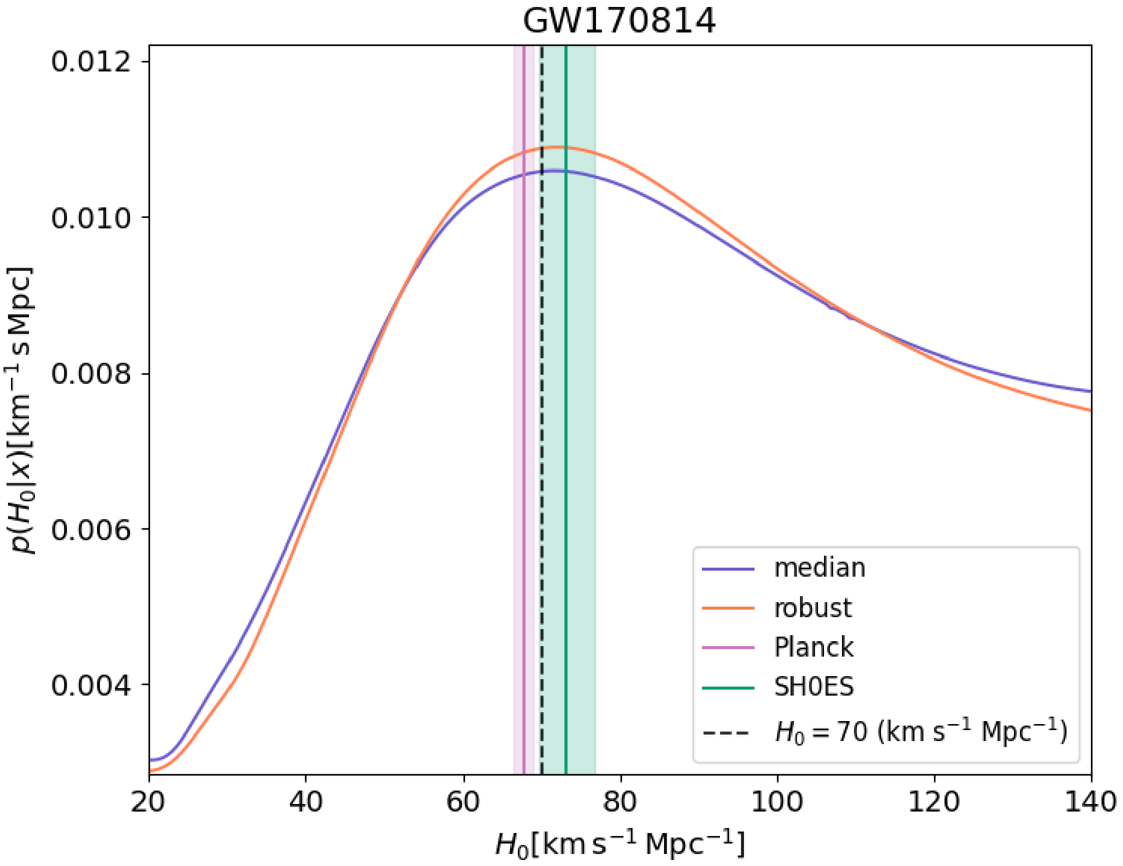

Figure 6.18: Posterior on H_0 for GW170814 using the DES catalogue. comparing results with the robust method and the median method

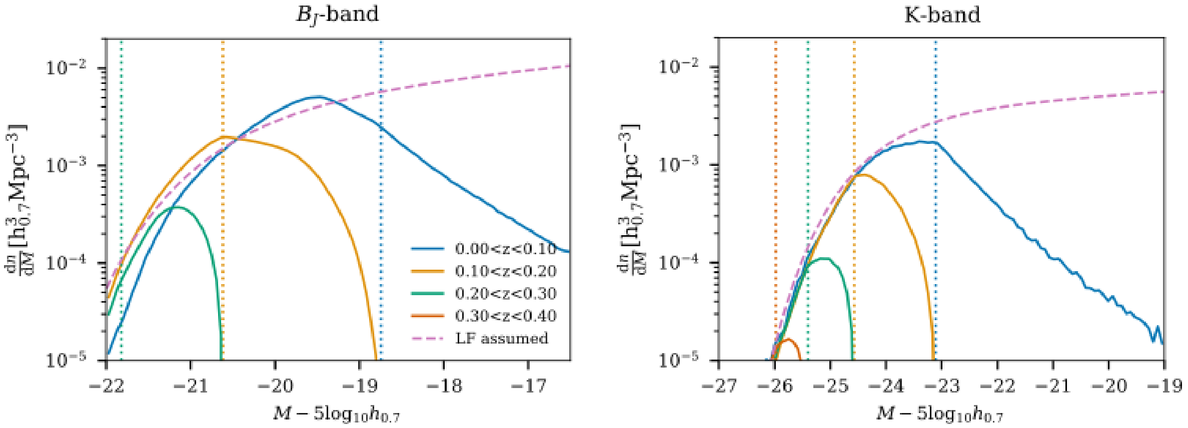

Figure 6.19: The assumed luminosity function against the actual distribution of B-band and K-band galaxies, with absolute median magnitude threshold (dotted vertical lines). Solid lines based on m_{thr}. While the K-band has a brighter apparent magnitude threshold, it is less affected by galactic dust, and its distribution is closer to the assumed luminosity function than the B-band. Figure from [156].

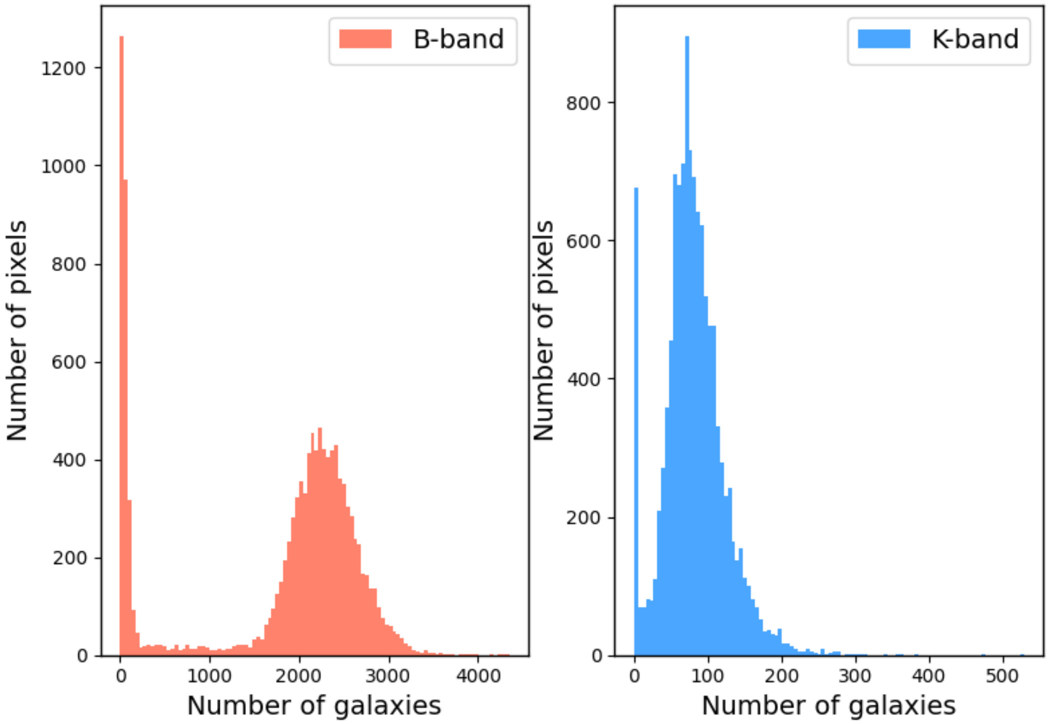

Figure 6.20: Histogram for the number of galaxies per pixel for GLADE+ for the B- and K-bands. $N_{side} = 32$. Empty pixels ($N_{gal} = 0$) are not included. There is a peak at low but non-zero $N_{gal} = 0$. This is due to near-empty pixels obscured by the Milky Way band.

the (m_i, z_i) samples, but also means any test of galaxy completeness will be less accurate. This applies not only to the robust method but also to the median method.

In the analysis of all GWTC-3 posteriors used for the current cosmology analysis, the difference is marginal compared to the analysis using the B-band of the GLADE catalogue with GWTC-1 events. This reflects the fact that GLADE+ is less complete in the K-band; for most events, even with a fainter and most accurate m_{thr}, the potential host galaxy still lies beyond the limits of GLADE+. However, as seen with the B-band analysis, a careful estimate of the magnitude threshold will be necessary as deeper galaxy catalogues are obtained and more events detected.

In the K-band analysis, most events are uninformative, with their posteriors being very similar to the posteriors for the "empty catalogue" case. Empty catalogue results are obtained solely from assumptions about the BBH population. [156] The most informative event is the well-localised GW190814A. GW190814A was a triple-coincident detection of a BBH at a distance of 241^{+41}_{-45}Mpc with a localisation area of 18.5 deg^2. [240] Figure 6.22 shows the skymap for the event against the map of robust magnitude thresholds for the GLADE+ K-band with a pixel size of $N_{side} = 32$.

Figure 6.23 shows a comparison for the posterior on GW190814A using robust and the median magnitude. The main difference when using the robust method is a slight shift towards a higher H_0, with support for $H_0 > 100$ km s^{-1} Mpc^{-1} being suppressed.

Figure 6.24 shows a comparison of the probability of the host galaxy being in the galaxy catalogue, $p(G|D_{GW}, x_{GW})$, for each pixel in the skymap. The figure shows that while the final posterior is almost identical, this is due to the probability of the host galaxy being in the catalogue still being very low, even when using the robust method. It does however show a clear trend towards increasing $p(G|D_{GW}, x_{GW})$.

The final results of the GWTC-3 analysis using the **`gwcosmo`** pipeline with the robust method and the GLADE+ K-band information are presented in figure 6.25. The results follow what is seen in individual events in figure 6.21; as most events are uninformative and lie beyond even the robust apparent magnitude limit of the GLADE+ K-band, there is no significant difference to the final posterior on H_0.

The final result on H_0 for the K-band GLADE+ GWTC-3 analysis is $H_0 = 69^{+8}_{-6}$ km s^{-1} Mpc^{-1} compared to $H_0 = 68^{+8}_{-6}$ km s^{-1} Mpc^{-1} for the GWTC-3 results using the median magnitude threshold. For dark sirens only, we get $H_0 = 68^{+14}_{-11}$ km s^{-1} Mpc^{-1} compared to $H_0 = 67^{+13}_{-12}$ km s^{-1} Mpc^{-1} for the GWTC-3 results using the median magnitude threshold. Using the robust method, the final posterior on H_0 is 2.8% wider with GW170817 and 2.2% wider for dark sirens only.

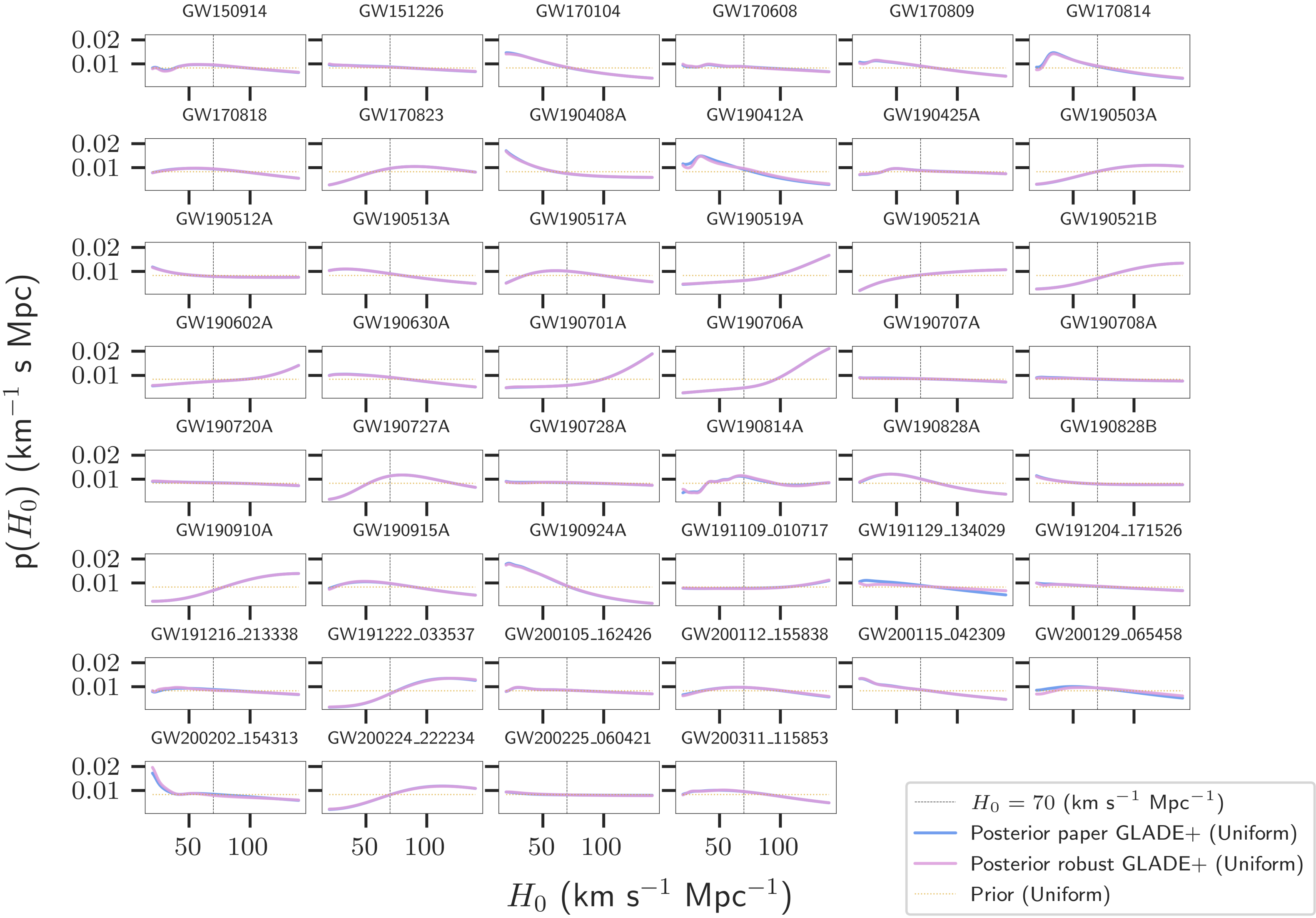

Figure 6.21: H_0 posteriors for all GWTC-3 dark sirens. The posterior using the robust method of estimating catalogue completeness is presented in pink, while the posteriors from the GWTC-3 cosmology paper are in blue. [156]. Most posteriors correspond to the "empty catalogue case", with all posteriors being very similar and uninformative.

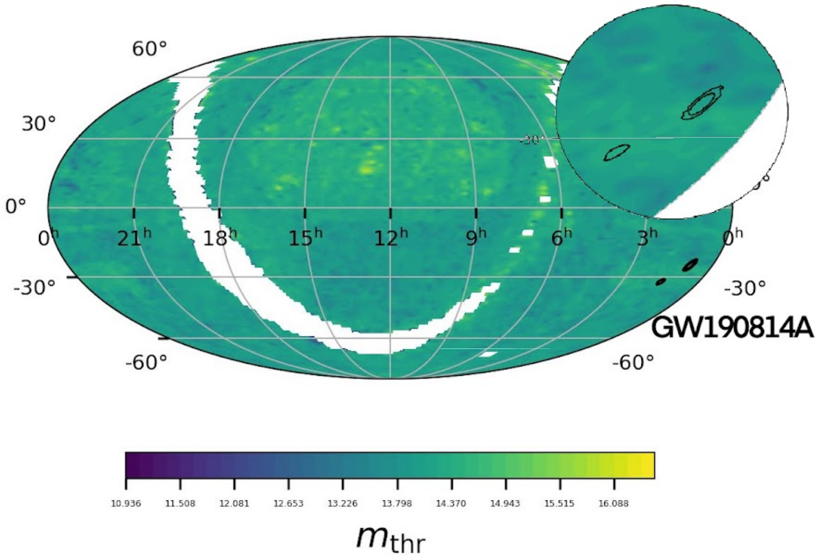

Figure 6.22: Skymap for GW190814A, against the robust m_{thr} map for the GLADE+ K-band, for a pixel size of $N_{side} = 32$. The contours shown are the 68% and 90% confidence intervals.

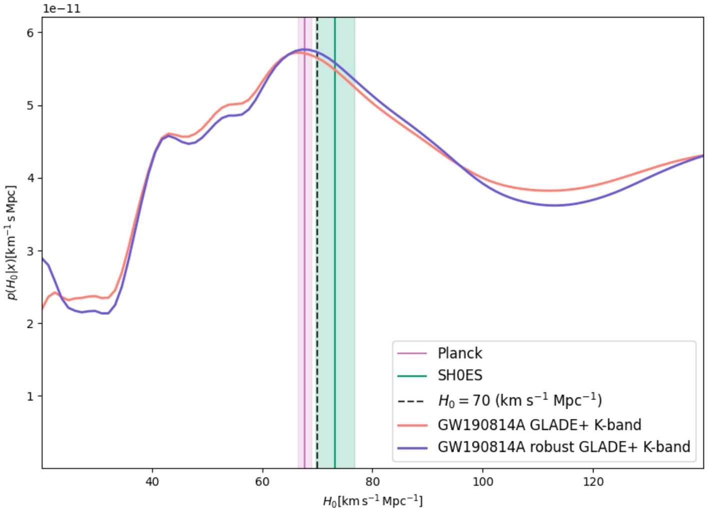

Figure 6.23: Posteriors on H_0 for the robust and median methods applied to the analysis of GW190814A, the most informative event of the GWTC-3 dataset.

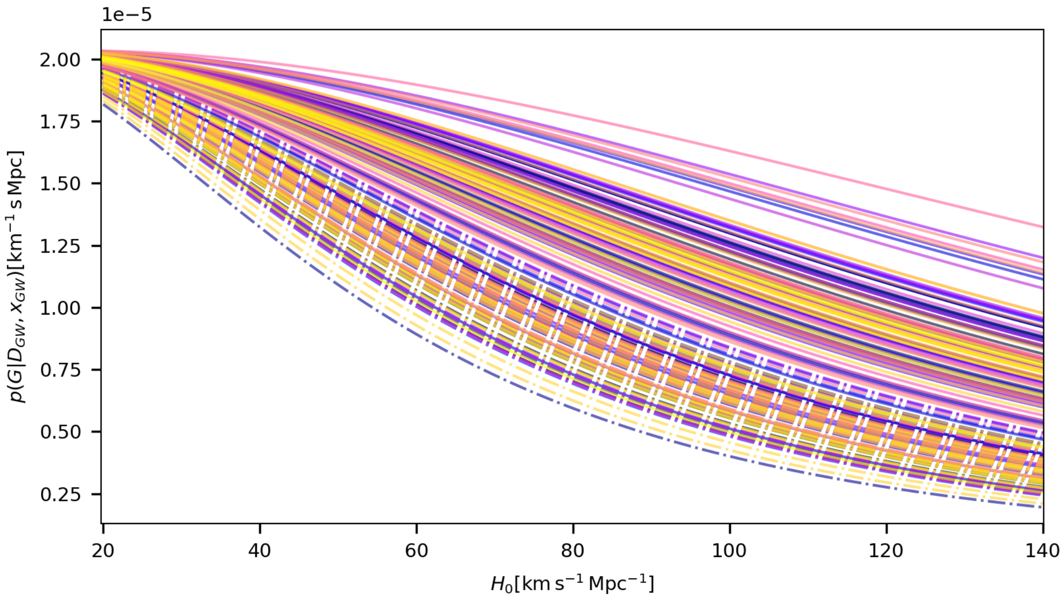

Figure 6.24: Probability of the host galaxy of the GW source being in the catalogue, $p(G|D_{GW}, x_{GW})$, for each pixel of the skymap corresponding to the event GW190814A. The dash-dotted lines show $p(G|D_{GW}, x_{GW})$ for the median method while the solid lines show $p(G|D_{GW}, x_{GW})$ for the robust method. Even where events are uninformative, it is clear that using the robust method increases the contribution from $p(G|D_{GW}, x_{GW})$.

6.7 Conclusions and Future Work

While the final results using the GWTC-3 catalogue do not show any improvement to the final H_0 posterior, this is due to most events lying outwith the GLADE+ galaxy catalogue in the K-band. GLADE and GLADE+ are more complete in the B-band, and a significant improvement can be seen in the GWTC-1 analysis using GLADE+. We also note that applying the robust test of completeness, or any test of completeness, is less informative in the K-band due to the low number of galaxies in each pixel.

The results highlight the importance of the careful treatment galaxy catalogue completeness when statistically inferring the Hubble constant from CBCs. While it is important not to introduce any biases by overestimating the completeness of a catalogue, information is thrown away when using an overly conservative estimate. This is an important consideration as the collaboration works towards compiling deeper, more complete galaxy catalogues for gravitational wave cosmology.

The result also highlights the important role of deep galaxy surveys for cosmological inference. This gives weight to the idea of carrying out dedicated deep EM follow-up within the sky localisation of loud and well-localised gravitational wave events.

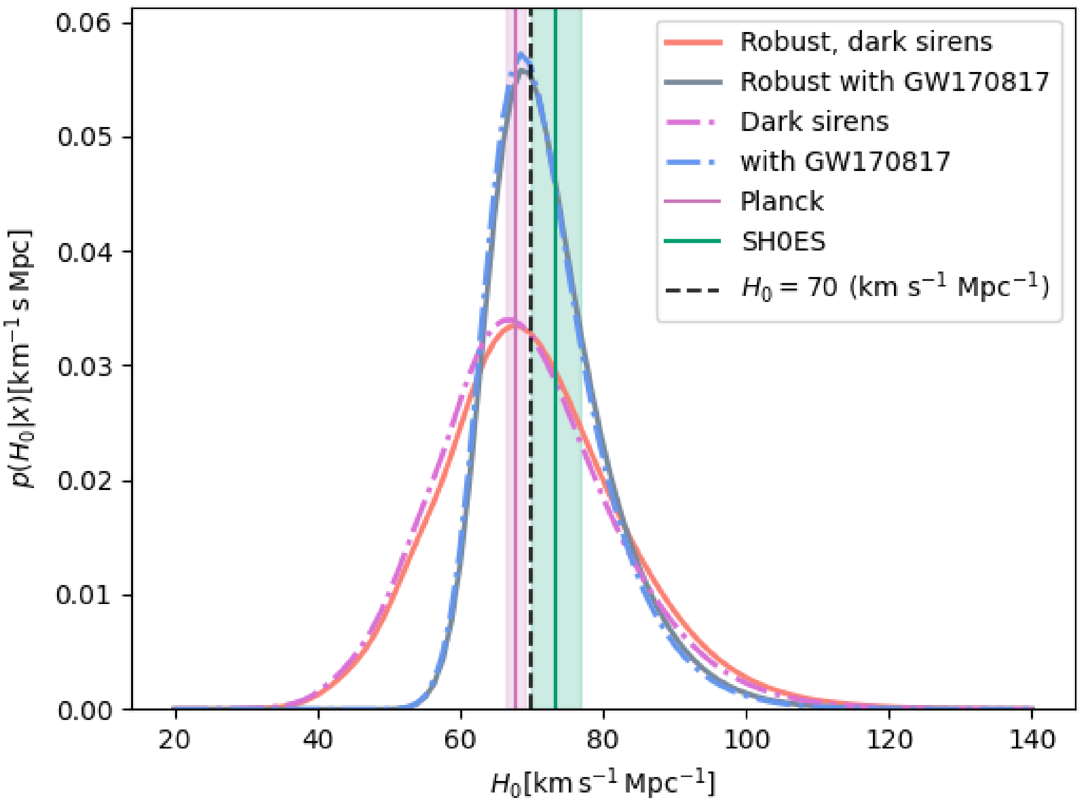

Figure 6.25: Final posterior on H_0 showing the difference between the robust analysis and the median analysis. The pink lines show the posterior only using dark sirens, while the blue lines show the posterior with GW170817.

6.7.1 Towards implementing uncertainties on the apparent magnitude threshold

The previous discussion highlights the fact that any rigorous estimate of the magnitude threshold m_{thr} will contain uncertainties due to the uncertainties on the measured apparent magnitudes and redshifts. This shows that for a rigorous cosmological analysis, implementing an uncertainty on m_{thr} in **gwcosmo** will be necessary. The work presented in this chapter paves the way for implementing m_{thr} into the **gwcosmo** pipeline. Implementing these uncertainties would require a re-write of the current equations used in the pipeline. Currently, the equations approximate $p(G|z,\Omega,M,m,D,s,H_0)$ to a Heaviside step function around m_{thr}. Implementing an uncertainty on the magnitude threshold would require to re-derive the equations following that step, and to implement them into the current pipeline.

The contributors to the uncertainty on m_{thr} with the robust method are:

- uncertainties on photometric redshifts z
- uncertainties on apparent magnitudes m
- uncertainties due to the re-sampling of galaxies for catalogue pixels with a large number of uncertainties

6.7.2 Other future work

At the time of writing, the **gwcosmo** pipeline computes pixel magnitude thresholds for each event. This is a legacy of the unpixelated method, for which a single magnitude threshold m_{thr} was obtained for each event skymap. As each area of the catalogue defined by an event skymap was unique, this was necessary for the unpixelated pipeline. However, with the galaxy catalogue being broken down into "pixels", one can simply choose the pixels contained within each event skymap, therefore bypassing the need for computing a new map of m_{thr} for every event. This is not yet implemented since the median method of determining m_{thr} is fast to compute, but plans are in place to implement the pre-computing of m_{thr} for the entire galaxy catalogue.

The robust method is computationally expensive, hence the need to re-sample galaxies for pixels with large numbers of galaxies. If all m_{thr} are pre-computed, this means a more sophisticated implementation of the robust method will be possible, without relying on re-sampling galaxies.

Currently, **gwcosmo** only takes in one pixel size as an input. This can mean that some pixels are emptier than others, which would make any test of m_{thr} less informative for low numbers of galaxies. Future work will focus on varying the N_{side} of pixels, amalgamating them with surrounding pixels for emptier areas.

Other areas of consideration for future work will be on the assumptions about the luminosity function. The robust method of determining the completeness of a catalogue does not take into account potential redshift-dependences of the luminosity function, since it assumes that the luminosity function is universal.

7 | The Newtonian Calibrator for LIGO detectors

> We demand rigidly defined areas of doubt and uncertainty!
>
> Douglas Adams, The Hitchhiker's Guide to the Galaxy

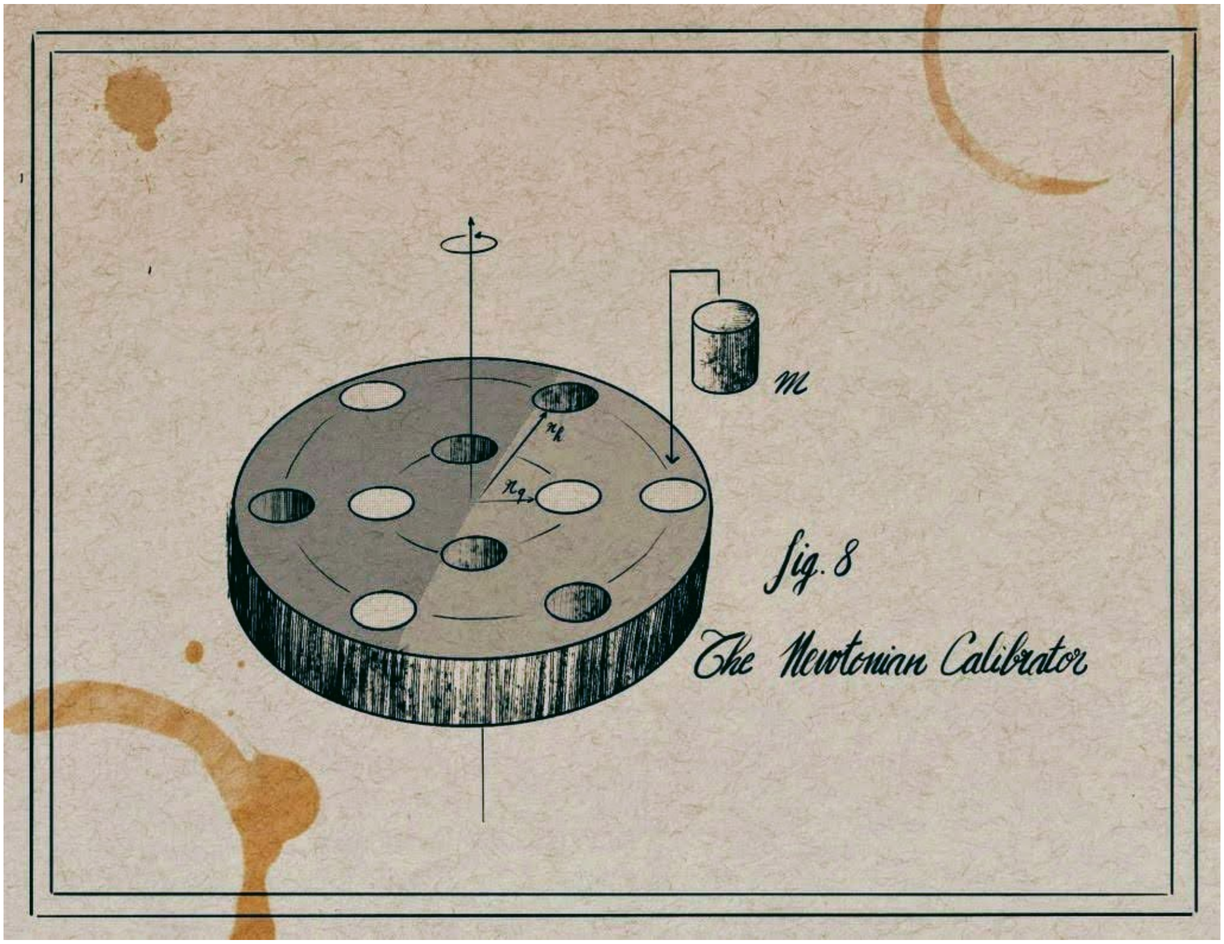

The previous chapters introduce a body of work that relies on LVK observations of compact binary coalescences. This work cannot be done without careful calibration of the LIGO detectors. Calibration fits into the framework of maximising scientific returns from CBC observations. Particularly, it has applications in cosmology, as the inferred parameters from CBCs depend on the accurate calibration of the detectors. The extraction of astrophysical parameters from gravitational wave data relies on the accurate calibration of the detectors. Accurate calibration is essential to gravitational wave astronomy and cosmology; without accurate calibration, the recovered waveform would be inaccurate.

The work presented in this section is the result of work published as part of the LIGO Calibration group. My contributions consisted of the derivation of a hexapole analytical model for the LIGO Newtonian Calibrator, along with re-deriving and implementing code for the quadrupole from first principles used in analytical models of the Virgo Calibrator. The derivations presented in this work are my own, while the derivations presented in [241, 242] have been re-arranged by Jeff Kissel and Martin Hendry for aesthetic purposes. The two are equivalent. My other contribution was on the Bayesian propagation of uncertainties for non-linear force coefficients. The methodology was applied to all models used in [241].

7.1 Calibrating the LIGO detectors

The LIGO detectors, along with other interferometric gravitational wave detectors, detect gravitational waves by measuring the differential arm length of the observatory. When a gravitational wave passes through the detector, a change in differential length is induced. This differential length variation of the interferometer arms is then measured through the ouput of the laser photodiode. [27]

While the interferometric gravitational wave detectors measure a displacement, the actual measured output will be the measured laser power at the photodiode. The output signal from the detectors are a time-series of calibrated differential length variations between the two arm cavities. They're reconstructed through applying a response function. [29]

Definition

Strain: In the context of gravitational wave detectors, the strain is the displacement of the observatory's arm compared to the arm length.

This means that in order to get the strain from the interferometer output, we need to know what the output looks like for a known displacement of the test masses. This is done through calibration. The calibration of interferometers requires the application of a known force to the test mass, which is then measured through the interferometer output. The displacement of the test mass results in a change in DARM (differential arm length).

The calibration of the detectors needs to be done across the entire sensitive band of the interferometer in order to accurately extract astrophysical source parameters from measured gravitational wave signals. For the LIGO detectors, that is 20-2000Hz. [243, 244]

There are several methods for calibrating the Advanced LIGO detectors. The main method is through Photon Calibrators (PCal). Two other methods, free-swinging Michelson and frequency modulation, provide cross-checks. [29] Here we discuss the calibration of the LIGO Hanford detector using another method, the Newtonian Calibrator (NCal).

7.2 Photon Calibrators

The Photon Calibrator (**PCal**) is a calibrating system which imparts a known, direct force on the detector's test mass through radiation pressure. This requires knowing the power of the laser precisely. Absolute laser power calibration is done through power sensors called integrating spheres, one of which, the *Gold Standard*, is calibrated annually at the National Institute of Standards and Technology (NIST). [245, 246] Photon calibrators use an auxiliary power-modulated laser at the end test mass (ETM). The beams shine slightly off-centre, imparting a displacement via photon recoil off of the test mass. [29, 245]

The PCal is the current, state-of-the-art calibration method used in the Advanced LIGO detectors. They provide continuous calibration while the detectors are observing, and provide the most precise calibration to date. [245] Virgo and KAGRA also make use of photon calibrators. [30, 247, 248]

7.3 Newtonian Calibrators

Newtonian Calibrators measure the response of the interferometer by imparting time-varying gravitational forces onto the detectors' test masses with an oscillating mass distribution. Rotors can be designed to impact force at any multiple of the rotational frequency f. [241]

Other calibrators which make use of gravitational forces on the test mass have been implemented at the Virgo and KAGRA detectors. These calibrators are known as Newtonian or gravitational calibrators.

One advantage of Newtonian Calibrators is that they are comparatively unintrusive. The forces induced by the PCal laser on the test mass can induce local and bulk deformations of the mirror. [249, 250]

7.3.1 Previous Newtonian Calibrators

Prior to the implementation of the LIGO NCal prototype at LIGO Hanford, both the KAGRA and Virgo detectors operated their own Newtonian calibrators.

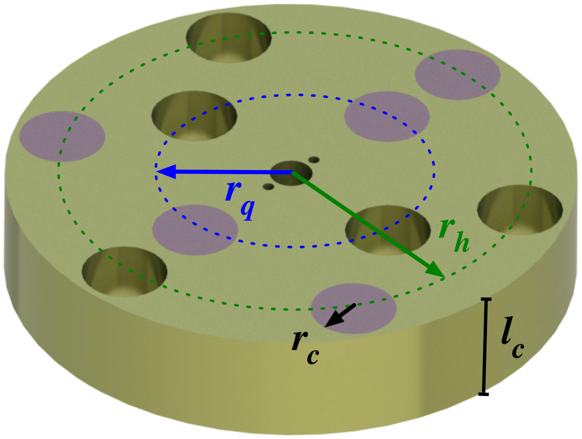

Figure 7.1: A render of the LIGO NCal. Figure from [241].

KAGRA

The design of the gravitational calibrator implemented at KAGRA, the Gcal, is similar to that of the LIGO NCal. The rotor has two mass distributions in a quadrupole and a hexapole configuration. [251]

Virgo

The Virgo Newtonian Calibrator (NCal) was first built as a simple prototype. Its rotor is symmetrical around its axis except for two sectors which have an opening angle of 45 degrees. It can be simplified as a rotor made out of two masses symmetrical around the axis of rotation for modelling purposes. [252] The set-up of the Virgo calibrator with regards to the test mass is similar to that of the LIGO NCal, with the rotor placed off-axis from the beam axis.

During O3, a more robust set-up was built, with two rotors made up of two 90 degree sectors. [253] The rotors were aligned with the same angle off-axis from the beam, with one "near" and one "far" rotor.

7.3.2 The LIGO Newtonian Calibrator (NCal)

The LIGO NCal prototype was installed at the X-end of the LIGO Hanford detector during the commissioning break between O3a and O3b, in October 2019.

It consists of a main body (disc) made out of aluminium (density 2.7 g cm^{-3}), with cylindrical cavities cut out in quadrupole and hexapole configurations. Two masses for the quadrupole configuration and three for the hexapole configuration are inserted into these cavities. The masses are tungsten masses (density 19.3 g cm^{-3}) set into the main aluminium disc of the NCal. [241] The design is similar to the design proposed in [254] and implemented at the KAGRA detector. [251] A full description of the hardware and installation can be found in [241].

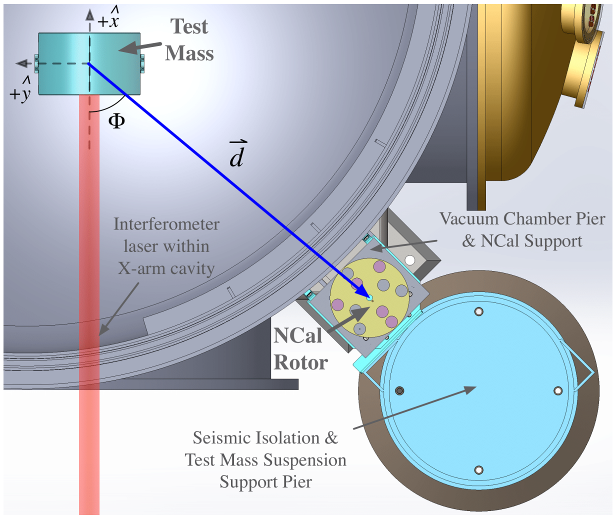

Figure 7.2: A render of the LIGO NCal at the LIGO Hanford X-end, showing its position relative to the end test mass. Figure from [241].

The quadrupole set-up, being a two-fold symmetric mass distribution, induces a force on the nearby test mass at twice the rotational frequency $2f$. Likewise the hexapole configuration, being three-fold symmetric, induces a force at $3f$.

7.4 Modelling the force coefficient of the Newtonian calibrator

In order to use the NCal for calibrating gravitational wave detectors, we must estimate the amplitude of the force it induces on the test mass. Modelling the force amplitude from the rotating prototype can be done in several ways. This work focuses on an analytical, point-mass expression for the NCal force coefficient. Other methods (Finite Element Analysis, Multipole) are outlined in [241].

The analytical, point mass form of the NCal force coefficient was built upon methods developed in [254], which were applied to the derivation of the force coefficient for the Virgo NCal. [252] The Virgo calibrator uses masses in a quadrupole set-up only. This force coefficient equation was re-derived and extended to a hexapole set-up.

7.4.1 Off-axis quadrupole

The following derivation is independently re-derived from the methodology described in [252]. From the description of the set-up, we arrive at the same expression for the force originating from the quadrupole configuration of the LIGO Newtonian calibrator. Another expression is presented, which is the equation presented in the published LIGO NCal paper. Results from the two expressions are equivalent to $\sim 0.01\%$. The second equation is presented in the paper for aesthetic purposes.

The LIGO Newtonian calibrator consists of masses in a quadrupole and in a hexapole configuration. In the LIGO Hanford configuration, the rotor position is off-axis from the centre of the test mass.

The two masses m_{q1} and m_{q2} in the quadrupole configuration are described by the following coordinates:

$$\begin{aligned}\mathbf{r_{x1}} &= d\cos\Phi + r_q\cos\theta, &(7.1)\\ \mathbf{r_{y1}} &= d\sin\Phi + r_q\sin\theta, &(7.2)\\ \mathbf{r_{z1}} &= z, &(7.3)\end{aligned}$$

and

$$\begin{aligned}\mathbf{r_{x2}} &= d\cos\Phi - r_q\cos\theta, &(7.4)\\ \mathbf{r_{y2}} &= d\sin\Phi + r_q\sin\theta, &(7.5)\\ \mathbf{r_{z2}} &= z. &(7.6)\end{aligned}$$

Starting with the first mass m_{q1}, the distance from the test mass to the rotor mass is:

$$\begin{aligned}L_1^2 &= (d\cos\Phi + r_q\cos\theta)^2 + (d\sin\Phi + r_q\sin\theta)^2 + z^2\\ &= d^2 + r_q^2 + 2dr_q(\cos\Phi\cos\theta + \sin\Phi\sin\theta) + z^2\\ &= d^2 + r_q^2 + z^2 + 2dr_q\cos(\Phi-\theta)\\ . \end{aligned} \tag{7.7}$$

Using

$$F = \frac{GMm}{L^2}, \tag{7.8}$$

we consider only the projection of the total force in the x-axis, $F_x = Fcos\Phi$ with Φ the angle between $\mathbf{F}$ and the x-axis. Projecting the force onto the x-axis:

$$F_{qx1} = F_{q1}(d\cos\Phi + r\cos\theta)(d^2 + r_q^1 + z^2 + 2dr_q\cos(\Phi-\theta))^{-1/2}, \tag{7.9}$$

which gives:

$$F_{qx1} = GMm_q(d\cos\Phi + r\cos\theta)(d^2 + r_q^1 + z^2 + 2dr_q\cos(\Phi-\theta))^{-3/2}. \tag{7.10}$$

We introduce the parameter $\varepsilon = \frac{r_q}{d} << 1$ and rewrite the equation above:

$$F_{qx1} = GMm\frac{d(\cos\Phi + \varepsilon\cos\theta)}{d^3(1+\varepsilon^2+\frac{z^2}{d^2}+2\varepsilon\cos(\Phi-\theta)^{3/2})}. \tag{7.11}$$

Setting $Z = 1+\frac{z^2}{d^2}$:

$$F_{qx1} = \frac{GMm_q}{d^2}(\cos\Phi + \varepsilon\cos\theta)(Z+\varepsilon_2^2\varepsilon\cos(\Phi-\theta))^{-3/2}. \tag{7.12}$$

Setting $X = \varepsilon^2 + 2\varepsilon\cos(\Phi-\theta)$ and using the following Taylor expansion up to the second order:

$$(Z+X)^{-3/2} \simeq \frac{1}{Z^{3/2}} - \frac{3X}{2Z^{5/2}} + \frac{15X^2}{8Z^{7/2}}. \tag{7.13}$$

We can re-write the force from the first test mass x-axis:

$$F_{qx1} = \frac{GMm}{d^2}Z^{-5/2}(Z-\frac{3}{2}X+\frac{15}{8Z}X^2)(\cos\Phi+\varepsilon\cos\theta). \tag{7.14}$$

The total force from the test mass m_{q1} projected onto the x-axis is:

$$F_{qx1} = \frac{GMm}{d^2}Z^{-5/2}(Z-\frac{3}{2}\varepsilon^2-3\varepsilon(\Phi-\theta)+\frac{15}{2Z}\varepsilon^2\cos^2(\Phi-\theta))(\cos\Phi+\varepsilon\cos\theta). \tag{7.15}$$

The derivation is similar for the second mass m_{q2}, where we set $X = \varepsilon^2 - 2\varepsilon\cos(\Phi-\theta)$. We arrive at a final expression

$$F_{qx2} = \frac{GMm_q}{d^2}Z^{-5/2}(Z-\frac{3}{2}\varepsilon^2+3\varepsilon\cos(\Phi-\theta)+\frac{15}{2Z}\varepsilon^2\cos^2(\Phi-\theta))(\cos\Phi-\varepsilon\cos\theta). \tag{7.16}$$

Adding the force contributions from both masses:

$$\begin{aligned}F_{qx} &= F_{qx1}+F_{qx2}\\ &= \frac{GMm_q}{d^2}Z^{-5/2}\big((2Z-3\varepsilon^2)\cos\Phi-6\varepsilon^2\cos\theta(\cos\theta\cos\Phi+\sin\theta\sin\Phi)\\ &\qquad+\frac{15}{Z}\varepsilon^2\cos\Phi(\cos\theta\cos\Phi+\sin\theta\sin\Phi)^2)\big).\end{aligned} \tag{7.17}$$

Taking only the θ-dependent terms gives:

$$\begin{aligned}F_{q\theta} = \frac{GMm_q^2}{d^4}Z^{-5/2}\big((-3\cos\Phi + \frac{15}{2Z}\cos^3\Phi - \frac{15}{2Z}\cos\Phi\sin^2\Phi)\cos 2\theta \\ + (-3\cos\Phi + \frac{15}{Z}\cos^2\Phi\sin\Phi)\sin 2\theta\big).\end{aligned} \tag{7.18}$$

Separating the two terms in $\cos 2\theta$ and $\sin 2\theta$ giving:

$$F_{q\theta} = \frac{GMm_q}{d^2}\varepsilon^2 Z^{-5/2}(\alpha\cos 2\theta + \beta\sin 2\theta). \tag{7.19}$$

Using $\cos^3\Phi = \frac{1}{4}(3\cos\Phi + \cos 3\Phi)$ and $\cos\Phi\cos 2\Phi = \frac{1}{2}(\cos\Phi + \cos 3\Phi)$:

$$\alpha = 3\cos\Phi + \frac{15}{4Z}(\cos\Phi + \cos 3\Phi), \tag{7.20}$$

and

$$\beta = -3\sin\Phi + \frac{15}{4Z}(\sin\Phi + \sin 3\Phi). \tag{7.21}$$

Using $a\cos x + b\cos x = \sqrt{a^2+b^2}\sin x$

$$\begin{aligned}F_{q\theta} = \frac{GMmr^2}{2d^4}Z^{-5/2}\sin(2\theta + \Phi) \\ \sqrt{\left(\cos\Phi\left(\frac{15}{2Z} - 6\right) + \frac{15}{2Z}\cos 3\Phi\right)^2 + \left(\sin\Phi\left(\frac{15}{2Z} - 6\right) + \frac{15}{2Z}\sin 3\Phi\right)^2},\end{aligned} \tag{7.22}$$

which can be written as:

$$F_{q\theta} = \frac{GMmr^2}{2d^4}Z^{-5/2}\sin(2\theta + \Phi)\sqrt{\left(\frac{15}{2Z}\right)^2 + \left(\frac{15}{2Z} - 6\right)^2 + \left(\frac{15}{2Z} - 6\right)\frac{15}{Z}\cos 2\Phi}. \tag{7.23}$$

The square-rooted term can be written as:

$$\begin{aligned}\frac{1}{2}(\frac{15}{Z})^2 - \frac{6\times 15}{Z} + 6^2(\cos^2\Phi + \sin^2\Phi) + \frac{1}{2}(\frac{15}{Z})^2 2\cos^2\Phi - \frac{1}{2}(\frac{15}{Z})^2 - \frac{6\times 15}{Z}2\cos^2\Phi + \frac{6\times 15}{Z} \\ = (\frac{15}{Z} - 6)\cos^2\Phi + 6^2\sin^2\Phi.\end{aligned} \tag{7.24}$$

Finally, the force from the quadrupole is:

$$F_q = \frac{GMm_q}{d^2}\varepsilon^2\sin(2\theta + \Phi)\sqrt{(\frac{15}{Z} - 6)^2\cos^2\Phi + 6^2\sin^2\Phi}, \tag{7.25}$$

which is the same expression seen in [252]. The final expression presented in [241] is

$$F_q = \frac{9}{2}\frac{GMm_q}{d^2}\varepsilon^2 Z^{-5/2}\big[(\frac{5}{6Z}-\frac{2}{3})\cos(2\theta-\Phi)+\frac{5}{6Z}\cos(2\theta-3\Phi)\big]. \tag{7.26}$$

The two expressions are equivalent to $\sim 0.01\%$.

7.4.2 Hexapole

On-axis hexapole

It is useful to start from an on-axis configuration (the NCal is aligned with the x-axis). Each rotor mass in this configuration has coordinates $\mathbf{r} = r\cos\theta_i$ with θ_i:

$$\theta_1 = \theta, \tag{7.27}$$

$$\theta_2 = \theta + \frac{2\pi}{3}, \tag{7.28}$$

$$\theta_3 = \theta - \frac{2\pi}{3}. \tag{7.29}$$

In this configuration, each mass contribution is given by:

$$F_{h_i} = \frac{GMm_h}{d^2}(1+\varepsilon\cos\theta_i)(1+\varepsilon^2+2\varepsilon\cos\theta_i)^{-3/2}. \tag{7.30}$$

Using the Taylor expansion

$$(1+X)^{-3/2} \simeq 1-\frac{3}{2}X+\frac{15}{8}X^2-\frac{35}{16}Z^3... \tag{7.31}$$

to the third order we get

$$\begin{aligned} F_{h_1} = {} & \frac{GMm_1}{d^2}(1+\varepsilon\cos\theta) \\ & (1-\frac{3}{2}(\varepsilon^2+2\varepsilon\cos\theta)+\frac{15}{2}(\varepsilon^2+2\varepsilon\cos\theta)^2-\frac{35}{16}(\varepsilon^2+2\varepsilon\cos\theta)^3), \end{aligned} \tag{7.32}$$

$$\begin{aligned} F_{h_i} = {} & \frac{GMm_h}{d^2}\big(1-\frac{3}{2}\varepsilon^2+3\varepsilon\cos\theta+\frac{15}{8}\varepsilon^4+\frac{15}{2}\varepsilon^3\cos\theta+\frac{15}{2}\varepsilon^2\cos^2\theta+\varepsilon\cos\theta \\ & +\frac{3}{2}\varepsilon^3\cos\theta+3\varepsilon^3\cos^2\theta+\frac{15}{8}\varepsilon^5\cos\theta+\frac{15}{2}\varepsilon^3\cos^2\theta+\frac{15}{2}\varepsilon^3\cos^3\theta\big). \end{aligned} \tag{7.33}$$

Summing over all angles θ_i for all mass contributions and taking terms only up to ε^3, all terms fall out except terms in $cos^3\theta$, giving a final expression:

$$F_h = -\frac{GMm_h}{d^2}\varepsilon^3\frac{15}{2}cos^3(\theta). \tag{7.34}$$

Off-axis hexapole

In the previous section, we re-derived the analytical model for a force from an off-axis quadrupole configuration, arriving at the same final equation for the force that is presented in [252]. The paper describes an analytical model for a rotor constituted of two masses.

The LIGO Newtonian Calibrator has two mass distributions, in a quadrupole and a hexapole configuration. The previous derivation is based on the force estimate for the Virgo NCal. Unlike the LIGO set-up, the Virgo calibrator does not have a hexapole mass configuration. Starting from the same principles as the off-axis quadrupole derivation, we derive an analytical expression for the force originating from the hexapole configuration of an off-axis rotor. This is the same configuration as above, adapted for a hexapole. For each mass n the coordinates are now:

$$\mathbf{r_x} = dcos\Phi + rcos(\theta + (n-1)\frac{2\pi}{3}), \tag{7.35}$$

$$\mathbf{r_y} = dsin\Phi + rsin(\theta + (n-1)\frac{2\pi}{3}), \tag{7.36}$$

$$\mathbf{r_z} = z. \tag{7.37}$$

giving:

$$\mathbf{r_{x1}} = d + rcos\theta \text{ and } \mathbf{r_{y1}} = rsin\theta, \tag{7.38}$$

$$\mathbf{r_{x2}} = d + rcos(\theta + \frac{2\pi}{3}) \text{ and } \mathbf{r_{y2}} = rsin(\theta + \frac{2\pi}{3}), \tag{7.39}$$

$$\mathbf{r_{x3}} = d + rcos(\theta - \frac{2\pi}{3}) \text{ and } \mathbf{r_{y3}} = rsin(\theta - \frac{2\pi}{3}). \tag{7.40}$$

The vertical component remains unchanged for all masses as it is not dependent on θ. The derivation then follows the same principles as previous derivations.

Using the following Taylor expansion up to the third order:

$$(Z+X)^{-3/2} \sim \frac{1}{Z^{3/2}} - \frac{3X}{2Z^{-5/2}} + \frac{15X^2}{8Z^{7/2}} - \frac{35X^3}{16Z^{9/2}}, \tag{7.41}$$

we get, for each mass i

$$
\begin{aligned}
F_{hx_i} = \frac{GMm}{d^2} Z^{-5/2} (\cos\Phi + \varepsilon\cos(\theta + (i-1)\frac{2\pi}{3})) \\
(Z - \frac{3}{2}(\varepsilon^2 + 2\varepsilon\cos(\Phi - (\theta + (i-1)\frac{2\pi}{3})) \\
+ \frac{15}{2Z}(\varepsilon^2 + 2\varepsilon\cos(\Phi - (\theta + (i-1)\frac{2\pi}{3}))^2 \\
- \frac{35}{16Z^2}(\varepsilon^2 + 2\varepsilon\cos(\Phi - (\theta + (i-1)\frac{2\pi}{3}))^3). \qquad (7.42)
\end{aligned}
$$

Finally, when adding all contributions and using:

$$
cos(\theta) + cos(\theta + \frac{2\pi}{3}) + cos(\theta - \frac{2\pi}{3}) = 0, \qquad (7.43)
$$

$$
cos^2(\theta) + cos^2(\theta + \frac{2\pi}{3}) + cos^2(\theta - \frac{2\pi}{3}) = \frac{3}{2}, \qquad (7.44)
$$

and

$$
\begin{aligned}
& \cos((\theta + \frac{2\pi}{3}) - \Phi) + \cos((\theta - \frac{2\pi}{3}) - \Phi) + \cos(\theta - \Phi), \\
= \; & \cos(\theta - \Phi) + 2\cos(\theta - \Phi)\cos(\frac{2\pi}{3}), \\
= \; & 0, \qquad (7.45)
\end{aligned}
$$

all terms fall out except

$$
\varepsilon^3 \big(\frac{15}{2Z} \sum \cos^2(\Phi - \theta_i)\cos\theta_i - \frac{35}{2Z} \sum \cos^3(\Phi - \theta_i) \big). \qquad (7.46)
$$

Summing over the contributions from each hexapole mass, we arrive at a final expression:

$$
\begin{aligned}
& F_h = \frac{GMm_h}{d^2}\varepsilon^3 Z^{-5/2} \\
& \big(\frac{15}{2Z}(\cos^2(\Phi - \theta + \frac{2\pi}{3})\cos(\theta - \frac{2\pi}{3}) + \cos^2(\Phi - \theta - \frac{2\pi}{3})\cos(\theta + \frac{2\pi}{3}) + \cos^2(\Phi - \theta)\cos(\theta)) \\
& - \frac{35}{2Z^2}\cos\Phi(\cos^3(\Phi - \theta + \frac{2\pi}{3})\cos(\theta - \frac{2\pi}{3}) + \cos^3(\Phi - \theta - \frac{2\pi}{3})\cos(\theta + \frac{2\pi}{3}) + \cos^3(\Phi - \theta)\cos(\theta))\big), \\
& \qquad (7.47)
\end{aligned}
$$

which becomes equivalent to 7.34 when setting the rotor coordinates so that it is on-axis with

Variable	Value	Uncertainty
Rotor Position x	723 mm	2 mm
Rotor Position y	933 mm	1 mm
Rotor Radial Position ρ	1180mm	2mm
Rotor Angle Φ	52.24 deg	0.08 deg
Rotor Vertical Position z	10 mm	3 mm
Test mass mass	39.680 kg	10 g
Tungsten cylinder mass	1.0558 kg	0.3 g
Quadrupole radius	6.033 cm	5 μm
Hexapole radius	10.476 cm	5 μm

Table 7.1: Parameters for the NCal along with 68% credible interval.

the test mass.

The equivalent expression presented in [241] is:

$$F_h = \frac{15}{2}\frac{GMm_h}{d^2}\varepsilon^3 Z^{-7/2}\big[(\frac{7}{8Z}-\frac{3}{4})\cos(3\theta-2\Phi)+\frac{7}{8Z}\cos(3\theta-4\Phi)\big]. \tag{7.48}$$

The two expressions are equivalent to $\sim 0.01\%$.

7.5 Uncertainty on the Force Coefficient

One advantage of the analytical model outlined previously is that it allows us to quickly recover the total uncertainty on the force coefficient, along with the contribution from each parameter.

In order to get our final calibration with its uncertainty, it is crucial to understand the uncertainty on the force estimate for whichever calibrator is used. Previous methods like the PCal propagate uncertainties linearly, through differential equations. This is suitable for linear force coefficients, which have a more straightforward uncertainty propagation.

However, the force from the NCal is not linear, and this type of propagation would not fully capture any degeneracies between the parameters of the force coefficient. We therefore apply a Bayesian framework to the propagation of uncertainties for the NCal force coefficient, simultaneously sampling over the whole distribution for each parameter. This is in turn done for the other two models used in the analysis, recovering a final uncertainty.

We use Monte Carlo methods to generate a distribution on the force coefficient, from which the final uncertainty is obtained. This method returns a posterior distribution on the NCal force coefficient.

The parameters necessary for calculating the force coefficient of the NCal, along with their associated uncertainties, are presented in table 7.1.

With the method outlined previously, one can estimate the contribution to the uncertainty from each component of the NCal force equation. This is only done using the analytical point-mass model, as this is the least computationally intensive model to run. This allows us to evaluate

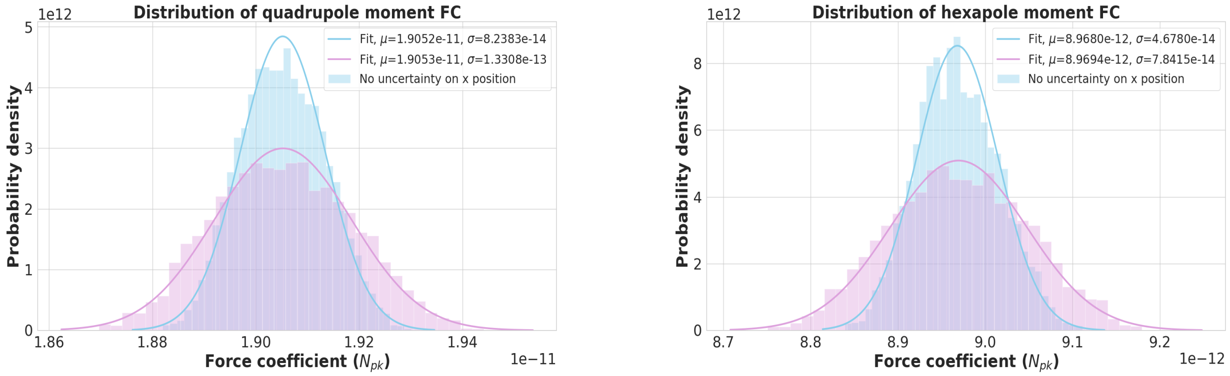

Figure 7.3: Force coefficient with all uncertainties for analytical model vs. no uncertainty on x position of rotor with regards to the test mass.

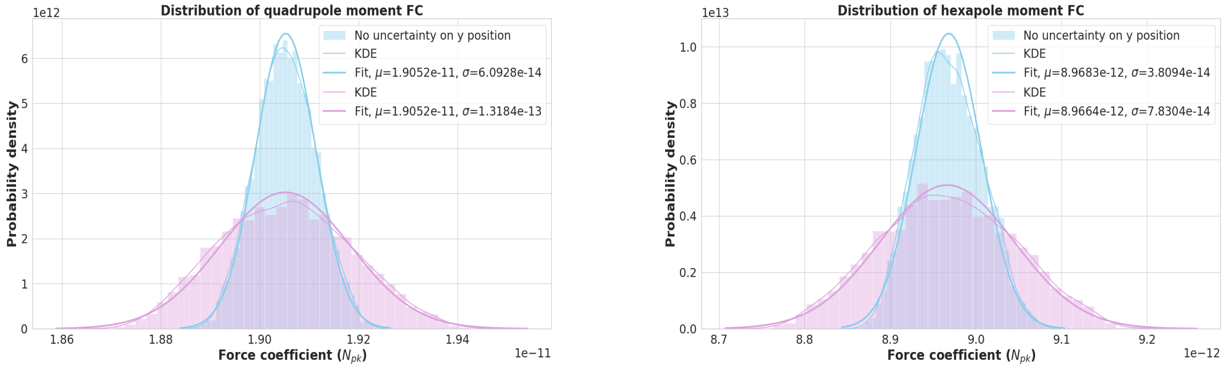

Figure 7.4: Force coefficient with all uncertainties for analytical model vs. no uncertainty on y position of rotor with regards to the test mass.

which aspect of the current set-up needs to improve in order to make the NCal competitive with other calibration methods.

Some uncertainties are negligible and/or below the numerical noise from the Monte Carlo sampling. These uncertainties are marked as "negligible" in table 7.2.

Although great effort was put into the surveying work for determining the position of the NCal accurately, the main driver of the uncertainty on the force coefficient remains the uncertainty on the position of the rotor in the x and y axes. [255]

7.6 Comparing the point-mass model to other models

This section briefly discusses the other two models used for the prediction of the NCal force coefficient, and compares results on the predicted force from each of the three models. The work on these two models was carried out by co-authors M.P. Ross and C. Weller and their

Variable	Value	Uncertainty	Contribution
Rotor Position x	723 mm	2 mm	$2f$: 0.27% (40% total) | $3f$: 0.35%(38% total)
Rotor Position y	933 mm	1 mm	$2f$: 0.37% (54% total) | $3f$: 0.45% (51% total)
Rotor position z	10.0 mm	3 mm	Negligible
Test mass mass	39.680 kg	10 g	Negligible
Tungsten cylinder mass	1.0558 kg	0.3 g	Negligible
Quadrupole radius	6.033 cm	5 μm	Negligible
Hexapole radius	10.476 cm	5 μm	Negligible

Table 7.2: Contributions to final uncertainty from each parameter for the analytical point mass model. The contributions are shown as a percentage of the mean of the force coefficient and as a percentage of the total uncertainty. Where uncertainties are negligible, they are below the numerical noise coming from the simulations.

group.

7.6.1 Finite Element Analysis

The Finite Element Analysis (FEA) model is the main model used in the analysis presented in [241]. It takes into account the full geometry of the NCal, making it the most realistic model of the three. While accurate, it is computationally expensive to run.

The FEA model works by approximating the geometry of the set-up as a cloud of finite-element point masses. This model was developed using the *PointGravity* algorithm presented in [256, 257].

7.6.2 Multipole

The multipole model calculates the force coefficient by breaking down each object into its gravitational multipole moments. This model is based on work presented in [258–262] and implemented using multipole algorithms found in in [257].

7.6.3 Comparison Between Models

Figure 7.5 shows a comparison of the force coefficients predicted by the three different models used in the analysis. All models are in good agreement, with the point-mass analytical model differing slightly from the other two due to not taking into account the full geometry of the NCal. Results are shown for the $2f$ (quadrupole) and $3f$ (hexapole) forces induced by the rotation of the NCal. The force coefficient is not expected to be frequency-dependent in this configuration.

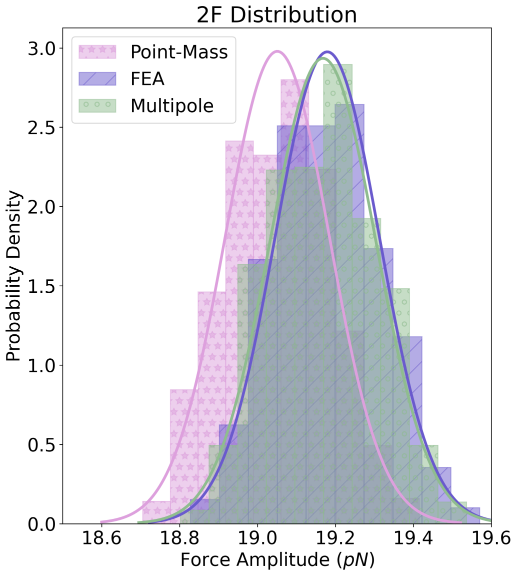

Figure 7.5: A comparison of the force coefficients obtained from all three models for the $2f$ and $3f$ forces.

7.7 Tests of the NCal

NCal injections were performed on 4 December 2019 at the X-end of the LIGO Hanford interferometer, while the detector was in its observation-ready state. The NCal was rotated at five different frequencies ranging from 4Hz to 10Hz, injecting $2f$ and $3f$ forces ranging from 8Hz to 30Hz. Each sweep lasted two minutes.

Figure 7.6 shows the amplitude spectra from the 2019 NCal injections, clearly showing the induced $2f$ and $3f$ signals for each $1f$ injection frequency.

From the NCal injection, we can extract a force coefficient and compare it to the one predicted by the models. The force amplitude was extracted from the injected signal using a Least-Squares Spectral Analysis. [241, 263] Statistical uncertainties from the fit dominate the uncertainty on the measured force coefficient.

Figure 7.7 shows a comparison between the measured force from the NCal and the predicted force coefficient from all three models. The first $2f$ measured force coefficient has a larger uncertainty due to the SNR being lower at that induced frequency. We can see that the measured force from the December 2019 injection is in agreement with the predicted force, which is predicted to $< 1\%$ relative uncertainty. This provides a good cross-check of the LIGO calibration, and could be combined with PCal in the future for increased accuracy.

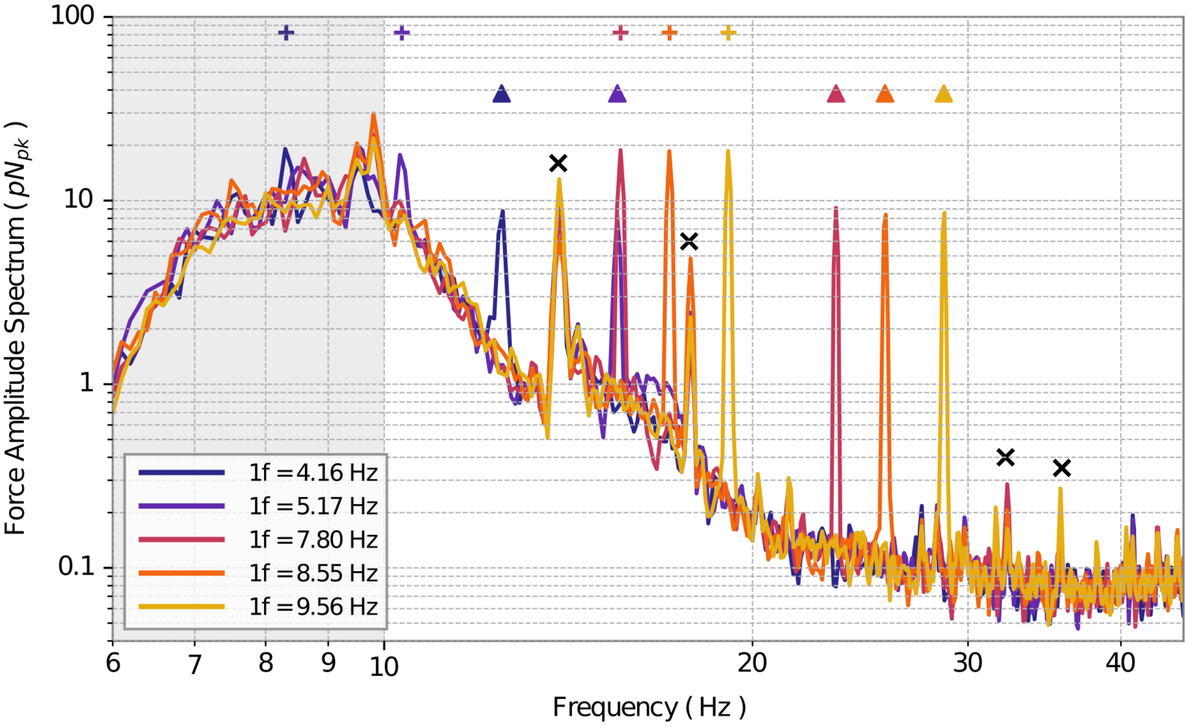

Figure 7.6: Amplitude spectra from the 4/12/2019 NCal injections at LIGO Hanford. Different colours represent different $1f$ injection frequencies, as detailed in the legend. The gray shaded area shows where the signal is aggressively high-passed and can be ignored. [241] The plus- and triangle-shaped markers indicate $2f$ and $3f$ frequencies, respectively. The black crosses indicate features unrelated to the NCal injection.

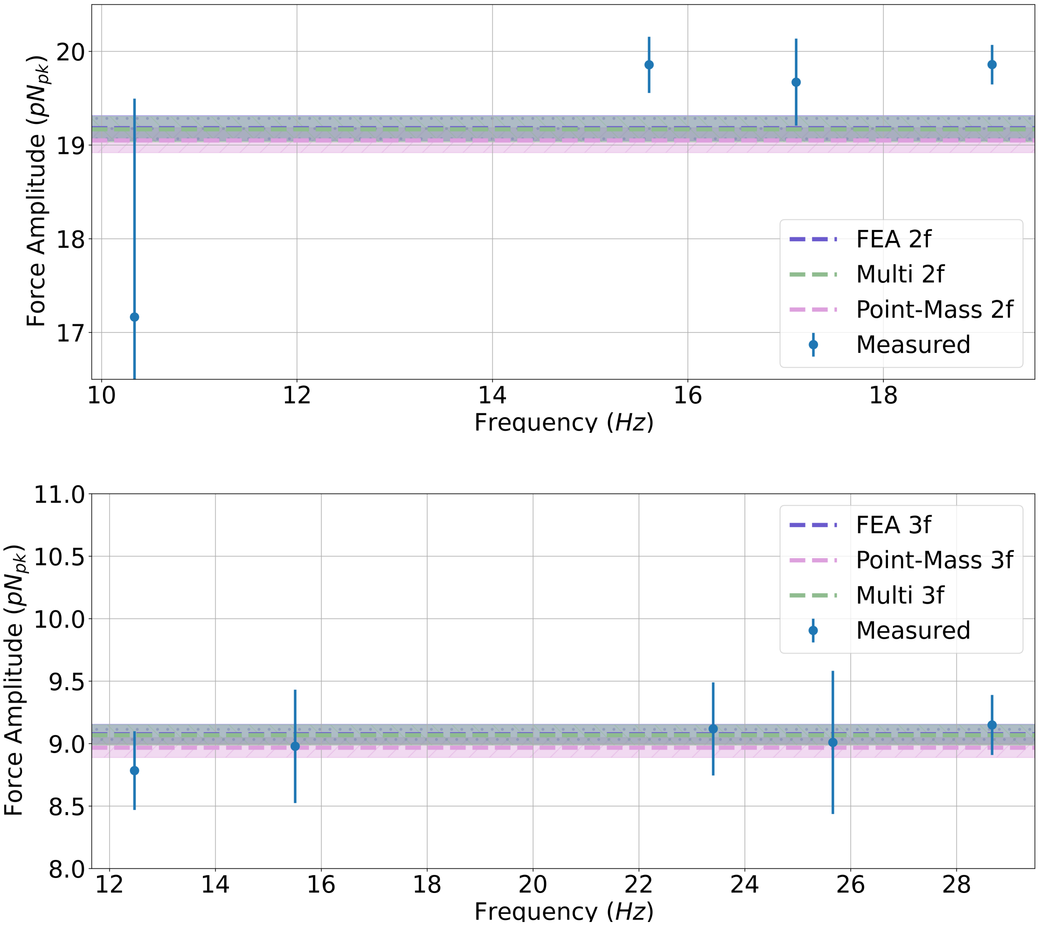

Figure 7.7: Force coefficients extracted from the NCal injections vs. force coefficients predicted by the models for both $2f$ and $3f$ signals.

8 | Conclusions

> Et j'aime la nuit écouter les étoiles.
>
> Antoine de Saint-Exupéry, Le Petit Prince

Since the first direct detection of gravitational waves in 2015, gravitational wave astronomy has grown to be a very active and rich field of astronomy. Between future observing runs of the LVK network, planned upgrades to the network, and new generations of instruments, we can expect gravitational wave astronomy to continue to blossom as a field.

The work presented in this thesis focused on maximising scientific returns from several fields related to gravitational wave astronomy. A lot of work remains to be done to fully take advantage of the data that will come out of future observing runs by the LVK network. In particular, this work has applications for gravitational wave cosmology. Here we will summarise the main results of the work presented in the previous chapters.

In chapters 3 to 5, we presented a framework for parameter estimation on kilonova light curves, presented results for recovering the merger time t_0 of a binary neutron star merger from incomplete light curves, and investigated the effect of neglecting some kilonova microphysics on the recovered parameters. Joint detections of compact binary coalescences and kilonovae are an extremely powerful tool for gravitational wave cosmology. While only one such bright siren has been detected to date, it dominates the current H_0 posterior obtained from the analysis of all detected standard sirens. It is therefore essential to maximise prospects for these joint detections, and to accurately infer the source's parameters.

The framework introduced in chapters 4 and 5 applied a methodology presented in chapter 3 for parameter estimation on kilonova light curves. In this chapter, we showed that Gaussian Processes are a useful tool for interpolating kilonova light curves from an existing set of models generated for a finite parameter grid. Realistic simulations of kilonovae are computationally expensive to generate, and research on model interpolation is an active field. The models used in this work are one dimensional, two component models, but the pipeline could be extended to future models.

We applied this framework to real data and obtained posteriors for the ejecta parameters of AT 2017gfo from the DECam observations in the *griz* bands. The recovered ejecta parameters were found to be in good agreement with other studies using the same models.

Results presented in chapter 4 focused on the recovery of a posterior on the merger time of a binary neutron star system from serendipitous, late time kilonova observations. We showed the importance of prompt, high cadence follow-ups for kilonovae. The most important aspect of recovering information on the merger time t_0 of a BNS was the cadence of the search. Obtaining a time window for a potential BNS could open the way for GW searches from serendipitous discoveries of kilonovae and maximise prospects for multi-messenger astronomy. This could also help link potential EM counterparts to sub-threshold or one-detector GW candidates. The results support previous work on optimal cadences that proposed nightly observations in wide surveys.

In chapter 5, we showed the importance of accurately modelling jet-ejecta interaction in kilonova light curves. The recovered ejecta mass from the kilonova m_{ej} could be overestimated by up to a factor of ~ 2 where the impact of a strong jet is neglected. The ejecta mass m_{ej} is related to the parameters of the BNS system and to the neutron star equation of state; it is therefore important to accurately infer this parameter.

The work presented in chapters 4 and 5 is, however, very model-dependent. Kilonova modelling is a very active field of research, and models will certainly by refined in the future as more detections are made. The principles of the pipeline can be applied to future models, incorporating more parameters.

In chapter 6, we presented results for the Hubble constant H_0 after implementing a rigorous treatment of galaxy catalogue completeness into the current pipeline for cosmology with dark sirens. While the final result on the GWTC-3 analysis was not improved by this method, improvements could be seen in the GWTC-1 analysis, when a deeper band of the GLADE and GLADE+ galaxy catalogues was used. This shows the importance of the careful treatment of galaxy catalogue incompleteness as they become deeper, and as more gravitational wave events are detected.

The GWTC-1 results using the B-band of the GLADE+ catalogue gave
$H_0 = 69.3^{+17}_{-8}$ km s^{-1} Mpc^{-1} when combining the dark sirens with GW170817, and
$H_0 = 67.4^{+36}_{-24}$ km s^{-1} Mpc^{-1} when considering only dark sirens. This is, respectively, a 5.1% and 7.1% improvement on the results using the median magnitude as the magnitude threshold.

While the inference of H_0 from standard sirens still relies heavily on bright sirens, with current measurements of H_0 being dominated by the posterior obtained from GW170817, dark sirens still provide an important contribution to the final posterior. This is especially true of well-localised, nearby dark sirens that could have strong galaxy catalogue support.

In past mock data challenges, a sample of ~250 injected binary neutron stars with no counterpart resulted in in a 2.21% uncertainty on the Hubble constant for a galaxy catalogue with an apparent magnitude threshold of 19.5, and 3.20 % for an apparent magnitude threshold of 16. For a complete catalogue, this uncertainty went down to 1.84%. [224] The completeness of the galaxy catalogue used for future gravitational wave catalogues will therefore be an important part of placing tighter constraints on H_0 from dark sirens.

The work presented in chapter 6 showed promising results, but future work will need to focus on applying the robust test of completeness to mock data challenges in order to quantify any potential systematics that the method would introduce.

The final chapter of this thesis presented results from a Newtonian calibrator that was prototyped at the LIGO Hanford detector in 2019. Calibrating the LIGO detectors is also an important aspect of gravitational wave cosmology, since without accurate calibration, an accurate luminosity distance cannot be obtained from GW waveforms. As the number of gravitational wave detections increases in upcoming runs, the impact of calibration uncertainties and unknown systematics could become greater, especially in fields like cosmology. [264]

Results from the first Newtonian calibrator prototype constrained the predicted force to $< 1\%$ relative uncertainty, which is a promising start for the LIGO NCal. The work presented in this thesis also outlines the importance of treating uncertainties in the modelling of force coefficients carefully.

The NCal was driven again on 3 September 2020 in nominal low noise. While it will not replace the PCal system, it could serve as a supplementary absolute reference for calibration. The calibration work started in 2019 with the NCal prototype is still ongoing, with plans to combine NCal calibration with PCal, and to improve the NCal set-up for increased accuracy. One such proposed set-up would use four smaller rotors placed around the end test mass. This set-up would improve the estimate on the distance of the NCal to the test mass, which is the main contributor to the current uncertainty on the predicted force from the system. The KAGRA and Virgo detectors also use gravitational calibrators, and there are ongoing developments to the technology.

The different chapters of this thesis all presented ways to maximise scientific returns for multi-messenger astronomy and gravitational wave cosmology. Future precise standard siren measurements of H_0 could help us understand whether or not discrepancies in current measurements of the Hubble constant indicate the presence of new physics. With the Hubble tension having recently passed the 5σ threshold, now is a crucial time for precision cosmology with gravitational waves.

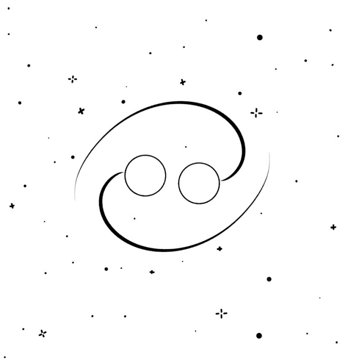

A | Wind Fence

This chapter summarises work that was carried out at LIGO Hanford during the Summer of 2019. This analysis was done in the context of a potential installation of a wind fence around the end stations of the LIGO detector. The original work can be found in the LIGO technical note that was posted to the LIGO Document Control Center (DCC). Several logs in the publicly accessible aLIGO LHO Logbook also summarise some of this work. [265–267] The wind fence installation started during the commissioning break between O3a and O3b, in October 2019 and was completed in December of the same year, during O3b.

Figure A.1: The wind fence at one of the end stations at LIGO Hanford. Photo credit: Corey Gray

A.1 Background

The duty cycles of the LIGO interferometers are affected by environmental factors such as earthquakes, thunder, and high winds. [268] Unlike LLO, when it comes to windy weather, LHO does not benefit from the protective effect of trees. Its shrub-steppe environment leaves the detector exposed to high winds, and gusts of wind can affect the alignments of its optics. The induced wind-tild cannot be separated from ground movement.

We looked at the impact of wind gusts on the observing range and duty cycle of LHO during the first two months of O3a at all three stations.

This analysis looks at the impact of wind speed at all three stations on the observing range for binary neutron stars and the interferometer duty cycle at LIGO Hanford during the first two months of O3. The wind speed, lock and range data analysed is obtained from the following channels:

`H1:PEM-EX_WIND_ROOF_WEATHER_MPH`
`H1:PEM-EY_WIND_ROOF_WEATHER_MPH`
`H1:PEM-CS_WIND_ROOF_WEATHER_MPH`
`H1:GRD-ISC_LOCK_STATE_N`
`H1:CDS-SENSMON_CAL_SNSW_EFFECTIVE_RANGE_MPC`

The first three channels record the wind speed at the three stations (End Station X, End Station Y and the Corner Station) while the other two give information about the lock state of the interferometer and its BNS observing range.

Data was obtained for GPS times 1238166018 (1 April 2019 15:00:00 UTC) to 1243566018 (3 June 2019 03:00:00 UTC). All data is obtained for maximum minute trends.

A.2 Wind Speed Data

The wind speed considered in this analysis is the maximum wind speed out of all three stations (End X, End Y and Corner Station) as measured by the wind sensors on the roof. We use maximum trends for the wind speed, as we want to account for the impact of gusts of wind, rather than sustained wind speed. Directionality of the wind is ignored for the purpose of this analysis. Other analyses focusing on the directionality of the wind during O3 have been carried out and are available on the LIGO DCC.

A.3 Duty Cycles

In the first part of the analysis, we look at the impact of wind speed on duty cycles. We use `H1:GRD-ISC_LOCK_STATE_N` for the lock status data, using 600 as the locked state. The average duty cycle for the first two months of O3 is **74.2%**.

Hourly maximum trends are considered for the wind speed. The maximum wind speed from all three stations is considered. Lock status is for one minute stretches (maximum minute trend). The wind hourly trends are obtained by using pandas' `pd.DataFrame.rolling(window=x).max()` on the wind speeds.

A.3.1 Hourly wind distributions

Table A.1 shows wind speed percentiles for the first two months of O3. The full distribution is plotted in blue in figure A.6.

percentile	**5**	**10**	**20**	**30**	**40**	**50**	**60**	**70**	**80**	**90**	**95**	**99**
wind speed [mph]	7	8	10	12	14	16	18	21	24	28	33	43

Table A.1: Wind speed percentile values for first two months of O3, maximum hour trends.

A.3.2 Duty cycle as a function of wind speed

The duty cycle at LHO shows a strong wind-dependence during the first two months of O3. Figure A.2 shows a histogram of duty cycles per percentile. Figure A.3 shows the same data plotted in a different way, with duty cycle as a function of wind speed quantile. Wind speed values for each percentile are defined in table A.1. Figures A.4 and A.5 show the duty cycle as a function of wind speed for the first two months of O3 and for all of O2. Comparing the results for O3 to the ones for O2, there is a much stronger wind-dependence during O3 for duty cycles.

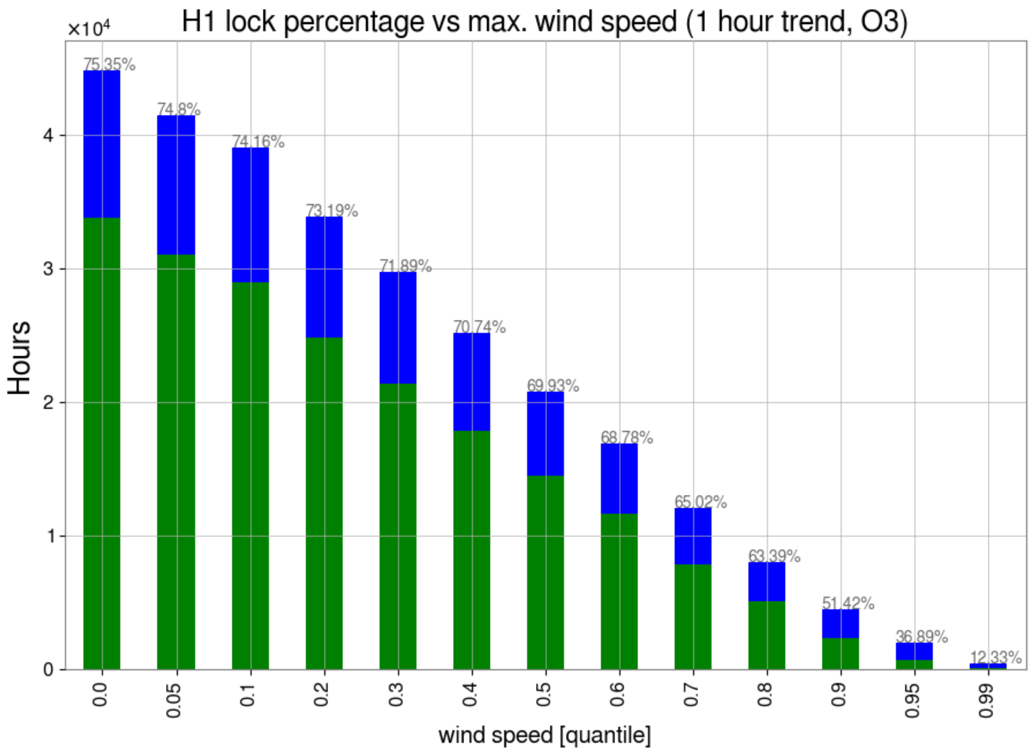

Figure A.2: Histogram of duty cycle as a function of wind speed quantile. Green is for time locked, blue is unlocked.

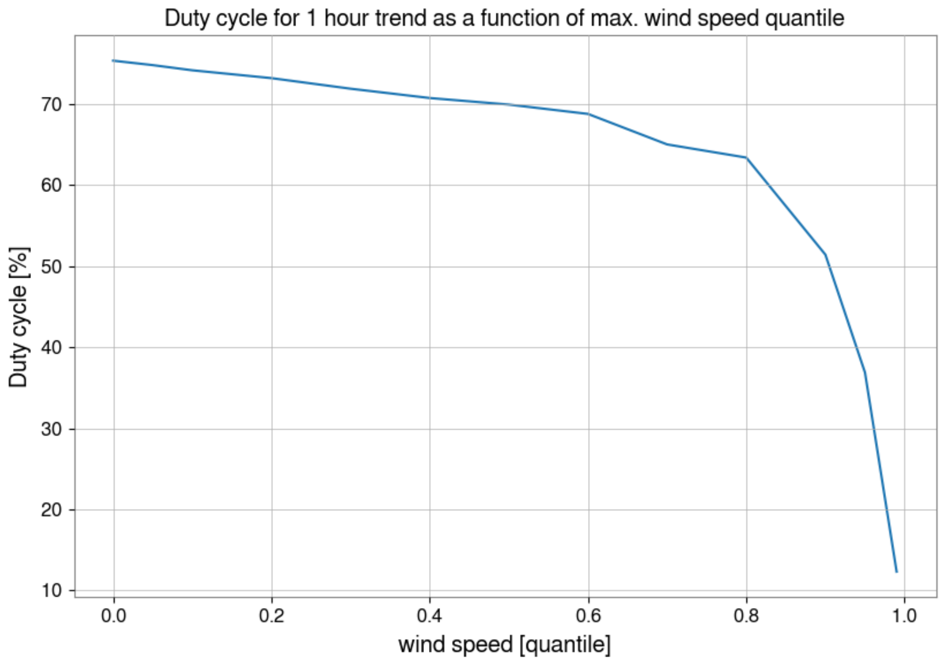

Figure A.3: Duty cycle as a function of wind speed quantile for the first two months of O3.

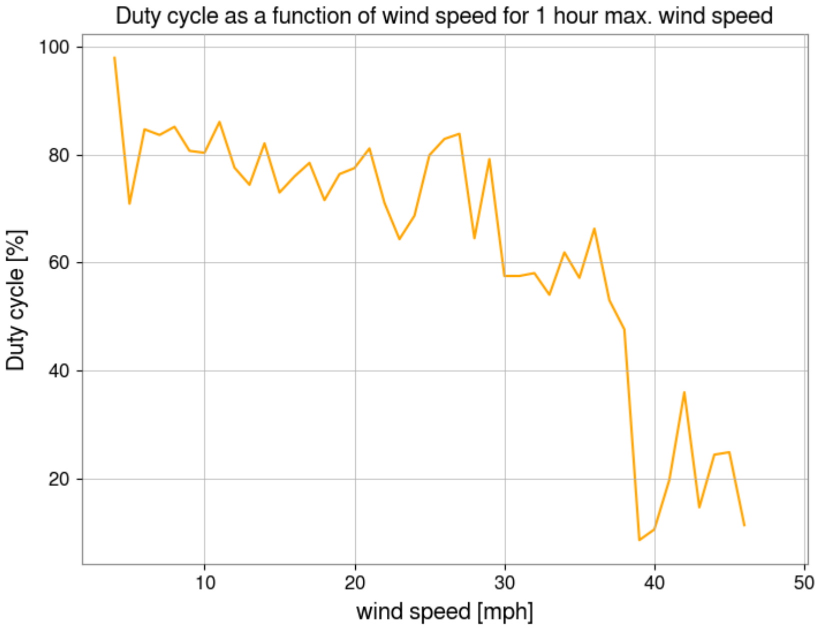

Figure A.4: Duty cycle as a function of wind speed for the first two months of O3.

In order to get the improvement in duty cycle , we approximate the duty cycle to the average duty cycle during low wind conditions. This ranges from **78.9%** (0-20mph, 70th percentile) to **84.1%** (0-7mph, 5th percentile) depending on how low wind conditions are defined.

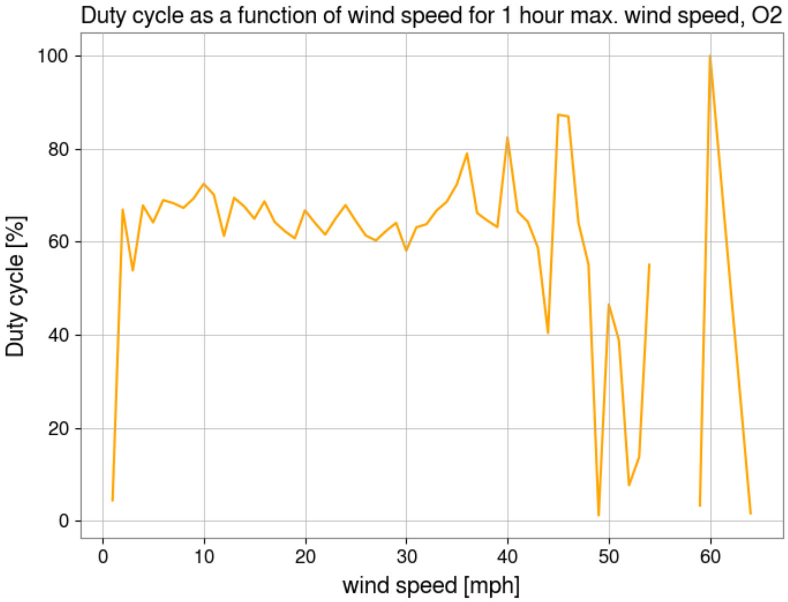

Figure A.5: Duty cycle as a function of wind speed for O2.

Another way to get the wind-independent duty cycle is to obtain the duty cycle for a wind distribution where all wind speeds are halved, to simulate the effects of a wind fence at both end stations. In order to do this, the wind speeds in the original distribution are halved, and the new distribution is convolved with the duty cycle as a function of wind speed. The resulting wind-independent duty cycle using this method is **81.6%**. Since we are dividing wind speeds by 2, there is no corresponding average duty cycle for hourly maximum wind speeds below 3mph. This is therefore taken to be equal to the average duty cycle for 3mph. The numbers remain approximate, as results may slightly differ depending on binning of wind data, length of trends used, etc.

Repeating this method on O2 data gives a wind-independent duty cycle of 66.8%, a 0.9% improvement from a baseline of 65.9%.

A.3.3 Wind speed and lockloss

We look at wind speeds around the time of lockloss. Figure A.6 shows the normalised distribution of wind speeds for all times against the normalised distribution of wind speeds when lock is lost. There is a significant tail above 30mph for the lockloss distribution. Figures A.7 and A.8 shows similar distributions for one minute and five minute maximum trends. While not as relevant for duty cycles, this distribution is used for BNS range.

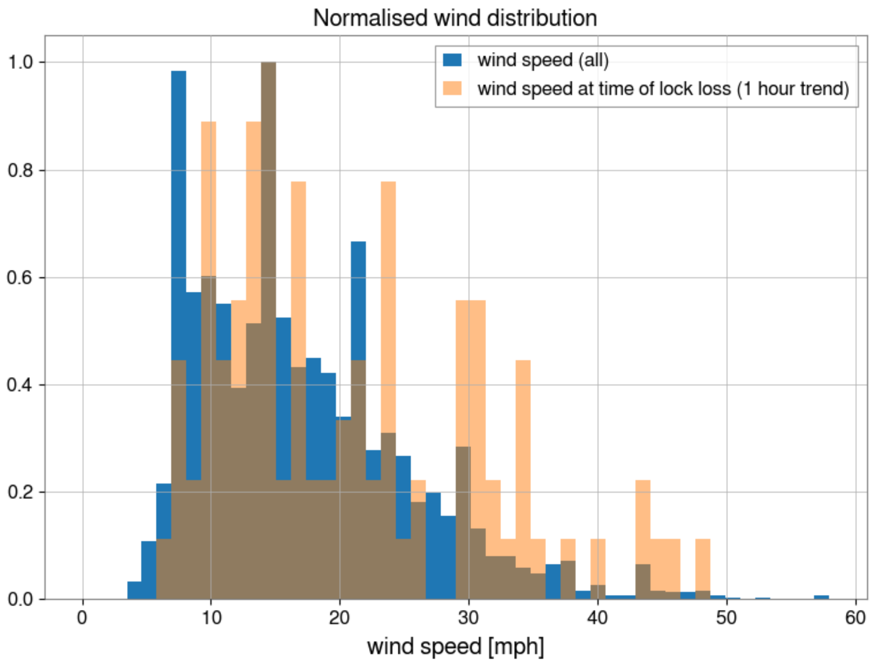

Figure A.6: Normalised ind speed distribution for all times (blue) and at instant of lockloss (orange), one hour maximum trend.

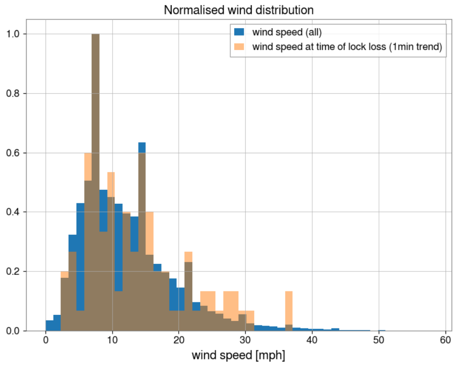

Figure A.7: Wind speed distribution for all times (blue) and at instant of lockloss (orange), one minute maximum trend.

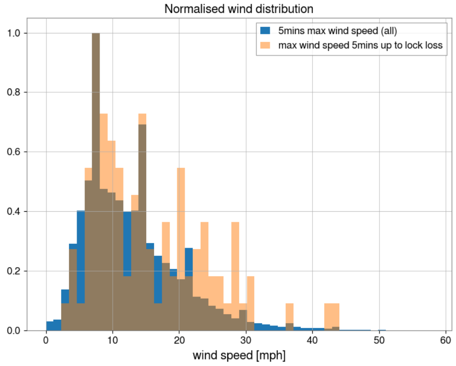

Figure A.8: Wind speed distribution for all times (blue) and at instant before lockloss (orange), 5min maximum trend.

A.4 BNS Range

The second part of this analysis looks at the impact of wind speed on BNS range while the interferometer is locked. Maximum minute trends instead of hourly trends are considered for this. The data is obtained from the output channel

`H1:CDS-SENSMON_CAL_SNSW_EFFECTIVE_RANGE_MPC`. Some unusual data points need to be discarded before starting the analysis as they record the range as being around 4000Mpc.

A.4.1 Minute maximum wind speed distribution

Figure A.2 shows the wind speed percentiles across all stations for maximum minute trends. The full distribution is in blue in figure A.7.

percentile	**5**	**10**	**20**	**30**	**40**	**50**	**60**	**70**	**80**	**90**	**95**	**99**
wind speed [mph]	4	5	6	8	9	11	12	14	17	21	25	35

Table A.2: Wind speed percentile values for first two months of O3, maximum minute trends.

A.4.2 Seasonal wind changes

Concerns have been raised over the use of the O3 wind distribution as the wind speed distribution to be convolved with the data to estimate potential improvements, as the first two months of O3 occurred during the "windy season". However the distribution is similar to wind distributions from O2.

percentile	**5**	**10**	**20**	**30**	**40**	**50**	**60**	**70**	**80**	**90**	**95**	**99**
wind speed [mph] (hour trend, O3)	7	8	10	12	14	16	18	21	24	28	33	43
wind speed [mph] (hour trend,O2)	5	6	8	9	11	13	15	19	22	28	33	43
wind speed [mph] (minute trend,O3)	4	5	6	8	9	11	12	14	17	21	25	35
wind speed [mph] (minute trend,O2)	3	4	5	6	7	9	11	13	16	21	25	33

Table A.3: Wind speed percentile values for O2 and O3.

A.4.3 BNS range as a function of wind speed

Figures A.10 to A.12 show the effect of wind speed on the BNS range. There is a wind-dependence, although it is not as marked as with duty cycles. Figures A.10 and A.12 inform us on the impact of wind based on the wind distribution. The dramatic drop in BNS range seen in figure A.9 occurs mostly at low-probability high winds.

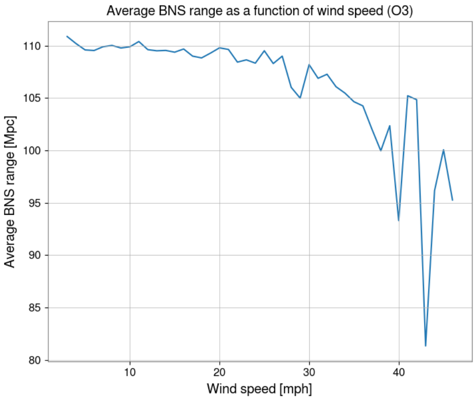

Figure A.9: Average BNS range as a function of wind speed.

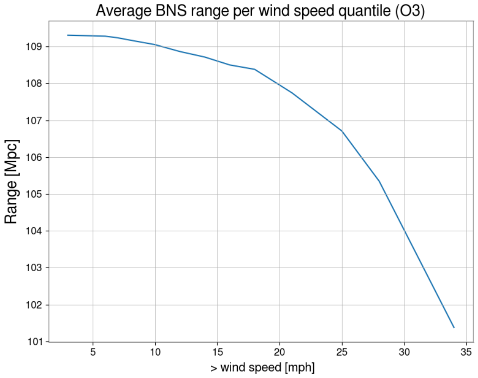

Figure A.10: Average BNS range as a function of wind speed quantile.

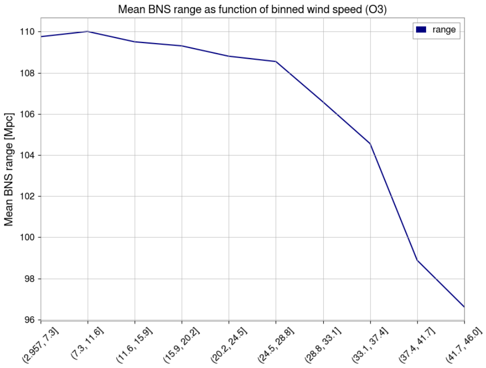

Figure A.11: Range per binned wind speed, for equal bins

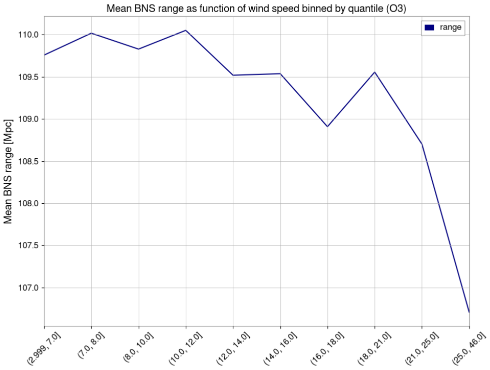

Figure A.12: Range per binned wind speed, for bins of equal probability

A.4.4 Improvement to BNS range if wind-independent

In order to get the improvement to BNS range if wind-independent we approximate the BNS range vs wind function to its value in low wind conditions (0-4mph).

Considering only wind at EX and EY, the improvement is **0.454Mpc**, or **1.48%** in detections based on improvement in observing volume.

Considering the maximum wind speed for all stations, the improvement is **0.46Mpc**, or **1.01%** in detections based on improvement in observing volume.

Using the method described in section A.3.2 and halving all wind speeds in the distribution, the improvement is **0.67Mpc**, or **1.85%** in detections based on improvement in observing volume.

A.5 Results Summary

Table A.4 presents a summary of improvements. While the improvement in BNS range is very modest, duty cycles could be significantly improved by being wind-independent.

	Average BNS range [Mpc]	Average duty cycle [%]
Current	109.31Mpc	74.2%
Wind-independent	109.77 to 109.85Mpc	78.9 to 84.1%
Improvement	**0.46** to **0.67Mpc**, **1.01** to **1.65%** in detections	**4.7** to **9.9%**

Table A.4: Summary of improvements from wind-independent duty cycle and BNS range.

A.6 O3b Results

Between O3a and O3b, the wind fence was commissioned and installed at the two end stations of the LIGO Hanford detector. We run the analysis above on the O3b data, using the wind speed measured at the corner station as the maximum wind speed for the site in order to measure the effect of the wind fence. We see in figure A.15 that the distribution of wind speeds at the time of lockloss no longer has the characteristic tail at higher wind speeds seen in the O3a data.

We also find that the duty cycles have improved during O3b, averaging $\sim\mathbf{83\%}.Thisisclosetothepredic$
$independentdutycycles.$

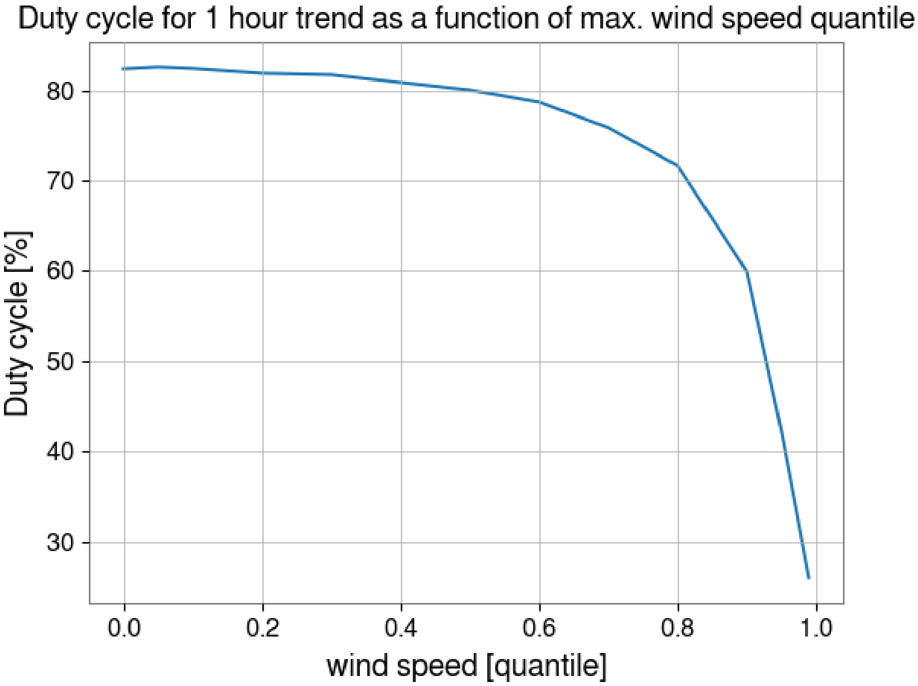

Figure A.13: Duty cycle as a function of maximum wind speed quantile for O3b.

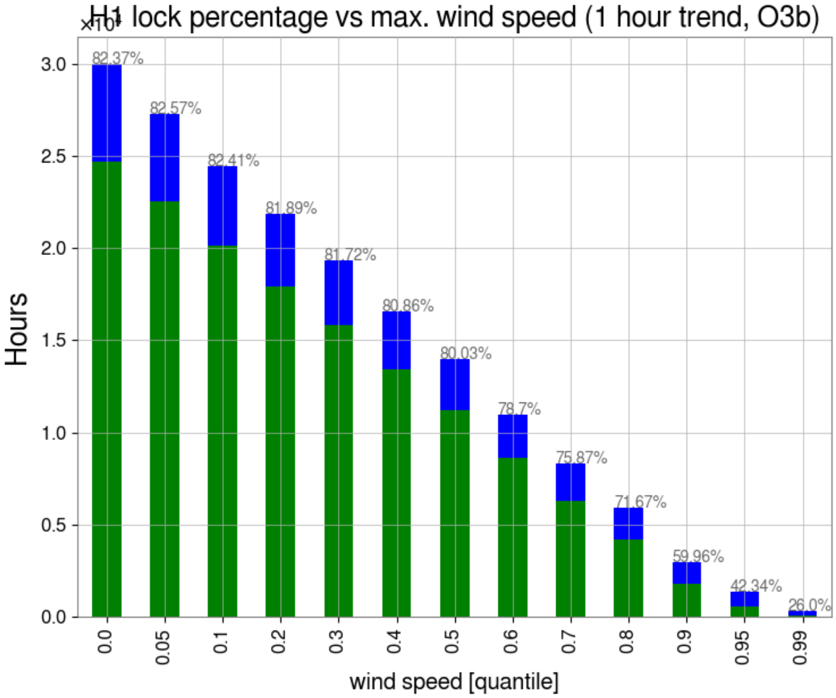

Figure A.14: Histogram of duty cycle as a function of wind speed quantile for O3b, using maximum wind speeds at the corner station. Green is for time locked, blue is out of lock.

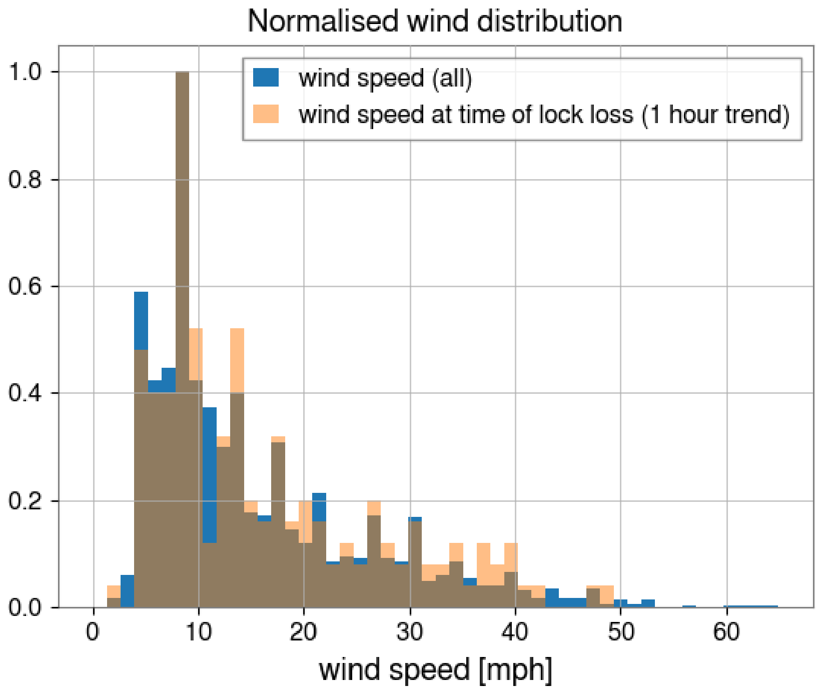

Figure A.15: Wind speed distribution for all times (blue) and during lockloss (orange) during O3b, 1hour maximum trend.

A.7 Relevant Links

The research presented here is summarised in the following LHO logbook entries:

- alog 50072 [267]
- alog 49682 [266]
- alog 49542 [265]

B | Supplementary Material for Chapter 4

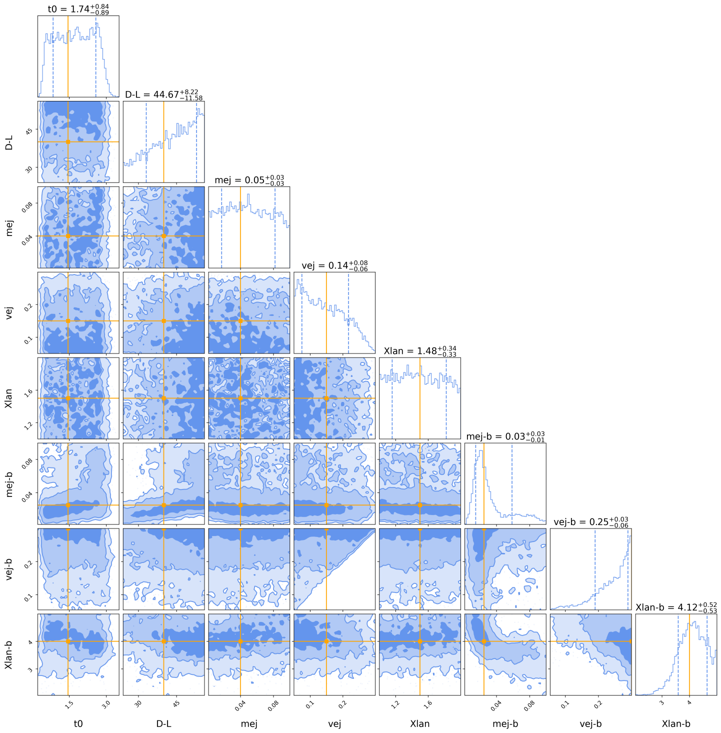

Figure B.1: Full parameter estimation for *gi* bands on AT 2017gfo DECam observations, with a starting time t_0 1.45 days post-merger. Real values for ejecta parameters are taken from Kasen(2017) [94]. True d_L taken to be 40 Mpc.

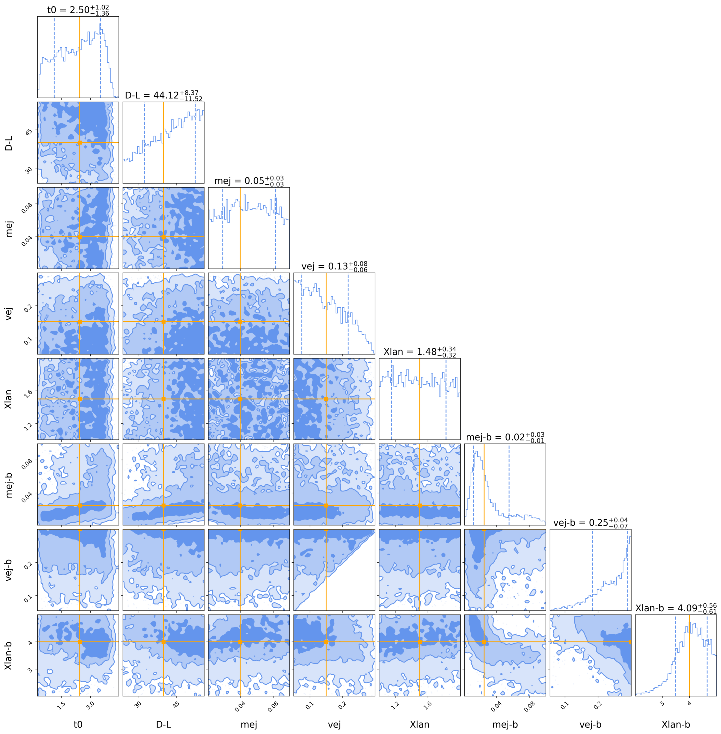

Figure B.2: Full parameter estimation for *gi* bands on AT 2017gfo DECam observations, with a starting time t_0 2.45 days post-merger. Real values for ejecta parameters are taken from Kasen(2017) [94]. True d_L taken to be 40 Mpc.

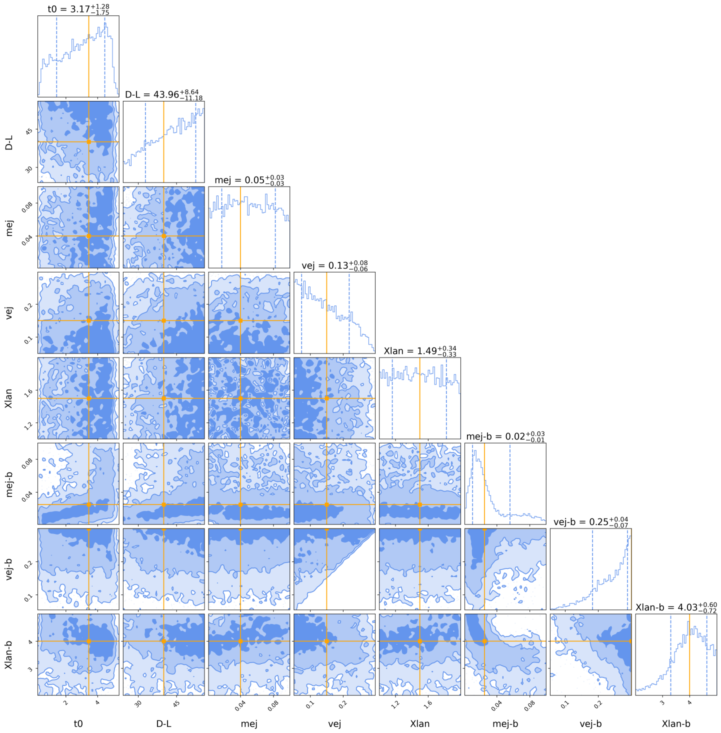

Figure B.3: Full parameter estimation for *gi* bands on AT 2017gfo DECam observations, with a starting time t_0 3.45 days post-merger. Real values for ejecta parameters are taken from Kasen(2017) [94]. True d_L taken to be 40 Mpc.

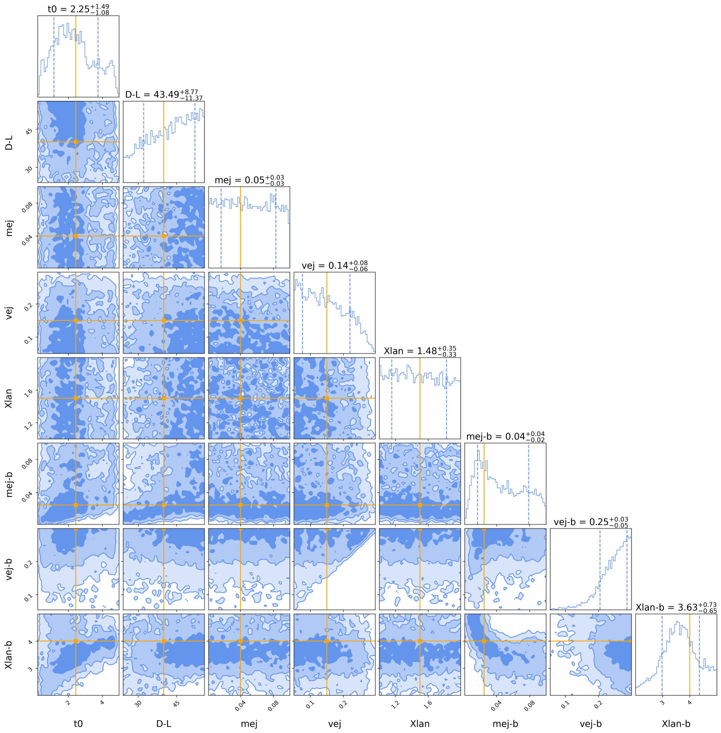

Figure B.4: Full parameter estimation for *gr* bands on AT 2017gfo DECam observations, with a starting time t_0 2.45 days post-merger. Real values for ejecta parameters are taken from Kasen(2017) [94]. True d_L taken to be 40 Mpc.

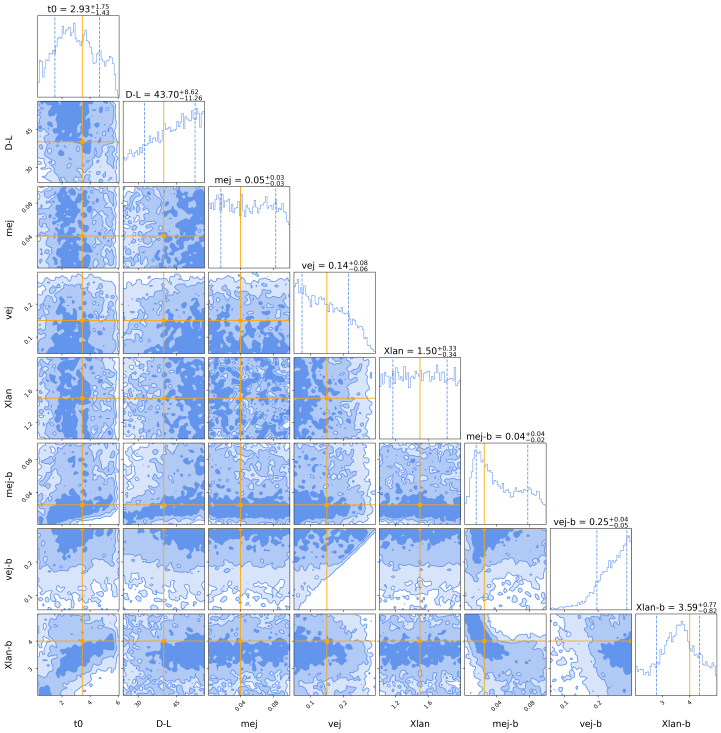

Figure B.5: Full parameter estimation for *gr* bands on AT 2017gfo DECam observations, with a starting time t_0 3.45 days post-merger. Real values for ejecta parameters are taken from Kasen(2017) [94]. True d_L taken to be 40 Mpc.

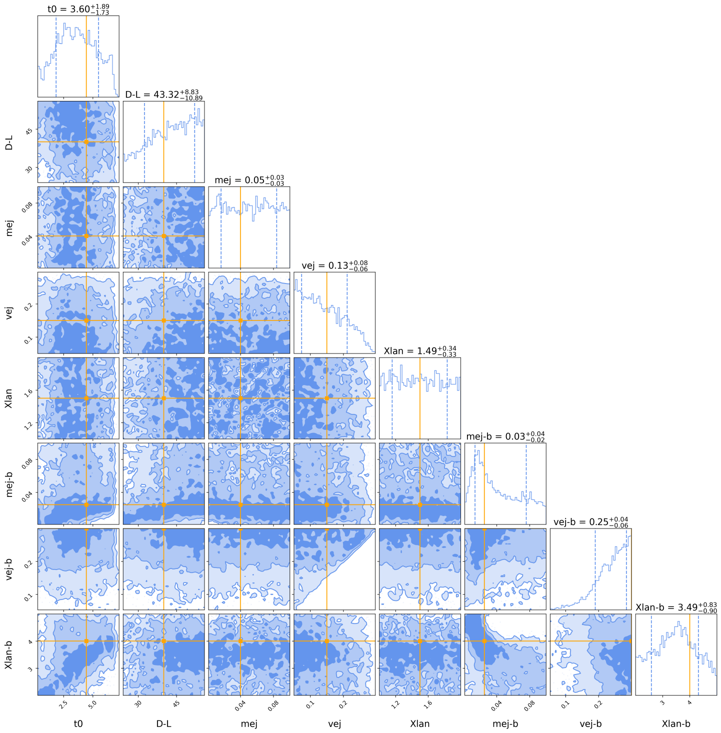

Figure B.6: Full parameter estimation for *gr* bands on AT 2017gfo DECam observations, with a starting time t_0 4.45 days post-merger. Real values for ejecta parameters are taken from Kasen(2017) [94]. True d_L taken to be 40 Mpc.

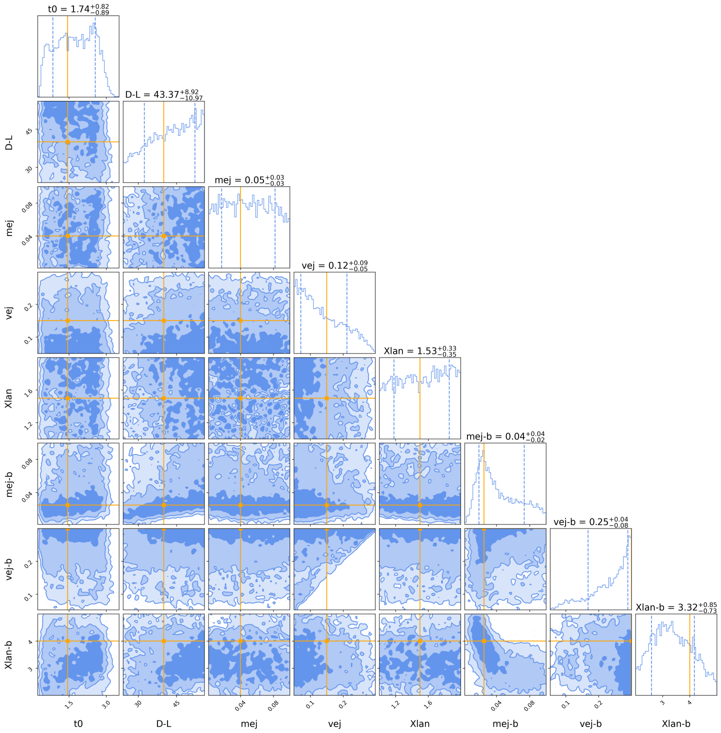

Figure B.7: Full parameter estimation for *ri* bands on AT 2017gfo DECam observations, with a starting time t_0 1.45 days post-merger. Real values for ejecta parameters are taken from Kasen(2017) [94]. True d_L taken to be 40 Mpc.

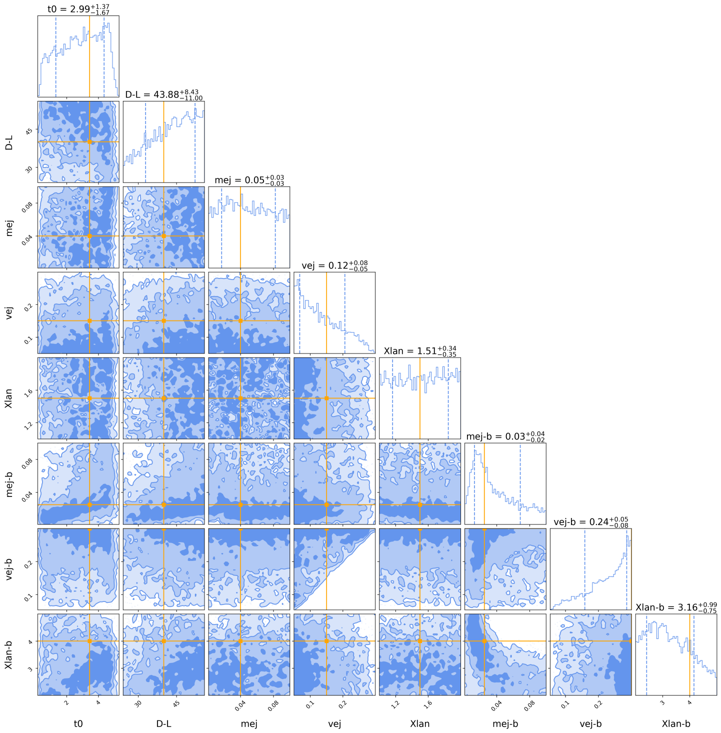

Figure B.8: Full parameter estimation for *ri* bands on AT 2017gfo DECam observations, with a starting time t_0 3.45 days post-merger. Real values for ejecta parameters are taken from Kasen(2017) [94]. True d_L taken to be 40 Mpc.

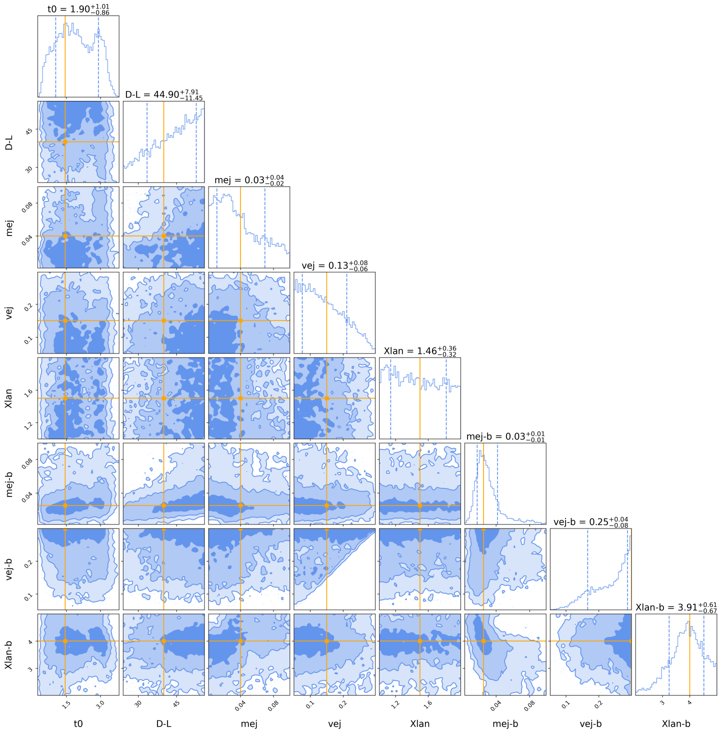

Figure B.9: Full parameter estimation for *rz* bands on AT 2017gfo DECam observations, with a starting time t_0 1.45 days post-merger. Real values for ejecta parameters are taken from Kasen(2017) [94]. True d_L taken to be 40 Mpc.

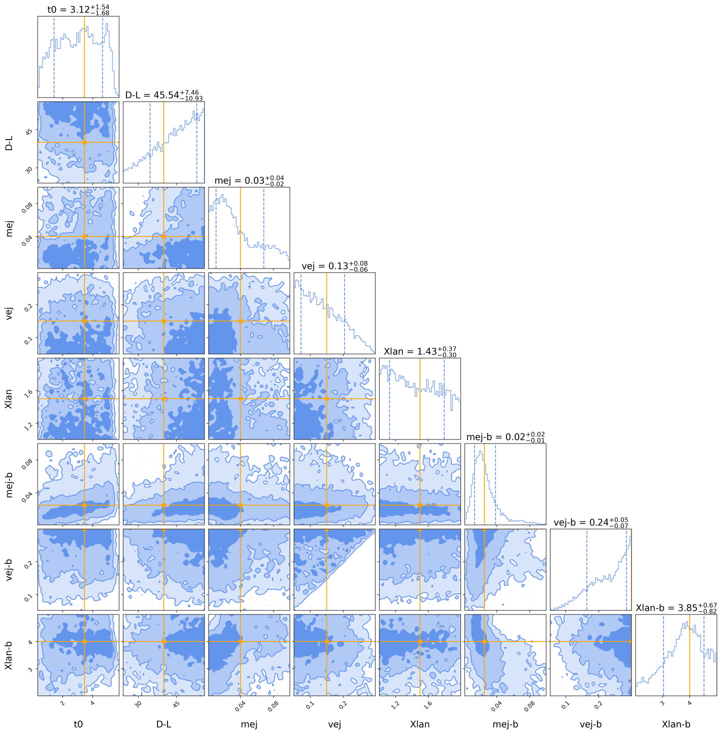

Figure B.10: Full parameter estimation for *rz* bands on AT 2017gfo DECam observations, with a starting time t_0 3.45 days post-merger. Real values for ejecta parameters are taken from Kasen(2017) [94]. True d_L taken to be 40 Mpc.

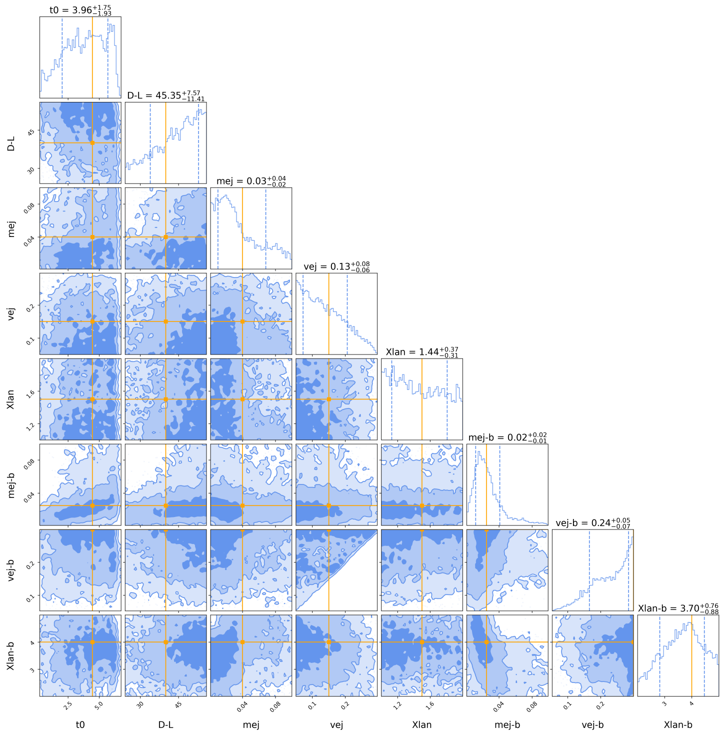

Figure B.11: Full parameter estimation for *rz* bands on AT 2017gfo DECam observations, with a starting time t_0 4.45 days post-merger. Real values for ejecta parameters are taken from Kasen(2017) [94]. True d_L taken to be 40 Mpc.

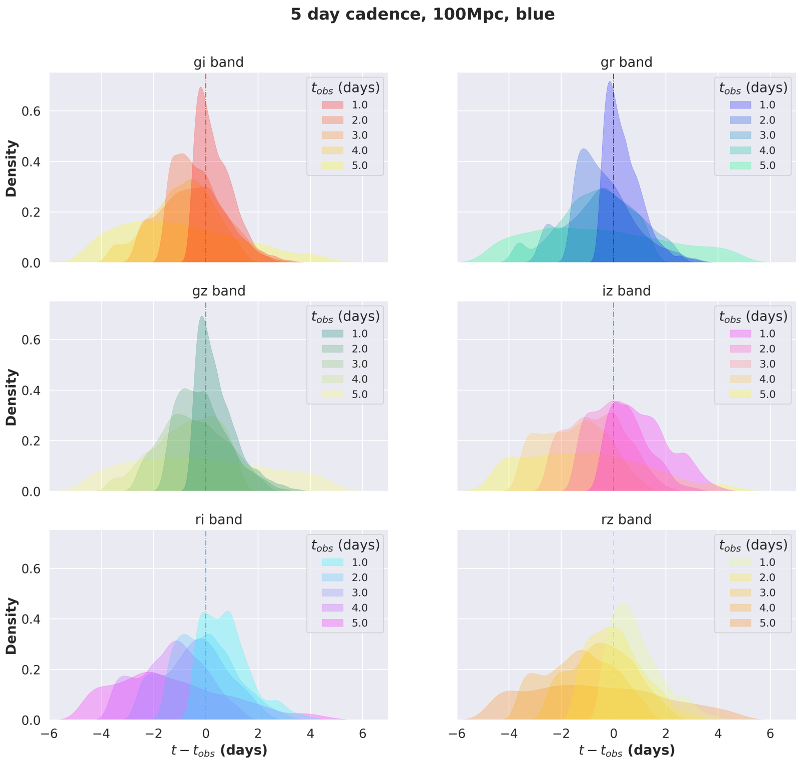

Figure B.12: Results on t_0 for the "blue" kilonova, with a 5 day cadence at 100 Mpc.

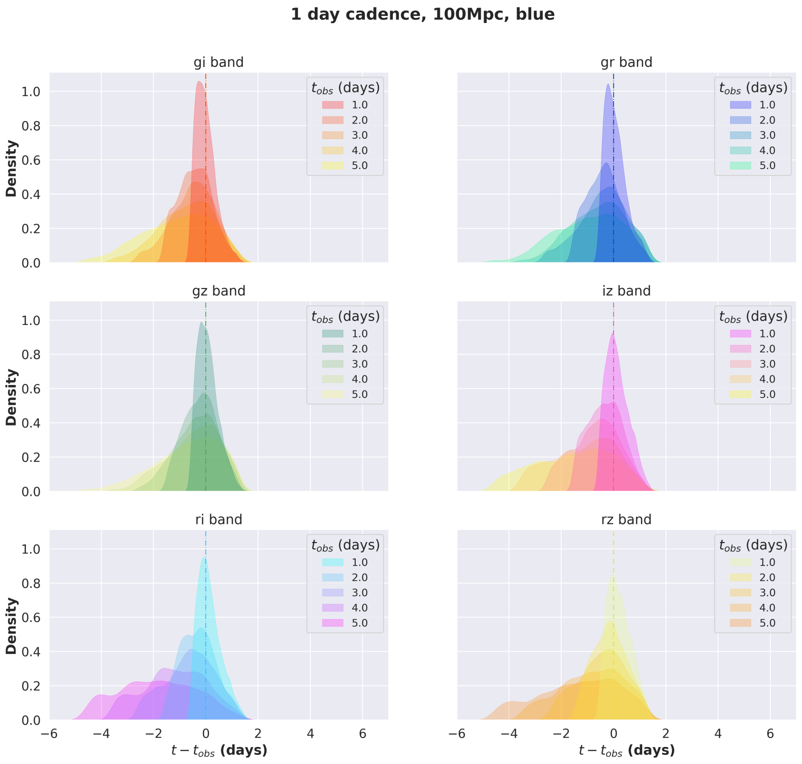

Figure B.13: Results on t_0 for the "blue" kilonova, with a 1 day cadence at 100 Mpc.

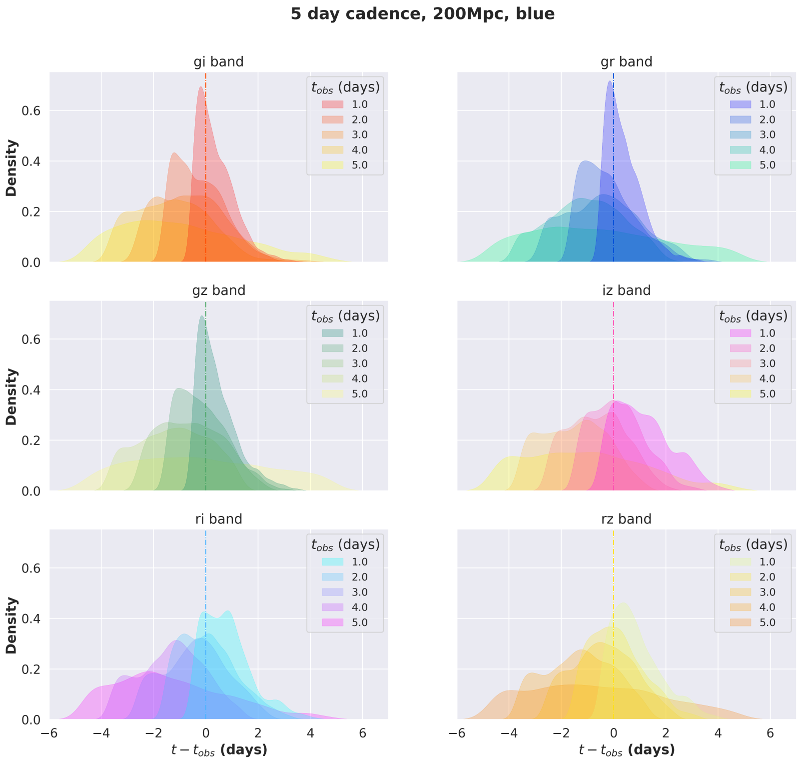

Figure B.14: Results on t_0 for the "blue" kilonova, with a 5 day cadence at 200 Mpc.

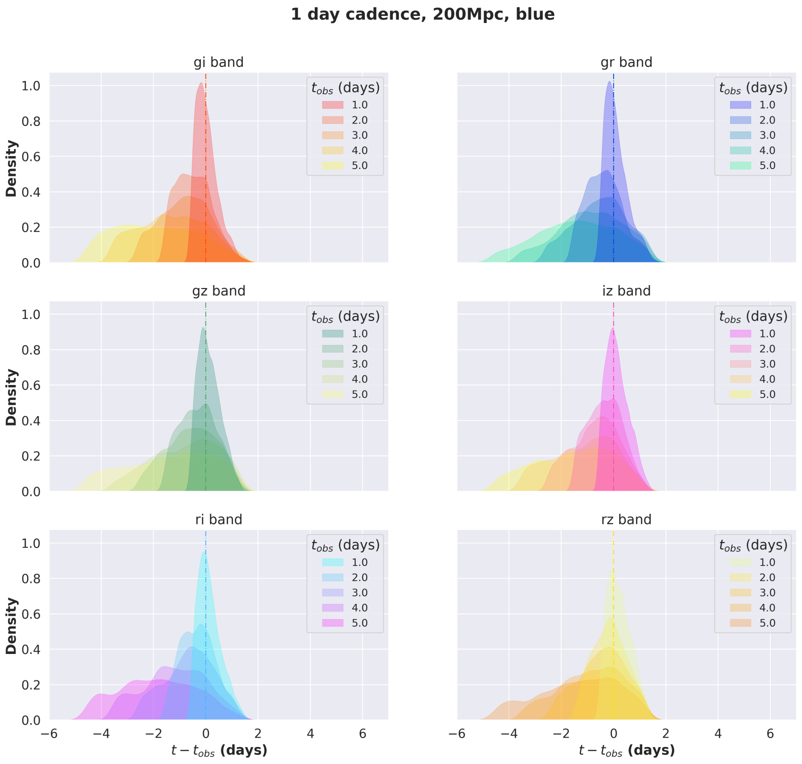

Figure B.15: Results on t_0 for the "blue" kilonova, with a 1 day cadence at 200 Mpc.

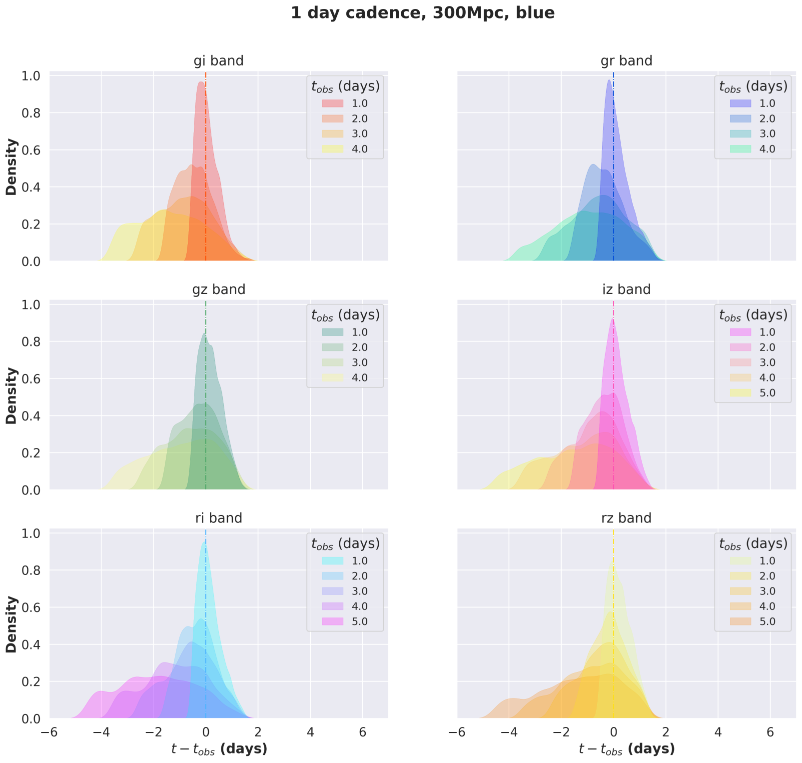

Figure B.16: Results on t_0 for the "blue" kilonova, with a 1 day cadence at 300 Mpc.

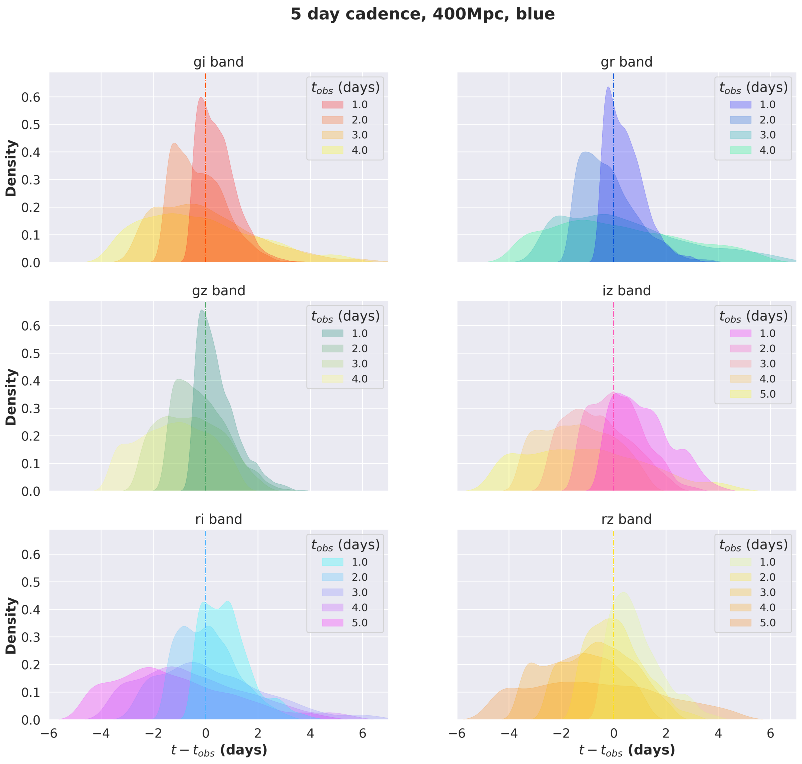

Figure B.17: Results on t_0 for the "blue" kilonova, with a 5 day cadence at 400 Mpc.

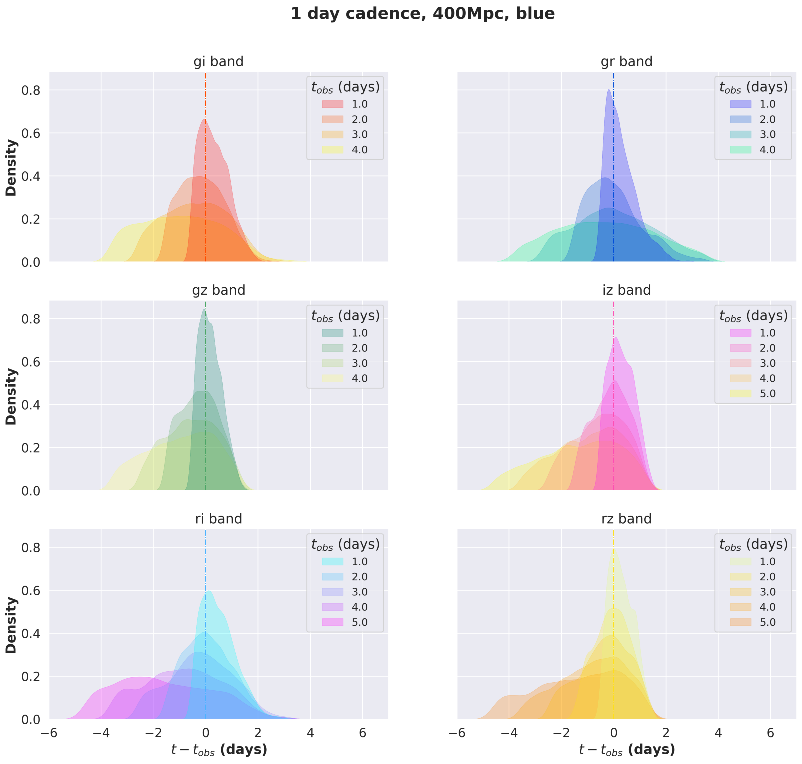

Figure B.18: Results on t_0 for the "blue" kilonova, with a 1 day cadence at 400 Mpc.

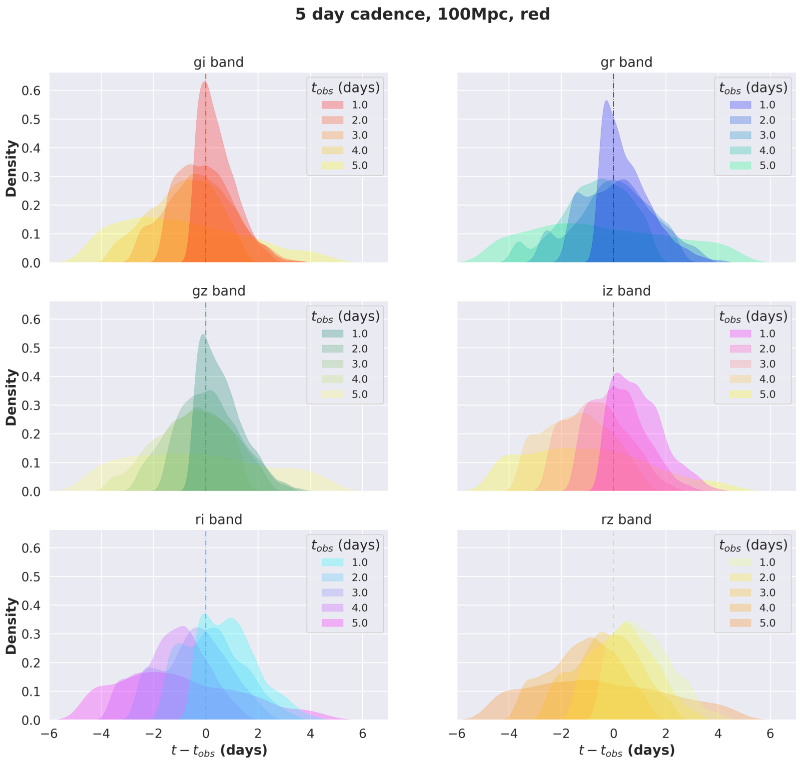

Figure B.19: Results on t_0 for the "red" kilonova, with a 5 day cadence at 100 Mpc.

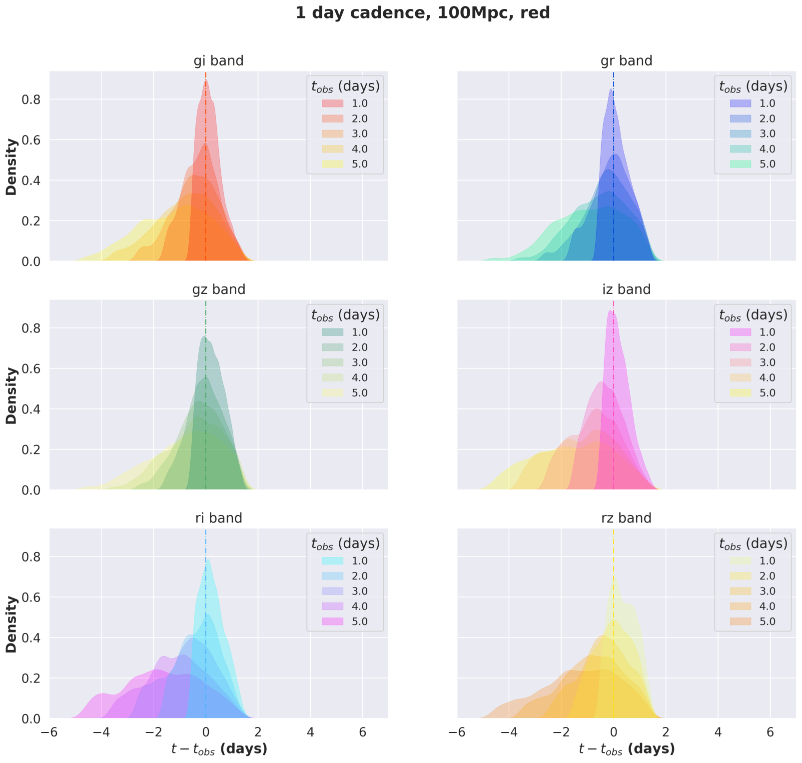

Figure B.20: Results on t_0 for the "red" kilonova, with a 1 day cadence at 100 Mpc.

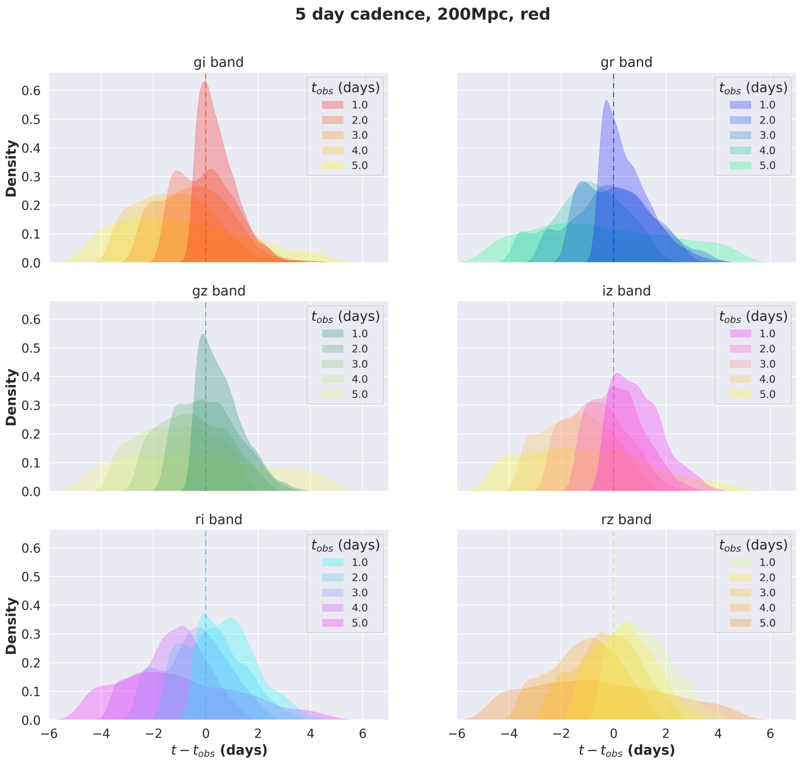

Figure B.21: Results on t_0 for the "red" kilonova, with a 5 day cadence at 200 Mpc.

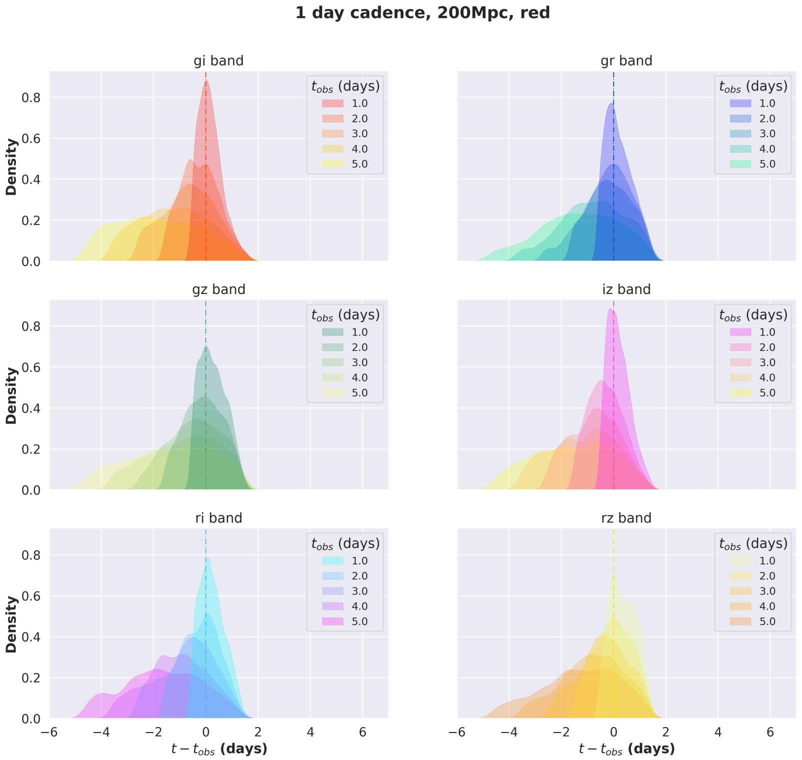

Figure B.22: Results on t_0 for the "red" kilonova, with a 1 day cadence at 200 Mpc.

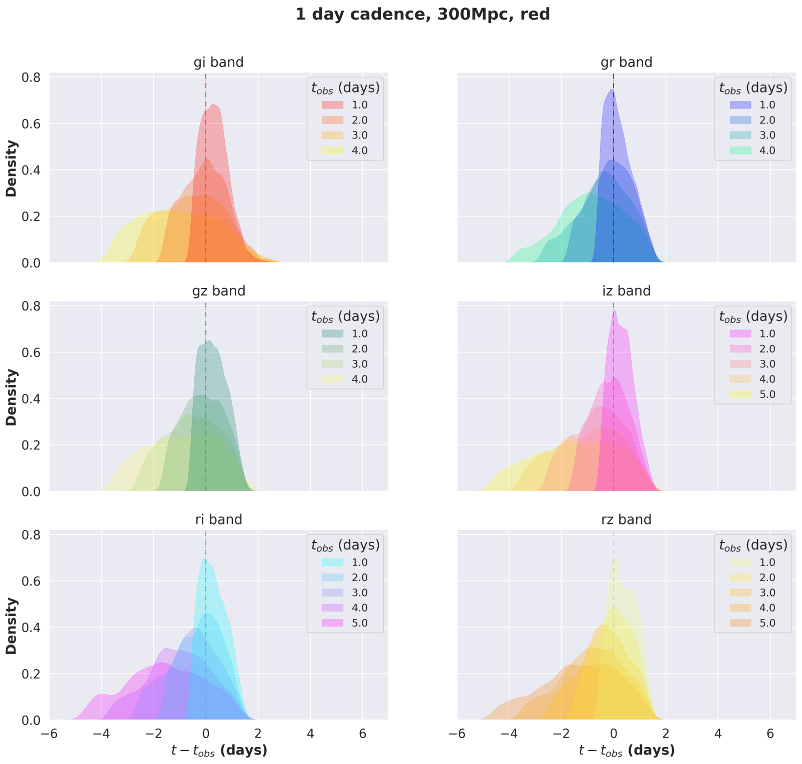

Figure B.23: Results on t_0 for the "red" kilonova, with a 1 day cadence at 300 Mpc.

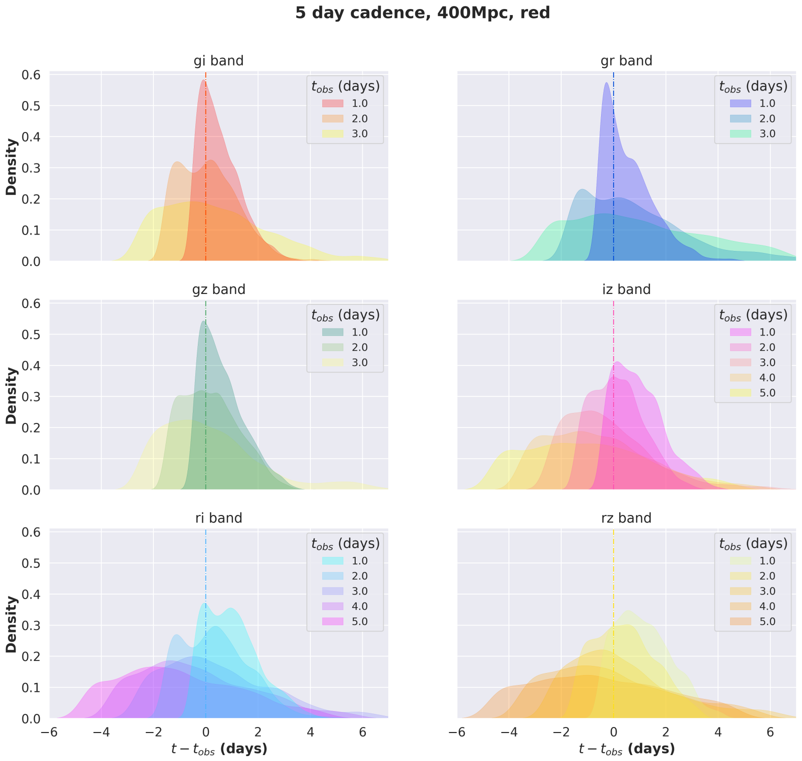

Figure B.24: Results on t_0 for the "red" kilonova, with a 5 day cadence at 400 Mpc.

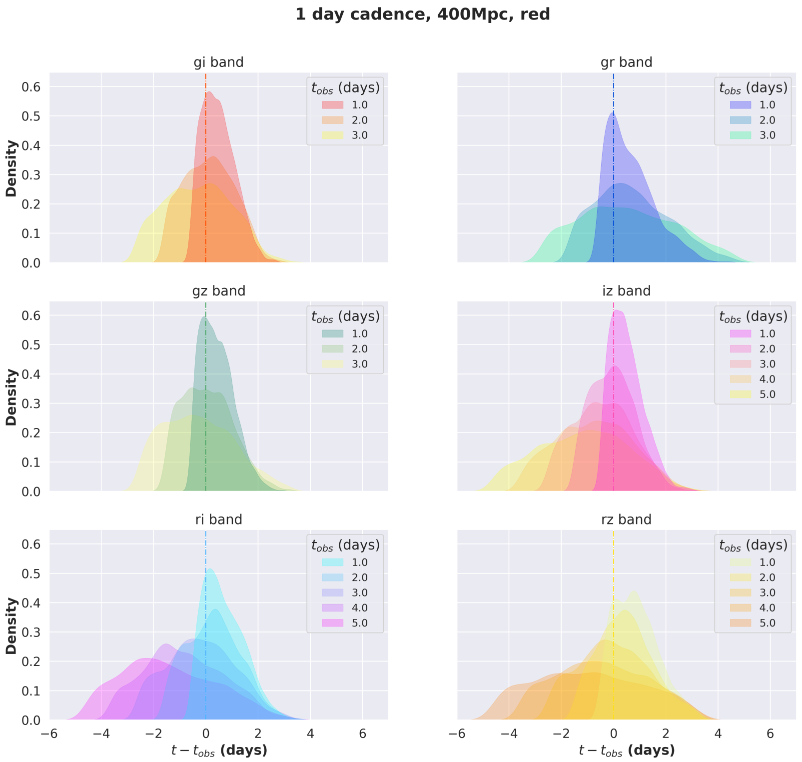

Figure B.25: Results on t_0 for the "red" kilonova, with a 1 day cadence at 400 Mpc.

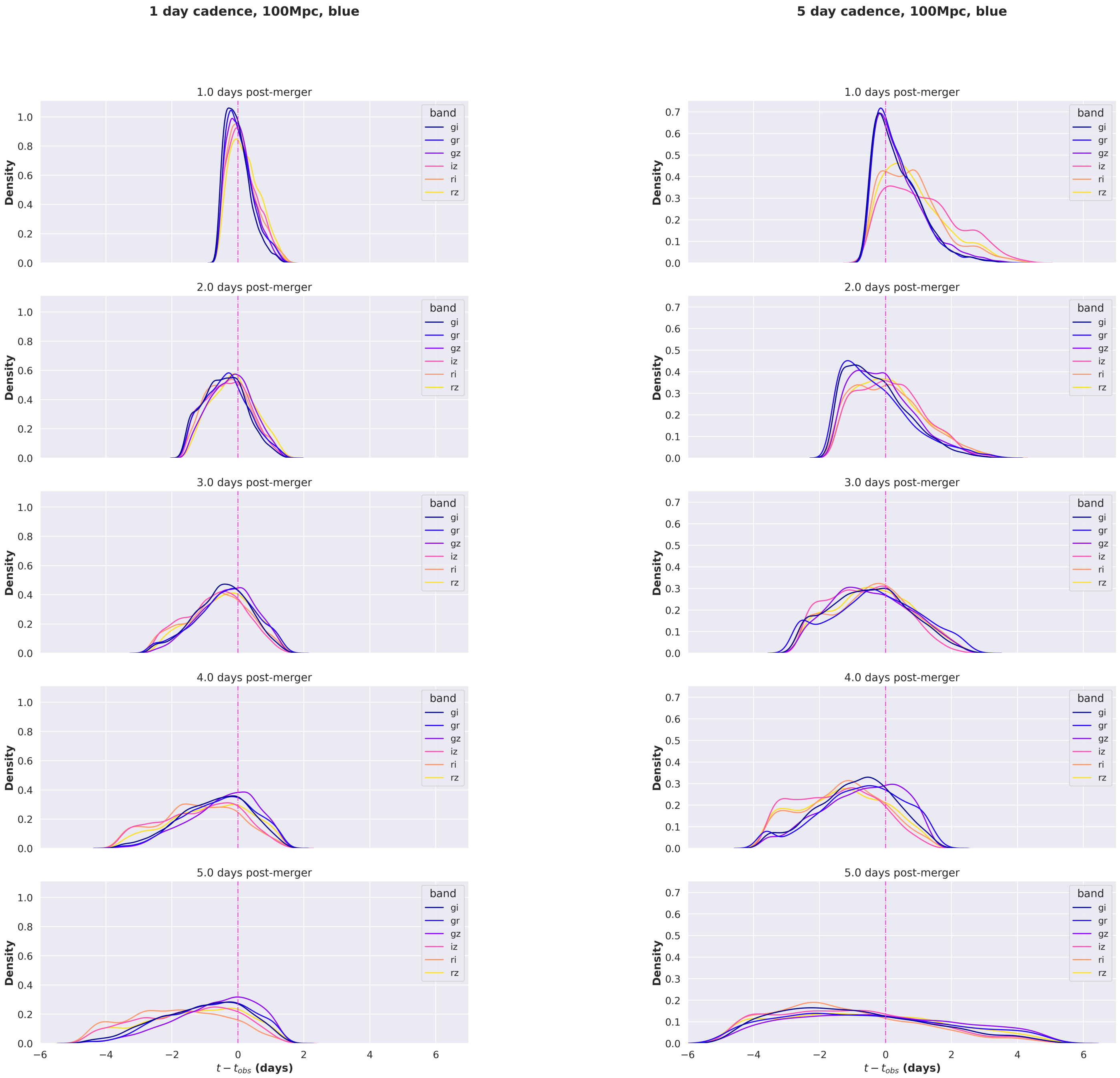

Figure B.26: Comparison of pairs of bands for a "blue" kilonova at 100 Mpc. The figures show results for a 1 day cadence and for a 5 day cadence. Where band combinations are not present, the kilonova did not meet the detection criteria.

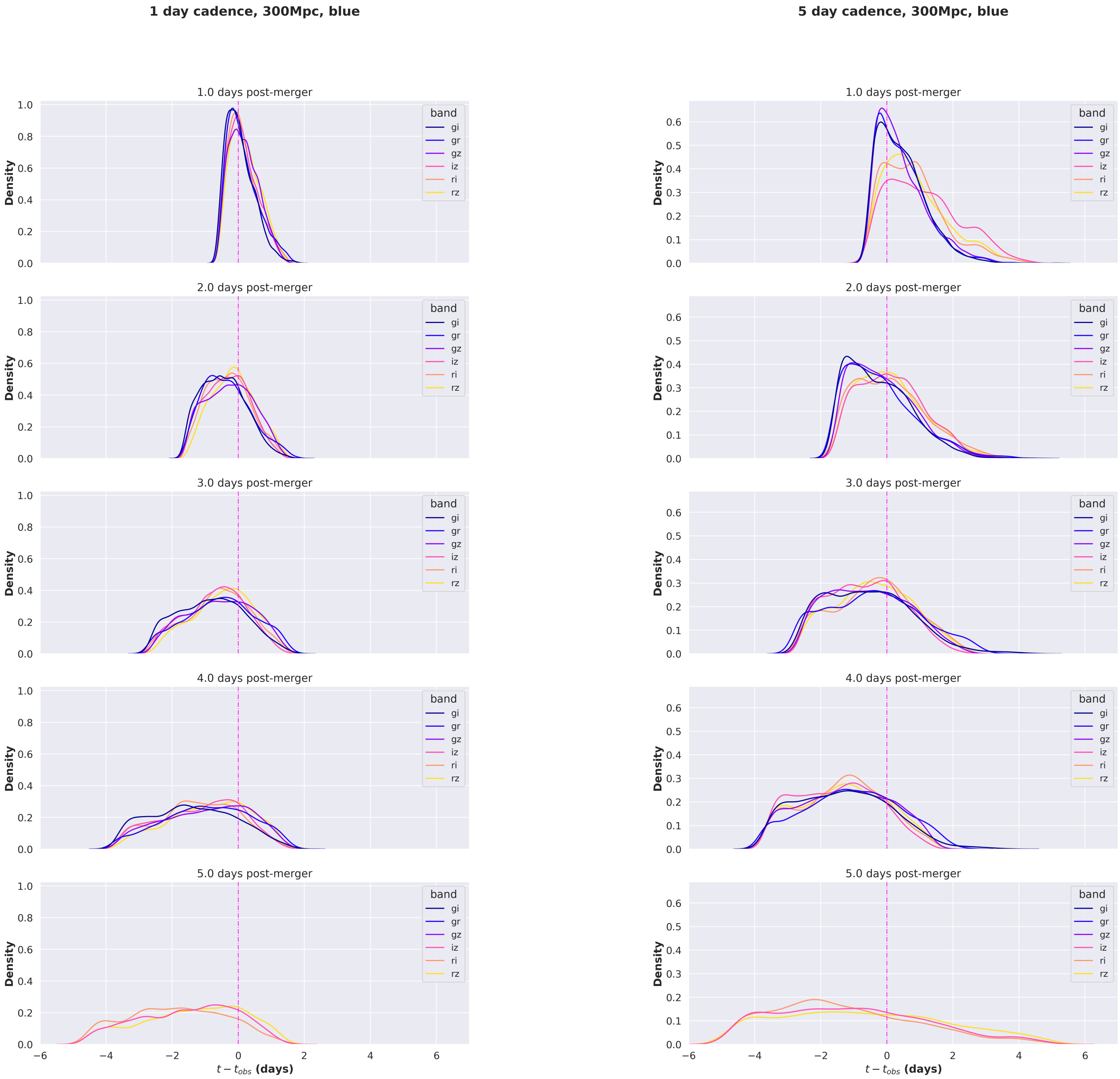

Figure B.27: Comparison of pairs of bands for a "blue" kilonova at 300 Mpc. The figures show results for a 1 day cadence and for a 5 day cadence. Where band combinations are not present, the kilonova did not meet the detection criteria.

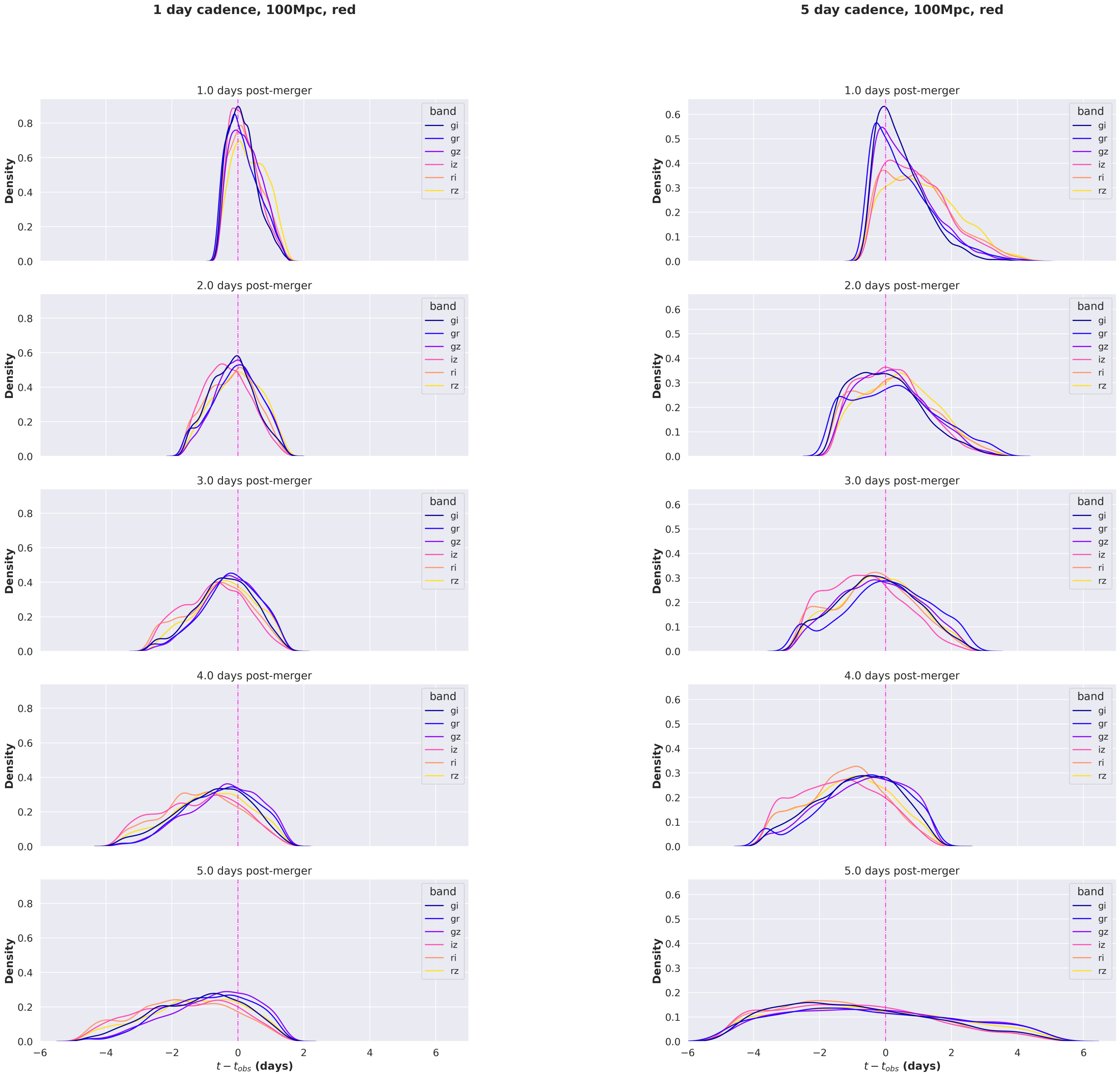

Figure B.28: Comparison of pairs of bands for a "red" kilonova at 100 Mpc. The figures show results for a 1 day cadence and for a 5 day cadence. Where band combinations are not present, the kilonova did not meet the detection criteria.

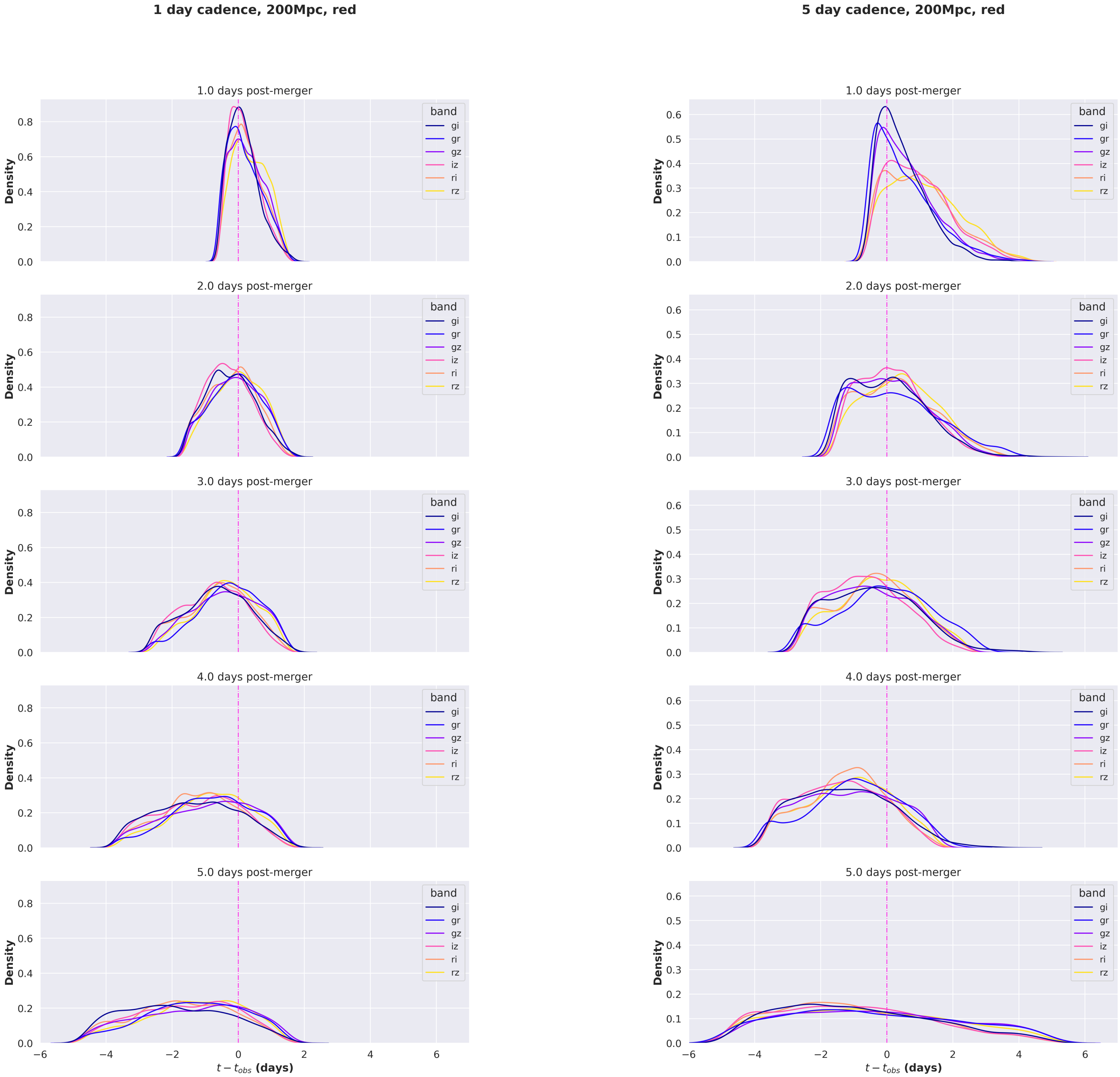

Figure B.29: Comparison of pairs of bands for a "red" kilonova at 200 Mpc. The figures show results for a 1 day cadence and for a 5 day cadence. Where band combinations are not present, the kilonova did not meet the detection criteria.

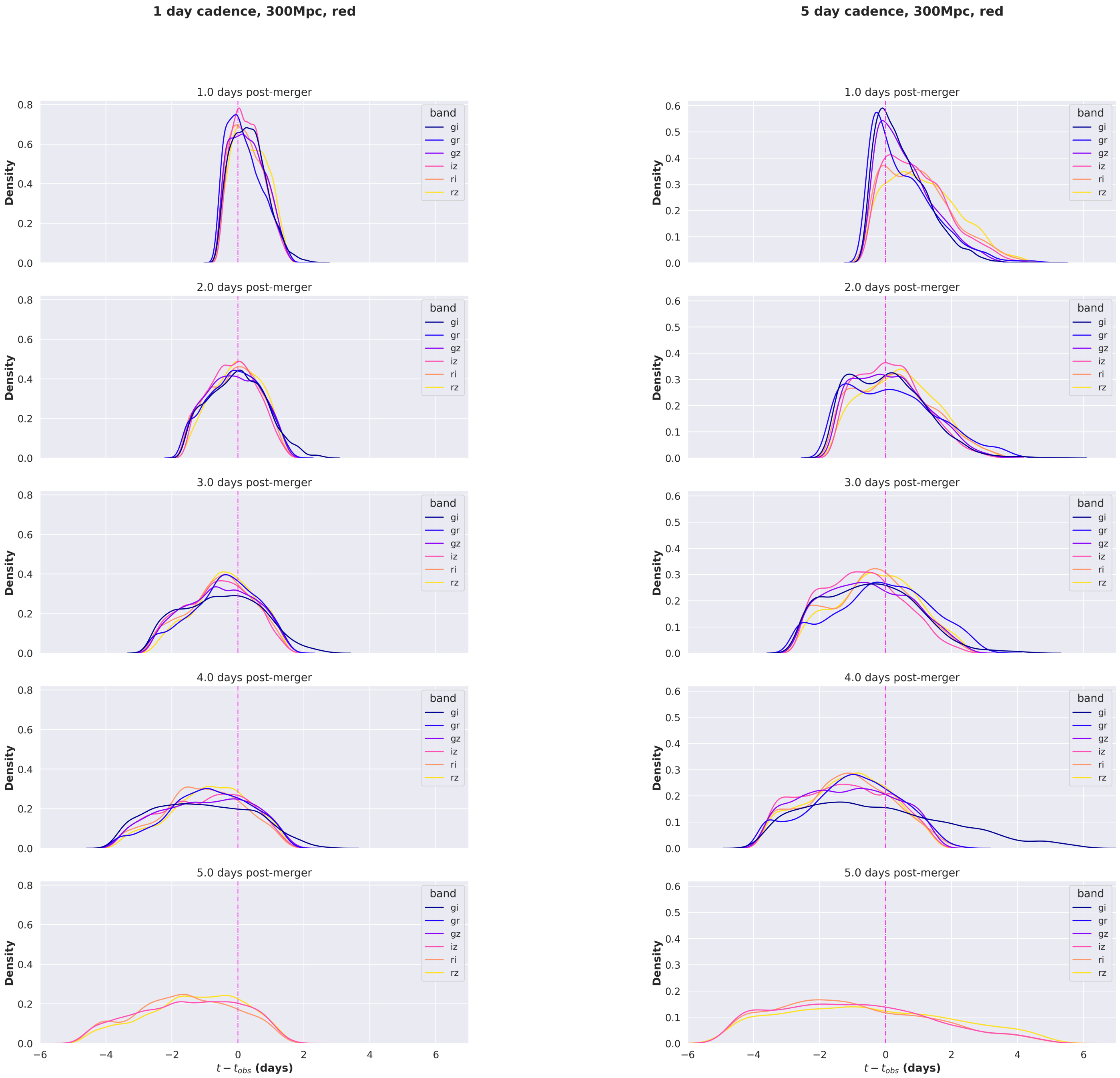

Figure B.30: Comparison of pairs of bands for a "red" kilonova at 300 Mpc. The figures show results for a 1 day cadence and for a 5 day cadence. Where band combinations are not present, the kilonova did not meet the detection criteria.

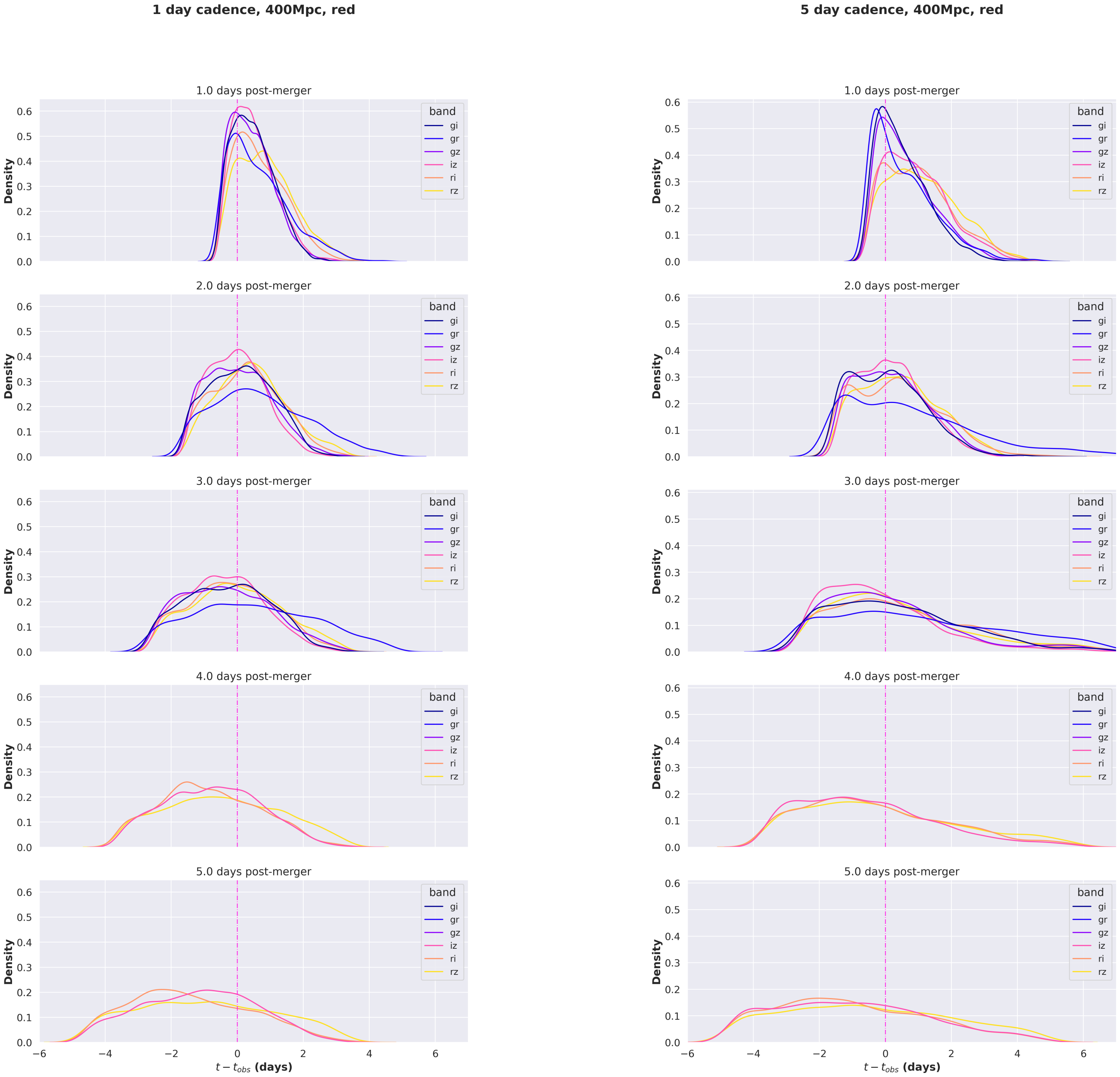

Figure B.31: Comparison of pairs of bands for a "red" kilonova at 400 Mpc. The figures show results for a 1 day cadence and for a 5 day cadence. Where band combinations are not present, the kilonova did not meet the detection criteria.

C | Supplementary Material for Chapter 5

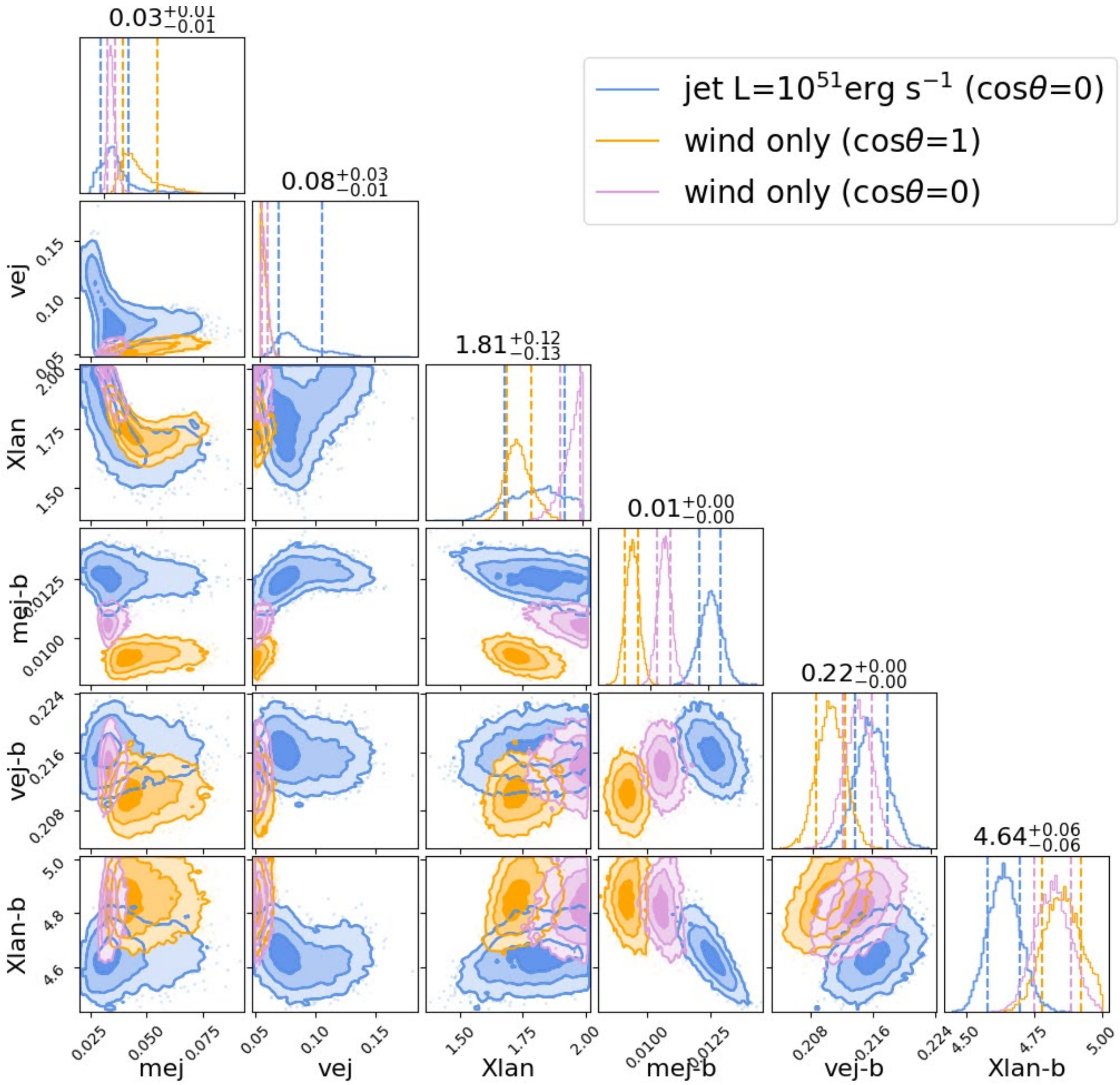

Figure C.1: Corner plot for parameter estimation on kilonova with and without a jet. Jet luminosity $L = 10^{51}$ erg s^{-1} with $\cos\theta_{obs} = 0$

Bibliography

[1] LIGO Scientific Collaboration, Virgo Collaboration, B. P. Abbott, *et al.*, "Observation of Gravitational Waves from a Binary Black Hole Merger," *Phys. Rev. Lett.* **116** (Feb, 2016) 061102. `https://link.aps.org/doi/10.1103/PhysRevLett.116.061102`.

[2] The LIGO Scientific Collaboration, The Virgo Collaboration, The KAGRA Collaboration, *et al.*, "GWTC-3: Compact Binary Coalescences Observed by LIGO and Virgo During the Second Part of the Third Observing Run,". `https://arxiv.org/abs/2111.03606`.

[3] B. Schutz, *A First Course in General Relativity, Second Edition*. Cambridge University Press, Cambridge, 2009.

[4] A. Einstein, "Die Feldgleichungen der Gravitation," *Sitzungsberichte der Königlich Preußischen Akademie der Wissenschaften (Berlin), Seite 844-847.* (1915) .

[5] J. A. Wheeler, *A Journey into Gravity and Spacetime*. Scientific American Library, New York, 1990.

[6] A. Einstein, "Approximative Integration of the Field Equations of Gravitation," Conference Proceedings of Prussian Academy of Sciences, 1916. Translated from German by Alfred Engel in *Volume 6: The Berlin Years: Writings, 1914-1917 (English translation supplement)*.

[7] J. A. Tyson and R. P. Giffard, "Gravitational-wave astronomy," **16** (1978) 521–554.

[8] K. Schwarzschild, "Über das Gravitationsfeld eines Massenpunktes nach der Einsteinschen Theorie," *Sitzungsberichte der Königlich Preußischen Akademie der Wissenschaften (Berlin), 1916, Seite 189-196* (1916) .

[9] F. Özel and P. Freire, "Masses, Radii, and the Equation of State of Neutron Stars," **54** (Sept., 2016) 401–440, `arXiv:1603.02698 [astro-ph.HE]`.

[10] T. A. Thompson, M. D. Kistler, and K. Z. Stanek, "A High Rate of White Dwarf-Neutron Star Mergers Their Transients," *ArXiv e-prints* (Dec., 2009) , `arXiv:0912.0009 [astro-ph.HE]`.

[11] P. Lorén-Aguilar, J. Guerrero, J. Isern, *et al.*, "Gravitational wave radiation from the coalescence of white dwarfs," **356** (Jan., 2005) 627–636, `astro-ph/0410356`.

[12] B. P. Abbott, R. Abbott, T. D. Abbott, *et al.*, "All-sky search for short gravitational-wave bursts in the first Advanced LIGO run," **95** no. 4, (Feb., 2017) 042003, `arXiv:1611.02972 [gr-qc]`.

[13] C. D. Ott, "TOPICAL REVIEW: The gravitational-wave signature of core-collapse supernovae," *Classical and Quantum Gravity* **26** no. 6, (Mar., 2009) 063001, `arXiv:0809.0695`.

[14] R. Abbott, T. Abbott, F. Acernese, *et al.*, "All-sky search for short gravitational-wave bursts in the third advanced LIGO and advanced virgo run," *Physical Review D* **104** no. 12, (Dec, 2021) . `https://doi.org/10.1103%2Fphysrevd.104.122004`.

[15] B. P. Abbott, R. Abbott, T. D. Abbott, *et al.*, "Prospects for Observing and Localizing Gravitational-Wave Transients with Advanced LIGO and Advanced Virgo," *Living Reviews in Relativity* **19** (Feb., 2016) 1, `arXiv:1304.0670 [gr-qc]`.

[16] T. Damour and A. Vilenkin, "Gravitational radiation from cosmic (super)strings: Bursts, stochastic background, and observational windows," **71** no. 6, (Mar., 2005) 063510, `hep-th/0410222`.

[17] C. Cutler and K. S. Thorne, "An Overview of Gravitational-Wave Sources," *ArXiv General Relativity and Quantum Cosmology e-prints* (Apr., 2002) , `gr-qc/0204090`.

[18] The LIGO Scientific Collaboration, the Virgo Collaboration, B. P. Abbott, *et al.*, "GW170817: Implications for the Stochastic Gravitational-Wave Background from Compact Binary Coalescences," *ArXiv e-prints* (Oct., 2017) , `arXiv:1710.05837 [gr-qc]`.

[19] R. Abbott, T. Abbott, F. Acernese, *et al.*, "All-sky, all-frequency directional search for persistent gravitational waves from advanced LIGO's and advanced virgo's first three observing runs," *Physical Review D* **105** no. 12, (Jun, 2022) . `https://doi.org/10.1103%2Fphysrevd.105.122001`.

[20] **LIGO Scientific Collaboration and Virgo Collaboration** Collaboration, J. Aasi, B. P. Abbott, R. Abbott, *et al.*, "Narrow-band search of continuous gravitational-wave signals

from Crab and Vela pulsars in Virgo VSR4 data," *Phys. Rev. D* **91** (Jan, 2015) 022004. `https://link.aps.org/doi/10.1103/PhysRevD.91.022004`.

[21] J. Aasi, B. P. Abbott, R. Abbott, *et al.*, "First low frequency all-sky search for continuous gravitational wave signals," **93** no. 4, (Feb., 2016) 042007, `arXiv:1510.03621 [astro-ph.IM]`.

[22] J. Weber, "Detection and Generation of Gravitational Waves," *Physical Review* **117** (Jan., 1960) 306–313.

[23] J. Weber, "Gravitational-Wave-Detector Events," *Physical Review Letters* **20** (June, 1968) 1307–1308.

[24] J. Weber, "Evidence for Discovery of Gravitational Radiation," *Physical Review Letters* **22** (June, 1969) 1320–1324.

[25] R. L. Forward, "Wideband laser-interferometer gravitational-radiation experiment," **17** (Jan., 1978) 379–390.

[26] R. Weiss, "Electromagnetically coupled broadband gravitational antenna," in *K.S. Thorne, "Gravitational radiation", 300 Years of Gravitation, S W Hawking and W Israel, pp 330–458*. University Press, 1972.

[27] P. R. Saulson, *Fundamentals of Interferometric Gravitational Wave Detectors*. World Scientific Publishing, Singapore, 1994.

[28] B. P. Abbott, R. Abbott, R. Adhikari, *et al.*, "LIGO: the Laser Interferometer Gravitational-Wave Observatory," *Reports on Progress in Physics* **72** no. 7, (July, 2009) 076901, `arXiv:0711.3041 [gr-qc]`.

[29] LIGO Scientific Collaboration, J. Aasi, B. P. Abbott, *et al.*, "Advanced LIGO," *Classical and Quantum Gravity* **32** no. 7, (Apr., 2015) 074001, `arXiv:1411.4547 [gr-qc]`.

[30] F. Acernese, M. Agathos, K. Agatsuma, *et al.*, "Advanced Virgo: a second-generation interferometric gravitational wave detector," *Classical and Quantum Gravity* **32** no. 2, (Jan., 2015) 024001, `arXiv:1408.3978 [gr-qc]`.

[31] Y. Aso, Y. Michimura, K. Somiya, *et al.*, "Interferometer design of the KAGRA gravitational wave detector," **88** no. 4, (Aug., 2013) 043007, `arXiv:1306.6747 [gr-qc]`.

[32] B. Willke, P. Aufmuth, C. Aulbert, *et al.*, "The GEO 600 gravitational wave detector," *Classical and Quantum Gravity* **19** no. 7, (2002) 1377. `http://stacks.iop.org/0264-9381/19/i=7/a=321`.

[33] R. A. Hulse and J. H. Taylor, “Discovery of a pulsar in a binary system,” *The Astrophysical Journal* **195** (1975) L51–L53.

[34] J. M. Weisberg, J. H. Tayler, and L. A. Fowler, “Gravitational waves from an orbiting pulsar,” *Scientific American* **245** (1981) 74–81.

[35] "GWOSC", “"o1 data set technical details".” `https://gwosc.org/o1_details/`. Accessed: 2023-04-29.

[36] **LIGO Scientific Collaboration and Virgo Collaboration** Collaboration, B. P. Abbott, R. Abbott, T. D. Abbott, *et al.*, “Binary black hole mergers in the first advanced ligo observing run,” *Phys. Rev. X* **6** (Oct, 2016) 041015. `https://link.aps.org/doi/10.1103/PhysRevX.6.041015`.

[37] B. P. Abbott, R. Abbott, T. D. Abbott, *et al.*, “GWTC-1: A Gravitational-Wave Transient Catalog of Compact Binary Mergers Observed by LIGO and Virgo during the First and Second Observing Runs,” *Physical Review X* **9** no. 3, (July, 2019) 031040, `arXiv:1811.12907 [astro-ph.HE]`.

[38] B. P. Abbott, R. Abbott, T. D. Abbott, *et al.*, “GW151226: Observation of Gravitational Waves from a 22-Solar-Mass Binary Black Hole Coalescence,” *Physical Review Letters* **116** no. 24, (June, 2016) 241103, `arXiv:1606.04855 [gr-qc]`.

[39] B. P. Abbott, R. Abbott, T. D. Abbott, *et al.*, “GW170817: Observation of Gravitational Waves from a Binary Neutron Star Inspiral,” *Physical Review Letters* **119** no. 16, (Oct., 2017) 161101, `arXiv:1710.05832 [gr-qc]`.

[40] B. P. Abbott, R. Abbott, T. D. Abbott, *et al.*, “Multi-messenger Observations of a Binary Neutron Star Merger,” *The Astrophysical Journall* **848** (Oct., 2017) L12, `arXiv:1710.05833 [astro-ph.HE]`.

[41] A. Goldstein, P. Veres, E. Burns, *et al.*, “An ordinary short gamma-ray burst with extraordinary implications: Fermi -GBM detection of GRB 170817a,” *The Astrophysical Journal* **848** no. 2, (Oct, 2017) L14. `https://doi.org/10.3847%2F2041-8213%2Faa8f41`.

[42] V. Savchenko, C. Ferrigno, E. Kuulkers, *et al.*, “INTEGRAL Detection of the First Prompt Gamma-Ray Signal Coincident with the Gravitational-wave Event GW170817,” *The Astrophysical Journall* **848** (Oct., 2017) L15, `arXiv:1710.05449 [astro-ph.HE]`.

[43] I. Arcavi, G. Hosseinzadeh, D. A. Howell, *et al.*, “Optical emission from a kilonova following a gravitational-wave-detected neutron-star merger,” *Nature* **551** (Nov., 2017) 64–66, `arXiv:1710.05843 [astro-ph.HE]`.

[44] P. S. Cowperthwaite, E. Berger, V. A. Villar, *et al.*, "The Electromagnetic Counterpart of the Binary Neutron Star Merger LIGO/Virgo GW170817. II. UV, Optical, and Near-infrared Light Curves and Comparison to Kilonova Models," *The Astrophysical Journall* **848** (Oct., 2017) L17, `arXiv:1710.05840 [astro-ph.HE]`.

[45] P. A. Evans, S. B. Cenko, J. A. Kennea, *et al.*, "<i>swift</i> and <i>nustar</i> observations of gw170817: Detection of a blue kilonova," *Science* **358** no. 6370, (2017) 1565–1570. `https://www.science.org/doi/abs/10.1126/science.aap9580`.

[46] S. J. Smartt, T. W. Chen, A. Jerkstrand, *et al.*, "A kilonova as the electromagnetic counterpart to a gravitational-wave source," *Nature* **551** no. 7678, (Nov., 2017) 75–79, `arXiv:1710.05841 [astro-ph.HE]`.

[47] N. R. Tanvir, A. J. Levan, C. González-Fernández, *et al.*, "The Emergence of a Lanthanide-rich Kilonova Following the Merger of Two Neutron Stars," *The Astrophysical Journall* **848** (Oct., 2017) L27, `arXiv:1710.05455 [astro-ph.HE]`.

[48] M. M. Kasliwal, E. Nakar, L. P. Singer, *et al.*, "Illuminating gravitational waves: A concordant picture of photons from a neutron star merger," *Science* **358** no. 6370, (2017) 1559–1565, `https://www.science.org/doi/pdf/10.1126/science.aap9455`. `https://www.science.org/doi/abs/10.1126/science.aap9455`.

[49] V. M. Lipunov, E. Gorbovskoy, V. G. Kornilov, *et al.*, "Master optical detection of the first ligo/virgo neutron star binary merger gw170817," *The Astrophysical Journal Letters* **850** no. 1, (Nov, 2017) L1. `https://dx.doi.org/10.3847/2041-8213/aa92c0`.

[50] M. Cantiello, J. B. Jensen, J. P. Blakeslee, *et al.*, "A precise distance to the host galaxy of the binary neutron star merger gw170817 using surface brightness fluctuations," *The Astrophysical Journal Letters* **854** no. 2, (Feb, 2018) L31. `https://dx.doi.org/10.3847/2041-8213/aaad64`.

[51] J. Hjorth, A. J. Levan, N. R. Tanvir, *et al.*, "The Distance to NGC 4993: The Host Galaxy of the Gravitational-wave Event GW170817," *The Astrophysical Journal Letters* **848** no. 2, (Oct., 2017) L31, `arXiv:1710.05856 [astro-ph.GA]`.

[52] M. Im, Y. Yoon, S.-K. J. Lee, *et al.*, "Distance and properties of ngc 4993 as the host galaxy of the gravitational-wave source gw170817," *The Astrophysical Journal Letters* **849** no. 1, (Oct, 2017) L16. `https://dx.doi.org/10.3847/2041-8213/aa9367`.

[53] S. Sakai, J. R. Mould, S. M. G. Hughes, *et al.*, "The Hubble Space Telescope Key Project on the Extragalactic Distance Scale. XXIV. The Calibration of Tully-Fisher Relations and the Value of the Hubble Constant," *The Astrophysical Journal* **529** no. 2, (Feb., 2000) 698–722, `arXiv:astro-ph/9909269 [astro-ph]`.

[54] W. L. Freedman, B. F. Madore, B. K. Gibson, *et al.*, "Final results from the hubble space telescope key project to measure the hubble constant*," *The Astrophysical Journal* **553** no. 1, (May, 2001) 47. `https://dx.doi.org/10.1086/320638`.

[55] D. A. Coulter, R. J. Foley, C. D. Kilpatrick, *et al.*, "Swope supernova survey 2017a (SSS17a), the optical counterpart to a gravitational wave source," *Science* **358** no. 6370, (Dec, 2017) 1556–1558. `https://doi.org/10.1126%2Fscience.aap9811`.

[56] D. Shoemaker, A. Rocchi, and S. Miyoki, "Observing scenario timeline graphic, post-o3." `https://dcc.ligo.org/LIGO-G2002127/public`. Accessed: 2022-11-02.

[57] D. Reitze, R. X. Adhikari, S. Ballmer, *et al.*, "Cosmic explorer: The u.s. contribution to gravitational-wave astronomy beyond ligo,". `https://arxiv.org/abs/1907.04833`.

[58] LIGO Scientific Collaboration, "Instrument Science White Paper," tech. rep., 10, 2016. `https://dcc.ligo.org/T1600119/public`.

[59] M. Maggiore, C. V. D. Broeck, N. Bartolo, *et al.*, "Science case for the einstein telescope," *Journal of Cosmology and Astroparticle Physics* **2020** no. 03, (Mar, 2020) 050–050. `https://doi.org/10.1088%2F1475-7516%2F2020%2F03%2F050`.

[60] P. Amaro-Seoane, H. Audley, S. Babak, *et al.*, "Laser Interferometer Space Antenna," *ArXiv e-prints* (Feb., 2017) , `arXiv:1702.00786 [astro-ph.IM]`.

[61] M. Armano, H. Audley, G. Auger, *et al.*, "Sub-Femto-g Free Fall for Space-Based Gravitational Wave Observatories: LISA Pathfinder Results," *Physical Review Letters* **116** no. 23, (June, 2016) 231101.

[62] K. G. Jansky, "Radio Waves from Outside the Solar System," *Nature* **132** (July, 1933) 66.

[63] F. S. Greus and A. S. Losa, "Multimessenger astronomy with neutrinos," *Universe* **7** no. 11, (Oct, 2021) 397. `https://doi.org/10.3390%2Funiverse7110397`.

[64] R. Davis, D. S. Harmer, and K. C. Hoffman, "Search for Neutrinos from the Sun," **20** no. 21, (May, 1968) 1205–1209.

[65] K. Hirata, T. Kajita, M. Koshiba, *et al.*, "Observation of a neutrino burst from the supernova sn1987a," *Phys. Rev. Lett.* **58** (Apr, 1987) 1490–1493. `https://link.aps.org/doi/10.1103/PhysRevLett.58.1490`.

[66] P. Mészáros, D. B. Fox, C. Hanna, and K. Murase, "Multi-messenger astrophysics," *Nature Reviews Physics* **1** no. 10, (Oct, 2019) 585–599. `https://doi.org/10.1038%2Fs42254-019-0101-z`.

[67] T. Baker, E. Bellini, P. Ferreira, *et al.*, "Strong constraints on cosmological gravity from GW170817 and GRB 170817a," *Physical Review Letters* **119** no. 25, (Dec, 2017) . `https://doi.org/10.1103%2Fphysrevlett.119.251301`.

[68] M. W. Coughlin, T. Dietrich, Z. Doctor, *et al.*, "Constraints on the neutron star equation of state from AT2017gfo using radiative transfer simulations," **480** no. 3, (Nov, 2018) 3871–3878, `arXiv:1805.09371 [astro-ph.HE]`.

[69] M. Nicholl, B. Margalit, P. Schmidt, *et al.*, "Tight multimessenger constraints on the neutron star equation of state from GW170817 and a forward model for kilonova light-curve synthesis," *Monthly Notices of the Royal Astronomical Society* **505** no. 2, (05, 2021) 3016–3032. `https://doi.org/10.1093/mnras/stab1523`.

[70] L.-X. Li and B. Paczyński, "Transient Events from Neutron Star Mergers," *The Astrophysical Journall* **507** (Nov., 1998) L59–L62, `astro-ph/9807272`.

[71] S. Rosswog, M. Liebendörfer, F. K. Thielemann, *et al.*, "Mass ejection in neutron star mergers," **341** (Jan., 1999) 499–526, `arXiv:astro-ph/9811367 [astro-ph]`.

[72] J. Barnes, D. Kasen, M.-R. Wu, and G. Martínez-Pinedo, "Radioactivity and Thermalization in the Ejecta of Compact Object Mergers and Their Impact on Kilonova Light Curves," *The Astrophysical Journal* **829** (Oct., 2016) 110, `arXiv:1605.07218 [astro-ph.HE]`.

[73] B. D. Metzger, "Kilonovae," *Living Reviews in Relativity* **20** (May, 2017) 3, `arXiv:1610.09381 [astro-ph.HE]`.

[74] J. Barnes and D. Kasen, "Effect of a High Opacity on the Light Curves of Radioactively Powered Transients from Compact Object Mergers," *The Astrophysical Journal* **775** no. 1, (Sep, 2013) 18, `arXiv:1303.5787 [astro-ph.HE]`.

[75] B. D. Metzger, "Kilonovae," *Living Reviews in Relativity* **23** no. 1, (Dec, 2019) . `https://doi.org/10.1007%2Fs41114-019-0024-0`.

[76] E. M. Burbidge, G. R. Burbidge, W. A. Fowler, and F. Hoyle, “Synthesis of the elements in stars,” *Rev. Mod. Phys.* **29** (Oct, 1957) 547–650. `https://link.aps.org/doi/10.1103/RevModPhys.29.547`.

[77] A. G. W. Cameron, “Nuclear reactions in stars and nucleogenesis,” *Publications of the Astronomical Society of the Pacific* **69** no. 408, (Jun, 1957) 201. `https://dx.doi.org/10.1086/127051`.

[78] T. Kajino, W. Aoki, A. Balantekin, *et al.*, “Current status of r-process nucleosynthesis,” *Progress in Particle and Nuclear Physics* **107** (Jul, 2019) 109–166. `https://doi.org/10.1016%2Fj.ppnp.2019.02.008`.

[79] C. Freiburghaus, S. Rosswog, and F.-K. Thielemann, “r-process in neutron star mergers,” *The Astrophysical Journal* **525** no. 2, (Nov, 1999) L121–L124. `https://doi.org/10.1086/312343`.

[80] J. M. Lattimer and D. N. Schramm, “Black-hole-neutron-star collisions,” *The Astrophysical Journall* **192** (Sept., 1974) L145–L147.

[81] J. M. Lattimer and D. N. Schramm, “The tidal disruption of neutron stars by black holes in close binaries,” *The Astrophysical Journal* **210** (Dec., 1976) 549–567.

[82] E. Symbalisty and D. N. Schramm, “Neutron star collisions and the r-process,” *Astrophysics Letters* **22** (1982) 143–145.

[83] S. Rosswog, F. K. Thielemann, M. B. Davies, *et al.*, “Coalescing Neutron Stars: a Solution to the R-Process Problem?,” in *Nuclear Astrophysics*, W. Hillebrandt and E. Muller, eds., p. 103. Jan., 1998. `arXiv:astro-ph/9804332 [astro-ph]`.

[84] D. A. Perley, B. D. Metzger, J. Granot, *et al.*, “GRB 080503: IMPLICATIONS OF a NAKED SHORT GAMMA-RAY BURST DOMINATED BY EXTENDED EMISSION,” *The Astrophysical Journal* **696** no. 2, (Apr, 2009) 1871–1885. `https://doi.org/10.1088%2F0004-637x%2F696%2F2%2F1871`.

[85] N. R. Tanvir, A. J. Levan, A. S. Fruchter, *et al.*, “A ‘kilonova’ associated with the short-duration γ-ray burst GRB 130603B,” *Nature* **500** (Aug., 2013) 547–549, `arXiv:1306.4971 [astro-ph.HE]`.

[86] G. P. Lamb, N. R. Tanvir, A. J. Levan, *et al.*, “Short GRB 160821B: A Reverse Shock, a Refreshed Shock, and a Well-sampled Kilonova,” **883** no. 1, (Sept., 2019) 48, `arXiv:1905.02159 [astro-ph.HE]`.

[87] S. R. Kulkarni, “Modeling supernova-like explosions associated with gamma-ray bursts with short durations,” 2005. `https://arxiv.org/abs/astro-ph/0510256`.

[88] B. D. Metzger, G. Martínez-Pinedo, S. Darbha, *et al.*, “Electromagnetic counterparts of compact object mergers powered by the radioactive decay of r-process nuclei,” *Monthly Notices of the Royal Astronomical Society* **406** no. 4, (08, 2010) 2650–2662. `https://doi.org/10.1111/j.1365-2966.2010.16864.x`.

[89] D. Kasen, N. R. Badnell, and J. Barnes, “OPACITIES AND SPECTRA OF THE r-PROCESS EJECTA FROM NEUTRON STAR MERGERS,” *The Astrophysical Journal* **774** no. 1, (Aug, 2013) 25. `https://doi.org/10.1088%2F0004-637x%2F774%2F1%2F25`.

[90] Wikimedia Commons, “Periodic table,” 2007. `https://commons.wikimedia.org/wiki/File:Periodic_Table_Armtuk3.svg`.

[91] R. Fernández and B. D. Metzger, “Electromagnetic signatures of neutron star mergers in the advanced ligo era,” *Annual Review of Nuclear and Particle Science* **66** no. 1, (2016) 23–45, `https://doi.org/10.1146/annurev-nucl-102115-044819`. `https://doi.org/10.1146/annurev-nucl-102115-044819`.

[92] M. Shibata and K. Hotokezaka, “Merger and mass ejection of neutron star binaries,” *Annual Review of Nuclear and Particle Science* **69** no. 1, (2019) 41–64, `https://doi.org/10.1146/annurev-nucl-101918-023625`. `https://doi.org/10.1146/annurev-nucl-101918-023625`.

[93] B. D. Metzger and R. Fernández, “Red or blue? A potential kilonova imprint of the delay until black hole formation following a neutron star merger,” *Monthly Notices of the Royal Astronomical Society* **441** no. 4, (05, 2014) 3444–3453, `https://academic.oup.com/mnras/article-pdf/441/4/3444/4055164/stu` `https://doi.org/10.1093/mnras/stu802`.

[94] D. Kasen, B. Metzger, J. Barnes, *et al.*, “Origin of the heavy elements in binary neutron-star mergers from a gravitational-wave event,” *Nature* **551** no. 7678, (Nov, 2017) 80–84, `arXiv:1710.05463 [astro-ph.HE]`.

[95] Z. Doctor, R. Kessler, H. Y. Chen, *et al.*, “A Search for Kilonovae in the Dark Energy Survey,” *The Astrophysical Journal* **837** (Mar., 2017) 57, `arXiv:1611.08052 [astro-ph.HE]`.

[96] M. Coughlin, T. Dietrich, K. Kawaguchi, *et al.*, “Toward Rapid Transient Identification and Characterization of Kilonovae,” *The Astrophysical Journal* **849** (Nov., 2017) 12, `arXiv:1708.07714 [astro-ph.HE]`.

[97] P. S. Cowperthwaite and E. Berger, "A Comprehensive Study of Detectability and Contamination in Deep Rapid Optical Searches for Gravitational Wave Counterparts," *The Astrophysical Journal* **814** (Nov., 2015) 25, `arXiv:1503.07869 [astro-ph.IM]`.

[98] J. C. Rastinejad, B. P. Gompertz, A. J. Levan, *et al.*, "A kilonova following a long-duration gamma-ray burst at 350 mpc," 2022. `https://arxiv.org/abs/2204.10864`.

[99] V. A. Villar, J. Guillochon, E. Berger, *et al.*, "The combined ultraviolet, optical, and near-infrared light curves of the kilonova associated with the binary neutron star merger GW170817: Unified data set, analytic models, and physical implications," *The Astrophysical Journal* **851** no. 1, (Dec, 2017) L21. `https://doi.org/10.3847%2F2041-8213%2Faa9c84`.

[100] M. R. Drout, A. L. Piro, B. J. Shappee, *et al.*, "Light curves of the neutron star merger GW170817/SSS17a: Implications for r-process nucleosynthesis," *Science* **358** no. 6370, (Dec, 2017) 1570–1574. `https://doi.org/10.1126%2Fscience.aaq0049`.

[101] Z. Ivezic, J. A. Tyson, B. Abel, *et al.*, "LSST: from Science Drivers to Reference Design and Anticipated Data Products," *ArXiv e-prints* (May, 2008) , `arXiv:0805.2366`.

[102] R. L. Jones, P. Yoachim, Z. Ivezic, *et al.*, "Survey Strategy and Cadence Choices for the Vera C. Rubin Observatory Legacy Survey of Space and Time (LSST)," Sept., 2020. `https://doi.org/10.5281/zenodo.4048838`.

[103] H.-Y. Chen, D. E. Holz, J. Miller, *et al.*, "Distance measures in gravitational-wave astrophysics and cosmology," *Classical and Quantum Gravity* **38** no. 5, (Jan, 2021) 055010. `https://doi.org/10.1088%2F1361-6382%2Fabd594`.

[104] E. A. Chase, B. O'Connor, C. L. Fryer, *et al.*, "Kilonova detectability with wide-field instruments," Mar, 2022. `https://dx.doi.org/10.3847/1538-4357/ac3d25`.

[105] A. S. Carracedo, M. Bulla, U. Feindt, and A. Goobar, "Detectability of kilonovae in optical surveys: *post-mortem* examination of the lvc o3 run follow-up," 2020.

[106] **LSST** Collaboration, Margutti, Raffaella and others, "Target of Opportunity Observations of Gravitational Wave Events with LSST," `arXiv:1812.04051 [astro-ph.HE]`.

[107] A. Loeb, "Electromagnetic counterparts to black hole mergers detected by ligo," *The Astrophysical Journal* **819** no. 2, (Mar, 2016) L21. `https://doi.org/10.3847%2F2041-8205%2F819%2F2%2Fl21`.

[108] S. E. de Mink and A. King, "Electromagnetic signals following stellar-mass black hole mergers," *The Astrophysical Journal* **839** no. 1, (Apr, 2017) L7. `https://doi.org/10.3847%2F2041-8213%2Faa67f3`.

[109] M. J. Graham, K. E. S. Ford, B. McKernan, *et al.*, "Candidate electromagnetic counterpart to the binary black hole merger gravitational-wave event s190521g," *Phys. Rev. Lett.* **124** (Jun, 2020) 251102. `https://link.aps.org/doi/10.1103/PhysRevLett.124.251102`.

[110] I. Arcavi, "The First Hours of the GW170817 Kilonova and the Importance of Early Optical and Ultraviolet Observations for Constraining Emission Models," *The Astrophysical Journall* **855** (Mar., 2018) L23, `arXiv:1802.02164 [astro-ph.HE]`.

[111] K. Mortensen, A. A. Miller, R. Margutti, and C. Pankow, "Is an LSST ToO mode necessary for kilonova discovery?," *Research Notes of the AAS* **3** no. 1, (Jan, 2019) 11.

[112] M. Almualla, S. Anand, M. W. Coughlin, *et al.*, "Towards regular serendipitous detections of kilonovae by wide-field surveys," `arXiv:2011.10421 [astro-ph.HE]`.

[113] I. Andreoni, S. Anand, F. Bianco, *et al.*, "A strategy for LSST to unveil a population of kilonovae without gravitational-wave triggers," *Publications of the Astronomical Society of the Pacific* **131** (06, 2019) 068004.

[114] C. N. Setzer, R. Biswas, H. V. Peiris, *et al.*, "Serendipitous discoveries of kilonovae in the LSST main survey: maximizing detections of sub-threshold gravitational wave events," *Monthly Notices of the Royal Astronomical Society* **485** no. 3, (02, 2019) 4260–4273. `https://doi.org/10.1093/mnras/stz506`.

[115] A. Liddle, *An Introduction to Modern Cosmology*. Wiley, West Sussex, 2003.

[116] W. Herschel, "On the Construction of the Heavens.," *Philosophical Transactions of the Royal Society of London Series I* **75** (1785) 213–266.

[117] E. Hubble, "A Relation between Distance and Radial Velocity among Extra-Galactic Nebulae," *Proceedings of the National Academy of Science* **15** (Mar., 1929) 168–173.

[118] G. Lemaître, "Un Univers homogène de masse constante et de rayon croissant rendant compte de la vitesse radiale des nébuleuses extra-galactiques," *Annales de la Société Scientifique de Bruxelles* **47** (Jan., 1927) 49–59.

[119] A. Friedmann, "Über die Krümmung des Raumes," *Zeitschrift fur Physik* **10** (1922) 377–386.

[120] A. Friedmann, “Über die Möglichkeit einer Welt mit konstanter negativer Krümmung des Raumes,” *Zeitschrift fur Physik* **21** (Dec., 1924) 326–332.

[121] A. Friedmann, “On the Curvature of Space,” *General Relativity and Gravitation* **31** (Dec., 1999) 1991.

[122] G. Lemaître, “Expansion of the universe, A homogeneous universe of constant mass and increasing radius accounting for the radial velocity of extra-galactic nebulae,” **91** (Mar., 1931) 483–490.

[123] G. Lemaître, “L’Univers en expansion,” *Annales de la Société Scientifique de Bruxelles* **53** (Jan., 1933) 51.

[124] H. P. Robertson, “Kinematics and World-Structure,” **82** (Nov., 1935) 284.

[125] A. G. Walker, “On Milne’s Theory of World-Structure*,” *Proceedings of the London Mathematical Society* **s2-42** no. 1, (01, 1937) 90–127. `https://doi.org/10.1112/plms/s2-42.1.90`.

[126] P. J. E. Peebles, *Principles of Physical Cosmology*. Princeton University Press, Princeton, New Jersey, 1993.

[127] C. Gordon, K. Land, and A. Slosar, “Cosmological Constraints from Type Ia Supernovae Peculiar Velocity Measurements,” *Physical Review Letters* **99** no. 8, (Aug., 2007) 081301, `arXiv:0705.1718`.

[128] N. Sugiura, N. Sugiyama, and M. Sasaki, “Anisotropies in Luminosity Distance,” in *Cosmological Parameters and the Evolution of the Universe*, K. Sato, ed., vol. 183 of *IAU Symposium*, p. 269. 1999.

[129] V. M. Slipher, “The radial velocity of the Andromeda Nebula,” *Lowell Observatory Bulletin* **2** (1913) 56–57.

[130] D. W. Hogg, “Distance measures in cosmology,” *ArXiv Astrophysics e-prints* (May, 1999) , `astro-ph/9905116`.

[131] T. Theuns, “Physical Cosmology.” `http://icc.dur.ac.uk/~tt/Lectures/UA/L4/cosmology.pdf`.

[132] A. Sandage, “Current Problems in the Extragalactic Distance Scale.,” *The Astrophysical Journal* **127** (May, 1958) 513.

[133] A. Sandage, “The Change of Redshift and Apparent Luminosity of Galaxies due to the Deceleration of Selected Expanding Universes.,” *The Astrophysical Journal* **136** (Sept., 1962) 319.

[134] S. Perlmutter, G. Aldering, G. Goldhaber, *et al.*, "Measurements of Ω and Λ using 42 High-Redshift Supernovae," *The Astrophysical Journal* **517** (1999) 565–586.

[135] A. G. Riess, A. V. Filippenko, P. Challis, *et al.*, "Observational evidence from supernovae for an accelerating universe and a cosmological constant," *The Astronomical Journal* **119** (1998) 1009–1038.

[136] J. L. Bernal, L. Verde, and A. G. Riess, "The trouble with H_0," **10** (Oct., 2016) 019, `arXiv:1607.05617`.

[137] C. Dreifus, "How Two Pigeons Helped Scientists Confirm the Big Bang Theory," Feb, 2004.

[138] R. Schofield, P. Covas, A. Effler, and R. Savage, "Why the GW channel detects thirsty black ravens along with colliding black holes," 2017. `https://alog.ligo-wa.caltech.edu/aLOG/index.php?callRep=37630`.

[139] A. A. Penzias and R. W. Wilson, "A Measurement of Excess Antenna Temperature at 4080 Mc/s.," *The Astrophysical Journal* **142** (July, 1965) 419–421.

[140] G. F. Smoot, C. L. Bennett, A. Kogut, *et al.*, "Structure in the COBE differential microwave radiometer first-year maps," *The Astrophysical Journall* **396** (Sept., 1992) L1–L5.

[141] R. K. Sachs and A. M. Wolfe, "Perturbations of a Cosmological Model and Angular Variations of the Microwave Background," *The Astrophysical Journal* **147** (Jan., 1967) 73.

[142] Planck Collaboration, P. A. R. Ade, N. Aghanim, *et al.*, "Planck 2015 results. XIII. Cosmological parameters," **594** (Sept., 2016) A13, `arXiv:1502.01589`.

[143] and N. Aghanim, Y. Akrami, M. Ashdown, *et al.*, "Planck 2018 results," *Astronomy & Astrophysics* **641** (Sep, 2020) A6. `https://doi.org/10.1051%2F0004-6361%2F201833910`.

[144] G. Hinshaw, D. Larson, E. Komatsu, *et al.*, "Nine-year Wilkinson Microwave Anisotropy Probe (WMAP) Observations: Cosmological Parameter Results," *The Astrophysical Journals* **208** (Oct., 2013) 19, `arXiv:1212.5226`.

[145] C. L. Bennett, D. Larson, J. L. Weiland, *et al.*, "Nine-year Wilkinson Microwave Anisotropy Probe (WMAP) Observations: Final Maps and Results," *The Astrophysical Journals* **208** (Oct., 2013) 20, `arXiv:1212.5225`.

[146] Planck Collaboration, P. A. R. Ade, N. Aghanim, *et al.*, "Planck 2013 results. I. Overview of products and scientific results," **571** (Nov., 2014) A1, `arXiv:1303.5062`.

[147] F. W. Bessel, "On the parallax of 61 Cygni," *Monthly Notices of the Royal Astronomical Society* **4** (Nov., 1838) 152–161.

[148] D. Branch and G. A. Tammann, "Type IA supernovae as standard candles," **30** (1992) 359–389.

[149] P. A. Mazzali, F. K. Röpke, S. Benetti, and W. Hillebrandt, "A Common Explosion Mechanism for Type Ia Supernovae," *Science* **315** (Feb., 2007) 825, `astro-ph/0702351`.

[150] A. G. Riess, W. Yuan, L. M. Macri, *et al.*, "A comprehensive measurement of the local value of the hubble constant with 1 km s-1 Mpc-1 uncertainty from the hubble space telescope and the SH0es team," *The Astrophysical Journal Letters* **934** no. 1, (Jul, 2022) L7. `https://doi.org/10.3847%2F2041-8213%2Fac5c5b`.

[151] B. F. Madore and W. L. Freedman, "The Cepheid distance scale," **103** (Sept., 1991) 933–957.

[152] H. S. Leavitt, "1777 variables in the Magellanic Clouds," *Annals of Harvard College Observatory* **60** (1908) 87–108.3.

[153] H. S. Leavitt and E. C. Pickering, "Periods of 25 Variable Stars in the Small Magellanic Cloud.," *Harvard College Observatory Circular* **173** (Mar., 1912) 1–3.

[154] W. Baade, "The Period-Luminosity Relation of the Cepheids," **68** (Feb., 1956) 5.

[155] V. Bonvin and M. Millon, "H0 tension." `https://github.com/vbonvin/H0_tension`. Accessed: 2022-10-30.

[156] T. L. S. Collaboration, the Virgo Collaboration, the KAGRA Collaboration, *et al.*, "Constraints on the cosmic expansion history from gwtc-3," 2021.

[157] B. F. Schutz, "Determining the Hubble constant from gravitational wave observations," *Nature* **323** (1986) 310–311.

[158] S. Nissanke, D. E. Holz, N. Dalal, *et al.*, "Determining the Hubble constant from gravitational wave observations of merging compact binaries," *ArXiv e-prints* (July, 2013) , `arXiv:1307.2638 [astro-ph.CO]`.

[159] B. P. Abbott, R. Abbott, T. D. Abbott, *et al.*, "Properties of the Binary Black Hole Merger GW150914," *Physical Review Letters* **116** no. 24, (June, 2016) 241102, `arXiv:1602.03840 [gr-qc]`.

[160] F. Pretorius, "Evolution of Binary Black-Hole Spacetimes," *Phys. Rev. Lett.* **95** (Sep, 2005) 121101. `https://link.aps.org/doi/10.1103/PhysRevLett.95.121101`.

[161] M. Campanelli, C. O. Lousto, P. Marronetti, and Y. Zlochower, "Accurate Evolutions of Orbiting Black-Hole Binaries without Excision," *Phys. Rev. Lett.* **96** (Mar, 2006) 111101. `https://link.aps.org/doi/10.1103/PhysRevLett.96.111101`.

[162] J. G. Baker, J. Centrella, D.-I. Choi, *et al.*, "Gravitational-wave extraction from an inspiraling configuration of merging black holes," *Phys. Rev. Lett.* **96** (Mar, 2006) 111102. `https://link.aps.org/doi/10.1103/PhysRevLett.96.111102`.

[163] D. E. Holz and S. A. Hughes, "Using Gravitational-Wave Standard Sirens," *The Astrophysical Journal* **629** (Aug., 2005) 15–22, `astro-ph/0504616`.

[164] S. R. Taylor, J. R. Gair, and I. Mandel, "Hubble without the Hubble: Cosmology using advanced gravitational-wave detectors alone," *Physical Review D* **85** no. 2, (2012) 023535.

[165] W. Del Pozzo, "Inference of cosmological parameters from gravitational waves: Applications to second generation interferometers," **86** no. 4, (Aug., 2012) 043011, `arXiv:1108.1317`.

[166] T. Bayes and R. Price, "An Essay Towards Solving a Problem in the Doctrine of Chances. By the late Rev. Mr. Bayes, communicated by Mr. Price, in a letter to John Canton, M.A. and F.R.S.," *Philosophical Transactions of the Royal Society* (January, 1763) .

[167] S. B. McGrayne, *The Theory That Would Not Die*. Yale University Press, New Haven & London, 2011.

[168] H. Jeffreys, *The Theory of Probability*. Oxford Classic Texts in the Physical Sciences. OUP Oxford, 1998. `https://books.google.co.uk/books?id=vh9Act9rtzQC`.

[169] P. Gregory, *Bayesian Logical Data Analysis for the Physical Sciences: A Comparative approach with Mathematica Support*. Cambridge University Press, Cambridge, UK, 2005.

[170] R. Trotta, “Bayes in the sky: Bayesian inference and model selection in cosmology,” *Contemporary Physics* **49** (Mar., 2008) 71–104, `arXiv:0803.4089`.

[171] E. T. Jaynes, *Probability Theory - The Logic of Science*. Cambridge University Press, Cambridge, UK, 2003.

[172] K. Kawaguchi, M. Shibata, and M. Tanaka, “Diversity of kilonova light curves,” *The Astrophysical Journal* **889** no. 2, (Feb, 2020) 171. `https://doi.org/10.3847%2F1538-4357%2Fab61f6`.

[173] D. Kasen, R. C. Thomas, and P. Nugent, “Time-dependent Monte Carlo Radiative Transfer Calculations for Three-dimensional Supernova Spectra, Light Curves, and Polarization,” **651** no. 1, (Nov., 2006) 366–380, `arXiv:astro-ph/0606111 [astro-ph]`.

[174] N. Roth and D. Kasen, “Monte carlo radiation-hydrodynamics with implicit methods,” *The Astrophysical Journal Supplement Series* **217** no. 1, (Mar, 2015) 9. `https://dx.doi.org/10.1088/0067-0049/217/1/9`.

[175] Y. Sekiguchi, K. Kiuchi, K. Kyutoku, *et al.*, “Dynamical mass ejection from the merger of asymmetric binary neutron stars: Radiation-hydrodynamics study in general relativity,” *Physical Review D* **93** no. 12, (Jun, 2016) . `https://doi.org/10.1103%2Fphysrevd.93.124046`.

[176] Oechslin, R., Janka, H.-T., and Marek, A., “Relativistic neutron star merger simulations with non-zero temperature equations of state* - i. variation of binary parameters and equation of state,” *A&A* **467** no. 2, (2007) 395–409. `https://doi.org/10.1051/0004-6361:20066682`.

[177] A. Perego, S. Rosswog, R. M. Cabezon, *et al.*, “Neutrino-driven winds from neutron star merger remnants,” *Monthly Notices of the Royal Astronomical Society* **443** no. 4, (Aug, 2014) 3134–3156. `https://doi.org/10.1093%2Fmnras%2Fstu1352`.

[178] O. Just, A. Bauswein, R. A. Pulpillo, *et al.*, “Comprehensive nucleosynthesis analysis for ejecta of compact binary mergers,” *Monthly Notices of the Royal Astronomical Society* **448** no. 1, (02, 2015) 541–567. `https://doi.org/10.1093/mnras/stv009`.

[179] B. D. Metzger, T. A. Thompson, and E. Quataert, “A magnetar origin for the kilonova ejecta in GW170817,” *The Astrophysical Journal* **856** no. 2, (Mar, 2018) 101. `https://doi.org/10.3847%2F1538-4357%2Faab095`.

[180] R. Fernández and B. D. Metzger, “Delayed outflows from black hole accretion tori following neutron star binary coalescence,” **435** no. 1, (Oct., 2013) 502–517, `arXiv:1304.6720 [astro-ph.HE]`.

[181] W. H. Lee, E. Ramirez-Ruiz, and D. López-Cámara, "Phase Transitions and He-Synthesis-Driven Winds in Neutrino Cooled Accretion Disks: Prospects for Late Flares in Short Gamma-Ray Bursts," *The Astrophysical Journal Letters* **699** no. 2, (July, 2009) L93–L96, `arXiv:0904.3752 [astro-ph.HE]`.

[182] L. Dessart, C. D. Ott, A. Burrows, *et al.*, "Neutrino Signatures and the Neutrino-Driven Wind in Binary Neutron Star Mergers," **690** no. 2, (Jan., 2009) 1681–1705, `arXiv:0806.4380 [astro-ph]`.

[183] L. Collaboration, "LSST throughputs." `https://github.com/lsst/throughputs/`. Accessed: 2020-04-08.

[184] C. E. Rasmussen and C. K. I. Williams, *Gaussian Processes for Machine Learning*. The MIT Press, 2006.

[185] S. Ambikasaran, D. Foreman-Mackey, L. Greengard, *et al.*, "Fast direct methods for gaussian processes," 2016.

[186] M. J. Williams, J. Veitch, and C. Messenger, "Nested sampling with normalizing flows for gravitational-wave inference," *Physical Review D* **103** no. 10, (May, 2021) . `http://dx.doi.org/10.1103/PhysRevD.103.103006`.

[187] I. Kobyzev, S. D. Prince, and M. A. Brubaker, "Normalizing flows: An introduction and review of current methods," *IEEE Transactions on Pattern Analysis amp; Machine Intelligence* **43** no. 11, (Nov, 2021) 3964–3979.

[188] W. D. Vousden, W. M. Farr, and I. Mandel, "Dynamic temperature selection for parallel tempering in Markov chain Monte Carlo simulations," **455** no. 2, (Jan, 2016) 1919–1937, `arXiv:1501.05823 [astro-ph.IM]`.

[189] D. J. Earl and M. W. Deem, "Parallel tempering: Theory, applications, and new perspectives," *Physical Chemistry Chemical Physics (Incorporating Faraday Transactions)* **7** (2005) 3910, `physics/0508111`.

[190] R. Magee, H. Fong, S. Caudill, *et al.*, "Sub-threshold binary neutron star search in Advanced LIGO's first observing run," *arXiv e-prints* (Jan, 2019) arXiv:1901.09884, `arXiv:1901.09884 [gr-qc]`.

[191] A. Goldstein, R. Hamburg, C. M. Hui, *et al.*, "Updates to the Fermi GBM Targeted Sub-threshold Search in Preparation for the Third Observing Run of LIGO/Virgo," *arXiv e-prints* (Mar, 2019) arXiv:1903.12597, `arXiv:1903.12597 [astro-ph.HE]`.

[192] B. P. Abbott, R. Abbott, T. D. Abbott, *et al.*, "Search for gravitational waves associated with gamma-ray bursts during the first advanced LIGO observing run and implications

for the origin of GRB 150906b," *The Astrophysical Journal* **841** no. 2, (May, 2017) 89. `https://doi.org/10.3847%2F1538-4357%2Faa6c47`.

[193] T. L. S. Collaboration, the Virgo Collaboration, B. P. Abbott, *et al.*, "An optically targeted search for gravitational waves emitted by core-collapse supernovae during the first and second observing runs of advanced ligo and advanced virgo," 2019.

[194] P. Marshall, W. Clarkson, O. Shemmer, *et al.*, "LSST science collaborations observing strategy white paper: "science-driven optimization of the LSST observing strategy"," 2017. `https://zenodo.org/record/842713`.

[195] M. Almualla, S. Anand, M. W. Coughlin, *et al.*, "Optimizing serendipitous detections of kilonovae: cadence and filter selection," *Monthly Notices of the Royal Astronomical Society* **504** no. 2, (04, 2021) 2822–2831. `https://doi.org/10.1093/mnras/stab1090`.

[196] I. Andreoni, M. W. Coughlin, M. Almualla, *et al.*, "Optimizing cadences with realistic light-curve filtering for serendipitous kilonova discovery with vera rubin observatory," *The Astrophysical Journal Supplement Series* **258** no. 1, (Dec, 2021) 5. `https://doi.org/10.3847/1538-4365/ac3bae`.

[197] M. Soares-Santos, D. E. Holz, J. Annis, *et al.*, "The electromagnetic counterpart of the binary neutron star merger LIGO/virgo GW170817. i. discovery of the optical counterpart using the dark energy camera," *The Astrophysical Journal* **848** no. 2, (Oct, 2017) L16. `https://doi.org/10.3847%2F2041-8213%2Faa9059`.

[198] S. Rosswog, U. Feindt, O. Korobkin, *et al.*, "Detectability of compact binary merger macronovae," *Classical and Quantum Gravity* **34** no. 10, (Apr, 2017) 104001. `https://dx.doi.org/10.1088/1361-6382/aa68a9`.

[199] M. Coughlin. Personal communication, Aug, 2019.

[200] D. Scolnic, R. Kessler, D. Brout, *et al.*, "How Many Kilonovae Can Be Found in Past, Present, and Future Survey Data Sets?," *The Astrophysical Journall* **852** (Jan., 2018) L3, `arXiv:1710.05845 [astro-ph.IM]`.

[201] The LSST Dark Energy Science Collaboration, R. Mandelbaum, T. Eifler, *et al.*, "The LSST dark energy science collaboration (desc) science requirements document," 2018. `https://arxiv.org/abs/1809.01669`.

[202] L. Nativi, M. Bulla, S. Rosswog, *et al.*, "Can jets make the radioactively powered emission from neutron star mergers bluer?," *Monthly Notices of the Royal Astronomical Society* **500** no. 2, (Oct, 2020) 1772–1783. `https://doi.org/10.1093%2Fmnras%2Fstaa3337`.

[203] W. Zhang, S. E. Woosley, and A. I. MacFadyen, "Relativistic jets in collapsars," *The Astrophysical Journal* **586** no. 1, (Mar, 2003) 356. `https://dx.doi.org/10.1086/367609`.

[204] A. Mizuta and M. A. Aloy, "Angular energy distribution of collapsar-jets," *The Astrophysical Journal* **699** no. 2, (Jun, 2009) 1261. `https://dx.doi.org/10.1088/0004-637X/699/2/1261`.

[205] A. Mizuta and K. Ioka, "Opening angles of collapsar jets," *The Astrophysical Journal* **777** no. 2, (Oct, 2013) 162. `https://dx.doi.org/10.1088/0004-637X/777/2/162`.

[206] A. Murguia-Berthier, G. Montes, E. Ramirez-Ruiz, *et al.*, "Necessary conditions for short gamma-ray burst production in binary neutron star mergers," *The Astrophysical Journal Letters* **788** no. 1, (May, 2014) L8. `https://dx.doi.org/10.1088/2041-8205/788/1/L8`.

[207] P. C. Duffell, E. Quataert, D. Kasen, and H. Klion, "Jet dynamics in compact object mergers: GW170817 likely had a successful jet," *The Astrophysical Journal* **866** no. 1, (Oct, 2018) 3. `https://doi.org/10.3847%2F1538-4357%2Faae084`.

[208] H. Nagakura, K. Hotokezaka, Y. Sekiguchi, *et al.*, "Jet collimation in the ejecta of double neutron star mergers: A new canonical picture of short gamma-ray bursts," *The Astrophysical Journal Letters* **784** no. 2, (Mar, 2014) L28. `https://dx.doi.org/10.1088/2041-8205/784/2/L28`.

[209] R. Harrison, O. Gottlieb, and E. Nakar, "Numerically calibrated model for propagation of a relativistic unmagnetized jet in dense media," *Monthly Notices of the Royal Astronomical Society* **477** no. 2, (03, 2018) 2128–2140. `https://doi.org/10.1093/mnras/sty760`.

[210] C. S. Kochanek and T. Piran, "Gravitational Waves and gamma -Ray Bursts," *The Astrophysical Journall* **417** (Nov., 1993) L17, `arXiv:astro-ph/9305015 [astro-ph]`.

[211] G. P. Lamb and S. Kobayashi, "GRB 170817A as a jet counterpart to gravitational wave trigger GW 170817," *Monthly Notices of the Royal Astronomical Society* **478** no. 1, (05, 2018) 733–740. `https://doi.org/10.1093/mnras/sty1108`.

[212] E. Berger, "Short-duration gamma-ray bursts," *Annual Review of Astronomy and Astrophysics* **52** no. 1, (2014) 43–105. `https://doi.org/10.1146/annurev-astro-081913-035926`.

[213] A. I. MacFadyen and S. E. Woosley, "Collapsars: Gamma-ray bursts and explosions in "failed supernovae"," *The Astrophysical Journal* **524** no. 1, (Oct, 1999) 262. `https://dx.doi.org/10.1086/307790`.

[214] J. Barnes, P. C. Duffell, Y. Liu, *et al.*, "A GRB and Broad-lined Type Ic Supernova from a Single Central Engine," *The Astrophysical Journal* **860** no. 1, (June, 2018) 38, `arXiv:1708.02630 [astro-ph.HE]`.

[215] D. Lazzati, B. J. Morsony, C. H. Blackwell, and M. C. Begelman, "Unifying the zoo of jet-driven stellar explosions," *The Astrophysical Journal* **750** no. 1, (Apr, 2012) 68. `https://dx.doi.org/10.1088/0004-637X/750/1/68`.

[216] V. Nedora, S. Bernuzzi, D. Radice, *et al.*, "Spiral-wave wind for the blue kilonova," *The Astrophysical Journal* **886** no. 2, (Nov, 2019) L30. `https://doi.org/10.3847%2F2041-8213%2Fab5794`.

[217] K. D. Alexander, E. Berger, W. Fong, *et al.*, "The electromagnetic counterpart of the binary neutron star merger LIGO/virgo GW170817. VI. radio constraints on a relativistic jet and predictions for late-time emission from the kilonova ejecta," *The Astrophysical Journal* **848** no. 2, (Oct, 2017) L21. `https://doi.org/10.3847/2041-8213/aa905d`.

[218] G. Hallinan, A. Corsi, K. P. Mooley, *et al.*, "A radio counterpart to a neutron star merger," *Science* **358** no. 6370, (2017) 1579–1583, `https://www.science.org/doi/pdf/10.1126/science.aap9855`. `https://www.science.org/doi/abs/10.1126/science.aap9855`.

[219] M. Bulla, "POSSIS: predicting spectra, light curves, and polarization for multidimensional models of supernovae and kilonovae," **489** no. 4, (Nov., 2019) 5037–5045, `arXiv:1906.04205 [astro-ph.HE]`.

[220] R. Gray, C. Messenger, and J. Veitch, "A pixelated approach to galaxy catalogue incompleteness: improving the dark siren measurement of the hubble constant," *Monthly Notices of the Royal Astronomical Society* **512** no. 1, (Feb, 2022) 1127–1140. `https://doi.org/10.1093%2Fmnras%2Fstac366`.

[221] B. P. Abbott, R. Abbott, T. D. Abbott, *et al.*, "A gravitational-wave standard siren measurement of the Hubble constant," *Nature* **551** (Oct., 2017) 85–88.

[222] H.-Y. Chen, C.-J. Haster, S. Vitale, *et al.*, "A standard siren cosmological measurement from the potential GW190521 electromagnetic counterpart ZTF19abanrhr," *Monthly Notices of the Royal Astronomical Society* **513** no. 2, (Apr, 2022) 2152–2157. `https://doi.org/10.1093%2Fmnras%2Fstac989`.

[223] S. Mastrogiovanni, K. Leyde, C. Karathanasis, *et al.*, "On the importance of source population models for gravitational-wave cosmology," *Physical Review D* **104** no. 6, (Sep, 2021) . `https://doi.org/10.1103%2Fphysrevd.104.062009`.

[224] R. Gray, I. M. Hernandez, H. Qi, *et al.*, "Cosmological inference using gravitational wave standard sirens: A mock data analysis," *Physical Review D* **101** no. 12, (Jun, 2020) . `https://doi.org/10.1103%2Fphysrevd.101.122001`.

[225] B. P. Abbott, R. Abbott, T. D. Abbott, *et al.*, "A gravitational-wave measurement of the hubble constant following the second observing run of advanced LIGO and virgo," *The Astrophysical Journal* **909** no. 2, (Mar, 2021) 218. `https://doi.org/10.3847%2F1538-4357%2Fabdcb7`.

[226] S. Rauzy, "A simple tool for assessing the completeness in apparent magnitude of magnitude-redshift samples," *Monthly Notices of the Royal Astronomical Society* **324** no. 1, (Jun, 2001) 51–56. `http://dx.doi.org/10.1046/j.1365-8711.2001.04078.x`.

[227] G. Dálya, G. Galgóczi, L. Dobos, *et al.*, "GLADE: A galaxy catalogue for multimessenger searches in the advanced gravitational-wave detector era," *Monthly Notices of the Royal Astronomical Society* **479** no. 2, (Jun, 2018) 2374–2381. `http://dx.doi.org/10.1093/mnras/sty1703`.

[228] G. Dálya, R. Díaz, F. R. Bouchet, *et al.*, "Glade+: An extended galaxy catalogue for multimessenger searches with advanced gravitational-wave detectors," 2021.

[229] A. Drlica-Wagner, I. Sevilla-Noarbe, E. S. Rykoff, *et al.*, "Dark energy survey year 1 results: The photometric data set for cosmology," *The Astrophysical Journal Supplement Series* **235** no. 2, (Apr, 2018) 33. `https://doi.org/10.3847/1538-4365/aab4f5`.

[230] T. M. C. Abbott, F. B. Abdalla, S. Allam, *et al.*, "The dark energy survey: Data release 1," *The Astrophysical Journal Supplement Series* **239** no. 2, (Nov, 2018) 18. `https://doi.org/10.3847/1538-4365/aae9f0`.

[231] **LIGO Scientific Collaboration and Virgo Collaboration** Collaboration, B. P. Abbott, R. Abbott, T. D. Abbott, *et al.*, "Gw170814: A three-detector observation of gravitational waves from a binary black hole coalescence," *Phys. Rev. Lett.* **119** (Oct, 2017) 141101. `https://link.aps.org/doi/10.1103/PhysRevLett.119.141101`.

[232] Z. Doctor, R. Kessler, K. Herner, *et al.*, "A search for optical emission from binary black hole merger gw170814 with the dark energy camera," *The Astrophysical Journal Letters*

873 no. 2, (Mar, 2019) L24.
https://dx.doi.org/10.3847/2041-8213/ab08a3.

[233] A. Finke, S. Foffa, F. Iacovelli, *et al.*, "Cosmology with LIGO/virgo dark sirens: Hubble parameter and modified gravitational wave propagation," *Journal of Cosmology and Astroparticle Physics* **2021** no. 08, (Aug, 2021) 026.
https://doi.org/10.1088/1475-7516/2021/08/026.

[234] K. M. Gorski, E. Hivon, A. J. Banday, *et al.*, "HEALPix: A framework for high-resolution discretization and fast analysis of data distributed on the sphere," *The Astrophysical Journal* **622** no. 2, (Apr, 2005) 759–771.
https://doi.org/10.1086/427976.

[235] B. Efron and V. Petrosian, "A Simple Test of Independence for Truncated Data with Applications to Redshift Surveys," *The Astrophysical Journal* **399** (Nov., 1992) 345.

[236] R. Gray, *Gravitational Wave Cosmology: measuring the Hubble constant with dark standard sirens*. PhD thesis, University of Glasgow, 2021.

[237] A. Zonca, L. Singer, D. Lenz, *et al.*, "healpy: equal area pixelization and spherical harmonics transforms for data on the sphere in Python," *The Journal of Open Source Software* **4** no. 35, (Mar., 2019) 1298.

[238] **LIGO Scientific Collaboration and Virgo Collaboration** Collaboration, B. P. Abbott *et al.*, "Gw190425: Observation of a compact binary coalescence with total mass $\sim$3.4 m$_\odot$," *The Astrophysical Journal* **892** no. 1, (Mar, 2020) L3.
http://dx.doi.org/10.3847/2041-8213/ab75f5.

[239] R. Abbott, T. D. Abbott, S. Abraham, *et al.*, "Observation of gravitational waves from two neutron star–black hole coalescences," *The Astrophysical Journal Letters* **915** no. 1, (Jun, 2021) L5. https://dx.doi.org/10.3847/2041-8213/ac082e.

[240] R. Abbott, T. D. Abbott, S. Abraham, *et al.*, "Gw190814: Gravitational waves from the coalescence of a 23 solar mass black hole with a 2.6 solar mass compact object," *The Astrophysical Journal Letters* **896** no. 2, (Jun, 2020) L44.
https://dx.doi.org/10.3847/2041-8213/ab960f.

[241] M. P. Ross, T. Mistry, L. Datrier, *et al.*, "Initial results from the LIGO newtonian calibrator," Oct, 2021.
https://link.aps.org/doi/10.1103/PhysRevD.104.082006.

[242] L. Datrier, J. Kissel, T. Mistry, and M. Ross, "Review of NCAL analytic force estimates, mathematical details," *LIGO DCC* (2020) .
https://dcc.ligo.org/LIGO-T2000238/public.

[243] S. Vitale, C.-J. Haster, L. Sun, *et al.*, "Physical approach to the marginalization of LIGO calibration uncertainties," *Physical Review D* **103** no. 6, (2021) 063016. `https://doi.org/10.1103/PhysRevD.103.063016`.

[244] E. Payne, C. Talbot, P. D. Lasky, *et al.*, "Gravitational-wave astronomy with a physical calibration model," *Physical Review D* **102** no. 12, (2020) 122004. `https://doi.org/10.1103/PhysRevD.102.122004`.

[245] S. Karki, D. Tuyenbayev, S. Kandhasamy, *et al.*, "The Advanced LIGO photon calibrators," *Review of Scientific Instruments* **87** no. 11, (2016) 114503. `https://doi.org/10.1063/1.4967303`.

[246] T. Sadecki, R. Savage, and D. Tuyenbayev, "Photon Calibrator Gold Standard NIST calibration," *LIGO DCC* (2018) . `https://dcc.ligo.org/LIGO-T1800104/public`.

[247] D. Estevez, P. Lagabbe, A. Masserot, *et al.*, "The advanced virgo photon calibrators," *Classical and Quantum Gravity* **38** no. 7, (2021) 075007. `https://iopscience.iop.org/article/10.1088/1361-6382/abe2db`.

[248] T. Akutsu, M. Ando, K. Arai, *et al.*, "Overview of KAGRA: Calibration, detector characterization, physical environmental monitors, and the geophysics interferometer," *Progress of Theoretical and Experimental Physics* **2021** no. 5, (02, 2021) . `https://doi.org/10.1093/ptep/ptab018`. 05A102.

[249] S. Hild, M. Brinkmann, K. Danzmann, *et al.*, "Photon-pressure-induced test mass deformation in gravitational-wave detectors," *Classical and Quantum Gravity* **24** no. 22, (Nov, 2007) 5681–5688. `https://doi.org/10.1088%2F0264-9381%2F24%2F22%2F025`.

[250] H. P. Daveloza, M. A. Badhan, M. Diaz, *et al.*, "Controlling calibration errors in gravitational-wave detectors by precise location of calibration forces," *Journal of Physics: Conference Series* **363** no. 1, (Jun, 2012) 012007. `https://dx.doi.org/10.1088/1742-6596/363/1/012007`.

[251] Y. Inoue, S. Haino, N. Kanda, *et al.*, "Improving the absolute accuracy of the gravitational wave detectors by combining the photon pressure and gravity field calibrators," *Phys. Rev. D* **98** (Jul, 2018) 022005. `https://link.aps.org/doi/10.1103/PhysRevD.98.022005`.

[252] D. Estevez, B. Lieunard, F. Marion, *et al.*, "First tests of a newtonian calibrator on an interferometric gravitational wave detector," *Classical and Quantum Gravity* **35** no. 23, (Nov, 2018) 235009. `https://doi.org/10.1088%2F1361-6382%2Faae95f`.

[253] D. Estevez, B. Mours, and T. Pradier, “Newtonian calibrator tests during the virgo o3 data taking,” *Classical and Quantum Gravity* (2021) . `https://iopscience.iop.org/article/10.1088/1361-6382/abe2da`.

[254] L. Matone, P. Raffai, S. Márka, *et al.*, “Benefits of artificially generated gravity gradients for interferometric gravitational-wave detectors,” *Classical and Quantum Gravity* **24** no. 9, (Apr, 2007) 2217–2229. `https://doi.org/10.1088/0264-9381/24/9/005`.

[255] T.Mistry, M.Ross, L.Datrier, *et al.*, “Ncal prototype h1 surveying distance measurement,” *LIGO DCC* (2021) . `https://dcc.ligo.org/LIGO-T2000417/public`.

[256] C. A. Hagedorn, *A Sub-Millimeter Parallel-Plate Test of Gravity*. PhD thesis, University of Washington, Jan., 2015.

[257] C. Hagedorn and J. Lee, “Newt (newtonian eot-wash toolkit),” *GitHub* (2021) . `https://github.com/4kbt/NewtonianEotWashToolkit`.

[258] J. Stirling, “Multipole calculation of gravitational forces,” *Phys. Rev. D* **95** (Jun, 2017) 124059. `https://link.aps.org/doi/10.1103/PhysRevD.95.124059`.

[259] J. Stirling and S. Schlamminger, “Closed form expressions for gravitational multipole moments of elementary solids,” *Physical Review D* **100** no. 12, (2019) 124053. `https://journals.aps.org/prd/abstract/10.1103/PhysRevD.100.124053`.

[260] N. A. C. E G Adelberger and C. D. Hoyle, “Analytic expressions for gravitational inner multipole moments of elementary solids and for the force between two rectangular solids,” *Classical and Quantum Gravity* **23** no. 17, (Aug, 2006) 5463–5464. `https://doi.org/10.1088%2F0264-9381%2F23%2F17%2Fc02`.

[261] C. Trenkel and C. C. Speake, “Interaction potential between extended bodies,” *Phys. Rev. D* **60** (Oct, 1999) 107501. `https://link.aps.org/doi/10.1103/PhysRevD.60.107501`.

[262] C. D’Urso and E. G. Adelberger, “Translation of multipoles for a $1/r$ potential,” *Phys. Rev. D* **55** (Jun, 1997) 7970–7972. `https://link.aps.org/doi/10.1103/PhysRevD.55.7970`.

[263] M.P.Ross, J. Kissel, L. Datrier, and T. Mistry, “Ncal least-squares spectral analysis,” *LIGO DCC* (2021) . `https://dcc.ligo.org/LIGO-T2100103/public`.

[264] Y. Huang, H.-Y. Chen, C.-J. Haster, *et al.*, "Impact of calibration uncertainties on hubble constant measurements from gravitational-wave sources," 2022. `https://arxiv.org/abs/2204.03614`.

[265] L. Datrier and S. Dwyer, "H1 down time due to wind," 2019. `https://alog.ligo-wa.caltech.edu/aLOG/index.php?callRep=49542`.

[266] L. Datrier and S. Dwyer, "Impact of wind on duty cycle and bns range for o3," 2019. `https://alog.ligo-wa.caltech.edu/aLOG/index.php?callRep=49682`.

[267] L. Datrier and S. Dwyer, "BNS range and duty cycle if wind-independent for O3," 2019. `https://alog.ligo-wa.caltech.edu/aLOG/index.php?callRep=50072`.

[268] D. Davis, J. S. Areeda, B. K. Berger, *et al.*, "LIGO detector characterization in the second and third observing runs," *Classical and Quantum Gravity* **38** no. 13, (Jun, 2021) 135014. `https://doi.org/10.1088%2F1361-6382%2Fabfd85`.